

# The legacy of the experimental hadron physics programme at COSY

C. Wilkin <sup>a</sup>

Physics and Astronomy Department, UCL, Gower Street, London, WC1E 6BT, UK

Received: May 26, 2022/ Revised version:

**Abstract.** The experimental hadronic physics programme at the COoler SYnchrotron of the Forschungszentrum Jülich terminated at the end of 2014. After describing the accelerator and the associated facilities, a review is presented of the major achievements in the field realized over the twenty years of intense research activity.

**PACS.** 13.75.-n Hadron-induced low- and intermediate-energy reactions and scattering (energy  $\leq 10$  GeV)

## Contents

1	Introduction . . . . .	2	4.3.3	Comparison of $pp \rightarrow pn\pi^+$ and $pp \rightarrow d\pi^+$	34
2	Facilities . . . . .	3	4.4	$\eta$ production in proton-proton collisions . . . . .	34
2.1	The COSY machine . . . . .	3	4.5	$\eta$ production in proton-neutron collisions . . . . .	36
2.2	Principal installations . . . . .	3	4.6	$\omega$ production in proton-proton scattering . . . . .	37
2.2.1	The COSY-11 spectrometer . . . . .	3	4.7	$\eta'$ production in proton-proton scattering . . . . .	38
2.2.2	The ANKE spectrometer . . . . .	4	5	Two-pion production in nucleon-nucleon collisions . . . . .	39
2.2.3	The WASA detector . . . . .	5	5.1	Two-pion production in proton-proton collisions	39
2.2.4	The Time-of-Flight detector . . . . .	6	5.2	Two-pion production in neutron-proton collisions	41
2.2.5	The Big Karl spectrometer . . . . .	7	6	Inclusive strangeness production . . . . .	43
2.2.6	The GEM detector . . . . .	8	6.1	The $pp \rightarrow K^+ X^+$ reaction . . . . .	43
2.2.7	The MOMO detector . . . . .	8	6.2	Hypernuclei lifetime measurements . . . . .	44
2.2.8	The ENSTAR detector . . . . .	9	6.3	Inclusive $K^+$ production on nuclei . . . . .	44
2.2.9	The EDDA detector . . . . .	9	7	Hyperon production . . . . .	45
2.3	Targets and equipment . . . . .	10	7.1	The $pp \rightarrow K^+ p\Lambda$ and $pp \rightarrow K^+ p\Sigma^0$ reactions . . . . .	45
2.3.1	The Atomic Beam Source . . . . .	10	7.2	Differential distributions . . . . .	47
2.3.2	Polarized gas cell targets . . . . .	11	7.3	Polarization and the $\Lambda p$ scattering length . . . . .	49
2.3.3	Silicon Tracking Telescopes . . . . .	12	7.4	The $\Lambda : \Sigma$ cusp effect . . . . .	50
2.3.4	The KOALA detector . . . . .	13	7.5	$pp \rightarrow K^+ n\Sigma^+$ . . . . .	51
2.4	Technical experiments . . . . .	13	7.6	$pp \rightarrow K^0 p\Sigma^+$ . . . . .	52
2.4.1	Determination of beam-target luminosity	14	7.7	The production of heavy hyperons . . . . .	53
2.4.2	Precision determination of beam momentum . . . . .	15	7.8	Pentaquarks . . . . .	54
2.4.3	Spin-filtering experiments . . . . .	16	7.9	Hyperon production in proton-neutron collisions	55
3	Nucleon-nucleon elastic scattering . . . . .	16	8	Kaon pair production . . . . .	56
3.1	Proton-proton elastic scattering . . . . .	16	8.1	Kaon pair production in nucleon-nucleon collisions	56
3.2	Neutron-proton elastic scattering . . . . .	22	8.2	$pp \rightarrow pp\phi$ and $pn \rightarrow d\phi$ reactions . . . . .	59
4	Single non-strange meson production in nucleon-nucleon collisions . . . . .	26	8.3	$pA \rightarrow K^+ K^- X$ and $pA \rightarrow \phi X$ . . . . .	60
4.1	Phenomenological description . . . . .	26	9	The $pd \rightarrow {}^3\text{He} X ({}^3\text{H} X')$ family of reactions . . . . .	61
4.2	Hard bremsstrahlung in proton-proton scattering	27	9.1	$pd \rightarrow {}^3\text{He} \pi^0$ and $pd \rightarrow {}^3\text{H} \pi^+$ . . . . .	61
4.3	Single pion production in nucleon-nucleon collisions . . . . .	29	9.2	$pd \rightarrow {}^3\text{He} \eta$ . . . . .	63
4.3.1	The $pp \rightarrow d\pi^+$ reaction . . . . .	30	9.2.1	Measurements of the mass of the $\eta$ meson	66
4.3.2	Partial wave analysis of the $NN \rightarrow \{pp\}_s \pi$ reaction . . . . .	32	9.3	The $pd \rightarrow {}^3\text{He} \pi^+ \pi^-$ reaction . . . . .	67
			9.4	The $pd \rightarrow {}^3\text{He} K^+ K^- (\phi)$ reactions . . . . .	69
			10	The $dd \rightarrow {}^4\text{He} X^0$ family of reactions . . . . .	71
			10.1	The $dd \rightarrow {}^4\text{He} \eta$ reaction . . . . .	71
			10.2	The $dd \rightarrow {}^4\text{He} \pi^0$ reaction and charge symmetry	72
			11	Rare decays of $\eta$ and $\pi^0$ mesons . . . . .	73
			11.1	$\eta$ decays . . . . .	74
			11.2	Dark photons . . . . .	75

<sup>a</sup> Email: c.wilkin@ucl.ac.uk

12 Conclusions . . . . .	76
References . . . . .	80

## 1 Introduction

At the end of 2014 the experimental priorities of the Institut für Kernphysik (IKP) Jülich switched from the study of hadronic reactions to precision measurements that are more in keeping with current particle physics. Since many interesting results had been found in the field of hadronic physics over the twenty years of operation of the laboratory’s COoler SYnchrotron COSY, it is clearly appropriate to try to describe some of these phenomena in the form of a review article.

Much of the programme at COSY was influenced by that of the SATURNE machine at the Saclay laboratory but, though the machines had similar maximum proton or deuteron beam energies, the accelerators had very different characteristics and so, before describing the physics programme at COSY, it is necessary to discuss in some detail the machine and the associated facilities that were available for experiments. The main difference is, of course, that COSY acts as a storage ring so that the various detectors described in sect. 2 are divided between those used for experiments inside the ring and those designed for use at external target stations. In contrast, SATURNE concentrated on the development of a whole series of state-of-the-art magnetic spectrometers for use at external beam lines.

The review is not intended merely to provide a synthesis of IKP Annual Reports but rather it hopefully gives a critical evaluation, while trying to make links between experiments carried out using some of the different facilities available around COSY or, indeed, at other laboratories. For this reason it was decided that the review should be prepared by a single person rather than follow the practice of the multi-author volume that described in 1998 the legacy of the SATURNE programme [1].

It is certainly impossible or even undesirable in this review to go into the details of all the several hundred research papers that have emerged from COSY over twenty years. In all cases of interest the reader is advised to go back to the original sources where, for example, systematic uncertainties and limitations or approximations are discussed at length. Since the aim is to present the COSY experimental programme, we have been rather cavalier in the discussion of the theoretical motivation for an experiment or its analysis. In general, in order to keep the length under control, we have confined ourselves to presenting only the phenomenology required to understand the experimental results at a rather basic level.

This review is concerned with the hadronic physics programme at COSY and so it omits any discussion of the extensive studies of spallation and nuclear breakup studies carried out by the Nessi [2], Jessica [3], and PISA [4] collaborations, especially in the first few years of COSY. The results in these early stages are summarized by an internal report in 2003 “10 years of COSY” and this shows the dominance of the experiments that were launched quickly,

most notably COSY-11. In contrast, only simple experiments from ANKE were described and, of course, WASA had not even arrived in Jülich by then. There were, of course, conference proceedings, such as those of Refs. [5, 6], but these only gave partial snapshots of the research that was current at the time. This review aims to present a more balanced picture over the twenty years. Also omitted is any description of tests of equipment for use at other facilities, in particular the extensive developments for the PANDA detector at the future FAIR complex.

In the space available, the brief descriptions of the machine and the facilities available at COSY are necessarily incomplete and biased. Thus there is no serious discussion of pellet or cluster-jet targets but, in contrast, space is devoted to the polarized targets that allow many refined experiments to be carried out at internal target stations. Technical experiments are then discussed which show, for example, how the beam momentum and the luminosity can be determined in a storage ring environment. Though by themselves not giving immediate hadronic physics results, they facilitated such experiments and are potentially important elements in the future precision physics programme at COSY.

The subsequent sections deal with the COSY experiments in the order given in the Table of Contents but it must be remembered that the final analysis of an experiment may come several years after the data had been taken. In one, hopefully extreme, example a paper was submitted for publication in 2015 based upon data that were taken at COSY seven years earlier. Hence some of the unpublished results presented in this review must be considered as being *preliminary*. Only results available by October 1<sup>st</sup> 2016 will be reported on, though some analyses currently being worked on might be indicated.

Although the hadronic physics programme has finished at COSY, the machine itself lives on as the basis for a challenging programme of precision physics. The most important element here is its use in putting constraints on the electric dipole moments of the deuteron and proton. The results obtained at COSY will be vital for the design of a dedicated ring that will lower the limits even further and possibly even find non-zero values. The TRIC experiment will search for the violation of time-reversal invariance in proton-deuteron collisions. It would therefore be remiss if we did not describe some of these exciting developments for the future, and this we do in the Conclusions.

Since we are interested in the “legacy of the experimental hadron physics programme at COSY”, in the Conclusions we also try to pick out ten experiments that we presently believe will have an influence on the field long after the termination of the hadron physics programme at COSY. This is necessarily a very speculative choice and we invite the readers to draw up their own lists of alternative experiments.

## 2 Facilities

### 2.1 The COSY machine

The first detailed description of the COoler SYnchrotron and storage ring COSY is almost twenty years old [7] but, despite several modifications, the underlying structure remains the same. The machine, which is capable of accelerating polarized or unpolarized protons or deuterons up to momenta of about 3700 MeV/c, is equipped with both electron cooling and stochastic cooling to provide quality beams.

A sketch of the overall layout of the facility is given in Fig. 1. This shows the 100 m long transfer beam line from the injector isochronous cyclotron to the ring and the cooler synchrotron itself, which has a circumference of about 184 m. This racetrack is made up of two arcs, each 52 m long, and two 40 m straight sections, where some of the larger experimental equipments are installed. In addition to the experimental detectors indicated<sup>1</sup>, the ring also contains accelerator-specific components, such as the accelerating *rf*-cavity, the electron cooler, scrapers, the stochastic pick-up and kicker tanks, Schottky pick-ups, and beam current monitors. There are also three extracted beam lines serving external experimental areas.

COSY has two ion sources, one for polarized and another for unpolarized beams, each of which yields H<sup>-</sup> and D<sup>-</sup> ion beams. By using different combinations of the *rf* transitions in the source, it is possible to produce deuteron beams with different mixtures of vector and tensor polarizations [8,9]. Unlike the SATURNE accelerator, no attempt was made to create beams of heavier nuclei, such as <sup>4</sup>He or <sup>6</sup>Li. The ions are pre-accelerated in the cyclotron JULIC, up to 295 MeV/c for H<sup>-</sup> and 539 MeV/c for D<sup>-</sup>, before being injected into the storage ring via charge exchange, using a carbon foil stripper. The low energy polarimeter in the injection line, which uses a carbon target, can determine the proton and deuteron vector polarizations but is insensitive to the deuteron tensor polarization.

Two different cooling techniques to shrink the beam phase space are implemented at COSY. Electron cooling [10]<sup>2</sup> is successful up to momenta of 600 MeV/c and this is complemented by a stochastic cooling system that covers the upper momentum range from 1.5 GeV/c to 3.3 GeV/c [11]. These cooling techniques significantly reduce the momentum spread of the COSY beam, such that a momentum resolution down to  $\Delta p/p = 10^{-3} - 10^{-5}$  has been achieved. The space charge limit on the number of stored protons or deuterons in the ring is about  $2 \times 10^{11}$  and, by using stacking injection, values as high as  $6 \times 10^{10}$  have been obtained in practice. Since the beam revolution frequency is of order 1 MHz, this would correspond to close to  $10^{17}$  particles per second passing an internal target.

<sup>1</sup> The PISA, Jessica, and Nessi (situated after TOF) detectors were used purely for nuclear reaction studies and will not be discussed in this review.

<sup>2</sup> A more powerful electron cooler is now installed at COSY but this was not available for the hadron physics programme described in this review.

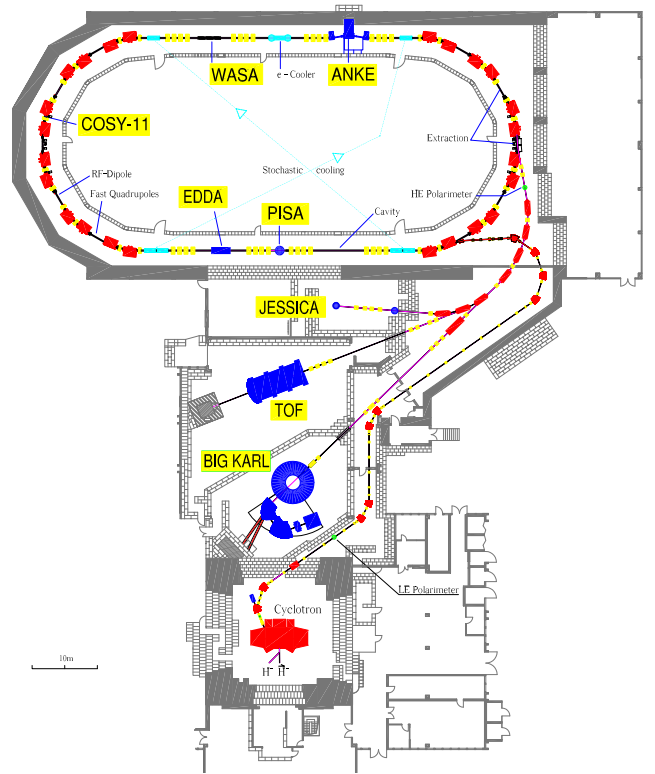


**Fig. 1.** Floor plan of the COSY facility, showing the injection cyclotron JULIC and the principal internal and external detectors. The PISA, Jessica, and Nessi (situated after TOF) detectors were used purely for nuclear reaction studies and will not be discussed in this review. The PISA location is now used for the PAX detector and the TRIC experiment that is discussed in sect. 12.

In a strong-focusing synchrotron, such as COSY, intrinsic or imperfection resonances can lead to losses of polarization of a proton beam during acceleration. In order to compensate for these effects, adiabatic spin-flip has been used to overcome the imperfection resonances and tune-jumping to deal with the intrinsic ones [12]. The situation is much simpler for deuteron beams since, because of the much smaller gyromagnetic anomaly, there are no resonances for deuterons throughout the whole of the COSY momentum range.

Both resonant (slow) and stochastic extraction have been used at COSY to populate the beam lines that serve the external experimental areas, whose locations are shown in Fig. 1. The maximum extracted proton beam momentum achieved was 3300 MeV/c, which is somewhat below the maximum circulating momentum of 3700 MeV/c.

### 2.2 Principal installations

#### 2.2.1 The COSY-11 spectrometer

COSY-11 [13] was one of the simpler facilities to be implemented at COSY and this allowed the collaboration

to carry out quite rapidly many near-threshold measurements. Its brilliant simplicity was that it used one of the existing dipoles of the COSY ring as an analyzing magnet of a spectrometer. Although this idea was also exploited at the CELSIUS storage ring [14, 15], the COSY-11 installation was far more ambitious.

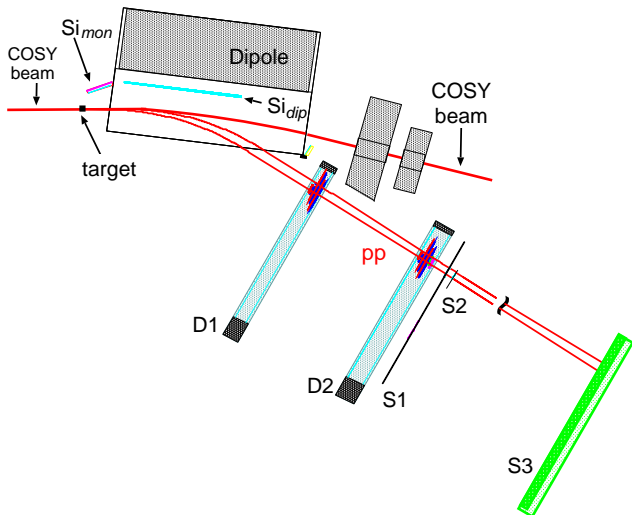


**Fig. 2.** Schematic view of the COSY-11 facility, as used for the measurement of the  $pp \rightarrow ppX^0$  reactions near threshold [16]. The proton trajectories are measured by means of hits in two sets of drift chambers D1 and D2. The scintillation hodoscopes S1 and S2 are used as start detectors and S3 as the corresponding stop detector for time-of-flight measurements. Si<sub>mon</sub> is a silicon pad monitor detector that is used to measure the recoil proton from  $pp$  elastic scattering for the normalization of cross sections and the calibration of the detection system. Si<sub>dip</sub> could be used to detect negatively charged particles.

The position of the detector inside COSY, which is shown in Fig. 1, is in a bending section of the ring in a dispersive region, so that the effective beam momentum spread *seen* by the target is much reduced. The basic principles of the facility are illustrated for the most straightforward  $pp \rightarrow ppX^0$  reaction [16] in Fig. 2. This shows the location of the hydrogen cluster target which, crucially, perturbs very little the circulating COSY beam. Due to their lower momenta, the two outgoing protons from a meson production reaction are separated from the beam in the magnetic field of the C-shaped dipole and are bent towards the centre of the COSY ring, where they can be seen by the COSY-11 detectors.

The proton trajectories are measured by means of hits in a set of two drift chambers (marked D1 and D2 in Fig. 2), which allow the momenta to be determined by ray tracing back through the precisely known magnetic field to the target position. Identification of the particles as protons is ensured by measuring also the times of flight over a distance of  $\approx 9.4$  m between the start and stop scintillator hodoscopes (S1 and S3). The neutral mesons,  $X^0 = \eta$  or  $\eta'$ , are not registered directly but are identified

by peaks in the missing-mass distributions. The isolation of these peaks is helped by looking at background data taken just below the threshold for the production of that meson. The geometrical acceptance of the COSY-11 detection system is limited, especially in the vertical direction, due to the narrow opening of the dipole gap with an internal height of 60 mm.

The beam and target parameters could be monitored and the cross sections normalized by measuring proton-proton elastic scattering in parallel [17]. This was achieved with the help of the silicon pad monitor detector Si<sub>mon</sub>, which measured the recoil proton.

Close to threshold the two protons from the  $pp \rightarrow pp\eta$  reaction must emerge with very similar momenta aligned close to the beam direction. In this case the geometric acceptance of COSY-11 is high but it falls quickly with increasing excess energy. It must be stressed that, unlike detectors such as WASA or Big Karl, where there is a hole that allows the passage of the beam, the COSY-11 coverage is essentially the highest near the forward direction. The detector is therefore well adapted to making measurements near threshold.

For other reactions involving three-body final states, such as  $K^+pA/K^+p\Sigma^0$ , the proton and kaon are registered in D1/D2 and S1/S2 and the hyperon isolated using the missing-mass method.

Though for certain experiments the facility was expanded by, for example, the addition of a neutron wall, COSY-11 was most successful when it was kept (comparatively) *simple* and the collaboration had a remarkable record in the measurement of near-threshold meson production that will be discussed in later sections

### 2.2.2 The ANKE spectrometer

The motivations for the COSY-11 and ANKE spectrometers have much in common since they were both designed as Zero Degree Facilities or, more accurately, as small angle facilities. However, in contrast to COSY-11, whose development was “straightforward”, ANKE has evolved into possibly the most complex detector at COSY. The basic design is described in Ref. [18] and the final layout shown in Fig. 3 allows much more space than is available at COSY-11.

As shown in Fig. 1, ANKE is placed in one of the two straight sections of COSY which means that, unlike COSY-11, it requires its own dedicated analyzing magnet. ANKE’s basic structure is built around three dipoles. D1 deflects the circulating COSY beam through an angle  $\alpha$  onto the target. A spectrometer dipole magnet D2, is used to analyze the momentum of the reaction products that originate from a beam-target interaction. D2 deflects the residual beam by an angle  $-2\alpha$ , which is then compensated by D3, which returns the beam back to the nominal orbit. For each value of  $\alpha$ , which is chosen optimally for a given experiment, D2 has to be moved perpendicularly to the COSY straight section and, for this purpose, D2 is installed on rails. The whole system thus forms a kind of chicane in the COSY racetrack.

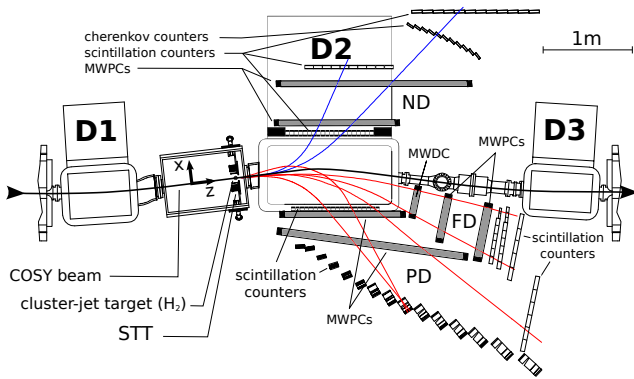


**Fig. 3.** The ANKE spectrometer setup [18], showing the positions of the three dipole magnets (D1,D2,D3), the hydrogen cluster-jet target, the Silicon Tracking Telescope (STT), and the Positive (PD), Negative (ND), and Forward (FD) detectors.

Although Fig. 3 indicates a  $H_2$  cluster-jet target, which may also be  $D_2$ , one can alternatively use a strip target, where the beam is steered onto it after injection and acceleration. For experiments requiring single- and double-polarization, there is also space in the ANKE target chamber for a polarized storage-cell gas target fed by an atomic beam source, which are discussed in sects. 2.3.2 and 2.3.1, respectively.

The silicon tracking telescopes (STT), described in sect. 2.3.3, which can be placed in the target chamber, are particularly helpful in ensuring some left-right symmetry and also in defining the vertex when using a storage cell.

The ANKE detection system consists of three distinct parts, viz.

- The forward detector (FD) measures high momentum particles.  $0.8 < p < 3.7$  GeV/ $c$ , close to the COSY beam orbit.
- The positive detector (PD) measures positive projectiles with  $0.3 < p < 0.8$  GeV/ $c$  and covers much larger angles than the FD.
- The negative detector (ND), which is located partially inside the D2 magnet frame, is used to measure negatively charged pions and kaons. Its momentum coverage is similar to that of the PD.

All three systems employ multiwire proportional chambers for track reconstruction and plastic scintillator counters to obtain time information.

In concept the forward detector is very similar to that used at COSY-11, being optimized to measure charged particles emitted near the forward direction, using tracking and time-of-flight information. Its angular acceptance is about  $12^\circ$  in the horizontal plane but only about  $3.5^\circ$  in the vertical.

Especially mention should be made of the 15 focal-surface telescopes placed after the PD, that are used to unambiguously identify  $K^+$ . Each of these telescopes is made up of a stop counter, an energy-loss counter, a delayed-veto counter, and two passive degraders chosen such that a  $K^+$  stops either at the edge of the first or in the second

degrader. The products from the  $K^+$  decay are registered in the delayed-veto counter, with the characteristic decay time of 12.4 ns. The delayed veto criterion leads to a suppression of better than  $10^{-5}$  in the non-kaon background for both inclusive and coincidence measurements [19].

### 2.2.3 The WASA detector

In its first decade of its operation, COSY was only equipped with detectors for charged particles. Although eventually some of the facilities, such as COSY-11 or TOF, were enhanced through the addition of neutron walls, no effort was made to construct a detector for photons or electrons. However this changed when it was realized in about 2002 that the already operational WASA detector would soon become available.

WASA was installed at the CELSIUS (Uppsala) storage ring and it was originally designed for the study of rare  $\pi^0$  decays but its remit was extended to look for the more interesting  $\eta$  decays. The operation of the detector at CELSIUS is described in Ref. [20]. Following the closure of the CELSIUS ring in 2004, the detector was transferred to Jülich and installed in the COSY ring. As envisaged in the WASA proposal [21], the much higher maximum proton energy available at COSY (2.9 GeV) compared to CELSIUS (1.4 GeV) meant that major upgrades were needed, especially in the forward detector. but also in the read-out system, to allow heavier mesons, such as the  $\eta'$ , to be studied. An up-to-date description of experiments using this detector is to be found in Ref. [22].

The forward detector of the WASA spectrometer is designed to measure hadronic ejectiles and the central detector to measure light mesons or their decay products. A cross-sectional view of the apparatus is shown in Fig. 4. The forward detector, which registers particles emitted with polar angles from about  $3^\circ$  to  $18^\circ$ , consists of an arrangement of thin and thick plastic scintillators and drift chambers covering the full azimuthal angle. Thick scintillators in the forward range hodoscope (FRH) are designed to measure energy loss via ionization. Thin scintillator layers in the forward window counter (FWC) and forward trigger hodoscope (FTH) provide precise timing information. The kinetic energy and the particle type can be determined from the pattern of energy deposits in the thin and thick scintillator layers. A proportional chamber system (FPC) consists of eight layers, each with 260 aluminized Mylar straws. Layers of the forward detector beyond the first layer of the FRH included the Forward Range Interleaving Hodoscope (FRI) detector and the Forward Veto Hodoscope (FVH). The kinetic energy  $T$  of a proton from say a  $pp \rightarrow pp\eta$  reaction can be reconstructed with a resolution of  $\sigma(T)/T \sim 1.5 - 3\%$  for  $T < 400$  MeV.

The central detector, which is designed to measure photons, electrons, and charged pions, is surrounded by a CsI(Na) electromagnetic calorimeter with 1012 elements (SEC). Contained within the calorimeter is a superconducting solenoid providing a uniform 1 T magnetic field in the space directly surrounding the interaction region. Charged particle tracking is provided by the mini drift

chamber (MDC), which is surrounded by an 8 mm thick plastic scintillator barrel (PSB) that provides precise timing and particle identification. The MDC consists of 4, 6, and 8 mm diameter straw tubes arranged in 17 layers that are alternately axial or skewed by  $+3^\circ$  or  $-3^\circ$  relative to the beam axis in order to provide three-dimensional tracking. An iron return yoke, shown in red in Fig. 4, surrounds the central detector and shields the photomultiplier tubes of the SEC from the magnetic field. As suggested in the figure, the polar angle range is from  $20^\circ$  to  $169^\circ$ , which represents about 96% of the geometrical acceptance. The energy resolution of the calorimeter is  $\sigma(E)/E \approx 5\%/\sqrt{E[\text{GeV}]}$ .

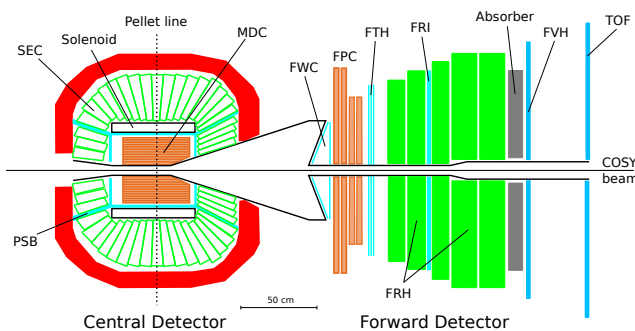


**Fig. 4.** A cross-sectional diagram of the WASA detector [21], with the beam coming from the left. Hadronic ejectiles are measured with the forward detector on the right while meson decay products are measured with the central detector on the left. The individual components are described in the text.

The WASA facility is equipped with an internal target, where frozen pellets of hydrogen or deuterium are injected at rates of several thousand per second [23] perpendicular to the COSY beam, as indicated in Fig. 4. The pellets have typical diameters of the order of  $30 \mu\text{m}$ , which provide a target density on the order of  $10^{15}$  atoms/cm<sup>2</sup>. Smaller pellets might be desirable but there is then the danger of blocking the nozzle producing the pellets. Though vacuum pumps are positioned as closely as possible to the interaction region, a certain amount of residual gas is present in the region around the target due to the evaporation of pellets. In tests with a deuterium target,  $pd \rightarrow {}^3\text{He} \pi^+ \pi^-$  events were selected and the vertex determined from the pion tracks [22]. Over 90% of these events originated within one centimetre of the centre of the interaction region.

In a reaction such as  $pp \rightarrow pp\eta$ , the two recoil protons are measured in the forward detector and this allows the  $\eta$  to be selected via the missing mass in the reaction. The  $\eta$  decay products are then measured in the central detector. Although this is the only facility at COSY that is capable of such measurements, it must be realized that, in the absence of a magnetic spectrometer, the missing-mass resolution is not optimal and that this might lead to extra background, depending upon the particular experiment.

## 2.2.4 The Time-of-Flight detector

Most of the spectrometers used at COSY rely on the analysis of trajectories in a magnetic field. In contrast, the COSY-TOF spectrometer is based on the measurements of the velocity vectors of all the charged products by combining the hit positions in various detectors together with very careful time-of-flight determinations [24]. The identification of the final particles is then achieved through the study of what reaction could produce such a velocity distribution at that particular energy and then optimizing through a kinematic fitting procedure.

Some of the most important advances achieved through the use of TOF have been in the field of strangeness production, where the delayed decays of neutral particles can lead to very characteristic patterns. Thus, in the reaction  $pp \rightarrow K^+ p \Lambda$ , there may initially be only two tracks, corresponding to the charged particles  $K^+$  and  $p$  but, after the decay  $\Lambda \rightarrow p \pi^-$ , four charged tracks can be seen in TOF. The design of COSY-TOF was certainly influenced by the experience gained with the PS185 spectrometer used at the CERN Low Energy Antiproton Ring (LEAR) [25]. In particular the technique to detect a  $\Lambda$  hyperon through its delayed decay was developed here.

The requirements that were set for the COSY-TOF spectrometer were [26]:

- Full geometrical reconstruction of all charged particles of a reaction,
- Reconstruction of the primary and secondary vertices,
- Reconstruction of the momenta through Time of Flight for additional kinematic information,
- High background rejection.

To fulfill all these requirements, TOF was built in a modular way such that it is possible to change the detector length and the position of different sub-detectors. A typical setting with the so-called long barrel is shown in Fig. 5 [27]; the calorimeter that gives energy information is generally only used in conjunction with the shorter barrel. It is seen from the figure that the diameter of the stainless steel barrel is also around 3 m, which makes it physically the largest detector installed at COSY.

Despite the large size, all the detectors as well as the liquid hydrogen or deuterium target are positioned inside the vacuum tank, where the residual pressure of less than  $7 \times 10^{-4}$  mbar minimizes the effects of secondary interactions and multiple scattering.

The charged particles produced in interactions in the target are registered in three different groups of detectors. The first consists of a set of plastic scintillators, providing a trigger and the start signal for the TOF measurement, and a silicon quirl detector for precise track information near the primary vertex. The latter is segmented into 128 Archimedian spirals, each of which covers an azimuthal angular range of  $180^\circ$ .

All the recent experiments at TOF were carried out with the next crucial element, the Straw Tube Tracker (STT), that is situated 25 cm downstream from the target. This consists of 2704 straw tubes, each of which is a cylindrical minidrift chamber. The STT actually gives the

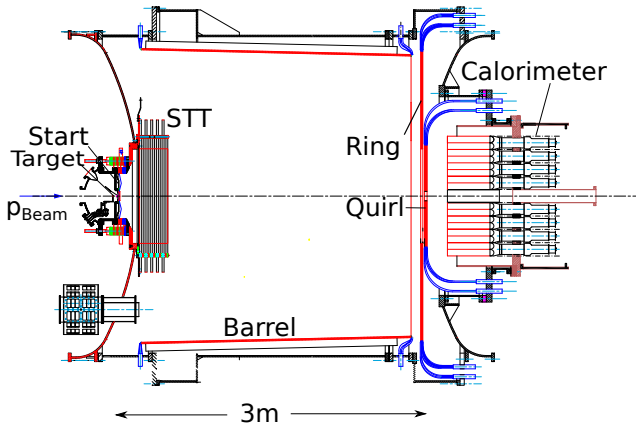


**Fig. 5.** Schematic drawing of the COSY-TOF detector, following the direction of the beam, after the target there are the start counter (Start), the straw tube tracker (STT), the barrel scintillators, the inner ring (Quirl), the outer ring (Ring), and the Calorimeter. All detectors and the liquid target are located inside the vacuum vessel [27].

most precise information for track and vertex reconstruction. For example, the achieved resolution in momentum and invariant mass of the  $pK^+\Lambda$  final state is significantly better than that obtained purely from the time-of-flight measurement.

The end detector region consists of scintillators covering the full cylindrical inner surface of the vacuum tank and the end cap (Quirl and Ring detector) and the calorimeter. The Quirl detector consists of three layers of scintillators, the first of which is structured in 48 wedge-shaped slices, with the other two being in the form of 24 Archimedean spirals, oriented in opposite directions. The structure of the Ring detector is similar to the Quirl but with twice the number of elements per layer,

Though, as seen clearly in Fig. 5, the TOF detector covers only a  $2\pi$  solid angle in the laboratory system, very few particles go backwards in this frame and so the geometric coverage is almost complete. The loss of events due to the hole that allows the primary beam to pass through the start and silicon quirl detectors can also be minimized. Charged particles can be triggered by the stop detector and evaluated by the straw detector starting from  $2^\circ$  but, for these low angles, the start timing and start trigger has to be provided by a second charged particle, for example the proton if the track of the kaon in a  $pK^+\Lambda$  final state lies very close to the forward direction.

Of course, without a magnetic field it is not possible to directly determine the sign of the charge of a meson and so it is then not possible to study the full structure in, for example,  $pp \rightarrow ppK^+K^-$ , which is discussed in sect. 8.1.

### 2.2.5 The Big Karl spectrometer

It was mentioned in the introduction that the SATURNE accelerator was equipped with a series of magnetic spectrometers placed on external beam lines. The only similar facility at COSY was the magnetic spectrometer Big

Karl [28]. This was actually designed as a QQDDQ facility for measurements at the JULIC cyclotron which, as discussed in sect. 2.1, is now used as the injector for COSY providing, for example, 45 MeV protons. Big Karl was used from about 1979 for studies of nuclear levels production in, for example,  $(p, p')$  or  $(p, d)$  reactions.

The spectrometer's design was subject to an initial modification in order to carry out experiments at the higher energies available at COSY [29]. In particular, the two entrance quadrupole magnets were replaced by three quadrupole magnets having larger geometrical acceptances and higher maximum magnetic field strengths. This resulted in a version of Big Karl that was a high resolution 3Q2DQ spectrometer, though the final quadrupole was often found not to be needed. The lay-out of the spectrometer is illustrated schematically in Fig. 6. It is equipped with two sets of multi-wire drift chambers (MWDC) for position measurement and two layers of scintillating hodoscopes for time-of-flight and energy loss information, used for particle identification.

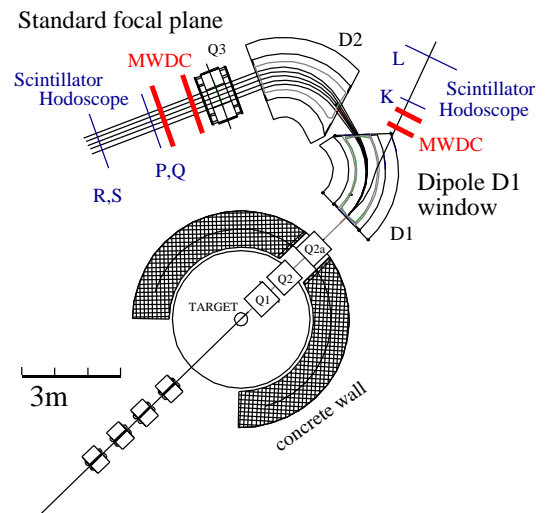


**Fig. 6.** Top view of the Big Karl magnetic spectrometer [30]. In the standard 3Q2DQ mode of operation, particles exiting from the target cell pass through the quadrupoles Q1, Q2 and Q2a and are bent to the focal plane by the dipoles D1 and D2. In the 3QD mode, high rigidity particles produced in the target are also registered emerging from the side hole of the first dipole D1.

The most important parameters of the 3Q2DQ version of Big Karl are summarized in Table 1 [29]. One feature that is clearly relevant for several of the experiments carried out at this facility is the momentum acceptance. Thus, when measuring, for example, inclusive  $\pi^+$  or  $K^+$  production in proton-proton collisions more than one setting of the central momentum is required in order to span the physics region of interest. In such cases it is important to ensure significant overlap between the settings.

However, the initial modifications described in Ref. [29] were not sufficient to exploit the full possibilities offered

Magnet structure	3Q2DQ
Central radius	1.94 m
Magnetic rigidity	$0 \leq B\rho \leq 3.6$ Tm
Max. proton momentum	1080 MeV/c
Momentum resolution	$\Delta p/p \approx 10^{-4}$
Dispersion	6.47 cm/%
Momentum acceptance	$\pm 4.5\%$
Max. horizontal angular acceptance	$\pm 28$ mrad
Max. vertical angular acceptance	$\pm 110$ mrad

**Table 1.** Selected properties of the 3Q2DQ version of the Big Karl magnetic spectrometer [29].

by the increased energy available at COSY. In particular, the maximum momentum per charge of 1080 MeV/c was too low, for example, to measure the fast tritons from the  $pd \rightarrow {}^3\text{H}\pi^+$  reaction over much of the COSY energy range. For such a two-body reaction, where the identification of one particle is sufficient to isolate the reaction and momentum resolution is less critical, a supplementary mode of Big Karl was installed [30]. As illustrated in Fig. 6, high rigidity particles could be measured by putting detectors after the exit of the first dipole so that for these particles Big Karl works as a 3QD spectrometer, where the momentum range is extended up to 3240 MeV/c. This would allow the measurement of the  $pd \rightarrow {}^3\text{H}\pi^+$  and  $pd \rightarrow {}^3\text{H}\pi^0$  cross sections under similar conditions to check charge independence, as discussed in sect. 9.1.

Additional detectors were often used in combination with Big Karl in order to register extra particles. The GEM detector of sect. 2.2.6 could also be used in a stand-alone mode but the MOMO detector of sect. 2.2.7 and the ENSTAR detector of sect. 2.2.8 were designed to be used in conjunction with Big Karl.

### 2.2.6 The GEM detector

Though the Big Karl spectrometer has excellent resolution, its limited angular acceptance meant that it has to be moved several times in order to produce an angular distribution. For two-body reactions, such as  $pd \rightarrow {}^3\text{H}\pi$ , a detector with lower resolution but larger angular coverage might be preferable. A sketch of the GEM detector, designed for this purpose, is shown in Fig. 7.

The first element in the GEM detector [31] (the so-called Quirl) measures the position and energy loss of penetrating particles. The active area of this diode is divided on both sides by 200 grooves. Each groove is shaped as an Archimedean spiral covering an angular range of  $2\pi$ , turning in opposite directions on the front and rear of the detector. This is followed by three high purity germanium detectors with radial symmetry with respect to the beam axis, as shown in the figure. These are mainly used for measuring the energy loss of penetrating particles or the total kinetic energy of stopped particles. These detectors are divided into 32 wedges to reduce the counting rate per division and this leads to a higher maximum total counting rate of the total detector.

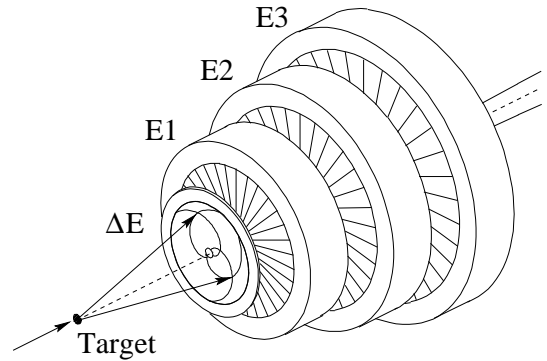


**Fig. 7.** Sketch of the GEM detector [31].

As used in experiments, GEM subtended an opening angle of about  $16.5^\circ$  at the target and this limited in particular the excess energies up to which it could be operated. In addition, in the centre of each detector there was a hole of angular size  $1.6^\circ$  that allowed the passage of the primary beam. Though GEM was designed primarily as a stand-alone facility, the presence of the central hole permitted it to be used in combination with Big Karl, which then worked as a zero-degree spectrometer. Thus the GEM collaboration worked with either the GEM detector or Big Karl, or with both.

### 2.2.7 The MOMO detector

The MOMO (Monitor-of-Mesonic-Observables) vertex detector was specifically designed for the measurement of the charged mesons  $X^\pm$  from the  $pd(dp) \rightarrow {}^3\text{H}X^+X^-$  reaction [32,33], where the  ${}^3\text{H}$  would be analyzed in Big Karl. A schematic view of the detector is shown in Fig. 8.

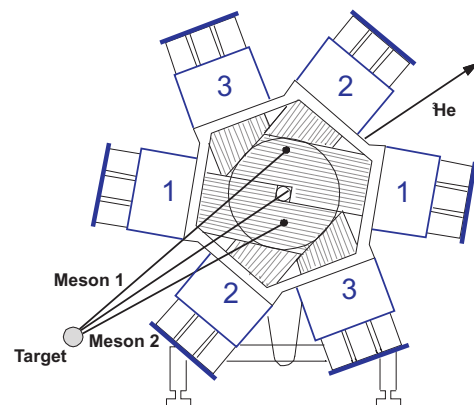


**Fig. 8.** Front view of the MOMO vertex detector [32,33], with the indication of a typical event. Both the primary beam and the recoil  ${}^3\text{H}$  detected in Big Karl pass through the central hole. The numbers denote the different layers and the three boxes at the end of each read-out symbolize the phototubes.

MOMO consists of 672 scintillating fibres, arranged in three planes, denoted by (1,2,3) in Fig. 8. The fibres are



individually read out by 16-anode multichannel photomultipliers. The fibres in the three planes are rotated by  $60^\circ$  with respect to each other and hits in three layers are required in order to avoid combinatorial ambiguities. It is important to note that the sign of the charge on each of the mesons  $X^\pm$  is not determined and this automatically leads to the symmetrization of some of the differential distributions.

In its applications, the MOMO detector was placed perpendicular to the beam direction 20 cm downstream of the target, outside a vacuum chamber, the end wall of which was a 5 mm thick aluminum plate. The central hole, which subtended an angle of  $6^\circ$  at the target, allowed the passage of the primary beam and also the  $^3\text{He}$  that were detected in Big Karl. The maximum angle of  $45^\circ$  was set by the physical dimensions of MOMO.

Each scintillating fibre is 2.5 mm thick but, when operating with a deuteron beam, these were too thin to provide reliable energy information. The MOMO wall was therefore complemented by a hodoscope consisting of 16 wedge-shaped 2 cm thick scintillators. This hodoscope was already used in the study of the  $pd \rightarrow ^3\text{He} K^+ K^-$  reaction [33]. High above threshold the acceptance for a  $pd \rightarrow ^3\text{He} X^+ X^-$  event is low, even for small  $^3\text{He}$  angles, because one of the mesons  $X$  would miss the MOMO detector. On the other hand, very close to threshold there are significant losses of events from mesons escaping through the central hole. Nevertheless, due to the forward boost, the acceptance of MOMO for  $\pi^+ \pi^-$  production is much higher for a deuteron beam than for a proton beam at the same c.m. energy.

### 2.2.8 The ENSTAR detector

The ENSTAR detector [34] was designed to detect a pair of relatively low energy particles emerging from a target, with a fast particle being measured in the Big Karl spectrometer. A typical example, discussed in sect. 10.1, is where a  $^3\text{He}$  is measured in Big Karl and a  $\pi^- p$  pair, emitted from the target almost back to back, is registered in ENSTAR [35]. The basic design of this detector [34] is illustrated in Fig. 9.

ENSTAR is cylindrically shaped, with three layers of plastic scintillators that are used to generate  $\Delta E - E$  spectra for particle identification and to obtain total energy information for the stopped particles. Each layer is divided into a number of pieces to obtain angular information. The detector consists of two identical half cylinders that are placed symmetrically on either side of the target. There is effectively full azimuthal angular coverage, but the modest resolution in  $\phi$  of about  $45^\circ$  is sufficient for the envisaged  $\eta$ -mesic nucleus search [34]. The corresponding limits for the polar angle are  $15^\circ < \theta_{\text{lab}} < 165^\circ$ .

Though, like MOMO, there is no magnetic field to help with the particle identification, the background could be suppressed by demanding strict timing coincidences between ENSTAR and Big Karl [34, 36].

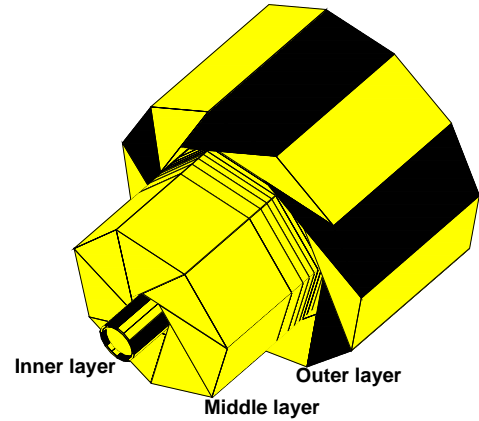


**Fig. 9.** One half of the ENSTAR detector [34] surrounding the target. It consists of wedges made of scintillating material and the read-out is ensured by scintillating fibres collecting the light in grooves milled in the wedges and transporting it to phototubes. For clarity, some elements of the middle and outer layers have been moved along the beam direction to provide an inner view.

### 2.2.9 The EDDA detector

It could be argued that EDDA has been the most successful detector employed at COSY because it was specifically optimized for one series of experiments. It relied on the stability and reproducibility of the circulating proton beam because data were taken at a continuum of energies during an acceleration or deceleration mode in COSY and the necessary statistics were acquired through the addition of data from many such cycles. Although designed for the measurement of proton-proton elastic scattering, the principles could be extended to other two-body reactions, such as  $pp \rightarrow d\pi^+$ , where two final particles are detected in coincidence and the resulting geometrical constraints eliminate much of the background.

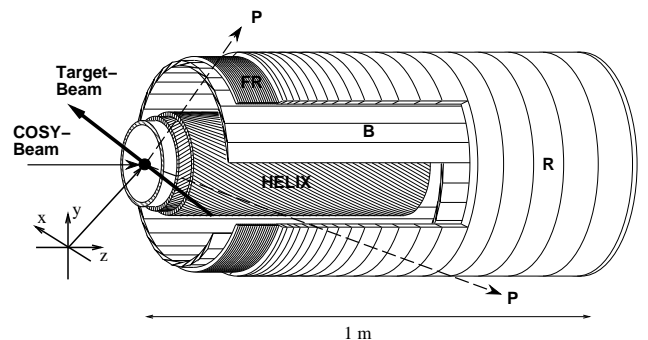


**Fig. 10.** Schematic drawing of the EDDA detector as used for the polarized target experiments [37]. The outer hodoscope consists of scintillator bars  $B$ , scintillator semi-rings  $R$  and semi-rings made of scintillating fibres  $FR$ . The inner hodoscope HELIX consists of four layers of scintillating fibres, helically wound in opposite directions.

The azimuthal symmetry of EDDA, which is so important when studying spin-dependent observables, is well illustrated by the drawing in Fig. 10. This shows the form of the detector used for measuring analyzing powers and spin correlations in  $pp$  elastic scattering [37]. Less redundancy was required in the measurement of the unpolarized cross section and an even simpler version could be used for the final EDDA incarnation as the default polarimeter for experiments at COSY. Since the detector was used only for the measurement of  $pp \rightarrow pp$ , most of the details of its application there are to be found in sect. 3.1 and we here concentrate on describing the relevant hardware.

The need to detect both final particles in a reaction puts strong constraints on the angular acceptance. Thus for very small angle  $pp$  scattering the recoil proton emerges almost perpendicular to the beam with low momentum and would not be detected. In practice, therefore, the EDDA  $pp$  elastic scattering measurements were restricted to c.m. angles  $30^\circ \lesssim \theta_{cm} \lesssim 150^\circ$ .

EDDA consists of two cylindrical detector shells, though only the outer shell was needed for the unpolarized cross section measurements. This shell consists of 32 scintillator bars ( $B$ ) which are mounted parallel to the beam axis. They are surrounded by scintillator semi-rings ( $R$ ) and semi-rings made of scintillating fibres ( $FR$ ). The resulting polar and azimuthal angular resolutions are about  $1^\circ$  and  $1.9^\circ$  FWHM, respectively.

In experiments involving polarized hydrogen, the target is far from point-like. There can be a non-negligible background associated with scattering events from the unpolarized hydrogen atoms surrounding the polarized hydrogen beam. This can be reduced significantly if the reaction vertex is well identified, which is achieved through the implementation of the inner detector shell, called HELIX in the figure. HELIX is a cylindrical hodoscope consisting of four layers of 640 plastic scintillating fibres of 2.5 mm diameter, helically wound in opposite directions so that a coincidence of hits in the two spirals determines the point where the ejectile traversed the hodoscope. Combined with the spatial resolution of the outer detector shell, the helix fibre detector allows vertex reconstruction with a FWHM resolution of 1.3 mm in the transverse directions and 0.9 mm in the COSY beam direction. Using a fit of the vertex and scattering angles with constraints imposed by  $pp$  elastic scattering kinematics the resulting polar and azimuthal angular resolutions are, respectively, about  $0.3^\circ$  and  $1.3^\circ$  FWHM.

After the completion of the EDDA physics programme, a stripped-down version of the detector has been used extensively at COSY as an on-line beam polarimeter. For this purpose the central helix shown in Fig. 10 was removed. Only carbon fibre targets were used and these could be moved remotely into the beam in order to measure the polarization. The resulting polarimeter consists of 29 pairs of half-rings placed to the left and right of the beam to detect coincidences from quasi-free scattering from the carbon. The asymmetry is determined individually for each pair of half-rings and the weighted average evaluated. This is converted into a value of the

beam polarization using dedicated C/CH<sub>2</sub> measurements and the EDDA values of the elastic  $pp$  analyzing powers at that particular energy [37]. The systematic uncertainty in the polarizations is estimated to be  $\approx \pm 3\%$  at each energy [38]. It should be noted that, unless great care is taken [39], the interaction of the beam with the target makes the residual beam unusable for precision experiments, so that the EDDA polarimeter is only employed at the end of a COSY cycle.

## 2.3 Targets and equipment

### 2.3.1 The Atomic Beam Source

For experiments with an external beam, the particles pass only once through the target so that, in order to obtain meaningful counting rates, the targets have to be “thick”. This causes particular problems for polarized targets because it has not been possible to produce a polarized target of pure hydrogen or deuterium on a macroscopic scale. For example, the alcohol pentanol, which has often been used for a polarized target, has a hydrogen content of less than 16% and this clearly reduces the figure of merit for any experiment [40].

The situation is very different for experiments carried out inside a storage ring such as COSY because the beam traverses the target a myriad of times and so much thinner targets must be used. Polarized hydrogen and deuterium ions are routinely produced using an Atomic Beam Source (ABS) and, although this may not lead to targets that are sufficiently thick, this can be compensated by using the ABS in combination with a gas cell, as described in sect. 2.3.2.

Several ABS systems have been used at COSY, including those at EDDA [37], ANKE [41], and PAX [42]. These are technologically very complex devices and the interested reader is directed to these references. Only the basic principles of an ABS, which are completely analogous to the devices used for producing polarized beams, are outlined here. In a static magnetic field the energy levels of an atom split into four (hydrogen) or six (deuterium) distinct lines though, as summarized by the Breit-Rabi diagrams [43], the relative separations between the lines change significantly with the field strength.

Transitions between the hyperfine states are induced by the magnetic component of an  $rf$  field, and this leads to changes in the populations of the states, and hence to a possible polarization. However, very different effects can be achieved in weak fields, where the total atomic spin is a good quantum number, from medium and strong fields. For hydrogen it is in principle possible to produce spin-“up” protons with transitions in a medium strength field whereas spin-“down” requires supplementary transitions in a weak field. It should therefore not come as a surprise if the polarizations ‘up’ and ‘down’ differed in magnitude.

The situation with deuterium is much more complicated because, in addition to the vector polarization  $p_z = (N_+ - N_-)/(N_+ + N_0 + N_-)$ , there is also the tensor polarization  $p_{zz} = (N_+ + N_- - 2N_0)/(N_+ + N_0 + N_-)$  to be

considered. Here the  $N_i$  are the populations of the three magnetic sub-states for a spin-one particle in the quantization direction of the source. In order to get different mixtures of vector and tensor polarizations, various combinations of hyperfine transitions in weak, medium, and strong fields must be introduced.

In the ideal case, the settings on the transition units would specify the polarizations of the source but, due to imperfections, this does not happen in practice and the resultant polarizations have to be measured independently. This can be done quite precisely with the help of a Lamb Shift Polarimeter (LSP) [44], which can also be used to optimize the polarization of the atomic hydrogen and deuterium beams delivered by the ABS.

Beam	$(p_z, p_{zz})_{\text{ideal}}$	$p_z$	$p_{zz}$
Hydrogen	(+1, -)	$+0.89 \pm 0.01$	—
	(-1, -)	$-0.96 \pm 0.01$	—
Deuterium	(+1, +1)	$+0.88 \pm 0.01$	$+0.88 \pm 0.03$
	(-1, +1)	$-0.91 \pm 0.01$	$+0.85 \pm 0.03$
	(0, +1)	$+0.005 \pm 0.003$	$+0.90 \pm 0.01$
	(0, -2)	$+0.005 \pm 0.003$	$-1.71 \pm 0.03$

**Table 2.** Values of the polarizations achieved for hydrogen and deuterium in a test experiment with the ABS used at ANKE [41].

In tests carried out on the ABS used at the ANKE target station, the values of the polarizations achieved for hydrogen and deuterium are reported in Table 2 [41]. However, these are just typical examples and the choices of hyperfine transitions, and hence polarizations, can be tailored to the needs of a particular experiment. Note also that there may be polarization losses when a beam from an ABS is used inside COSY.

### 2.3.2 Polarized gas cell targets

Though an ABS can produce high quality polarized beams of hydrogen and deuterium, they are generally too weak to provide acceptable luminosities in a storage ring such as COSY. The general solution to this dilemma is to use the ABS beam to supply a storage cell that holds the polarized atoms in the vicinity of the passage of the high energy circulating beam. In this way the target density can be increased by up to two orders of magnitude compared to the direct ABS beam [45]. Such a storage cell was routinely used by the HERMES collaboration working at the DESY electron storage ring [46] and at COSY they have formed parts of the EDDA, ANKE, and PAX programmes.

The basic design of the T-shaped system illustrated on the left of Fig. 11 is fairly general. There is a vertical feeding tube that catches the gas flow from the ABS to guide it into the horizontal tube of the storage cell that lies along the circulating beam of the accelerator. The minimum feeding tube diameter, which is of the order of 10 mm, is determined by the extension of the focused gas

beam from the ABS. The areal density of the target increases roughly like  $L^2/d^3$ , where  $d$  is the diameter of the storage cell and  $L$  its length [45]. The highest density is therefore achieved with a long target cell with the smallest possible diameter.

The minimum diameter of the storage cell is defined by the beam extension and, depending on the beam energy and the cooling capabilities of the machine, diameters  $d$  from 10 to 12 mm are reasonable. With a storage cell of length  $L = 390$  mm, this would lead to target areal densities from  $3$  to  $6 \times 10^{13} \text{ cm}^{-2}$  compared to the  $1 \times 10^{12} \text{ cm}^{-2}$  obtained directly from the ABS.

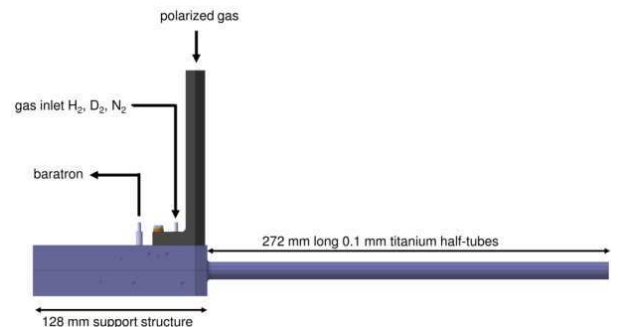


**Fig. 11.** Design for the openable storage cell for use at ANKE [47] showing the typical T-shape layout, with the vertical feeding tube that connects to the ABS and the storage cell itself that lies along the COSY beam. Unpolarized hydrogen and deuterium gas can be introduced through the smaller tube to the left, as can the nitrogen used for background studies. There is also an outlet to the baratron pressure monitor. The cell can be opened (or closed) vertically along its length with the use of a precision piezoelectric drive.

A storage cell with a diameter of 10-12 mm would, however, pose a serious obstacle for the COSY beam at injection and during electron cooling. This would restrict the beam intensity and hence the luminosity. One way to overcome this limitation is to design a cell that is open at the start of a COSY cycle and only closes once the beam has been well prepared and is stable. Such a cell is illustrated on the right of Fig. 11, which shows the open two halves of the cell. These close and open around the beam at each cycle of the accelerator and in this way the storage cell is not the limiting factor in the COSY beam intensity.

The choice of material for the walls of the storage cell is critical. Aluminium is suitable for a rigid cell because the target polarization is not destroyed and all but the lowest energy ejectiles can pass through the 0.2 mm walls. However, for an openable cell, such walls are too flexible to provide firm closure over the 272 mm length shown in Fig. 11. Stainless steel has the necessary rigidity but, even after coating with PTFE, there is serious loss of polarization due to recombination effects on the walls. The successful cell was made from titanium, which was as thin as 0.1 mm in the region of interest, coated with a 0.005 mm

layer of PTFE. The rigid support structures allow the precise and reproducible positioning of the half-tubes of the cell [48].

The cell polarizations were measured for both  $\vec{H}$  and  $\vec{D}$  targets with the 580 MeV proton beam, using the free or quasi-free  $pp \rightarrow d\pi^+$  reaction for the polarimetry, with both the  $d$  and  $\pi^+$  being measured in ANKE, with identification made on the basis of time of flight. The value of the polarization for hydrogen in the cell was  $86 \pm 5\%$ , which is only slightly lower than the highest ABS jet polarization observed in laboratory tests. As expected, the polarization of the rest-gas around the cell was very low. The vector polarization of the deuterium target was  $61 \pm 10\%$ , which is also consistent with there being little polarization loss on the titanium walls [47].

It therefore seems that the openable storage cell technology represents a major advance for the use of polarized targets in storage rings.

### 2.3.3 Silicon Tracking Telescopes

The original motivation for the design of the Silicon Tracking Telescope (STT) was the detection of low energy protons emerging from a deuterium target [49]. In a hard process, such as  $pd \rightarrow p_{sp}d\eta$ , a recoiling proton with a momentum less than say 150 MeV/c might be considered to be a *spectator*,  $p_{sp}$ , which only influences the reaction through the kinematic changes that it induces. In this case the reaction can be interpreted in terms of quasi-free  $pn \rightarrow d\eta$ .

Spectator detection in internal measurements at storage rings is made easier because the low energy protons are not lost in a liquid target and an initial trial of the method was carried out at the CELSIUS ring [50]. However, more dedicated equipment has been constructed at COSY [49] and the STT have found other uses, such as the measurement of recoil protons from  $pp$  elastic scattering or facilitating the vertex location when using a long polarized cell target.

The COSY STT have been developed to trigger, identify, and track low energy protons and deuterons. Three layers of silicon-strip detectors act as a range telescope, combining particle trigger and time-of-flight information with particle tracking and energy-loss determination over a wide dynamic range. Stopped particles are unambiguously identified by the  $\Delta E/E$  method and their four-momentum determined. With the STT acting as modular building blocks, an extended vertex detector covering a large acceptance can be setup depending on the needs of an individual experiment.

A single STT is made up of three layers of 70, 300 and 5000  $\mu\text{m}$  thick double-sided structured silicon-strip detectors to guarantee particle triggering and tracking over the full energy-loss range of 0.05–50 MeV. Each detector has an active area of  $64 \times 64 \text{ mm}^2$ . The 70 and 300  $\mu\text{m}$  thick detectors have 128 strips (0.5 mm pitch) per side whereas the 5000  $\mu\text{m}$  thick detector has 64 segments (1 mm pitch) on each side. The segmentation and geometry have been chosen taking into account the limitations due to small

angle scattering within the detector planes. The electronics that provide information for each individual strip are placed behind the detectors so as not to disturb the particle detection. There are independent cooling branches so that the electronics can be kept at room temperature whereas the detectors can be cooled down to  $-20^\circ\text{C}$ .

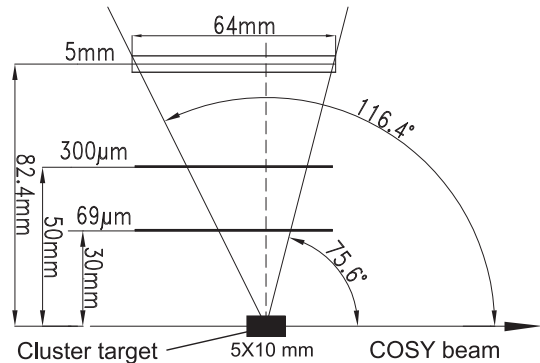


**Fig. 12.** Schematic diagram of one possible layout of the three STT layers inside the ANKE target chamber when used in conjunction with a cluster-jet target [49].

The layout of the STT inside the high vacuum of the ANKE target chamber is shown schematically in Fig. 12. There is some flexibility in the location of the detector but the first silicon layer could be placed as close as 1 cm from the cluster-jet target so that the angular acceptance would then be even larger than that indicated in the figure. In order to pass through the three layers, the protons must have kinetic energies of at least 2.5 MeV, 6 MeV, and 30 MeV, respectively. The first of these criteria is the most severe because about half the spectator protons from a deuterium target have energies below this and so such events cannot be reconstructed.

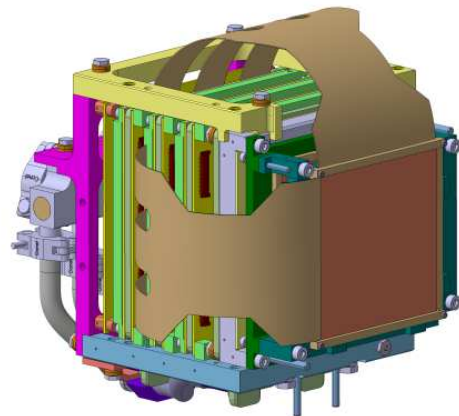


**Fig. 13.** A fully assembled STT detector [49].

For stopping protons with energies below 30 MeV the particle identification is unambiguous and greater precision in the angle of the recoiling proton is achieved by deducing it from the energy measured in the telescope rather than from a direct angular measurement. However, by studying the energy deposited principally in the third layer, it is also possible to deduce the energy of punch-through protons up to 90 MeV, thus expanding considerably the angular coverage of the telescope. The fully assembled STT detector illustrated in Fig. 13 is compact and transportable.

The demand that the STT identifies and determines the track of a charged particle means that this must pass through the first layer and hit (and possibly stop) in the second layer of the detector. This allows the STT to be used with a long target, such as the cell filled with polarized gas. The downside is the fact that a proton must have a minimum momentum of about 70 MeV/ $c$  to pass through the first layer. In the case of elastic proton-proton scattering it can only be used for momentum transfers  $|t| > 0.005 (\text{GeV}/c)^2$ . To access smaller momentum transfers requires changed criteria and a different design, an example of which is the KOALA detector.

### 2.3.4 The KOALA detector

The prime motivation for the development of the KOALA (Key experiment fOr pAnda Luminosity determinAtion) detector by the PANDA collaboration is the study of anti-proton-proton scattering at small momentum transfers at HESR. Since the evaluation of the pure Coulomb differential cross section, which proportional to  $1/t^2$ , is unambiguous, a measurement in the region of Coulomb dominance would determine the  $\bar{p}p$  luminosity in an independent way and allow parameters of the  $\bar{p}p$  interaction to be extracted. For this to be feasible the device must allow smaller values of momentum transfers to be studied than is possible with the STT. This in turn requires that the particle be registered on the front layer of a detector and that the track be determined by demanding the beam-target interaction to be point-like. As described in sect. 3.1, such a detector could also be used to investigate proton-proton elastic scattering at COSY.

The general layout of the KOALA detector is shown in Fig. 14 [51]. In order to optimize the settings for different beam momenta, it is possible to adjust remotely the distance of the detector plane from the interaction point. The recoil detector will measure both the kinetic energy and the polar angle of the recoil protons which will provide two determinations of the momentum transfer  $t$ .

As used at COSY, the KOALA detector plane, containing two  $76.8 \text{ mm} \times 50 \text{ mm} \times 1 \text{ mm}$  silicon strip sensors, was positioned about 1 m from the target. Each silicon detector has 64 strips with 1.2 mm pitch. In order to measure higher energy protons, two germanium strip detectors with 5 and 11 mm thickness were also added. These each have 67 readout strips and a strip pitch of 1.2 mm.

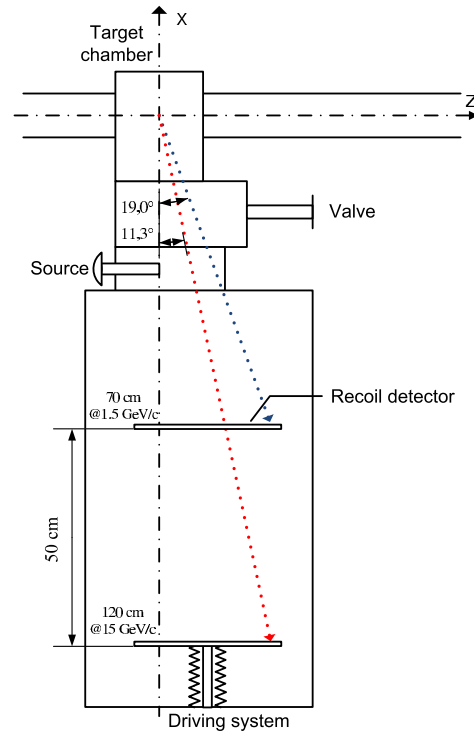


**Fig. 14.** Schematic view of the KOALA recoil detector [51], showing the complete setup with a movable detector plane in order to cover the desired range of recoil angles depending upon the chosen beam momentum.

## 2.4 Technical experiments

Two of the more difficult challenges that must be faced when carrying out experiments inside a storage ring are the evaluation of the beam-target luminosity  $\mathcal{L}$  and the precise determination of the beam momentum. At an external target position the beam is generally much smaller than the area of the target and, by taking a target of uniform thickness,  $\mathcal{L}$  will not depend on fine details of the beam properties. If the fluxes of the incident and scattered particles are measured, the absolute cross section of a reaction can be determined. Even here there may be complications due, for example, to the bulging of the windows of a liquid target.

In an internal experiment the beam-target overlap and the target thickness are very hard to estimate from macroscopic measurements and so another method to determine the luminosity must be sought. To avoid the associated normalization uncertainties, many experiments at COSY have derived cross sections by comparing production rates with those for processes with known differential cross sections, often elastic or quasi-elastic scattering.

A much more ingenious method was implemented by the EDDA collaboration in their measurement of proton-proton scattering. As described in sect. 3.1, this involved evaluating the numbers of electrons knocked out of the target by the proton beam. Since this is an electromagnetic process, its cross section can be calculated quite reliably. A different approach to the problem, which is also based

upon electromagnetic processes, viz. the energy losses of energetic charged particles as they pass through matter, is discussed in sect. 2.4.1. The energy loss of the stored beam, which is proportional to the target thickness, builds up steadily in time and leads to a shift in the revolution frequency of the machine, which can be determined by measuring the Schottky spectra. If the characteristics of the machine are known, the effective target thickness can be deduced [52].

Regarding the second challenge, when performing a precision measurement, such as determining the mass of the  $\eta$  meson discussed in sect. 9.2, it is important to know the COSY beam momentum to a fraction of a MeV/c. Though the circulation frequency is known to better than  $10^{-5}$ , the same cannot be said for the length of the COSY orbit because there may be small but significant and uncontrolled deviations from the ideal path. An alternative approach, such as that described in sect. 2.4.2, is necessary if great accuracy is required.

The momentum of a stored polarized proton or deuteron beam in COSY can be determined by sweeping an *rf* magnetic dipole or solenoid field over a spin resonance. This perturbation induces a beam depolarization that is maximal at the resonance frequency. Taken together, the resonance and beam revolution frequencies completely determine the beam's Lorentz  $\gamma$  factor. This allows the corresponding beam momentum to be determined at least one order of magnitude more precisely than with macroscopic methods [53].

There were other *technical* experiments, especially several carried out by the SPIN@COSY collaboration [54, 55], but these had less direct influence on the hadron physics programme and will not be described here. The one that is described explicitly is the PAX programme to study the production of polarized protons by spin filtering. Though the PAX experiments could have no direct influence on the hadronic physics programme at COSY, it has been suggested that such a technique could be used to produce polarized antiproton beams at FAIR.

#### 2.4.1 Determination of beam-target luminosity

When the particles in a closed orbit in COSY lose energy in passing through the target, the fractional change in the momentum  $p$  is proportional to the fractional change in the frequency  $f$  of the machine:

$$\frac{1}{p} \frac{dp}{dt} = \frac{1}{\eta} \frac{1}{f} \frac{df}{dt}, \quad (2.1)$$

where  $\eta$  is the so-called *frequency-slip parameter*. Once this constant of proportionality is known, the rate of change of frequency determines the effective target thickness  $n_T$  through [52]:

$$n_T = \left( \frac{1 + \gamma}{\gamma} \right) \frac{1}{\eta} \frac{1}{(dE/dx)m} \frac{T}{f^2} \frac{df}{dt}, \quad (2.2)$$

where  $T$  is the kinetic energy of the beam particles of mass  $m$ ,  $\gamma$  the Lorentz factor, and  $dE/dx$  the stopping power of the target material.

The  $\eta$ -parameter, which reflects a competition between the slowing down due to the energy loss and an apparent speeding up following an orbit adjustment, is a property of COSY that is quite independent of the particular target. Though it can be estimated from the general machine parameters, it is best measured by varying the field strength in the bending magnets by a few parts per thousand. As seen from Fig. 15a, obtained for a proton beam with a momentum of about 3.463 GeV/c, the resulting frequency change is quite linear and the slope  $\alpha$  leads to a value of  $\eta = 1/\gamma^2 - \alpha = -0.115 \pm 0.003$  [52].

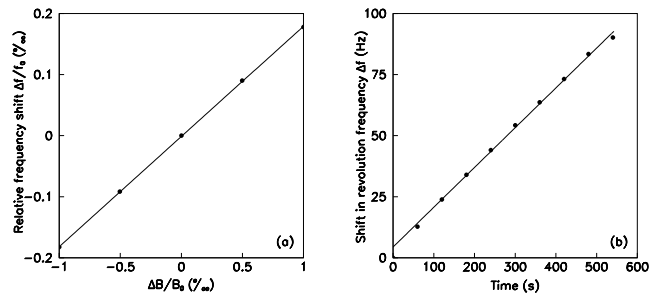


**Fig. 15.** (a) Variation of the revolution frequency with field strength in the bending magnets, both in parts per thousand. (b) Typical mean frequency shifts derived from the Schottky power spectra at ten equally spaced intervals of time. Both measurements were conducted for settings corresponding to protons with momenta 3.463 GeV/c [52].

The frequency shift is measured by analyzing the Schottky noise power spectrum of the coasting proton beam at a sequence of times. The origin of the Schottky noise is the statistical distribution of the particles in the beam, which gives rise to current fluctuations that induce a voltage signal at a beam pick-up. The centroids of these power spectra are shown in Fig. 15b at ten equally spaced intervals in time. After neglecting the first and last points, the slope of these data gives  $df/dt = (0.163 \pm 0.003)$  Hz/s for *pp* interactions at 3.463 GeV/c [52]. By inserting the values of  $df/dt$  and  $\eta$  into Eq. (2.2), a value of the effective target thickness can be deduced which, without any loss of precision, can be converted into one of luminosity by multiplying by the number of beam particles measured in the same cycle with a high precision beam current transformer.

The measurement relies on the particles in the beam passing through the target more or less the same number of times so that they build up similar energy shifts. This is confirmed by the Schottky spectrum at the end of a cycle being similar in shape to that at the beginning. Several corrections, described in detail in Ref. [52], have to be applied before a reliable value of the luminosity can be obtained. The biggest of these is to account for the energy loss caused by the interactions with the residual gas in the ring. After making such corrections, the uncertainty

in the luminosity in this initial experiment was estimated to be on the 5% level [52].

Even greater precision was achieved when the Schottky technique was used in the normalization of the ANKE measurements of the proton-proton differential cross section described in sect. 3.1. However, it is important to note that, with the actual settings in COSY,  $\eta$  changes sign for a proton kinetic energy around 1.3 GeV. Due to the resulting large error bars, the Schottky technique is of little value for energies in this neighbourhood.

#### 2.4.2 Precision determination of beam momentum

The determination of the momentum of a polarized electron beam through the study of induced depolarizing resonances was used at the VEPP accelerator to measure the masses of a variety of neutral mesons from the  $\phi$  to the  $\Upsilon$  [56]. A similar technique has also been used at COSY to measure the momentum of a vector polarized deuteron beam [53]. If  $f_{\text{res}}$  is the frequency of the depolarizing  $rf$  field and  $f_0$  the revolution frequency of the beam in COSY then the total energy  $E_d$  of a deuteron in the beam is given by

$$E_d = \frac{m_d c^2}{|G_d|} \left( k - \frac{f_{\text{res}}}{f_0} \right), \quad (2.3)$$

where  $k$  is an integer. Under the actual conditions of COSY,  $k = 1$ . Thus, by measuring the two frequencies it is possible to determine  $E_d$  in terms of the deuteron mass  $m_d$  and its gyromagnetic anomaly  $G_d = -0.1429873$ .

The revolution frequency  $f_0$  was measured by using once again the Schottky noise of the beam. From all the spectra taken over five days that were measured under the same conditions at a particular energy, one mean spectrum was constructed, an example of which is presented in Fig. 16. The small tail at lower frequencies is well understood. The FWHM of the peak is below 50 Hz and an average revolution frequency of  $\overline{f_0} = 1403831.75 \pm 0.12$  Hz was deduced [53]. The tiny statistical error here is dwarfed by the systematic uncertainty of  $\Delta f_0 \approx 6$  Hz that arose from the limited preparation of the Schottky analyzer used in the experiment. As a consequence the value of  $\overline{f_0}$  was only determined with a relative precision  $\approx 4 \times 10^{-6}$ .

At COSY a horizontal  $rf$  field from a solenoid was used to induce a depolarizing resonance in the deuteron beam [53]. The polarization was measured with the EDDA polarimeter discussed in sect. 3.1 using deuteron-proton elastic scattering. The absolute calibration of this polarimeter is unimportant because it is only the frequency dependence of the signal that is relevant. Figure 16 shows the measured deuteron beam polarization as a function of the  $rf$  solenoid frequency  $f_{\text{res}}$  with statistical errors. The major contribution to the width of the signal comes from the momentum spread of the deuteron beam inside COSY, which is about  $\delta p/p \approx 2 \times 10^{-4}$ . This value agrees with that deduced from the study of the kinematics of the  $dp \rightarrow {}^3\text{He}\eta$  reaction described in sect. 9.2.

The structure in the middle of the resonance frequency scan of Fig. 16 is due to the interaction with a broad-band

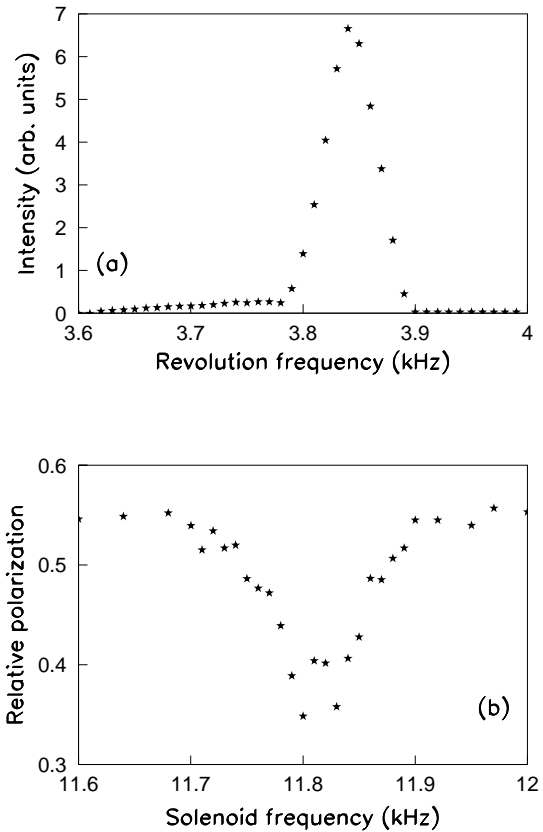


**Fig. 16.** (a) Mean Schottky power spectrum extracted from measurements over five days at a single energy. (b) Spin-resonance measurements at a single energy. The frequencies shown were displaced by (a) 1.4 MHz and (b) 1.0 MHz. The measurements were carried out with a deuteron beam of momentum  $\approx 3.1$  GeV/c [53].

barrier-bucket (stabilizing) cavity in COSY and does not affect the mean position of the resonance frequency, which was determined with a precision of  $\approx 1.5 \times 10^{-5}$ . It is this uncertainty that dominates the error in the extraction of the deuteron energy, and hence its momentum, on the basis of Eq. (2.3). This resulted in a limit of  $\Delta p_d/p_d \leq 6 \times 10^{-5}$  for  $p_d \approx 3.1$  GeV/c [53]. This is over an order of magnitude better than ever reached before for a standard experiment in the COSY ring and is quite sufficient for measuring the  $\eta$  mass, as discussed in sect. 9.2.

The method described here is far more general than the one applied on an external proton beam using the Big Karl spectrometer [57]. This technique was specific for the momentum 1930.477 MeV/c, where the forward-going pion from the  $pp \rightarrow d\pi^+$  reaction has the same momentum as the backward-going deuteron. An experiment based upon this principle resulted in a precision of about  $5 \times 10^{-5}$ , though small corrections had to be made to account for the energy losses in the target and its windows.

### 2.4.3 Spin-filtering experiments

The ultimate aim of the PAX (Polarized Antiproton eXperiment) collaboration is to produce beams of polarized antiprotons that can be used to study a variety of double-polarized  $\bar{p}p$  interactions [58,59]. Of particular interest here is the transversity distribution that can be measured in the Drell-Yan production of lepton pairs in double-polarized  $\bar{p}p$  collisions. The basic principle of the PAX approach is quite straightforward but the methodology should first be refined for proton beams.

For beam and target polarized transversally in the  $y$  direction, the proton-proton total cross section has the spin structure

$$\sigma_{\text{tot}} = \sigma_0 + \sigma_1 PQ, \quad (2.4)$$

where  $P$  is the beam polarization and  $Q$  that of the target. Thus, if  $\sigma_1$  is non-zero, the  $pp$  total cross section will depend on the relative orientations of the beam and target spin orientations. In this case, when an unpolarized beam passes through a polarized target, one of the beam spin orientations is preferentially absorbed and the residual beam thus acquires a polarization. The obvious disadvantage of this spin-filtering method is that, unless  $\sigma_1/\sigma_0$  is very large, the beam intensity would be much reduced before a significant polarization could be built up. There are some similarities here with the measurements of the beam lifetime discussed in connection with the TRIC experiment, the difference being that in the study of  $A_{y,y}$  the beam was initially polarized [60].

A proof-of-principle experiment was carried out at the Test Storage Ring at Heidelberg using 23 MeV protons passing through a cell filled with transversally polarized hydrogen supplied by an atomic beam source. Beam polarizations (both “up” and “down”) of over 1% were achieved after about 80 min of spin filtering [61].

A similar experiment was carried out by the PAX collaboration at COSY close to the injection energy of 45 MeV [62]. The polarized hydrogen target cell was installed in one of the straight sections of COSY, in the position previously taken by the PISA detector shown in Fig. 1. As at Heidelberg, this was fed from an atomic beam source but the target polarization was controlled much more precisely through the inclusion of a Breit-Rabi polarimeter. The electron cooler was used to compensate for multiple small-angle Coulomb scattering and the energy loss in the target and the residual gas in the machine [42]. The beam polarization was measured in the other straight section of COSY using the ANKE facility, which does not seriously affect the beam quality. The setup for this was very similar to that used for the measurement of the analyzing power in  $pp$  scattering [63], except that the target was in the form of a deuterium cluster jet. The asymmetry of elastically scattered deuterons was measured in a pair of STT placed on either side of the target.

The rate of polarization build-up through spin filtering was much slower in the COSY experiment compared to that of Heidelberg, due mainly to the differences in the machine frequencies and the relative sizes of the spin-dependent cross sections. Thus about 0.8% was achieved

after 270 min. It is important to realize that a beam proton has to scatter through some minimum angle in order to leave the ring acceptance and this has to be taken into account when making estimates of  $\sigma_1$  from phase-shift amplitudes [64]. After making this correction, there is good agreement with the COSY data at 49.3 MeV [62].

Faster polarization build-up would be possible with an increased target thickness and this would be allowed with an openable cell of the type discussed in sect. 2.3.2. Also, in order to be independent of the ANKE facility, a dedicated polarimeter, with better azimuthal coverage is under construction. Although the COSY experiment has shown that spin filtering works and is well understood, the test only applies to transverse polarizations. Any test of longitudinal spin filtering would involve a rotation of the beam polarization and this will require the use of the new Siberian snake.

## 3 Nucleon-nucleon elastic scattering

A good understanding of the nucleon-nucleon ( $NN$ ) interaction is one of the principal goals of nuclear and hadron physics. Apart from their intrinsic importance for the study of nuclear forces,  $NN$  elastic scattering data are also necessary ingredients in the modeling of meson production and other nuclear reactions at intermediate energies. It is therefore clear that all facilities must try to fill in any remaining gaps in our knowledge in the area. In this respect COSY has certainly taken its responsibilities seriously because the measurements of proton-proton elastic scattering carried out at this machine have completely revolutionized the  $pp$  database above 1 GeV, where previously there had been relatively few systematic experiments [65]. However, as shown in sect. 3.2, significant advances in the measurements of neutron-proton elastic scattering have also been made at COSY.

### 3.1 Proton-proton elastic scattering

It is important at the outset to realize that the beam intensities at COSY are not sufficient to make the study of the polarizations of recoil particles through double scattering experiments a very attractive proposition. On the other hand, the possibility of using a thin windowless target at an internal target station of COSY offers significant advantages over the methods used in standard external experiments. By exploiting the repeated passage of the recirculating polarized or unpolarized proton beam through such a polarized or unpolarized target in COSY it was possible to measure the differential cross section [66,67], the proton analyzing power [68,37], and spin-correlations [69,70] with the EDDA detector described in Section 2.2 and illustrated in Fig. 10. This approach allowed these observables to be studied over effectively a continuum in energy though, for presentational reasons, the final results were necessarily published in finite energy bins. Though a similar technique was used earlier at the SATURNE synchrotron, the measurements there were restricted to the



unpolarized cross section and only at centre-of-mass angles close to  $\theta_{cm} = 90^\circ$  [71].

Proton-proton elastic scattering can be cleanly identified by geometry if the directions of the two recoiling protons are measured. In this case the laboratory polar angles of fully coplanar events must satisfy

$$\cot \theta_{lab}^1 \cot \theta_{lab}^2 = 1 + T_p/2m_p, \quad (3.1)$$

where  $T_p$  is the laboratory kinetic energy of the beam and  $m_p$  the proton mass. Imposing this condition suppresses significantly the contributions of multibody final states, such as meson production. In contrast to the single-arm measurements that are discussed later in this section, a detailed study of the recoil energies is not required.

In all measurements of a differential cross section in an internal experiment at an accelerator, a crucial element is the determination of the absolute normalization, i.e., of the beam-target luminosity  $\mathcal{L}$ . The technique used at EDDA involved the evaluation of the numbers of electrons kicked out of the target through purely electromagnetic proton-electron scattering. The requirements of this procedure had a significant influence on the target design, to which we now turn.

The EDDA targets for the cross section measurements were made of strips of polypropylene ( $\text{CH}_2$ ) of dimension  $4 \times 5 \mu\text{m}^2$  coated with a very thin layer of aluminium. These were then strung horizontally between the prongs of a metal fork such that they could be moved remotely into the path of the COSY beam. The carbon background under the  $pp$  elastic scattering peak was already much reduced by the coplanarity cut and the correlation requirement of Eq. (3.1). In addition, the shape of the residual background could be determined with high accuracy by using similar carbon fibres as targets.

A key feature of the EDDA cross section measurement is that it possessed two independent methods to determine the electron loss from the target fibres. Though these studied electrons in widely different kinematic regions, on average the deviations between the two methods was below 1.5%. The secondary electron monitor (SEM) measured the electric current through the metal supporting fork of the target. This current of electrons replaced the low-energy secondary electrons emanating from the target surface due to the interaction with the proton beam. The alternative technique involved detecting higher energy  $\delta$  electrons kicked out of the target in two PIN-diodes placed downstream of the target. It must be stressed that, due to uncertainties in the geometry etc., neither of these could give reliable absolute normalizations. However, since the proton-electron cross section and its energy dependence are calculable, both methods provide excellent relative luminosity determinations.

Since the target used for the differential cross section experiment was relatively narrow, the inner shell of the EDDA detector, called the helix in Fig. 10, was not needed for the vertex reconstruction and so only the outer shell was left in position. There are, of course, many detailed refinements in the very careful analysis of the EDDA data [67] but, by normalizing the results on an angular

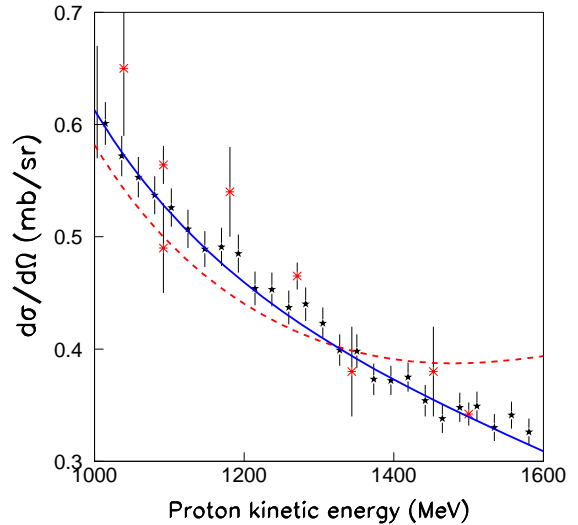


**Fig. 17.** Differential cross section for elastic proton-proton scattering at a centre-of-mass angle  $\theta_{cm} = 89^\circ$ . The (black) stars are EDDA points [67] whereas the (red) crosses are a selection of earlier results taken from the SAID database [65]. The (red) dashed curve represents SAID solution SM94 before taking the EDDA data into account whereas the (blue) solid line is that of SP07, where all the EDDA data are included [65].

integral of the precise LAMPF measurements at  $T_p = 793$  MeV [72], values of the  $pp$  elastic differential cross section could be obtained from 230 to 2590 MeV with a 1% overall systematic uncertainty. In total about  $4 \times 10^7$  good  $pp$  elastic scattering events were registered and so the statistical uncertainties were also very low.

To illustrate the influence of the (combined) EDDA results on the phase shift analysis, we show in Fig. 17 these data at  $\theta_{cm} = 89^\circ$  compared to SAID solutions before and after the EDDA results were available [65]. It should be noted that the earlier SAID solution was only valid up to 1.6 GeV. Also shown are a selection of results from previous experiments. The improvements in the data and their representation are manifest. The complete EDDA  $89^\circ$  data set is shown in Fig. 18, where deviations from the SAID SP07 are only evident at very low energies, where many results from other experiments are available to constrain the solution.

Due to the necessity to detect both protons in the detector, the major drawback in all the EDDA data sets is the lack of acceptance near the forward or backward directions. The lowest c.m. angle for the differential cross sections was typically  $\theta_{cm} \approx 35^\circ$ , depending upon the beam energy, though this was reduced to  $\approx 32.5^\circ$  for the spin-dependent observables.

The proton-proton differential cross sections measured with the EDDA detector at two beam energies are shown in Fig. 19, where they are compared with the SP07 and, at the lower energy, with a pre-EDDA partial wave solution [65]. It must be stressed that these are just two out

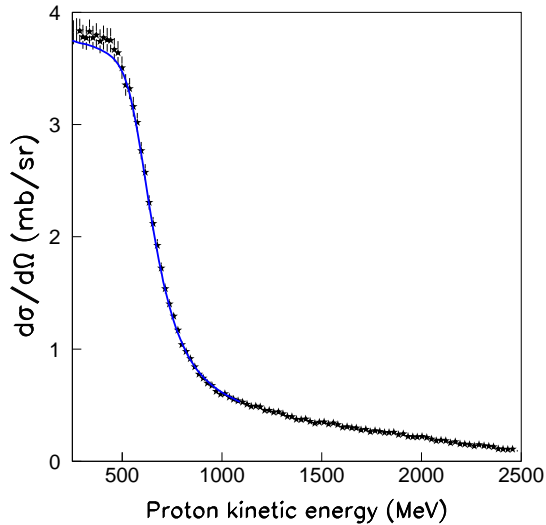


**Fig. 18.** Differential cross section for elastic proton-proton scattering at  $\theta_{cm} = 89^\circ$ . The EDDA data [67] are compared to the SP07 SAID partial wave solution [65].

of the very many EDDA measurements, as already indicated by the  $89^\circ$  data set shown in Fig. 18. The change between the SM94 and SP07 solutions is clear and the fact that the SP07 SAID solution passes through almost all of the EDDA points proves that these data completely dominate the SAID database above about 1 GeV. One reason for this may, of course, be the limitations of the other data shown in Fig. 19.

A full partial wave analysis clearly needs information from spin-dependent measurements and so we now turn to the contributions in this field made by the EDDA collaboration. The EDDA proton analyzing power,  $A_y$ , measurements were carried out using the unpolarized COSY proton beam incident on a polarized hydrogen target [68,37]. This approach avoids the difficulties associated with the depolarizing resonances in COSY so that all the EDDA  $A_y$  results are inversely proportional to the same factor, namely the polarization of the target. Its value can be most reliably deduced by comparing the EDDA data at 730 MeV with the results of a precise external target experiment in the angular range  $45 \lesssim \theta_{cm} \lesssim 70^\circ$  [75].

The target used in the EDDA experiments was a polarized hydrogen gas jet fed from the atomic beam source (ABS). The typical width of the jet in the region of intersection with the COSY beam was about 12 mm. The resulting luminosities of almost  $10^{28} \text{ cm}^{-2}\text{s}^{-1}$  were adequate for the programme because of the comparatively large cross section for proton-proton elastic scattering. The effective polarization seen by the COSY beam was diluted by the background of unpolarized hydrogen gas in the COSY ring. This resulted in a variation of the effective polarization across the jet width and its effects in the longitudinal direction were especially important at small angles and had to be taken into consideration.

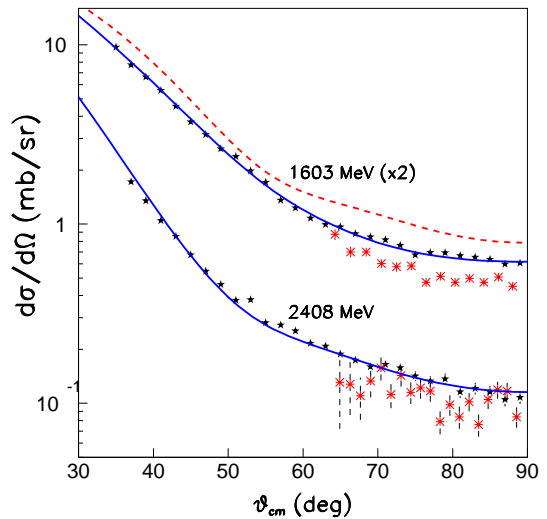


**Fig. 19.** Differential cross sections for elastic proton-proton scattering. The EDDA data (stars) [67] at the two marked beam energies are compared with the SP07 SAID solution and, at the lower energy, with the SM94 solution (dashed curve) [65]. Early data from Ref. [74] are also shown as (red) crosses.

Because of the symmetry of the detector in the azimuthal angle  $\phi$  shown in Fig. 10, EDDA is ideally suited for measuring asymmetries. The polarized differential cross section may be written

$$\frac{d\sigma}{d\Omega} = \left( \frac{d\sigma}{d\Omega} \right)_0 [1 + A_y(Q_y \cos \phi + Q_x \sin \phi)], \quad (3.2)$$

where  $(d\sigma/d\Omega)_0$  is the unpolarized cross section and  $Q_y$  and  $Q_x$  are the target polarizations in the (transverse)  $y$  and  $x$  directions, respectively, which were cycled around the  $+x$ ,  $-x$ ,  $+y$ , and  $-y$  directions. Since, using the  $\phi$  dependence of Eq. (3.2), each of these polarizations would be sufficient for the extraction of  $A_y$ , the extra redundancy allowed the authors to eliminate the false asymmetries that would still be observed with no target polarization.

A typical excitation function at  $\theta_{cm} = 56^\circ$  of the EDDA  $pp$  elastic analyzing power above 1 GeV is shown in Fig. 20, where it is compared to pre- and post-EDDA solutions. This is just a small fraction of the total EDDA data set and the statistical fluctuations would be reduced if wider energy bins were used. However, such a wider binning would not be of any real benefit for the partial wave fits. As an extra consistency check, data were also taken during the deceleration of the COSY proton beam as well as in the acceleration mode.

Angular distributions of  $A_y$  are shown at two energies in Fig. 21, where the EDDA results [37] are compared with small-angle data obtained at ANKE [63] and partial wave solutions [65,73], which will be discussed later in this section.

The culmination of the innovative EDDA campaign was provided by measurements of the spin correlations

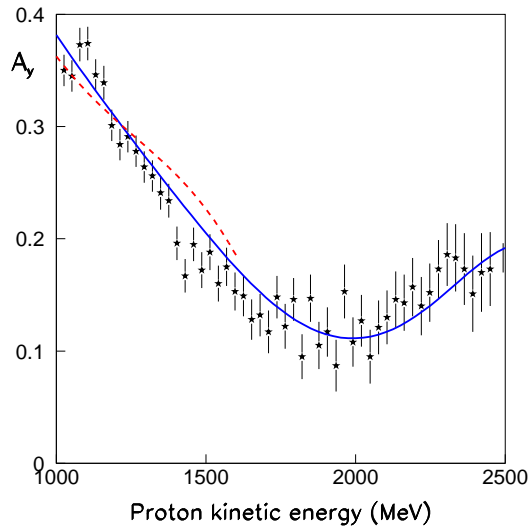


**Fig. 20.** Proton analyzing power in  $pp$  elastic scattering measured by the EDDA collaboration at  $\theta_{cm} = 56^\circ$  as a function of the proton beam energy [37]. The curves correspond to the SAID SP07 (blue solid line) and SM94 (red dashed line) solutions, though the latter is only valid up to 1.6 GeV.

$A_{yy}$ ,  $A_{xx}$ , and  $A_{xz}$  in  $pp$  elastic scattering [69, 70]. For this purpose the operation of the polarized gas jet target described for the  $A_y$  measurements was extended so that the polarization cycle included also  $\pm z$  modes as well as  $\pm y$  and  $\pm x$ . When using a polarized proton beam in conjunction with such a target, the dependence on the azimuthal angle  $\phi$  is more complicated than that of Eq. (3.2) [69]. However, by studying the  $\phi$  variation for different target polarizations it was possible to extract the value of the asymmetry due to the beam in terms of that of the target. Since the target polarization, or equivalently the target proton analyzing power, had been precisely measured in the  $A_y$  studies with an unpolarized beam [37], this led to accurate values of the beam polarizations.

The spin-correlation measurements were carried out using two modes, either as a study of excitation functions with a quasi-continuous beam energy or as a series of ten fixed energies, the so-called flat tops. One critical problem when accelerating polarized protons in a circular machine is handling the depolarizing resonances which, in the most serious cases, is achieved by flipping the proton polarization. Thus, in the vicinity of the  $p_p = 2443$  MeV/ $c$  ( $T_p = 1678$  MeV) resonance the statistics in the excitation functions are rather poor, due to the low beam polarization. The data for  $A_{yy}$  and  $A_{xx}$  shown in Fig. 22 were those obtained at the nine flat tops above 1 GeV at the fixed c.m. angle of  $\theta_{cm} = 57.5^\circ$  [70] compared to the SAID SP07 solution [65].

The angular distributions of  $A_{yy}$  and  $A_{xx}$  at 1.8 GeV are shown in Fig. 23 as functions of the scattering angle. Note that both these observables are symmetric about  $90^\circ$ . The EDDA  $A_{yy}$  results are in reasonable agreement

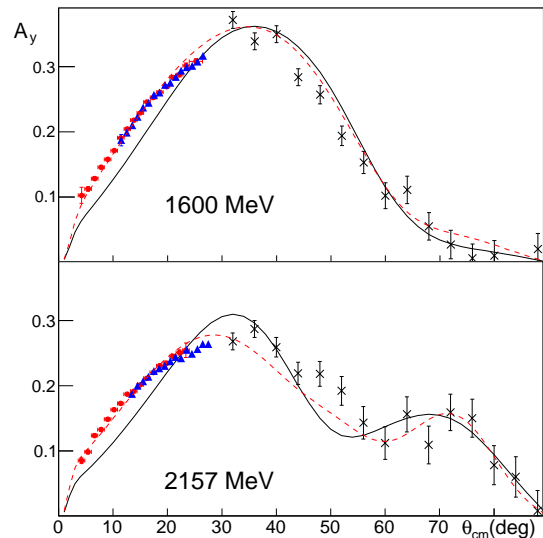


**Fig. 21.** Comparison of the ANKE measurements of the proton analyzing power in  $pp$  elastic scattering at two (out of six) energies using the STT (red filled circles) and FD (blue filled triangles) systems [63] with results from EDDA (black crosses) [37] for energies that differed by no more than 7 MeV. If continuity in energy were imposed, many of the EDDA statistical fluctuations would be significantly diminished. The curves correspond to the SAID SP07 (solid black line) solution [65] and a revised one (dashed red) [73].

with the earlier SATURNE experiment [76] but far less so with the later one [77]. There are no other data to which one could compare the  $A_{xx}$  results. It is seen from both Figs. 22 and 23 that the SAID SP07 solution still needs further refinement if it is to accommodate the EDDA transverse spin correlations. Though considerable effort was put into the measurement of  $A_{xz}$ , all the EDDA results for this observable are consistent with zero and this is in accord with the SAID partial wave analysis [65].

It is hard to overstate the impact that the EDDA data have had on the partial wave analysis of proton-proton elastic scattering above 1 GeV. However, the basic design of EDDA means that measurements could not be carried out with this apparatus for c.m. angles below about  $30^\circ$ . To fill some of the void left by EDDA in this region, measurements of the unpolarized differential cross section [78] and proton analyzing power [63] have been carried out at small angles at several discrete energies at the ANKE facility.

The ANKE measurements differed from those carried out with EDDA in several important respects. At ANKE a polarized proton beam was incident on a hydrogen cluster-jet target so that no C/CH<sub>2</sub> subtraction was required. Furthermore, the ANKE experiments involved single-arm measurements, where the energy of one of the final protons as well as its direction were measured. This allowed the second proton to be identified through the peak in the missing-mass distribution.

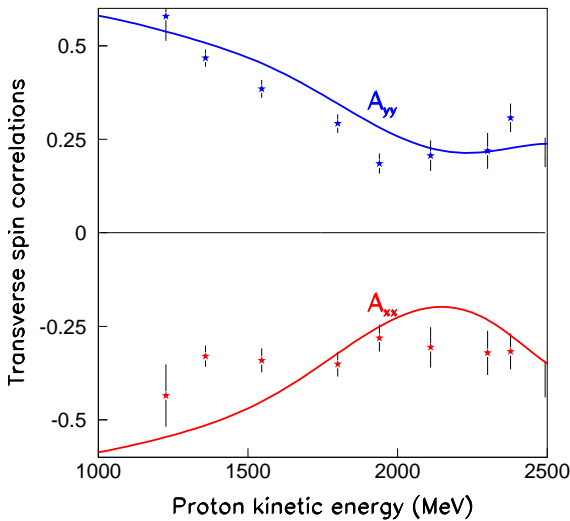


**Fig. 22.** Transverse spin correlations measured by the EDDA collaboration at nine flat tops above 1 GeV at the fixed angle of  $\theta_{cm} = 57.5^\circ$  [70]. These are compared to the results of SAID solution SP07 [65].

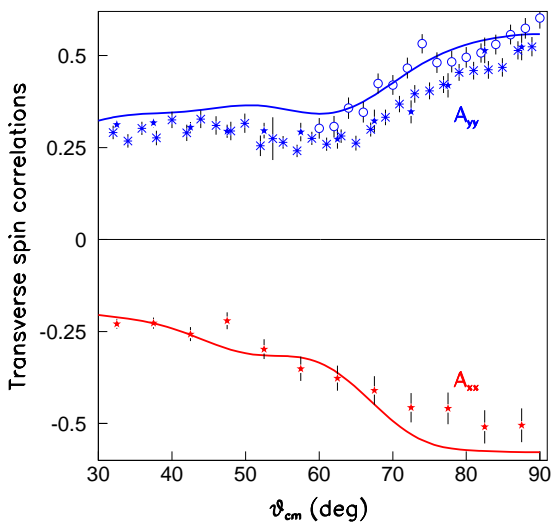


**Fig. 23.** Transverse spin correlations measured by the EDDA collaboration at 1.8 GeV as functions of the scattering angle  $\theta_{cm}$  (stars) [70]. The crosses [76] and open circles [77] represent  $A_{yy}$  data taken in external target experiments at SATURNE. The results are compared to the SAID solution SP07 [65].

Fast protons were measured in the forward detector, which covered  $10^\circ - 30^\circ$  in c.m. polar angles for  $pp$  elastic scattering and  $\pm 30^\circ$  in azimuth, though the polar angle range was cut in order to minimize acceptance uncertainties. In the analyzing power experiment the slower recoil protons were detected in one of the Silicon Tracking Tele-

scopes (STT), described in sect. 2.3. These were placed inside the vacuum chamber near the target, symmetrically to the left and right of the beam. Although there was a large overlap in acceptance angle between the FD and STT data, the latter allowed measurements in c.m. angle down to  $\approx 5^\circ$ . For protons stopping in the third layer of the STT, greater precision in the angle of the recoiling proton was achieved by deducing it from the energy measured in the telescope rather than from a direct angular measurement.

Although there were events where one proton was measured in the FD and the other in the STT, unlike the EDDA experiment, such a coincidence requirement was not placed on the trigger. However, for events where both of the protons were simultaneously measured in the two detectors it was possible to make two determinations of the scattering angle and typically  $\theta_{cm}(\text{STT}) - \theta_{cm}(\text{FD}) \approx 0.3^\circ$ . This offset is fortunately much smaller than the bin width used to present the data.

Just as for the EDDA spin-correlation experiments [69, 70], the use of a (vertically) polarized proton beam necessitated overcoming the depolarizing resonances in COSY. The analyzing power measurements were carried out at 796 MeV and five other fixed beam energies between 1.6 and 2.4 GeV that were well away from the resonances. The values of the six beam polarizations were determined at the end of each COSY cycle using the EDDA polarimeter that was discussed in sect. 2.2.9 [38].

Though not possessing the same azimuthal acceptance as the EDDA detector, the symmetric positioning of the STT did allow the left-right asymmetry to be robustly evaluated. On the other hand, the ANKE forward detector only covered part of one hemisphere and an asymmetry could only be deduced if the relative luminosities for polarizations “up” and “down” could be determined to high precision. This was achieved by comparing the rates of charged particle production in angular regions where the beam polarization could have no influence. As is seen in Fig. 21, the two very different methods gave remarkably consistent results in the overlap region, differences being typically on the 1% level. This agreement suggests that most of the systematic errors in the asymmetry determinations are under control and that the dominant uncertainty arises from the  $\pm 3\%$  of the EDDA polarimeter [38].

Figure 21 also compares the small-angle ANKE results at two beam energies with larger angle taken with EDDA at neighbouring energies. Such a presentation does not reflect fairly the EDDA statistics because their data were obtained at many closely spaced energies. Although there is no overlap in angle between the EDDA and ANKE data, there is no obvious discrepancy between the two experiments. The solid lines represent the predictions of the SAID solution SP07 [65], which was heavily influenced by the combined EDDA data set. Since these curves do not reproduce the rapid variation of the ANKE measurements at small angles, partial wave solutions were sought that included these results along with the EDDA and other data in the fitting process. This resulted in the broken curves in Fig. 21, which reproduce far better the *shapes* defined

by the ANKE points, though even here there seem to be systematic differences at the larger ANKE angles [73].

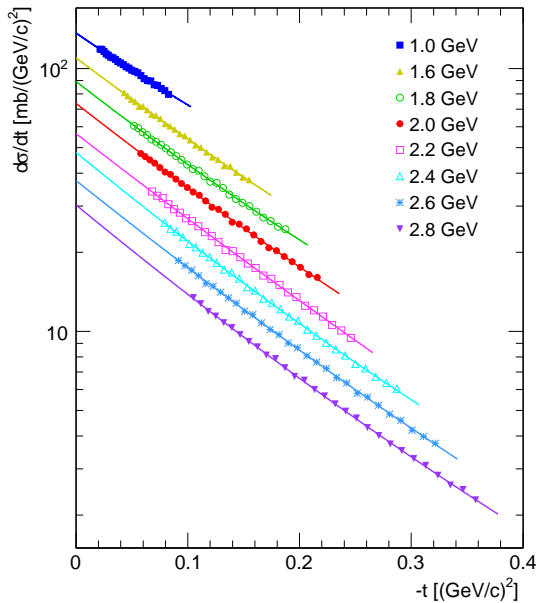


**Fig. 24.** Combined ANKE data set at eight beam energies of  $pp$  elastic differential cross sections with respect to the four-momentum transfer  $t$  [78] compared to fits made on the basis of Eq. (3.3). The correct values are shown at 1.0 GeV but, for clarity of presentation, the data are scaled down sequentially in energy by factors of 1.2. The typical systematic uncertainty is of the order of 3%.

The luminosity in the ANKE measurement of the differential cross section for elastic  $pp$  scattering was evaluated using the so-called Schottky technique discussed in sect. 2.4.1. It was shown here that this was even more accurate than the  $\pm 4\%$  found in the initial experiment [52]. Though the cross section can be deduced from the count rates in either the FD or STT, the acceptance can be more reliably estimated for the forward detector and the results shown in Fig. 24 were obtained using this system.

The energy dependence of the ANKE measurements of the  $pp$  elastic differential cross sections [78] can be seen most clearly in terms of the four-momentum transfer  $t$  and the results at the eight energies are shown in Fig. 24. The data in the measured region vary very smoothly on this logarithmic plot and can be well represented by

$$\frac{d\sigma}{dt} = A \exp(-B|t| + C|t|^2). \quad (3.3)$$

Good fits could be obtained at low energies with  $C = 0$ .

The perfect agreement with the ANL data at 2.2 and 2.83 GeV [79] may be fortuitous because these measurements have a quoted normalization uncertainty of  $\pm 4\%$ . The other data that overlap the ANKE results were obtained at Gatchina at several energies up to 992 MeV using the IKAR recoil detector [80]. These 992 MeV points are about 8% lower in normalization than the ANKE 1000 MeV values.

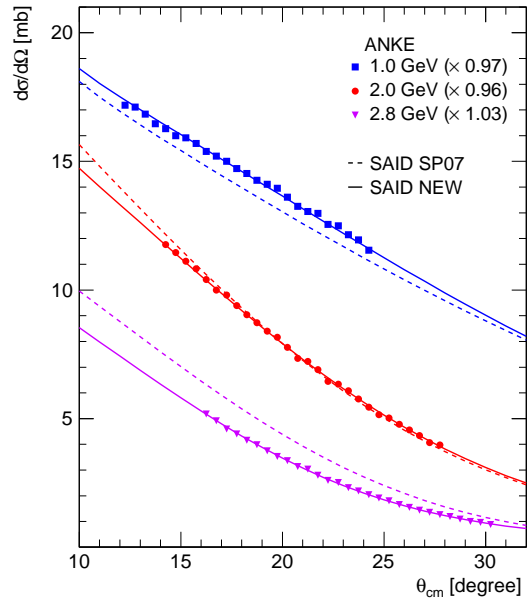


**Fig. 25.** Scaled ANKE proton-proton elastic differential cross sections at 1.0, 2.0, and 2.8 GeV with statistical errors [78] compared to the SAID SP07 solution [65] and a “new” partial wave solution where the ANKE data have been taken into account. For presentational reasons the 2.0 and 2.8 GeV data and curves have been reduced by factors of 0.5 and 0.25, respectively. The best agreement with the new partial wave data was achieved by scaling the ANKE data with factors 0.97, 0.96, and 1.03 at the three energies. The deviations from unity are consistent with the overall systematic uncertainties.

Although the ANKE results are not inconsistent with the EDDA data [66,67], the gap in angle between the two data sets means that one cannot use this as direct evidence in favour of the ANKE normalization. On the other hand, the modified (“new”) SAID partial wave solution of Fig. 25 can describe both data sets provided that the ANKE results are scaled by factors that are consistent with the overall systematic uncertainties [73].

In the forward direction the number of proton-proton elastic scattering amplitudes reduces from five to three and the imaginary parts of these amplitudes are determined completely by the spin-averaged and spin-dependent total cross sections through the generalized optical theorem. The corresponding real parts have been estimated from forward dispersion relations, where these total cross sections provide the necessary input [81]. All the terms contribute positively to the value of  $A$  and, using the optical theorem, the lower bound,  $A \geq (\sigma_{\text{tot}})^2/16\pi$ , is obtained by taking the  $pp$  spin-averaged total cross section  $\sigma_{\text{tot}}$ . This lower bound and the full Grein and Kroll estimates for  $A$  [81] are both shown in Fig. 26.

Before extrapolating to  $t = 0$  the data have to be corrected for Coulomb effects. In the Gatchina case this was done by adding a spin-independent Coulomb amplitude [80] whereas the “new” SAID fit with and without Coulomb provided a means to correct the ANKE data [78]. Both sets of extrapolated values are shown in Fig. 26 and the agreement of the ANKE results with the theoretical

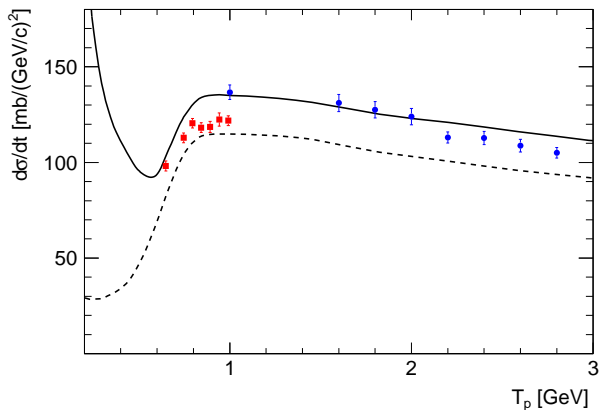


**Fig. 26.** The predictions of Grein and Kroll [81] for the values of the forward  $pp$  elastic differential cross section (solid line), the corresponding lower limit provided by the spin-independent optical theorem being indicated by the broken line. The extrapolated ANKE data are shown with their quoted errors by the (blue) circles [78], whereas the (red) squares are the published Gatchina values obtained with the IKAR recoil detector [80].

curve is very encouraging, It is, however, unfortunate that similar data were not taken below 1 GeV.

The KOALA detector described in sect. 2.3.4 is capable of studying the proton recoils from  $pp$  or  $\bar{p}p$  elastic scattering in the momentum transfer range  $10^{-3} \lesssim |t| \lesssim 10^{-1} (\text{GeV}/c)^2$  [51] so that it covers different regions where the Coulomb, the Coulomb-nuclear interference, and the nuclear are all significant. The detector was tested at COSY by investigating proton-proton elastic scattering at 2.5, 2.8, and 3.2 GeV/ $c$  [82]. The preliminary values obtained for the differential cross sections are shown in Fig. 27, where they are compared with the results from ANL at 2.2 GeV [79]. The overall normalizations of the KOALA data have not yet been determined because the completely pure Coulomb region was not fully accessed and the analysis is still proceeding [83].

It is intriguing to note that, if two KOALA arms had been used at small momentum transfers in the ANKE proton-proton analyzing power experiment [63], the resulting data could have been sensitive to magnetic moment effects and this would have provided extra constraints on the amplitude analysis.

### 3.2 Neutron-proton elastic scattering

Since COSY was not designed for the production of external neutron beams, the only contributions that could be made in neutron-proton elastic scattering have been through quasi-free scattering with a deuterium target or a deuteron beam and several measurements of interest have been performed in this way.

As part of their programme to study the properties of the possible dibaryon found in two-pion production described in sect. 5.2, the WASA-at-COSY collaboration measured the analyzing power in  $np$  quasi-elastic scattering in the vicinity of the dibaryon mass of 2.38 GeV/ $c^2$  [84,

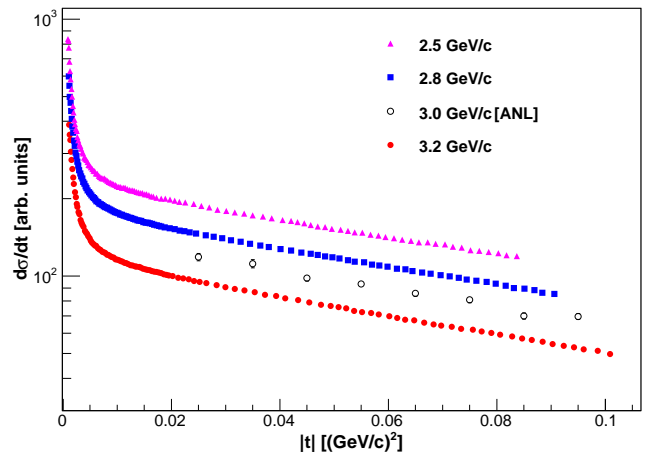


**Fig. 27.** Elastic proton-proton differential cross sections at small momentum transfers  $t$ . The preliminary values measured by the PANDA collaboration with the KOALA detector at 2.5, 2.8, and 3.2 GeV/ $c$  [82] are compared to the angular dependence measured at ANL at 3.0 GeV/ $c$  [79]. The normalizations of the KOALA data at the three momenta are still under study [83] and all data are given in arbitrary units.

85]. For this they used a polarized deuteron beam of the maximum energy available at COSY, viz. 2.27 GeV, and detected the recoil proton in coincidence with the *spectator* proton. The values of the vector and tensor polarizations of the beam were determined using deuteron-proton elastic scattering that had been measured at ANKE [86]. The methodology was also checked by studying in parallel the analyzing power in  $pp$  quasi-elastic scattering.

The design of the WASA detector, with its azimuthal symmetry, makes it very suitable for measuring analyzing powers and the full set of results is shown in Fig. 28. Although the SAID  $np$  analysis has been used up to a beam energy of 1.3 GeV [65], the data upon which it is based are rather sparse above 1.0 GeV and this leads to large uncertainties in its application at the higher energies.

By detecting the spectator proton it is also possible to separate the data into intervals in the total c.m. energy  $\sqrt{s}$ , as for the dibaryon studies in sect. 5.2. However, this was not done for the results shown in Fig. 28 and, instead, the SP07 predictions [65] have been averaged over the c.m. energies produced by the deuteron Fermi momenta, as moderated by the WASA acceptance. It is immediately clear that the SP07 partial wave solution does not reproduce satisfactorily the new WASA measurements. A modified solution that does take these data into account is shown by the dashed curve [87]. The major change compared to SP07 is in the  ${}^3D_3$  wave, where a pole has been generated. This structure therefore gives extra evidence in support of the dibaryon hypothesis discussed in sect. 5.2.

In summary, the WASA results show that the isoscalar part of the SP07 solution is in conflict with data in the 1.135 GeV region. Given the limited number of other measurements available above 1 GeV, it was possible to modify this solution to yield the satisfactory agreement shown in Fig. 28 though, it must be stressed, there may still

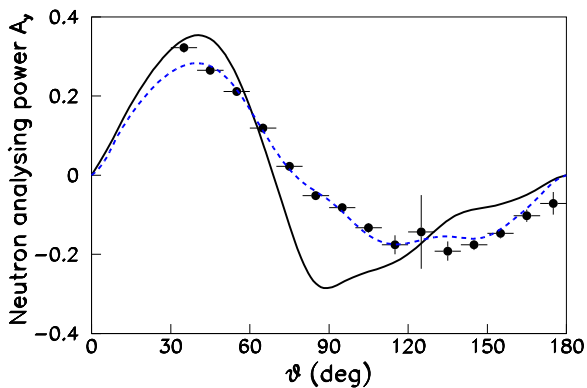


**Fig. 28.** Angular distribution of the neutron analyzing power measured in  $np$  quasi-elastic scattering in the  $\sqrt{s} = 2.377$  GeV region by the WASA-at-COSY collaboration [84]. Also shown by the (black) solid line are the SP07 predictions [65], averaged over the deuteron momentum distribution and the WASA acceptance. An updated SAID solution, similarly averaged, is shown by the (blue) dashed line.

be ambiguities in this revised solution. The partial wave solutions are considered in Ref. [87], where double-spin experiments that might clarify the dibaryon hypothesis are discussed. There are, in fact, other measurements at COSY that have questioned the validity of the SAID  $np$  SP07 partial wave solution at 1.135 GeV, and we now turn to these.

It has been known for many years that the charge exchange of deuterons on hydrogen,  $\vec{d}p \rightarrow \{pp\}_s n$ , is very sensitive to the deuteron tensor polarization provided that the excitation energy  $E_{pp}$  in the recoiling proton pair is low [88]. In this case the diproton is dominantly in an  $S$ -wave and the Pauli principle then demands that the proton spins are antiparallel in the  $^1S_0$  configuration. There is therefore a spin-isospin flip from the  $(S, I) = (1, 0)$  of the deuteron to  $(0, 1)$  of the diproton. At small momentum transfers between the deuteron and diproton the transition amplitudes are well described in impulse approximation in terms of the three spin-spin small angle neutron-proton charge-exchange amplitudes, i.e., the three spin-spin large angle neutron-proton elastic amplitudes [88, 89].

There has been an extensive programme at ANKE to study the charge exchange of polarized deuterons on hydrogen and, by using a polarized target, this was also extended to include measurements of deuteron-proton spin correlations. The polarized deuterium ion source at COSY is capable of producing beams with a variety of vector ( $p_z$ ) and tensor ( $p_{zz}$ ) polarizations. The  $z$ -direction indicated here is the quantization axis in the polarized source system and this is relabeled as the  $y$ -direction in the COSY frame. This is perpendicular to the COSY ring, i.e., along the direction of the holding fields, and it is only in this direction that the polarization is not modified by the spin precession.

Although some information on the beam polarizations was available from the low energy and EDDA polarime-

ters at 75.8 MeV and 270 MeV, respectively, the ANKE collaboration wished to measure the polarizations at the energy of the primary experiment. This was achieved by comparing the results for various nuclear reaction, viz.  $\vec{d}p \rightarrow {}^3\text{He} \pi^0$ ,  $\vec{n}p \rightarrow d \pi^0$ , and  $\vec{d}p$  elastic scattering, with values obtained in external target experiments [90]. Following this procedure, no evidence was found for deuterons being depolarized during acceleration and this is completely consistent with the absence of depolarizing resonances for deuterons over the entire COSY energy range. Using these values of the beam polarization, together with neutron-proton elastic scattering amplitudes taken from the SAID PWA [65], the impulse approximation described well the  $dp \rightarrow \{pp\}_s n$  differential cross section and tensor analyzing powers at 1.17 GeV [91]. Since this reaction is easily identified, and has a large figure of merit, the results at the neighbouring energy of 1.2 GeV were used in all the subsequent ANKE experiments to determine the tensor polarization of the beam. This is very much in the spirit of the original work, which proposed that the reaction could be used as the basis of a tensor polarimeter for deuterons [88].

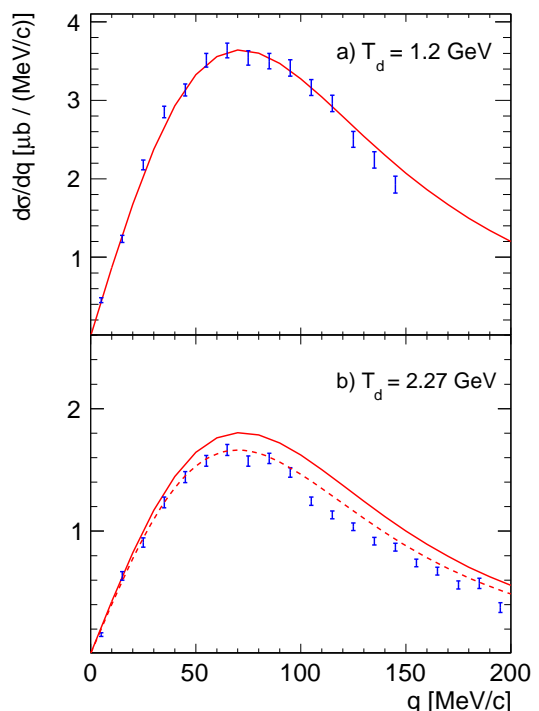


**Fig. 29.** Differential cross sections for the  $dp \rightarrow \{pp\}_s n$  reaction at 1.2 and 2.27 GeV [92] compared with impulse approximation predictions based upon the SAID SP07 solution [65]. The data are integrated over  $E_{pp} < 3$  MeV. Only statistical errors are shown; The systematic uncertainty of  $\approx 5\%$  is particularly large at 2.27 GeV. The dashed curve at this energy corresponds to the longitudinal  $np$  spin-spin amplitude being reduced by 25%.

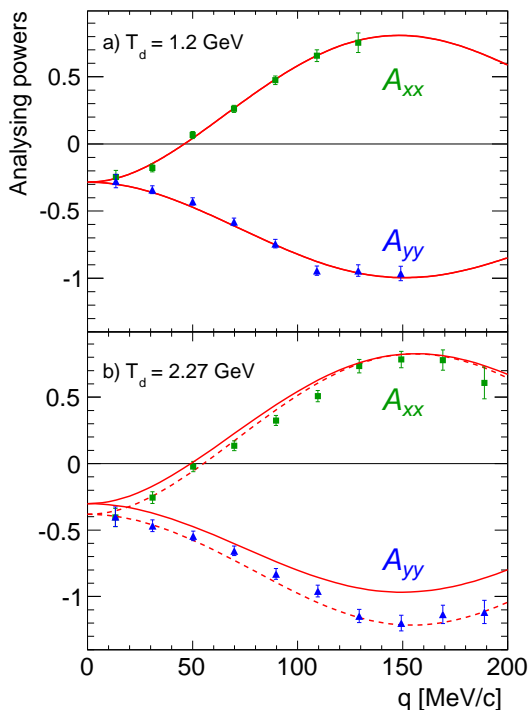


**Fig. 30.** Tensor analyzing powers  $A_{xx}$  (squares) and  $A_{yy}$  (triangles) of the  $\vec{d}p \rightarrow \{pp\}_s n$  reaction at 1.2 and 2.27 GeV for  $E_{pp} < 3$  MeV [92] compared to impulse approximation predictions based upon the SAID SP07 solution [65]. The dashed curves at 2.27 GeV correspond to a uniform reduction of the spin-longitudinal amplitude by 25%. In addition to the error bars shown, there could be an overall uncertainty of up to 4% in the beam polarization at 2.27 GeV.

Measurements of the differential cross section and tensor analyzing powers of the  $\vec{d}p \rightarrow \{pp\}_s n$  reaction were made at 1.2, 1.6, 1.8, and 2.27 GeV at ANKE using an unpolarized hydrogen cluster-jet target [92,93]. The results at the lowest and highest energy are shown in Figs. 29 and 30, where they are compared to impulse approximation predictions based upon the SAID SP07 solution [65]. Whereas the data are well reproduced at 1.2 GeV, as they are also at 1.6 GeV and 1.8 GeV, serious discrepancies are evident at 2.27 GeV, despite the fact that the impulse approximation approach should get better as the energy is increased. In order to see whether these could be explained as arising from the  $np$  input, the spin-longitudinal input amplitude at 1.135 GeV was reduced uniformly by an *ad hoc* factor of 0.75. This results in much better agreement for the analyzing powers and reduces significantly the discrepancy for the cross section at 2.27 GeV, though it should be noted that the systematic uncertainty in the luminosity (5%) is particularly large at this energy.

The spin-correlation experiments were carried out at 1.2 and 2.27 GeV, with a deuteron beam with a limited set of polarization modes, incident on a teflon-coated (closed) aluminum storage cell target, fed with a jet of polarized atomic hydrogen [92,93]. The polarization of the target was flipped between “up” and “down” every five

seconds. Both the polarization of the hydrogen target and the vector polarization of the deuteron beam were determined from measurements of the analyzing power of the  $\vec{n}p \rightarrow d\pi^0$  reaction.

By using a polarized gas target, it was possible to measure also the proton analyzing power in the  $d\vec{p} \rightarrow \{pp\}_s n$  reaction. The impulse approximation model reproduces the  $A_y^p$  data very well at 1.2 GeV but fails completely at 2.27 GeV, which is a strong indication of problems with the spin-orbit amplitude in the isospin-zero part of the SP07 solution [65].

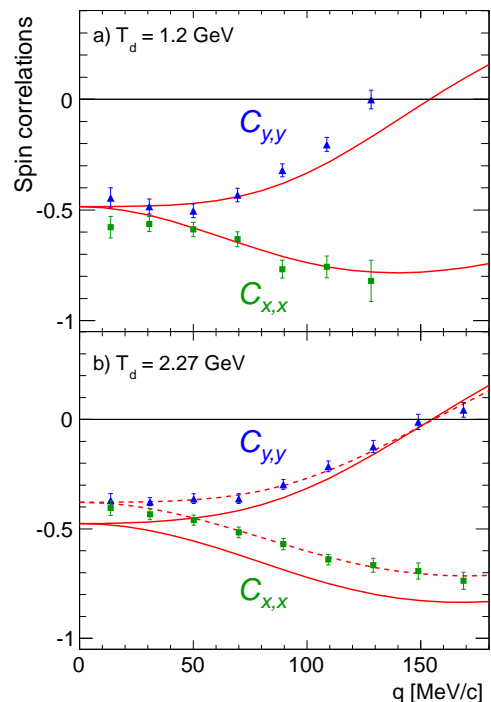


**Fig. 31.** Spin-correlations  $C_{x,x}$  and  $C_{y,y}$  for the  $dp \rightarrow \{pp\}_s n$  reaction at  $T_d = 1.2$  GeV and 2.27 GeV for  $E_{pp} < 3$  MeV [92] compared to impulse approximation predictions [89]. The dashed curves at 2.27 GeV correspond to the longitudinal  $np$  spin-spin amplitude being reduced by 25%.

The spin-correlation results are shown in Fig. 31 and the message here is very similar to that given by the other ANKE data. Though there is broad agreement with the model at 1.2 GeV, at 2.27 GeV the theoretical description is improved significantly if the longitudinal  $np$  spin-spin input is reduced by 25%.

It is immediately obvious from looking at the four figures that the ANKE data are reasonably well described by the model at 600 MeV per nucleon but the agreement is less satisfactory at 1.135 GeV, where the model should be more reliable. The deviations in the differential cross section are on the 10-15% level, as they are also for the deuteron tensor analyzing powers and the spin correlations. These discrepancies can be largely eliminated if the  $np$  longitudinal spin-spin amplitude is reduced by a factor



of 0.75. This should not be taken as proof of the validity of such a reduction; rather it indicates that a revised  $np$  partial wave solution could give a much better description of the ANKE data. The situation is even more extreme for the proton analyzing power since this shows that the spin-orbit term is very badly described in the SP07 solution.

To put some of these discrepancies into context, and to link up to the WASA neutron analyzing power experiment [85], one sees from Figs. 30 and 31 that the measured values of  $A_{xx}$  and  $C_{x,x}$ , extrapolated to  $q = 0$ , are  $-0.38 \pm 0.03$  and  $-0.39 \pm 0.05$ , respectively, where uncertainties in the beam and target polarizations have been included. These are to be compared to the SP07 predictions shown in the figures of  $-0.30$  and  $-0.48$ . On the other hand, the revised  $np$  partial wave solution discussed in connection with the WASA data [85] yields rather  $-0.42$  and  $-0.31$ , respectively. Given that the new solution is far from being unambiguous with respect to observables in this region, the fact that the changes from SP07 are both in the right direction and are of the right order of magnitude, is very promising. Thus both the WASA  $np$  analyzing power measurement and the ANKE deuteron charge-exchange data indicate in similar ways that the SAID SP07 solution [65] requires modification at 1.135 GeV.

In order to go to higher energies in quasi-free interactions on the deuteron at COSY one must use a deuterium target rather than a deuteron beam. A feasibility test was carried out at ANKE with a 600 MeV unpolarized proton beam incident on the cell target that had been fed with polarized deuterium atoms from the ABS [94]. Protons from a charge exchange then had very low energies and these were detected in STT placed to the left and right of the target. The values of  $A_{yy}$  extracted from these data at low  $E_{pp}$  showed good continuity in three-momentum transfer  $q$  with those obtained with a deuteron beam [92]. The major drawback of the deuterium target approach is that it is not possible with the current STT to investigate the region where  $E_{pp}$  and  $q$  are simultaneously small.

Since there were successful measurements at ANKE of the analyzing power in elastic  $pp$  scattering at small angles that were shown in Fig. 21 [63], it is natural to wonder whether similar data could be obtained in quasi-free  $\bar{p}n$  elastic scattering. For this purpose the collision of a polarized proton beam with a deuterium cluster-jet target was studied at 796 MeV and five other beam energies from 1.6 to 2.4 GeV and these data are still under analysis [95]. The fast proton was measured in the forward detector and the supposed *spectator* proton in one of the two STT that were placed symmetrically inside the vacuum chamber to the left and right of the beam. The  $\bar{p}d \rightarrow \bar{p}pn$  reaction could then be identified through the missing-mass peak corresponding to the undetected neutron. Just as in the  $pp$  case, the proton beam polarization was established on the basis of measurements with the EDDA polarimeter. Although the data are broadly similar to the measured free  $np$  elastic analyzing power at 796 MeV, the paucity of the database above 1.3 GeV has limited the influence of the ANKE results.

The deuteron charge exchange reactions discussed in this section so far are *soft* processes, where the momentum transfer between the initial deuteron and the final diproton is very low. These are not to be confused with the large momentum transfer  $pd \rightarrow \{pp\}_s n$  reactions where, in the c.m. frame, the diproton emerges in the backward direction with respect to the incident deuteron. The kinematics are then very similar to those of proton-deuteron backward elastic scattering. The unpolarized differential cross section for *hard* proton-deuteron breakup was measured at ANKE at ten proton beam energies from 0.5 GeV to 2.0 GeV with the standard  $E_{pp} < 3$  MeV cut [96,97] and the results are shown in Fig. 32.

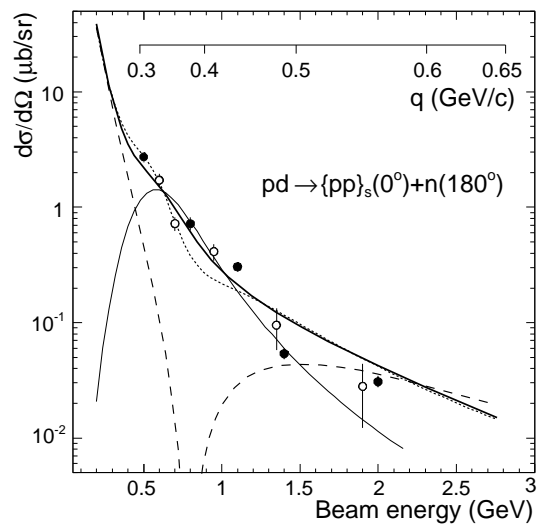


**Fig. 32.** Differential cross section in the c.m. frame for the  $pd \rightarrow \{pp\}_s n$  reaction averaged over the angular interval  $172^\circ - 180^\circ$  versus the beam energy. The experimental points are taken from the ANKE experiments of Ref. [96] (open circles) and Ref. [97] (closed circles). The predictions of one nucleon exchange are shown by the dashed line and those of the  $\Delta$  mechanism by the thin solid line. The total predictions of the model, including small single-scattering contributions, are shown by the thick solid line [97]. The upper scale shows the internal momentum  $q$  of the nucleons in the deuteron (or diproton) for the one nucleon exchange.

It should be noted that, throughout the energy range shown in Fig. 32, the differential cross section for the backward  $pd \rightarrow \{pp\}_s n$  reaction is about two orders of magnitude less than that for  $pd \rightarrow dp$ . However, it was suggested many years ago that backward proton-deuteron elastic scattering at high energies may be driven by the virtual excitation of the  $\Delta(1232)$  isobar and estimates of its effects were derived in a phenomenological model using a  $\pi^+ d \rightarrow pp$  input [98,99] and a similar approach was initiated for diproton production [100].

At low energies one would expect the reaction to be dominated by purely nucleonic degrees of freedom, so that the main driving term is that of one proton exchange, which depends on the wave functions of the deuteron and

diproton. In the calculations of Ref. [97], this predicts a node for  $T_p \approx 0.8$  GeV and in this region the  $\Delta$  provides the main contribution. Taking into account also small effects from impulse approximation terms, the overall theoretical description given in Fig. 32 is reasonable and it reinforces the suggestion that  $\Delta$  degrees of freedom cannot be ignored in high momentum transfer reactions even if they only involve initial and final nucleons.

In a further investigation, the proton analyzing power  $A_y$  in the  $\bar{p}d \rightarrow \{pp\}_s n$  reaction was also measured near the backward direction at 0.5 GeV and 0.8 GeV [101]. It is interesting to note that at 0.8 GeV  $A_y$  remains small over the measured angular range from  $167^\circ$  to  $180^\circ$  whereas at 0.5 GeV it becomes very large below  $170^\circ$ . This different behaviour might be linked to the dominance of different driving terms seen in Fig. 32. However, since  $A_y$  represents an interference between amplitudes, it is hard to draw firm conclusions from such data.

#### 4 Single non-strange meson production in nucleon-nucleon collisions

The energy range of COSY is such that it is possible to produce non-strange mesons in nucleon-nucleon collisions with masses up to that of the  $\phi$ . This section will detail the COSY efforts in this field, though the  $\phi$  itself will be considered in sect. 8.2 since its detection is intimately connected with kaon pair production.

However, before we go into details of specific reactions, we show in Fig. 33 the total cross sections for meson production near threshold in proton-proton scattering in terms of the total c.m. energy  $W$  minus twice the proton mass. This figure, which is an update of that presented in a 2002 review [102], shows the overwhelming contribution that COSY has made in the field from the  $\eta$  to kaon pair production. It is extended even further in sect. 7 to encompass hyperon production, where the COSY data are completely dominant.

##### 4.1 Phenomenological description

In a reaction such as  $pn \rightarrow pn\eta'$  near threshold, the interaction of the  $\eta'$  with either of the two recoiling nucleons is quite weak. In contrast there is a very strong Final State Interaction (FSI) between the neutron and proton which might even lead to the formation of a deuteron. Although this could be taken into account by constructing an  $np$  final-state wave function, it is nevertheless useful to have simple closed-form expressions that describe semi-quantitatively the main effects observed in the production of both non-strange and strange mesons. This has been achieved in a series of papers [103,104,105,106] and the principal results of the approach are outlined here before the individual experiments are discussed.

The starting point is the observation that for a real local potential the bound state wave function  $u(r)$  and scattering state wave function  $v(k, r)$  are intimately linked. If

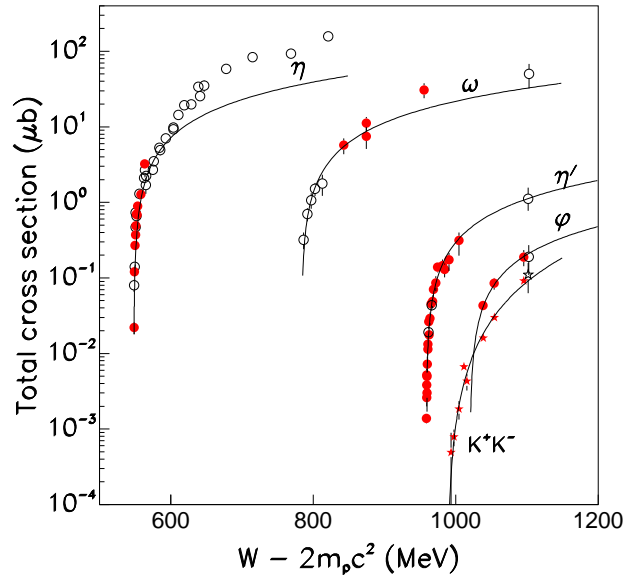


**Fig. 33.** Total cross sections near threshold for  $pp \rightarrow pp\eta$ ,  $pp \rightarrow pp\omega$ ,  $pp \rightarrow pp\eta'$ ,  $pp \rightarrow pp\phi$ , and  $pp \rightarrow ppK^+K^-$  as functions of the total c.m. energy available for meson production. The (red) circles and stars represent COSY measurements while the open (black) symbols were obtained at other laboratories. The phenomenological curves are discussed with the specific reactions.

these are chosen to satisfy real boundary conditions, then in the  $S$ -wave

$$v(k, r) \approx -\frac{1}{\sqrt{2\alpha(\alpha^2 + k^2)}} u(r). \quad (4.1)$$

Here  $k$  is the relative momentum in the scattering state and  $\alpha^2 = m_{\text{red}}B$ , where  $B$  is the binding energy of two particles with reduced mass  $m_{\text{red}}$ . The result is exact when extrapolated to the pole at  $k^2 = -\alpha^2$ , but it is generally a good first approximation at small  $r$  and  $k$ .

If the meson production operator is of short range, Eq. (4.1) shows that the final  $S$ -wave triplet contribution to the differential cross section for  $pp \rightarrow np\pi^+$  should be related to that for  $pp \rightarrow d\pi^+$  through

$$\frac{d^2\sigma}{d\Omega dx}(pp \rightarrow np\pi^+) \approx \frac{q(x)}{q(-1)} \frac{\sqrt{x}}{2\pi(x+1)} \frac{d\sigma}{d\Omega}(pp \rightarrow d\pi^+). \quad (4.2)$$

The dimensionless variable  $x$  is defined as  $x = Q_{pn}/B_{I=0} = k^2/2m_{\text{red}}B_{I=0}$ , where  $q(x)$  and  $q(-1)$  are the momenta of the pion in the three- and two-body reactions, respectively. The excess energy  $Q_{pn}$  is the total c.m. energy in the  $pn$  system minus the rest masses. In some of the literature it is denoted by  $\varepsilon$ .

It is important to note that Eq. (4.2) only predicts the  $S$ -wave spin-triplet  $np$  production in a truly model-independent way as  $x \rightarrow -1$ . Thus it breaks down at large

$x$  when  $P$  and higher waves become important and the shape dependence of the  $S$ -wave is significant. It also assumes that the distortion introduced by pion-nucleon scattering is similar for the two- and three-body final states. More subtly, it ignores the coupling between the  $S$  and  $D$  waves through the  $np$  tensor force. These drawbacks will come to the fore when discussing the Big Karl experiment in sect. 4.3.3.

Equation (4.2) is useful in the description of the high energy tail of inclusive pion production, i.e., small  $x$ , even away from threshold but it can also be integrated analytically to predict the energy dependence of the total cross section near threshold. If the deuteron production cross section varies like phase space,  $\sigma_d \approx D\sqrt{Q}$ , then, using non-relativistic integration, the three-body total cross section behaves as

$$\sigma_{I=0}(Q) \approx \frac{1}{4}D\sqrt{Q} \left( \frac{Q}{B_{I=0}} \right)^{3/2} \left( 1 + \sqrt{1 + Q/B_{I=0}} \right)^{-2}, \quad (4.3)$$

where  $Q$  is the excess energy for either the two- or three-body final state. It is, however, important to repeat that this formula only corresponds to  $S$ -wave spin-triplet  $np$  final states. The formula can be extended to take into account the more complex energy dependence seen in  $pp \rightarrow d\pi^+$  near threshold [106].

For the spin-singlet final states, which are relevant in the  $pp \rightarrow pp\pi^0$  reaction, there is no bound state to which one can normalize the cross section, i.e., there is no equivalent of Eq. (4.3). Nevertheless there is a pole corresponding to a virtual state very close to threshold with a “binding” energy  $B_{I=1} \approx 0.5$  MeV. We would then expect this feature to dominate the  $pp \rightarrow pp\pi^0$  reaction close to threshold to give an energy dependence of the form

$$\sigma_{I=1}(Q) \approx C \left( \frac{Q}{B_{I=1}} \right)^2 \left( 1 + \sqrt{1 + Q/B_{I=1}} \right)^{-2}, \quad (4.4)$$

Equation (4.4) is often used to describe reactions such as  $pp \rightarrow K^+ \Lambda p$  or  $pp \rightarrow ppn'$  but in the latter case one must realize that there is some ambiguity in the value chosen for  $B_{I=1}$  because the formula neglects the Coulomb repulsion between the two protons.

The approach can easily be extended to the case where the final state interaction is described by the more complete Jost function  $(k-i\alpha)/(k+i\beta)$ . The results of Eq. (4.2) should be multiplied by  $(\beta^2+k^2)/(\beta^2-\alpha^2)$  and an analytic formula has been derived for the near-threshold energy dependence of the corresponding total production cross section [107].

## 4.2 Hard bremsstrahlung in proton-proton scattering

The photon is clearly not a meson, but it is nevertheless convenient to consider its production here because the principle of measuring the  $pp \rightarrow pp\gamma$  reaction by detecting the two protons and reconstructing a missing-mass peak is identical to that used extensively at COSY for several mesons. Indeed the cross section for hard bremsstrahlung

production is often obtained as a by-product of a study of the  $pp \rightarrow pp\pi^0$  reaction.

The threshold for  $\pi^0$  production in  $pp$  collisions is at about 280 MeV and so, when the first  $pp \rightarrow pp\gamma$  experiment was carried out at COSY-TOF at 293 MeV [108], pion production was much reduced by the proximity to threshold. Since no large-acceptance photon detector was then available at COSY, the reaction was studied by detecting the two protons in the most basic version of the COSY-TOF spectrometer. Peaks in the  $pp$  missing-mass distribution were seen that corresponded to the production of the  $\pi^0$  and the  $\gamma$ . The latter suffered from a large random background, whose shape was determined from empty-target measurements.

In most of the earlier hard bremsstrahlung experiments carried out at other laboratories, the two protons were measured in pairs of counters placed on either side of the beam line and, as a consequence, they had little or no acceptance at small  $pp$  excitation energy. A total cross section was estimated by summing data taken at different angles. In contrast, a large fraction of the  $pp \rightarrow pp\gamma$  phase space was covered in a single setting at COSY-TOF and this allowed a Dalitz plot to be constructed. For low  $pp$  invariant masses, i.e., energetic photons, there was a coverage of over 95%. The coplanar photon angular distributions that could be extracted from the COSY-TOF data were shown to be in good agreement with earlier results, though there was an overall 20% normalization uncertainty.

A notable feature of these data is that there was no obvious evidence for the production of the  $^1S_0$  enhancement of the  $pp$  final state, which was seen in the TOF data on pion production. This could of course be a statistical fluctuation arising from the small number ( $< 1500$ ) of events, of which only a tiny fraction would fall in the FSI region. Alternatively, it was argued that the effect might be caused by the electromagnetic transition operator coupling only weakly to a spin-singlet  $pp$  state [108]. This latter possibility was excluded by a later experiment at CELSIUS, where a large FSI enhancement was seen in the 58,000  $pp \rightarrow pp\gamma$  events measured using a similar missing-mass technique [109,110]. The beam energy of 310 MeV was only slightly higher than that used at COSY-TOF and the windowless target in the CELSIUS experiment meant that the random background was almost non-existent. However, it must be noted that the CELSIUS data at small  $pp$  excitation energy are strongly forward peaked [109] and this might affect the measured COSY-TOF statistics [108].

In complete contrast to the large geometric acceptance of the COSY-TOF detector, the ANKE facility can only measure fast protons emerging at small angles with respect to the beam direction. This means that the acceptance for two protons from a  $pp \rightarrow ppX$  reaction is maximal when these have similar momentum vectors, i.e., the excitation energy  $E_{pp}$  in the final  $pp$  rest frame is small. In such cases the Pauli principle requires the diproton to be in the  $^1S_0$  configuration. Taking a cut with  $E_{pp} < 3$  MeV, the group made small angle measurements of  $pp \rightarrow \{pp\}_s\gamma$

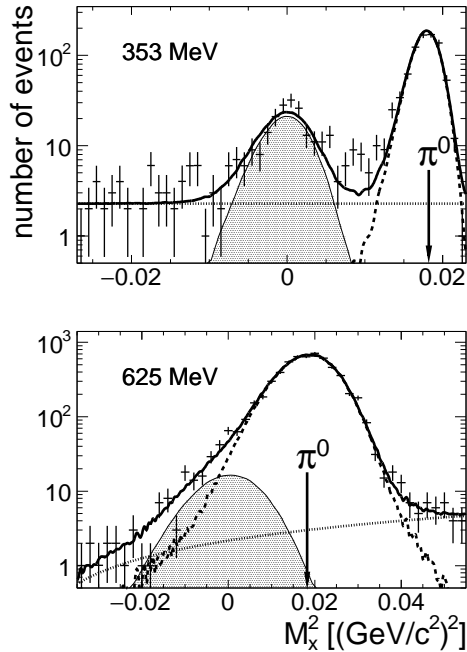


**Fig. 34.** Distributions in the square of the missing mass in the  $pp \rightarrow \{pp\}_s X$  reaction at beam energies of 353 and 625 MeV for proton pairs with  $\theta_{pp} < 20^\circ$  [111,112]. The expected  $\pi^0$  position is indicated by the arrow. In the fits, the shaded area corresponds to the  $\gamma$  peak, the dashed line to the  $\pi^0$  peak, the dotted to the linear accidental background, and the solid to the sum of these three contributions.

at six energies between 353 MeV and 800 MeV [111,112]. Such small angle studies were possible at ANKE because of the absence of a beam-pipe hole.

Missing-mass distributions from the ANKE experiment are shown for two beam energies in Fig. 34 [111,112]. Although there is no real difficulty in identifying the  $\gamma$  peak at 353 MeV, the same is not true at 625 MeV where, for kinematic reasons, the  $\pi^0$  peak is considerably wider. The bremsstrahlung reaction could then only be isolated through a careful fitting process.

The luminosity  $\mathcal{L}$  in the ANKE experiments was determined from the number of elastically scattered protons detected in parallel and these led to normalization uncertainties that varied between about 3% and 5%, depending upon the energy. In the c.m. frame the  $\gamma$  polar angle  $\theta_\gamma$  is  $180^\circ$  minus the diproton angle and in Fig. 35 the ANKE data at four energies are shown in terms of  $\cos^2 \theta_\gamma$ . The CELSIUS 310 MeV data have also been evaluated for the  $E_{pp} < 3$  MeV cut [109] and the one point that falls within the ANKE domain is also shown. At 310 MeV it might be reasonable to keep just the lowest multipoles, viz.  $E1$  and  $M2$ , and these would lead to a linear dependence of the cross section on  $\cos^2 \theta_\gamma$ . The fit to the CELSIUS data,  $0.27 + 4.27 \cos^2 \theta_\gamma$ , which is also plotted, corresponds to a forward enhancement, whereas the ANKE higher energy data show evidence for some suppression for small  $\theta_\gamma$ .

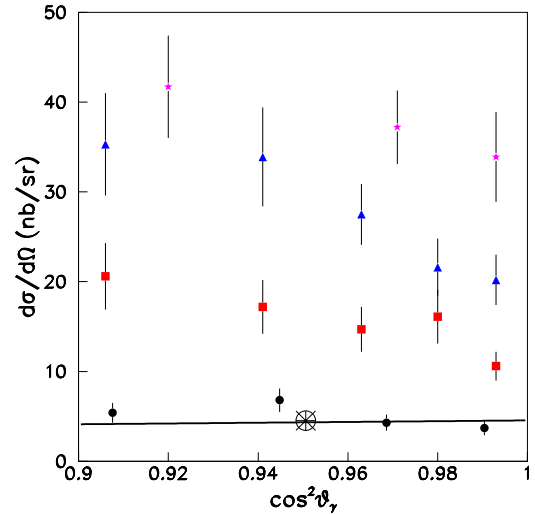


**Fig. 35.** Angular dependence of the differential cross section for the  $pp \rightarrow \{pp\}_s \gamma$  reaction at four beam energies measured at ANKE [111,112]. Experimental results are shown at 353 MeV by (black) circles, at 500 MeV by (red) squares, at 550 MeV by (blue) triangles, and at 700 MeV by (magenta) stars. Also shown by the (black) circled cross is the one point in this angular domain measured at CELSIUS at 310 MeV [109]; the straight line is the fit to all the 35 CELSIUS points .

The integral of the ANKE cross section for  $0^\circ < \theta_\gamma < 20^\circ$  is maximal for a beam energy at around 650 MeV and the authors [112] argue that this might be associated with a  $\Delta(1232)N$  intermediate state in a relative  $P$ -wave, the  $S$ -wave being forbidden by selection rules.

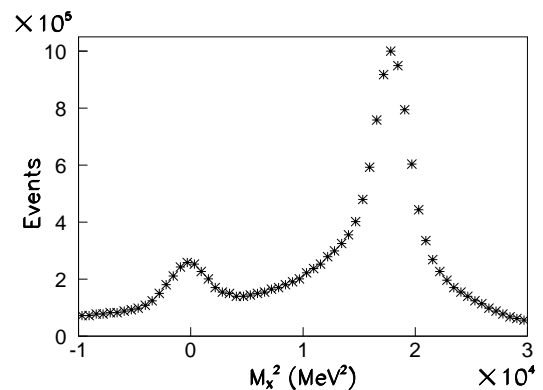


**Fig. 36.** Missing-mass-squared distribution for the two protons from the  $pp \rightarrow pp \gamma$  measured with the COSY-WASA detector at 550 MeV [113]. These preliminary results were obtained by measuring the photon in coincidence and putting a cut on its c.m. energy relative to that of the two protons.

It is clear from looking at Fig. 34 that the identification of the  $pp \rightarrow pp\gamma$  reaction through the missing-mass peak becomes more difficult as the beam energy is raised. This problem can be circumvented by measuring directly the photon as well as the two protons in the WASA detector. In the preliminary missing-mass spectrum taken at a beam energy of 550 MeV and shown in Fig. 36 there is a peak containing about  $1.3 \times 10^6$  events at zero missing mass sitting on a smooth background associated mainly with photons that come from  $\pi^0$  decay [113]. Here both protons were detected in the WASA Forward Detector and about the same statistics are available where one of the protons was measured in the Central Detector, though it must be realized that the resolution on the momentum of this proton is poorer than that of the one entering the Forward. The only cut applied to these data is that the missing energy of the two protons in the c.m. frame should be at least 100 MeV bigger than the photon energy. This criterion, which does not eliminate good  $pp \rightarrow pp\gamma$  events, is responsible for producing the clear bremsstrahlung peak in Fig. 36 at 550 MeV despite there being little sign of it in Fig. 34 at 625 MeV.

Though the energy cut is useful way of obtaining a reliable estimate on the number of bremsstrahlung events, a much more robust way of eliminating the background comes from noting that, in the c.m. frame, a single photon should move in the opposite direction to the proton pair. Thus, in a two-dimensional plot of  $\theta_{pp} + \theta_\gamma$  versus  $|\phi_{pp} - \phi_\gamma|$  there is a clear island of  $pp \rightarrow pp\gamma$  events centred at  $180^\circ \times 180^\circ$  which extends only a few degrees in either direction.

This data set probably represents the largest collection of clean  $pp \rightarrow pp\gamma$  events ever obtained above the pion production threshold but results are not yet available on the differential cross sections [113].

### 4.3 Single pion production in nucleon-nucleon collisions

At the start up of most new accelerators some of the first experiments that are performed involve pion production from nuclear targets. The general aim of such tests is to find optimal conditions for the creation of pion beams but, since at COSY there were no plans to use secondary pion beams, all research in this area was focussed on the understanding of the underlying reaction mechanisms. A useful description of meson production more generally is to be found in Ref. [114].

It has already been stressed that COSY-TOF has the big advantage of a large geometric acceptance which is so important when measuring reactions with three or more particles in the final state far away from threshold. The only other spectrometer at COSY with large acceptance is WASA, but this has a hole in the detector to allow the unscattered beam to emerge. This subtends an angle of about  $3^\circ$  in the laboratory and, if either proton from say a  $pp \rightarrow ppX$  reaction is produced within this cone, the event is lost. This becomes more problematic at low energies where, as threshold is approached, more and

more events fall into the beam pipe trap. Since there is a strong proton-proton final state interaction, it has been argued [115] that results of the near-threshold missing-mass measurements carried out at IUCF [116] and the PROMICE-WASA facility at CELSIUS [117] have significant model dependence caused, in part, by uncertainties in the Monte Carlo estimation of the acceptance.

A  $pp \rightarrow pp\pi^0$  experiment was carried out at three energies very close to threshold by detecting the two final protons at COSY-TOF [115]. The luminosity was established by measuring in parallel elastic proton-proton scattering for which the uncertainty in the differential cross section is less than 5%. Since the cross section for pion production varies very fast with energy in the near-threshold region, it was equally important to establish this energy to high precision. This was achieved by measuring both final particles in the two-body  $pp \rightarrow d\pi^+$  reaction, which determined the proton beam energy to 0.3 MeV.

The measured total cross sections for excess energies between about 6 and 9 MeV seem to be about 50% higher than those found at IUCF [116] and CELSIUS [117] and the COSY-TOF authors speculated that this might be associated with the beam-pipe problem in these two experiments. This could have significant implications for the value of the  $s$ -wave  $\pi^0$  production amplitudes but a greater energy range would be needed to confirm this. Such a programme was indeed carried out for  $\eta$  and  $\eta'$  production at COSY11, and this will be discussed in sect. 4.4.

Pion production in unpolarized proton-proton collisions was also studied well away from threshold at a beam energy of 397 MeV [118,119]. Since the momenta of all three particles in the  $pp \rightarrow pp\pi^0$  reaction were measured or reconstructed over a very large fraction of phase space, an intrinsic problem was choosing which variables to use in the presentation of the data. One that is of great interest to other experiments at COSY and CELSIUS is that of the angular distribution of the pion in bins of the excitation energy  $E_{pp}$  in the final two-proton system.

If the data in the c.m. frame are parameterized in the form  $d\sigma/d\Omega \sim 1 + b \cos^2 \theta_\pi$ , the COSY-TOF data yield  $b = -1.00 \pm 0.02$  for  $E_{pp} < 3$  MeV and  $b = -0.17 \pm 0.01$  for the whole data sample. The corresponding numbers obtained in the PROMICE-WASA (CELSIUS) experiment at 400 MeV [117] are  $b = -0.58 \pm 0.03$  and  $b = +0.19 \pm 0.01$ , respectively. There are therefore unresolved systematic differences that are much larger than the statistical uncertainties. As discussed in sect. 4.3.2, the ANKE data at 353 MeV [120] seem to be consistent with the PROMICE-WASA results at 360 MeV [117].

Since the two incident protons are identical, the pion c.m. angular distribution must be symmetric about  $90^\circ$  and this is one test of whether systematic effects are under control. Although this was successfully passed for the  $\pi^0$  at COSY-TOF [118], the group only measured  $\pi^+$  data in one hemisphere. There were also clearly problems in one hemisphere of the CELSIUS experiment when the two photons from the  $\pi^0$  decay were detected in coincidence with the two protons [121].

Though the experimental procedures were very similar for the  $pp \rightarrow pn\pi^+$  reaction measured in parallel at 397 MeV [119], the results were significantly different because the data were dominated by the onset of the  $J^P = 2^+ \Delta(1232)N$  intermediate state. A cut had to be imposed to stop leakage from the  $pp \rightarrow d\pi^+$  reaction, where the deuteron broke up in a secondary reaction. The strong angular dependence, where the pion is produced preferentially along the beam direction, which is illustrated in Fig. 37, is very similar to that of  $pp \rightarrow d\pi^+$ . The measured slope parameter is  $b = 2.8 \pm 0.1$  compared to  $b \approx 3.6$  for the  $pp \rightarrow d\pi^+$  reaction [122].

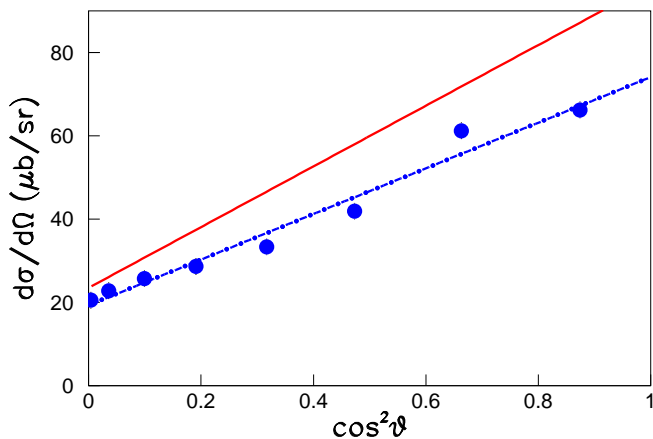


**Fig. 37.** Differential cross section for the  $pp \rightarrow pn\pi^+$  reaction at 397 MeV in terms of the pion angle  $\theta$  [119]. The best straight line fit (dashed blue) gives an integrated cross section of  $(470 \pm 20) \mu\text{b}$  whereas the FSI model of Ref. [106] (solid red) predicts about  $600 \mu\text{b}$ .

Of course, in the case of the three-body final state there are also  $S$ -wave spin-singlet  $pn$  contributions and these have been estimated from the  $pp \rightarrow pp\pi^0$  data in the phenomenological model presented in sect. 4.1 [106], whose results are also shown in Fig. 37. In this approach it is assumed that the  $\pi^+d$  final state is produced by a fusion of the spin-triplet proton and neutron pair in the three-body  $\pi^+pn$  channel in a final state interaction. Starting from experimental data on  $pp \rightarrow d\pi^+$ , an evaluation of the final state interaction model at 397 MeV gives  $b \approx 3.1$ , which is very close to the COSY-TOF value [119].

The FSI model also predicts [106] a  $pp \rightarrow pn\pi^+$  total cross section of about  $600 \mu\text{b}$  at 397 MeV compared to an experimental value of  $(470 \pm 20) \mu\text{b}$  [119], where the error bar is the authors' estimate of the systematic uncertainty. Given the uncertainties in both the measurement and the calculation, the experimental result could be consistent with the theoretical estimate. This reinforces the COSY-TOF conclusion that it is the same intermediate state that governs both the  $d\pi^+$  and  $pn\pi^+$  channels. While accepting this, it may be a step too far to agree with the authors' suggestion that both production are associated with an isovector  $2^+$  dibaryon [119]!

To obtain information on pion production in the isospin-zero channel requires data from neutron-proton collisions and, in the absence of neutron beams at COSY, this necessarily involves the use of a deuteron beam or target. The former is clearly more suitable for COSY-TOF because the *spectator* proton is then fast and all four charged particles from  $dp \rightarrow ppp\pi^-$  can be measured. In an initial experiment [123] the group showed that it was possible to isolate the spectator proton ( $p_{\text{sp}}$ ) so that the resulting data could be interpreted in terms of quasi-free  $np \rightarrow pp\pi^-$  production.

Due to the Fermi motion of the neutron inside the deuteron, a measurement of  $dp \rightarrow p_{\text{sp}}pp\pi^-$  provides a scan of  $np \rightarrow pp\pi^-$  over a range of excess energies. This was exploited in the second COSY-TOF experiment [124], which was carried out at a beam energy of 759 MeV. The value of the excess energy  $Q$  depended primarily on the momentum vector of the spectator proton and the overall energy resolution was estimated to be about 8 MeV. The data were therefore put into six bins in  $Q$  between 0 and 90 MeV.

The pion angular distributions for the six mean values of  $Q$  are shown in Fig. 38. It should be noted that the angle is here defined with respect to the direction of the incident (virtual) neutron and not the proton that was used for the ANKE data [125] shown in Fig. 42, where only events with the final  $pp$  excitation energy  $E_{pp} < 3$  MeV were considered. After taking this angle definition into account, one sees some similarities between the COSY-TOF and ANKE data.

It is seen from Fig. 38 that, even at the highest excess energy, the data can be represented by a quadratic in  $\cos\theta_\pi$ , which is a reflection of the dominance of low partial waves in this reaction. No attempt was made to determine the absolute luminosity and the data were normalized to PSI measurements with free neutrons [126] that are shown in the figure at 54 MeV.

Though the COSY-TOF data show evidence for a  $pp$  FSI, the data do not allow the angular distributions to be displayed in bins of  $pp$  excess energy. A simple estimate of the total cross section for  $E_{pp} < 3$  MeV from the  $pp$  effective mass distributions of Ref. [124] would suggest a somewhat lower value than the ANKE result [125] discussed in sect. 4.3.2, but such an evaluation is very crude.

#### 4.3.1 The $pp \rightarrow d\pi^+$ reaction

Over the last sixty years there have been countless measurements of the  $pp \rightarrow d\pi^+$  or the inverse  $\pi^+d \rightarrow pp$  reaction. One therefore has to wonder if it is possible for COSY to add useful information in this field. Nevertheless, there are two experiments that are worthy of note.

The GEM collaboration measured the  $pp \rightarrow d\pi^+$  differential cross section with the Big Karl spectrometer at five c.m. energies up to 3.6 MeV [128,29]. They checked isospin invariance by comparing the integrated Coulomb-corrected cross sections with those obtained for  $np \rightarrow d\pi^0$ . This is clearly not without problems because, unless one has a good reaction model, Coulomb corrections are

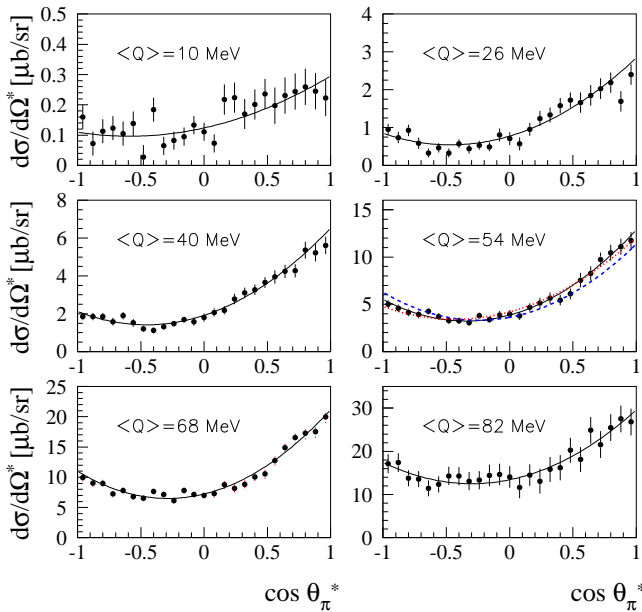


**Fig. 38.** Angular distributions of the  $\pi^-$  from the quasi-free  $np \rightarrow pp\pi^-$  reaction with respect to the neutron direction for selected mean excess energies  $\langle Q \rangle$ . The COSY-TOF data [124] are shown together with quadratic fits in  $\cos\theta_\pi$ . The data are normalized at  $\langle Q \rangle = 54$  MeV to the PSI results [126], shown by the dashed (blue) curve. The earlier results of Handler [127] at this energy are parameterized by the dotted (red) curve.

somewhat ambiguous and pion mass differences are significant. Furthermore, absolute cross sections always present a challenge with neutron beams.

Far less contentious were the group's measurements of the angular distributions, an example of which is shown in Fig. 39. Due to having identical protons in the initial channel, the cross section is symmetric about  $90^\circ$  in the c.m. frame, so that it is a function of  $\cos^2\theta$ . It also means that there can be no interference between even and odd pion waves so that the first deviations from isotropy must arise from either  $s$ - $d$  interference or the squares of  $p$ -wave amplitudes. Since  $s$ -wave pion production is expected to be generally weak, the second of these options would seem to be the more likely.

The data in Fig. 39 are consistent with a linear behaviour,  $d\sigma/d\Omega = a_0 + a_2 \cos^2\theta$  and the same is true for the GEM data at lower energies. At 3.6 MeV the parameters are  $a_0 = (3.31 \pm 0.59) \mu\text{b/sr}$  and  $a_2 = (1.54 \pm 0.33) \mu\text{b/sr}$  so that, even very close to threshold, the differential cross section displays significant anisotropy. The near-threshold GEM data are consistent with  $a_2/a_0 \approx 11\eta^2$ , where  $\eta$  is the pion c.m. momentum in units of the pion mass. The ratio is, of course, independent of the uncertainties in the absolute normalization, and may provide a more robust method to check charge independence. Some evidence of isospin breaking in the pion  $p$ -waves was shown many years ago in measurements of  $\pi^\pm p$  and  $\pi^\pm d$

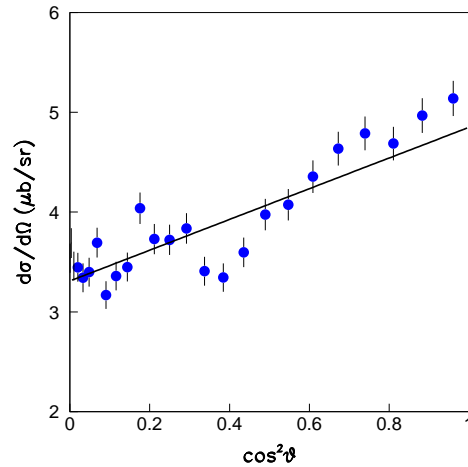


**Fig. 39.** The differential cross section for the  $pp \rightarrow d\pi^+$  reaction 3.6 MeV above threshold in the c.m. frame [128,29]. The curve is the group's straight line fit to the data in terms of  $\cos^2\theta$ .

total cross sections [129] and this might be relevant for the value of  $a_2$ .

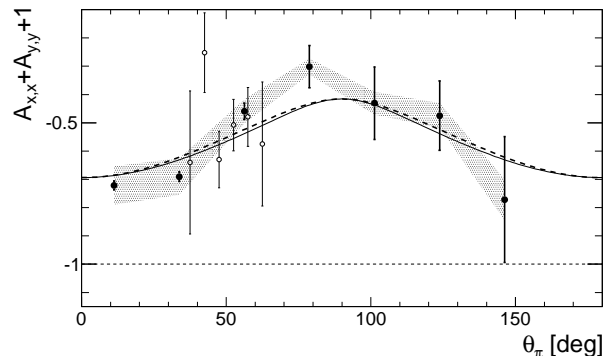


**Fig. 40.** The combination  $1 + A_{x,x} + A_{y,y}$  measured in the  $\bar{n}\bar{p} \rightarrow d\pi^+$  reaction at 353 MeV [130] as a function of the pion c.m. angle  $\theta_\pi$  (closed circles) compared with the SAID  $\bar{p}\bar{p} \rightarrow d\pi^+$  predictions (dashed curve) [122]. Statistical uncertainties are shown with error bars; systematic uncertainties are illustrated with shaded bands. Also presented are IUCF data for  $A_{z,z}$  taken at 350 MeV for the  $\bar{p}\bar{p} \rightarrow d\pi^+$  reaction (open circles) [131] and the SAID prediction for this observable (solid curve).

Since there is only one isospin amplitude, all the spin observables in the  $pp \rightarrow d\pi^+$  and  $np \rightarrow d\pi^0$  reactions should be identical. As by-products of other studies, there were measurements at ANKE of the spin correlations  $A_{x,x}$  and  $A_{y,y}$  in the quasi-free  $np \rightarrow d\pi^0$  reaction at 353 and 600 MeV [130]. Figure 40 shows the ANKE measurements of the combination  $1 + A_{x,x} + A_{y,y}$  at 353 MeV, together with the SAID prediction [122] of this observable. If one

neglects pion  $d$ -waves, which the SAID analysis suggests is a very good approximation at 353 MeV, this observable is identical to the longitudinal spin-correlation parameter  $A_{z,z}$ , for which there are some measurements from IUCF [131]. Though these have large error bars, they are not incompatible with the ANKE results. All the ANKE data [130] are consistent with the current SAID  $pp \rightarrow d\pi^+$  solution and no sign was found for any breaking of isospin invariance.

#### 4.3.2 Partial wave analysis of the $NN \rightarrow \{pp\}_s\pi$ reaction

There were pioneering measurements of the  $pp \rightarrow \{pp\}_s\pi^0$  differential cross section carried out at the CELSIUS storage ring at a series of beam energies from close to threshold up to 425 MeV [117]. Here the  $\{pp\}_s$  denotes a proton-proton pair with low excitation energy  $E_{pp}$  such that the Pauli principle forces them to be in the  $^1S_0$  state. The CELSIUS group chose to impose the cut  $E_{pp} < 3$  MeV and, even if this is a little arbitrary, it became the standard for most subsequent experiments carried out at ANKE.

In some ways the  $pp \rightarrow \{pp\}_s\pi^0$  reaction is an ideal one to study at COSY because the  $^1S_0$  diproton configuration means that there are no spin degrees of freedom in the final state that have to be determined through a double-scattering measurement. The differential cross section was measured at 800 MeV at ANKE [132] by detecting both protons in the Forward Detector, with the  $\pi^0$  being recognized from the peak in the missing-mass spectrum. However, this restricted the angular coverage to diproton c.m. angles less than about  $15.4^\circ$ . The measurements were later extended to cover the energy range from about 500 MeV to 2.0 GeV, but always in a similar small angle region [133].

The quasi-two-body  $pp \rightarrow \{pp\}_s\pi^0$  reaction is kinematically very similar to that of  $pp \rightarrow d\pi^+$ , though it must be noted that an intermediate  $S$ -wave  $\Delta(1232)N$  state, which is so important for  $\pi^+$  production, is not allowed in the  $\pi^0$  case. As a consequence, it is expected that the maximum cross section would occur at a somewhat higher energy, and that was precisely what was seen in the ANKE data [133]. Furthermore, the ratio of  $\pi^0$  production to that of  $\pi^+$  through these (quasi) two-body processes increases with energy, albeit from a very low base. However, the only *ab initio* theoretical estimation of  $\pi^0$  production with a low  $E_{pp}$  cut [134] fails completely to describe the experimental data. It should be noted though that there can be delicate cancellations between different partial waves. This was shown more clearly in an amplitude analysis that took into account new ANKE measurements of the analyzing power. This provided evidence for resonance structure in both  $s$ - and  $d$ -wave  $\pi^0$  production [135].

The most ambitious programme of measurements was carried out at 353 MeV per nucleon, where the aim was to perform a full spin-isospin analysis of pion production leading to the  $^1S_0$  diproton state. It was then hoped that this would lead to the isolation of a term that was relevant for chiral perturbation theory [136]. Such experiments are only possible at ANKE close to threshold where the spectrometer acceptance covers a large fraction of the

solid angle. The programme involved the measurement of the differential cross section and analyzing power in  $pp \rightarrow \{pp\}_s\pi^0$  [120], the differential cross section and analyzing power in quasi-free  $\vec{p}\vec{n} \rightarrow \{pp\}_s\pi^-$  with a deuterium target [137], and the analyzing powers and spin-correlations in quasi-free  $\vec{n}\vec{p} \rightarrow \{pp\}_s\pi^-$  with a polarized deuteron beam and a polarized hydrogen cell target [125].

The  $pp \rightarrow \{pp\}_s\pi^0$  study was carried out in a similar manner to the earlier  $\pi^0$  experiments at ANKE [132, 133], but it is important to realize that the differential cross section is symmetric about  $90^\circ$  and the analyzing power is antisymmetric. This feature provides a useful extension to the limited ANKE acceptance. So close to threshold one would expect only low partial waves to contribute and the ANKE data shown in Fig. 41 are consistent with the behaviour  $d\sigma/d\Omega = a_0 + a_2 \cos^2 \theta$  and  $A_y d\sigma/d\Omega = b_1 \sin 2\theta$ . Even if one only considers terms up to pion  $d$ -waves, there are three complex amplitudes that can contribute and the information from the three real parameters must be supplemented by other constraints in order to achieve a full amplitude decomposition.

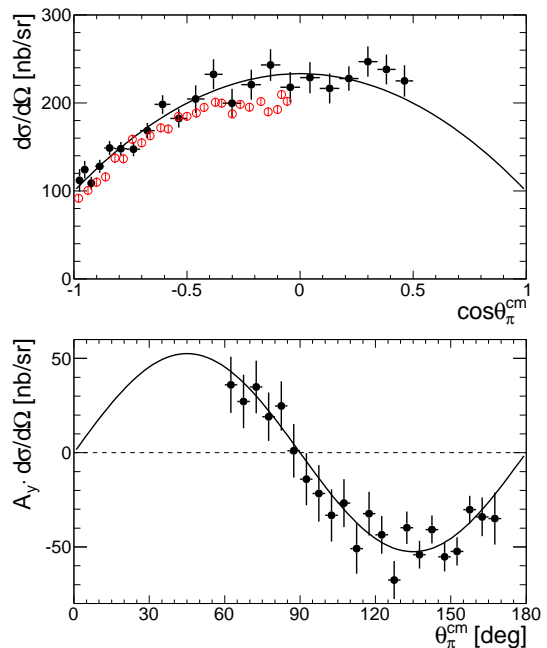


**Fig. 41.** Upper panel: Differential cross section for the  $pp \rightarrow \{pp\}_s\pi^0$  reaction at 353 MeV as a function of the cosine of the pion c.m. angle. The solid (black) circles represent the ANKE measurements [120] whereas the open (red) circles are CELSIUS data obtained at 360 MeV [117]. The curve is a linear fit in  $\cos^2 \theta_\pi$  to the ANKE data. Lower panel: The corresponding product of the measured analyzing power and differential cross section for the  $\vec{p}\vec{p} \rightarrow \{pp\}_s\pi^0$  reaction [120]. The curve is of the form  $b \sin 2\theta$ , where the parameter  $b$  is fitted to the data.

Studies of the  $pn \rightarrow \{pp\}_s\pi^-$  reaction were carried out in two stages, the first with a polarized proton beam incident on a deuterium pellet target [137]. The full kinematics were determined by detecting either the spectator



proton in an STT or the produced  $\pi^-$  in the negative detector, in coincidence with the diproton pair. In the subsequent experiment, a polarized deuteron beam collided with a polarized hydrogen cell [125]. In this case the fast spectator proton was measured in the forward detector of ANKE and the diproton pair in the positive detector. In both cases the momentum of the spectator in the deuteron rest frame was restricted such that the spread in effective energies was not as wide as in the COSY-TOF experiment [124].

The most important information obtained from the  $np$  experiments is summarized in Fig. 42. This shows the measurements of the differential cross section, the proton analyzing power  $A_y^p$ , and the transverse spin correlation  $A_{x,x}$ , where  $x$  lies in the horizontal COSY plane, perpendicular to the beam direction  $z$ . Also shown are the predictions of three possible amplitude analyzes.

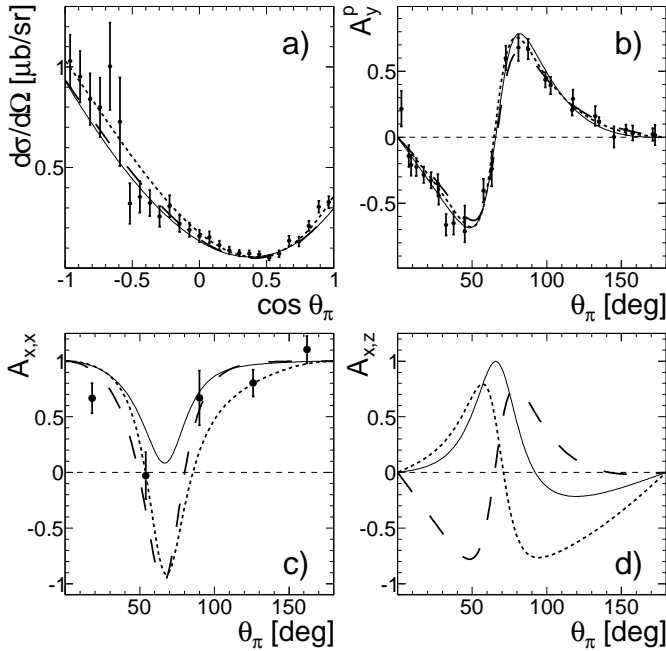


**Fig. 42.** Predictions of the partial wave analysis for the polarized  $pn \rightarrow \{pp\}_s \pi^-$  reaction at 353 MeV with the  $E_{pp} < 3$  MeV cut. The full, long-dashed, and short-dashed lines correspond to solutions 1, 2, and 3, respectively. The ANKE experimental data with statistical errors correspond to a) the differential cross-section [137], b)  $A_y^p$  [125], and c)  $A_{x,x}$  [125]. There are no experimental data to compare with the predictions for  $A_{x,z}$  shown in panel d).

In addition to the three isospin-one amplitudes needed to describe the  $pp \rightarrow \{pp\}_s \pi^0$  observables up to pion  $d$  waves, two more isospin-zero amplitudes are required for the  $pn \rightarrow \{pp\}_s \pi^-$  data. Since the  ${}^3P_0$ ,  ${}^3P_2$ , and  ${}^3F_2$   $pp$  waves are either uncoupled or weakly coupled, the authors [120] assumed the Watson theorem and took the phases of the pion production amplitudes to be the same as those of elastic proton-proton scattering. Taken together with the data shown in Fig. 41, this fixes com-

Amplitude	Real	Imaginary
Solution 1: $\chi^2/ndf = 101/82$		
${}^3P_0 \rightarrow {}^1S_0s$	$53.4 \pm 1.0$	$-14.1 \pm 0.3$
${}^3P_2 \rightarrow {}^1S_0d$	$-25.9 \pm 1.4$	$-8.4 \pm 0.4$
${}^3F_2 \rightarrow {}^1S_0d$	$-1.5 \pm 2.3$	$0.0 \pm 0.0$
${}^3S_1 \rightarrow {}^1S_0p$	$-37.5 \pm 1.7$	$16.5 \pm 1.9$
${}^3D_1 \rightarrow {}^1S_0p$	$-93.1 \pm 6.5$	$122.7 \pm 4.4$
Solution 2: $\chi^2/ndf = 103/82$		
${}^3P_0 \rightarrow {}^1S_0s$	$52.7 \pm 1.0$	$-13.9 \pm 0.3$
${}^3P_2 \rightarrow {}^1S_0d$	$-28.9 \pm 1.6$	$-9.4 \pm 0.5$
${}^3F_2 \rightarrow {}^1S_0d$	$3.4 \pm 2.6$	$0.0 \pm 0.0$
${}^3S_1 \rightarrow {}^1S_0p$	$-63.7 \pm 2.5$	$-1.3 \pm 1.6$
${}^3D_1 \rightarrow {}^1S_0p$	$-109.9 \pm 4.2$	$52.9 \pm 3.2$
Solution 3: $\chi^2/ndf = 106/82$		
${}^3P_0 \rightarrow {}^1S_0s$	$50.9 \pm 1.1$	$-13.4 \pm 0.3$
${}^3P_2 \rightarrow {}^1S_0d$	$-26.3 \pm 1.5$	$-8.5 \pm 0.5$
${}^3F_2 \rightarrow {}^1S_0d$	$2.0 \pm 2.5$	$0.0 \pm 0.0$
${}^3S_1 \rightarrow {}^1S_0p$	$-25.4 \pm 1.9$	$-7.3 \pm 1.5$
${}^3D_1 \rightarrow {}^1S_0p$	$-172.2 \pm 5.6$	$92.0 \pm 6.2$

**Table 3.** Values of the real and imaginary parts of the amplitudes for the five lowest partial waves deduced from fits to the ANKE measurements at 353 MeV.

pletely the values of the three complex  $I = 1$  amplitudes given in Table 3. Particularly striking is the fact that the production from the initial  ${}^3F_2$  state is consistent with zero.

On the other hand the  ${}^3S_1$  and  ${}^3D_1$  waves are strongly coupled by the tensor force and so it is much harder to justify invoking the Watson theorem in this case. Fortunately, the extra  $np$  information contained in Fig. 42 allows a complete amplitude reconstruction, apart from some discrete ambiguities. The three possible solutions are listed in Table 3 and the resulting predictions for the observables are shown in Fig. 42.

The phase assumptions in the  $I = 1$  case mean that there are no discrete ambiguities in the  $pp \rightarrow \{pp\}_s \pi^0$  analysis and the three solutions presented in Table 3 lead to indistinguishable curves in the two panels of Fig. 41. In contrast, in the  $np$  case there are three solutions that are statistically very similar. As shown in Fig. 42d, a measurement of the spin correlation parameter  $A_{x,z}$  in the  $pn \rightarrow \{pp\}_s \pi^-$  reaction would allow one to resolve these discrete ambiguities. However, such a measurement could only be carried out with a polarized deuterium cell and would require a Siberian snake to rotate the spin of the incident proton into the beam direction. The latter facility was not available before the termination of the hadron physics programme at COSY.

It is nevertheless interesting to study the phases of the two pion  $p$ -wave amplitudes from the three solutions given in Table 3, which are  $(\text{Im}({}^3S_1 \rightarrow {}^1S_0p)/\text{Re}({}^3S_1 \rightarrow {}^1S_0p), \text{Im}({}^3D_1 \rightarrow {}^1S_0p)/\text{Re}({}^3D_1 \rightarrow {}^1S_0p)) = (-0.44, -1.32), (0.02, -0.48),$  and  $(0.29, -0.53)$  for solutions 1, 2, and 3, respectively<sup>3</sup>. These can be compared with the nucleon-

<sup>3</sup> We are here using the standard notation of  $L\ell$ , where  $L$  is the angular momentum in the  $NN$  system and  $\ell$  is the angular momentum of the meson with respect to the  $NN$ .

nucleon phase-shift analysis values of  $(\tan \delta_{3S_1}, \tan \delta_{3D_1}) = (0.03, -0.46)$  [65], which are well within the error bars of Solution 2. If Solution 2 were indeed the correct one, then it would suggest that the concerns over the use of the Watson theorem for coupled channels might be less serious than feared and this can have important consequences for the modeling of meson production. However, if the *truth* corresponded to one of the other solutions, one would have to explain why the phases had suffered such severe modifications.

#### 4.3.3 Comparison of $pp \rightarrow pn\pi^+$ and $pp \rightarrow d\pi^+$

The FSI approach discussed in sect. 4.1 predicts the differential cross sections for  $S$ -wave spin-triplet  $np$  production in the  $pp \rightarrow \pi^+pn$  reaction in terms of the cross section for  $pp \rightarrow \pi^+d$  [104], as shown in Eq. (4.2). The theorem is derived on the assumption that the  $np$  potential is local and that the coupling induced by the tensor force can be neglected. Though, under these conditions, the theorem is exact when extrapolated to the bound state pole, deviations in the physical region are minimized if the pion production operator is of short range. The relation given in Eq. (4.2) was tested in several experiments at COSY.

The ANKE  $pp \rightarrow \pi^+np$  experiment at 492 MeV [138] used a  $\text{CH}_2$  target but isolated the production on the proton by measuring the final  $p\pi^+$  pairs in coincidence. The normalization was assured by measuring also pions coming from the  $\pi^+d$  final state, though greater care had to be taken here with the carbon background and this was one contributor to the overall systematic uncertainties of approximately 8%. The width of any spin-singlet contribution was determined by the angular integration in the ANKE data rather than the intrinsic energy resolution of the apparatus.

The ANKE results were successfully discussed in the framework of the FSI theorem of Eq. (4.2). The shape of the  $np$  spectrum for an excitation energy  $E_{np} < 3$  MeV can be explained in terms of pure spin-triplet production and an upper limit of any spin-singlet production of about 10% was found. This limit is not really competitive with the direct measurements of spin-singlet production in the  $pp \rightarrow pp\pi^0$  channel discussed earlier in this section. To improve on this limit requires better effective resolution and also the simultaneous measurement of the  $\pi^+d$  and  $\pi^+np$  final states under identical conditions in order to eliminate any normalization ambiguities. A pure hydrogen target is clearly preferable for this purpose. These criteria were met in experiments carried out by the GEM collaboration using the Big Karl spectrometer [139,140].

The Big Karl experiments were carried out at 401, 601, and 951 MeV. Only the  $\pi^+$  was detected in the spectrometer, set close to the forward direction. In order to optimize the resolution, a liquid hydrogen target of only 2 mm thickness was used, with windows made of  $1 \mu\text{m}$  Mylar. As can be seen from the 951 MeV data [139] shown in Fig. 43, a resolution of  $\sigma = 97$  keV was achieved on the deuteron peak and this was sufficient to put stringent bounds on the

production of the very narrow peak that would correspond to the  $np$  spin-singlet final state.

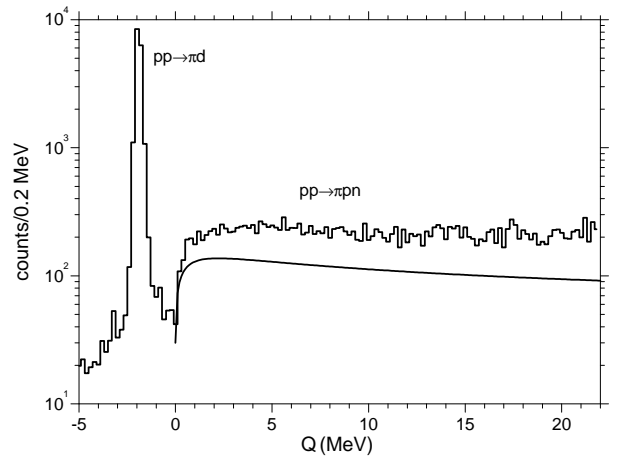


**Fig. 43.** The results from the first Big Karl experiment (histogram) [139] compared with the prediction (curve) of the  $S$ -wave final state interaction theorem of Eq. (4.2) [104] for pure spin-triplet  $pn$  production.

Though corrections for acceptance, etc., were included, these varied relatively little for  $Q < 20$  MeV so that the data provide a robust measurement of the ratio of the production of the  $\pi^+pn$  and  $\pi^+d$  final states. Also shown in the figure is the prediction of Eq. (4.2), where the normalization was taken from the area of the deuteron peak. Though the shape is similar to that of the experimental spectrum, it is too low by a factor of  $N = 2.2 \pm 0.1$ . This factor is reduced to about 1.8 if the model-dependent term  $(\beta^2 + k^2)/(\beta^2 - \alpha^2)$  is included with the value of  $\beta = 0.927 \text{ fm}^{-1}$ , taken from the spin-triplet scattering length and effective range.

Deviations from Eq. (4.2) were also studied at the two lower energies measured, where normalization factors of  $N = 0.51 \pm 0.06$  and  $1.06 \pm 0.04$  were required at 401 MeV and 601 MeV, respectively [140]. The authors could not explain the energy dependence of  $N$  in terms of the  $np$  tensor force and the resulting deuteron  $D$ -state. Instead they suggested that the culprit might be the long-range part of the pion production operator associated with on-shell intermediate pions. It should be noted in this context that  $N$  changes from below to above unity at an energy that corresponds to the  $\Delta$  threshold.

#### 4.4 $\eta$ production in proton-proton collisions

By far the most extensive series of measurements of the  $pp \rightarrow pp\eta$  reaction near threshold was undertaken by the COSY-11 collaboration [16,145,146] and this has led to the bulk of the low energy points shown in Fig. 44. The two emerging protons were identified and their momenta measured and the reaction isolated by finding the missing-mass peak corresponding to the production of the  $\eta$  meson. Very close to threshold this peak stands out clearly

from the multipion background, though more care has to be taken at the higher excess energies.

Fully reconstructed  $pp \rightarrow pp\eta$  events were also obtained in a COSY-TOF experiment at 15 MeV and 41 MeV [155] and at the higher energy these seem to show an even larger fraction of events at large  $pp$  invariant masses.

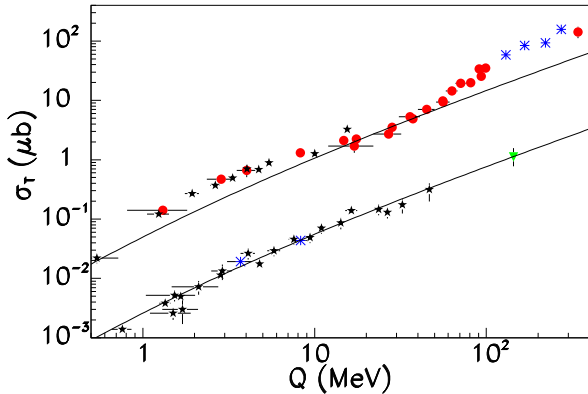


**Fig. 44.** Total cross sections for  $pp \rightarrow pp\eta$  (upper points) and  $pp \rightarrow pp\eta'$  (lower points). The  $\eta$  data are taken from Refs. [141, 142, 143, 144] (closed red circles), COSY-11 [16, 145, 146] (closed black stars), [147] (blue crosses), and [148] (green star). The  $\eta'$  data are from Ref. [143, 144] (blue crosses), [149] (green star), and COSY-11 [150, 151, 152, 153] (closed black stars). The solid curves are arbitrarily scaled  $pp$  FSI predictions of Eq. (4.4).

Also shown in Fig. 44 is a curve corresponding to the energy dependence expected according to the  $pp$  FSI model of Eq. (4.4). This assumes that the data are dominated by  $S$ -wave  $pp$  final states but this is in conflict with the differential data at  $Q = 72$  MeV, where the valley along the diagonal of the Dalitz plots shows strong evidence for the production of  $Pp$  or higher waves [154]. This suggests that the deviations from the curve in Fig. 44 for  $Q \gtrsim 40$  MeV might be associated with the excitation of higher partial waves. This cannot be the explanation of the relatively high cross sections at low  $Q$ , which are probably driven by the strong  $\eta p$  interaction, which is already well known in the  $pd \rightarrow {}^3\text{He}\eta$  reaction to be discussed in sect. 9.2.

More detailed information can be obtained from looking at differential distributions and the spectrum of the excitation energy  $E_{pp}$  in the  $pp$  system in Fig. 45 at an excess energy of  $Q \approx 15.5$  MeV [145]. What is immediately striking here is the sharp peaking of the experimental data at very low  $E_{pp}$  that is due to the dominance of the  $Ss$  wave and the very strong final state interaction between the two protons. There are minor differences in the literature on how the FSI is modeled and the curve shown in Fig. 45 does not include Coulomb repulsion or experimental resolution, Nevertheless, it is clear that the model falls well below the data at large  $E_{pp}$ . A natural assumption is that at large  $E_{pp}$  there are contributions associated with  $Ps$  final waves and the combination of  $Ss$  and  $Ps$  final waves describes the COSY-11 data very well.

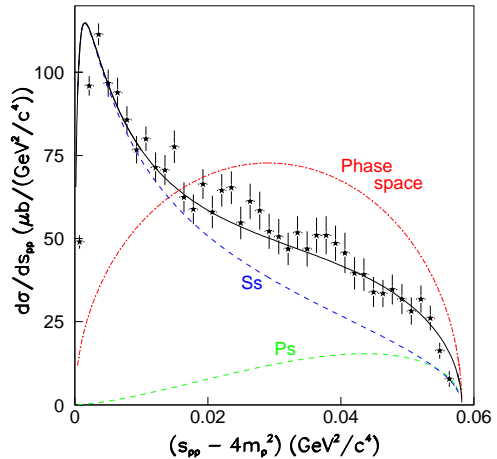


**Fig. 45.** One-dimensional distribution measured in the  $pp \rightarrow pp\eta$  reaction by the COSY-11 collaboration at  $Q = 15.5$  MeV [145]; to a very good approximation the abscissa represents  $4m_p E_{pp}$ . The (red) chain curve corresponds to a phase space distribution and weighting this arbitrarily with the  $pp$   $S$ -wave FSI or a  $P$ -wave factor gives the (blue or green) dashed curves. The sum of  $Ss$  and  $Ps$  contributions (solid black curve) describes well the shape of the data.

The COSY-TOF experiment also produced angular distributions of both the  $\eta$  and the  $pp$  relative momentum [155] and the  $\eta$  differential cross section at 41 MeV is shown in Fig. 46, where it is compared with CELSIUS-WASA measurements at 40 MeV and 72 MeV [154]. The shape of the distribution seems to be better defined by the CELSIUS experiment.

Data were also obtained at ANKE in a missing-mass experiment at  $Q = 55$  MeV and 270 MeV, where a cut of  $E_{pp} < 3$  MeV was placed on the excess energy of the outgoing  $pp$  pair [156]. At such high excess energies only data at small  $\eta$  angles were accessible and, putting a further cut of  $\cos\theta_\eta > 0.95$ , a preliminary cross section of  $(4.3 \pm 0.8)$  nb at 55 MeV could be extracted, where only the statistical error is quoted. The CELSIUS-WASA experiment [154] was not very sensitive to this kinematic region but the ANKE value does raise questions regarding the restricted amplitude analysis used at CELSIUS to extrapolate into this region.

Although the WASA programme on  $pp \rightarrow pp\eta$  was primarily directed towards the study of the rarer  $\eta$  decays described in sect. 11.1, the azimuthal symmetry of the detector makes it an ideal instrument with which to measure analyzing powers. In order to avoid unwelcome rotations of the proton spin and the consequent loss of beam polarization, the field in the solenoid was switched off [157]. This

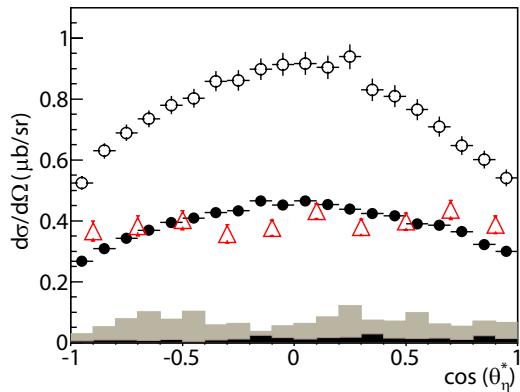


**Fig. 46.** The  $pp \rightarrow pp\eta$  cross section as a function of the cosine of the  $\eta$  polar angle in the overall CM frame. The data from the CELSIUS-WASA experiment [154] at  $Q = 72$  MeV (open circles) and  $Q = 40$  MeV (filled circles) are compared with those of COSY-TOF [155] at  $Q = 41$  MeV (triangles). The  $Q = 72$  MeV points have been shifted down by a factor 0.5 for ease of presentation. The systematic uncertainties in the CELSIUS data are shown by the grey and black histograms, where the black corresponds to the  $Q = 40$  MeV data.

was possible because at WASA the  $\eta$  could be detected through the  $\eta \rightarrow 2\gamma$  and  $\eta \rightarrow 3\pi^0$  decays as well as a missing-mass peak. The beam polarizations were deduced from measurements of elastic  $pp$  scattering, with one proton being registered in the forward detector and the other in the central detector. These asymmetries were converted into polarizations using the analyzing powers measured by the EDDA collaboration [37]. The experiments, which were carried out at  $Q = 40$  MeV and 72 MeV, complemented the earlier COSY-11 measurements at 10 MeV and 36 MeV, which showed no significant signal [158, 159].

Figure 47 shows the WASA data on the analyzing power of the  $\bar{p}p \rightarrow pp\eta$  reaction at an excess energy of  $Q = 72$  MeV as a function of the c.m. polar angle of the  $\eta$  [157]. Near threshold we can expect  $A_y d\sigma/d\Omega$  to be a linear combination of  $\sin\theta_\eta$  and  $\sin 2\theta_\eta$ . Taking the unpolarized angular distribution at this energy from the earlier WASA measurement at CELSIUS [154] shown in Fig. 46, the  $A_y$  data are well described by

$$A_y = (C_1 \sin\theta_\eta + C_2 \sin 2\theta_\eta)/(0.88 + 0.92 \sin^2\theta_\eta), \quad (4.5)$$

where  $C_1 = 0.208 \pm 0.008$  and  $C_2 = 0.018 \pm 0.009$ . The error bars are statistical but there may be systematic effects in  $C_2$  arising from slightly different acceptances in the two hemispheres. The fit is shown in Fig. 47 along with separate curves corresponding to the  $\sin\theta_\eta$  and  $\sin 2\theta_\eta$  components. It is clear from this that the former, which arises principally from  $Ps$  interfering with  $Pp$  waves, is much bigger than the latter, which is probably driven mainly by  $Ss : Sd$  interference. This is not a total surprise since the CELSIUS data [154] have shown that the  $Pp$  contribution is very strong at 72 MeV and there is evidence in Fig. 45 for a  $Ps$  contribution already at 15.5 MeV. In con-

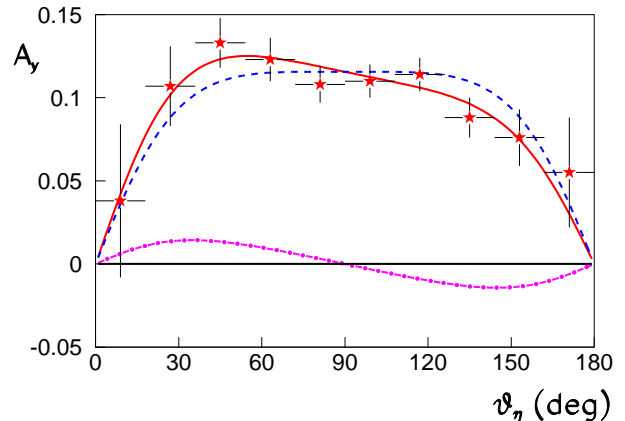


**Fig. 47.** Measurement of the proton analyzing power in the  $\bar{p}p \rightarrow pp\eta$  reaction with respect to the  $\eta$  polar angle in the c.m. frame at  $Q = 72$  MeV [157]. Only statistical errors are shown. The fits on the basis of Eq. (4.5) used differential cross sections measured at CELSIUS [154]. The dashed (blue) curve represents the  $\sin\theta_\eta$  component, the dot-dashed (magenta) curve corresponds to the  $\sin 2\theta_\eta$  term, whereas the solid (red) curve is their sum. It appears from these data that the analyzing power is driven mainly by  $Ps : Pp$  interference.

trast, the group found no significant analyzing power at  $Q = 15$  MeV [157] but this is also not unexpected so close to threshold.

#### 4.5 $\eta$ production in proton-neutron collisions

Although there were measurements of the cross section for the quasi-free  $pn \rightarrow pn\eta$  reaction at CELSIUS [14], these were not carried out in the immediate vicinity of the threshold. What is remarkable in these data is the large ratio of  $\eta$  production in  $pn$  compared to  $pp$  collisions, with cross section ratios being typically  $R_{pn/pp} \approx 7$ . The  $pd \rightarrow p_{sp}pn\eta$  reaction was measured closer to threshold by adding the neutral particle detector to the standard COSY-11 facility [160]. The outgoing neutron was then measured in this detector, which delivered information about the position and time at which the registered neutron induced a hadronic reaction. By using a single beam energy (1.34 GeV) and exploiting the spread in excitation energies  $Q$  caused by the deuteron Fermi motion, the COSY-11 authors extracted values of the  $pn \rightarrow pn\eta$  total cross section in three bins in  $Q$ . Although the value of  $R_{pn/pp}$  was consistent with the CELSIUS results for  $10 < Q < 15$  MeV, the COSY-11 results closer to threshold were much lower than the CELSIUS factor of seven.

As the authors pointed out [160], much of this variation could arise from the different final state interactions in the nucleon-nucleon  $I = 1$  and  $I = 0$  channels. Following the arguments given in sect. 4.1, if this factor alone is included, one might expect that near threshold the ratio should vary

as [103]

$$R_{pn/pp} = 0.5 + C \frac{B_{I=1}}{B_{I=0}} \left( \frac{1 + \sqrt{1 + Q/B_{I=1}}}{1 + \sqrt{1 + Q/B_{I=0}}} \right)^2, \quad (4.6)$$

where  $B_{I=0} = 2.23$  MeV and the authors assumed  $B_{I=1} \approx 0.68$  MeV. The 0.5 corresponds to the  $I = 1$  component in the initial  $pn$  wave and the parameter  $C$  reflects the basic production mechanism that is outside the remit of the FSI approach. By taking  $C \approx 7$ , which is consistent with high energy data, much of the near-threshold decrease in  $R_{pn/pp}$  could be explained, though more refined data would be required to isolate clearly this effect [160].

An attempt was made at ANKE to measure the cross section for  $np \rightarrow d\eta$  by using a deuteron beam with the maximum COSY energy of 2.27 GeV. Since the central neutron energy is below the  $d\eta$  threshold, which is at about 1.26 GeV, only the upper part of the Fermi momentum contributed to  $\eta$  production. As can be judged from the missing-mass distribution shown in Fig. 48, it is straightforward to identify the reaction but, being so far below threshold, it has not been possible to separate quasi-free production cleanly from more complicated three-nucleon effects.

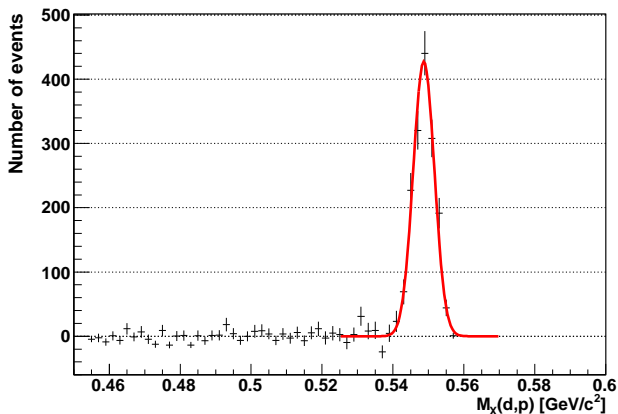


**Fig. 48.** Missing-mass spectrum after background subtraction for the  $dp \rightarrow dpX$  reaction at 2.27 GeV from preliminary ANKE data for  $5 < Q < 10$  MeV [161].

To go higher in energy at COSY, the experiment must use a deuterium target and isolate the  $pd \rightarrow p_{sp}d\eta$  by detecting explicitly the spectator proton. Such an experiment was undertaken at ANKE, where the spectator proton was detected in one of the two STT [162]. The data, which covered the range  $0 < Q < 100$  MeV in excess energy, are still under analysis but preliminary results in the range below 20 MeV indicate an  $\eta d$  scattering length of magnitude  $|a_{\eta d}| \approx 1.2$  fm [163].

#### 4.6 $\omega$ production in proton-proton scattering

With the possible exception of the  $\eta'$ , the natural widths of the other mesons discussed in this section are much less than the resolution of the detectors available at COSY. As a consequence, any improvement in the resolution automatically improves the signal-to-background ratio. This is no longer true for  $\omega$  production because in the COSY experiments the missing-mass peak is dominated by the natural meson width of  $\Gamma_\omega = 8.49 \pm 0.08$  MeV/ $c^2$  [164]. There is therefore a large background of mainly two- and three-pion production that has to be mastered.

In some experiments only the two final protons were measured [165,166] but in more refined approaches the  $\pi^+$  and  $\pi^-$  from the three-pion decay of the  $\omega$  were detected in coincidence [167,168,169,170,171]. However, in all cases one is still faced with the problem of separating the  $\omega$  signal from the background. Although this can be done by fitting smooth curves on either side of the  $\omega$  peak, there are two other procedures that deserve closer attention.

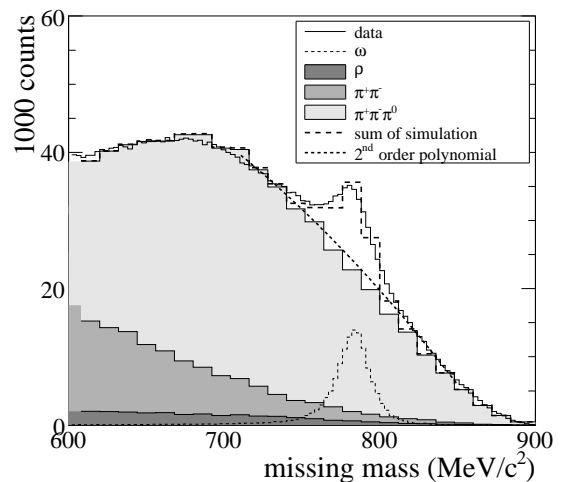


**Fig. 49.** Proton-proton missing-mass spectra at an excess energy of  $Q = 128$  MeV with respect to the nominal  $\omega$  threshold [171]. Also shown are normalized Monte Carlo distributions obtained for resonant  $pp \rightarrow pp(\rho \rightarrow \pi^+\pi^-)$  and plane-wave two- and three-pion production. The sum describes the non- $\omega$  background very well.

In the COSY-TOF missing-mass spectrum of Fig. 49, the background was explicitly modeled in terms of  $\rho$  production and decay plus larger contributions coming from direct two- and three-pion production. By allowing each of these contributions to be included with fitted weights, a good overall description of the multipion background could be achieved. However, it was assumed in this analysis that these non- $\rho$  pion productions followed phase space although in reality the spectra would be distorted in some way by  $\Delta$  or  $N^*$  isobar production.

In an alternative, more empirical approach, it was assumed that in experiments with magnetic spectrometers

the shape of the multipion background was determined mainly by the limited spectrometer acceptance, so that the shape of the background was taken from sub-threshold measurements. Rather than simply shifting the data from negative  $Q$  to positive  $Q$ , in the Saclay experiment the sub-threshold data were analyzed as if they had been taken at the energy of the  $\omega$  signal [165]. The ANKE data were taken at only two energies, well above threshold, but a similar procedure was adopted, taking the background away from the  $\omega$  peak at one energy and using it under the  $\omega$  peak at the other [166]. The practice of using sub-threshold data to determine the shape of multipion background is quite common at COSY, for example in the measurement of  $dp \rightarrow {}^3\text{He}\eta$  at COSY-11 [172] and ANKE [173].

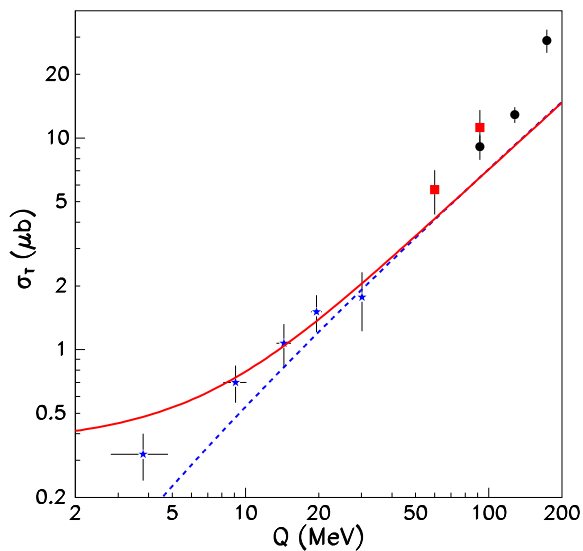


**Fig. 50.** Total cross sections for  $pp \rightarrow pp\omega$  in terms of the nominal value of  $Q$ , i.e., neglecting the  $\omega$  width. The data are taken from Refs. [165] (blue stars), [166] (red squares), and [171] (black circles). The (blue) dashed curve is an arbitrarily scaled  $pp$  FSI prediction of Eq. (4.4), whereas the (red) solid one has been smeared over the  $\omega$  width.

The values of the low energy  $pp \rightarrow pp\omega$  total cross sections extracted from the COSY and earlier Saclay experiments are shown in Fig. 50 along with the arbitrarily normalized pure  $pp$  FSI prediction of Eq. (4.4). This assumes that the final  $pp$  pair is in the  ${}^1S_0$  state and the deviations at large  $Q$  are, like the  $\eta$  production data of Fig. 44, due to  $P$  and higher waves in the  $pp$  system. The deviations close to threshold probably arise from the finite width of the  $\omega$  and smearing the  $pp$  FSI predictions over this width gives the modified curve that is also shown in the figure.

Apart from reducing somewhat the multipion background, detecting the decay products of the  $\omega$  allows one to determine the tensor polarization (the alignment)  $\rho_{00}$  of this meson. At threshold the only transition allowed

is  ${}^3P_1 \rightarrow {}^1S_0s$  and this leads to  $\omega$  spin projections of  $m_\omega = \pm 1$  along the beam axis and hence  $\rho_{00} = 0$ . The COSY-TOF collaboration has measured  $\rho_{00}$  at excess energies of  $Q = 92, 128, \text{ and } 173$  MeV and seen a significant departure from the threshold value towards the unpolarized value of  $\rho_{00} = 1/3$  [171]. The results at the three energies could be parameterized as  $\rho_{00} = Q/3(Q + A)$ , where  $A = 90 \pm 35$  MeV.

In principle the various angular distributions in the  $pp \rightarrow pp\omega$  reaction could be investigated by just measuring the two final protons but the large data sample of relatively clean  $\omega$  events in the COSY-TOF experiments, especially at 128 MeV, has allowed angular distributions to be extracted in the c.m., the helicity, and the Jackson frame [171]. At this energy the proton angular distribution is relatively flat in all three frames though the  $\omega$  c.m. dependence is quite strong, varying like  $1 + (0.97 \pm 0.21)\cos^2\theta_\omega$ . These two facts suggest that the other important final wave is  ${}^1S_0p$ , though this would give an angular dependence to  $\rho_{00}$ .

The other valuable piece of evidence that is relevant for the presence of higher partial waves comes from the measurements of the proton analyzing power of the  $\bar{p}p \rightarrow pp\omega$ , where a value consistent with zero was found at  $Q = 129$  MeV [174]. This would follow if the extra partial waves were spin-triplet since there would then be no interference with the threshold spin-singlet for the analyzing power. However, this would also be the case for the differential cross section, so that this may not be the origin of the observed non-isotropy in  $\theta_\omega$ . Of course, the vanishing of the analyzing power could be the result of an accident in the phases of the production amplitudes. The rich COSY-TOF  $pp \rightarrow pp\omega$  data set [171,174] will certainly provide a challenge for modelers.

There was one measurement of quasi-free  $pn \rightarrow d\omega$  production, where the spectator proton in the  $pd \rightarrow p_{\text{sp}}d\omega$  was measured in two energy regions in an early version of a Silicon Tracking Telescope [175]. Though the total cross sections could be a little larger than those for  $pp \rightarrow pp\omega$ , the error bars are large, due to the limited statistics and the very significant multipion background.

#### 4.7 $\eta'$ production in proton-proton scattering

A particularly interesting case of near-threshold meson production is the COSY-11 study of the  $pp \rightarrow pp\eta'$  reaction. This is because the meson has a natural width of some hundreds of  $\text{keV}/c^2$ , which is comparable to the resolution of the spectrometer. The COSY-11 measurement of the  $pp \rightarrow ppX$  missing-mass distribution at an excess energy of  $Q = 0.8$  MeV with respect to the  $\eta'$  threshold is shown in Fig. 51 [177]. Since the COSY beam momentum was not known with sufficient precision from macroscopic measurements, it could be fixed to  $\pm 0.2$  MeV/ $c$  by using the standard value of the  $\eta'$  mass, as given in the PDG tables [164].

The acceptance of the COSY-11 or ANKE spectrometer for such reactions increases as threshold is approached from above because the two final protons are then squeezed

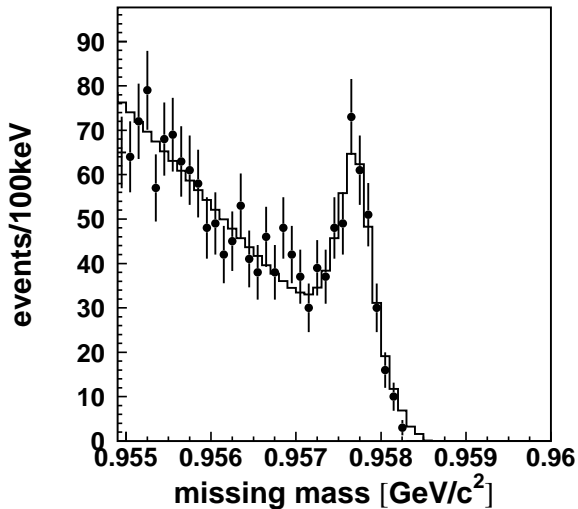


**Fig. 51.** The missing-mass spectrum for the  $pp \rightarrow ppX$  reaction at an excess energy of  $Q = 0.8$  MeV with respect to the  $pp\eta'$  threshold [177]. The experimental data are presented as points while the line corresponds to the sum of the Monte Carlo generated signal for the  $pp \rightarrow pp\eta'$  reaction with  $\Gamma_{\eta'} = 0.226$  MeV/ $c^2$  and the background obtained from another energy. Having a reliable parametrization of the background, it is straightforward to extract the numbers of  $\eta'$  mesons produced from the missing-mass peak.

into a smaller and smaller forward cone. This advantage no longer holds for, e.g., the MOMO and WASA detectors where particles are lost down the beam pipe. The missing-mass resolution also improves near threshold because, just as for the  $pd \rightarrow {}^3\text{He}\eta$  reaction discussed in sect. 9.2, the value of  $M_X$  is stationary at threshold. As a consequence, the missing-mass peak in Fig. 51 stands out very clearly.

The background in the figure is mainly due to multi-pion production which changes very smoothly with beam energy. The shape of the background, which is fixed dominantly by the characteristics of the spectrometer, can be determined by fitting data taken at a different energy and then shifting the spectrum so that the kinematic limits coincide. This method gave a very good description of the background at all the energies studied and it allowed the  $\eta'$  peak to be isolated for the different values of  $Q$ . Even at the highest COSY-11 energy of  $Q = 46.6$  MeV, the rather flat angular distribution was consistent with pure  $s$ -wave production [152].

The series of measurements at COSY-11 [153,176,177] yielded two important Physics results. The 21 COSY-11 points completely dominate the energy dependence of the  $pp \rightarrow pp\eta'$  total cross section displayed in Fig. 44, where the values are typically a factor of 30 or more below those for  $\eta$  production. It is also immediately apparent from this figure that any enhancement of the cross section at low  $Q$  is much less than that for  $\eta$  production. It would therefore seem that the magnitude of the  $\eta'p$  scattering length,  $a_{\eta'p}$ , must be significantly smaller than that of  $\eta p$ . Numerical estimates of  $a_{\eta'p}$  were given in Ref. [153],

though there is some model dependence in the imaginary part. The relatively weak interaction of the  $\eta'$  with the proton has significant consequences for the chances of this meson binding to nuclei.

The Particle Data Group obtained a value of the natural width of the  $\eta'$  by making fits to 51 measurements of partial widths, integrated cross sections, and branching ratios. The existing direct measurements of the line width had very large uncertainties and a more accurate one was clearly highly desirable. This was achieved with the COSY-11 data [177]. In the  $\eta'$  threshold region the circulating proton beam has a momentum spread of FWHM = 2.5 MeV/ $c$ . However, due to the position of the COSY-11 target in a dispersive region of COSY, the momentum spread seen at the target could be reduced down to a mere  $\pm 0.06$  MeV/ $c$ . This therefore gave a negligible contribution to the total experimental missing-mass resolution of FWHM  $\approx 0.33$  MeV/ $c^2$ .

By analyzing simultaneously data taken at five excess energies, from 0.8 to 4.8 MeV, the width was determined to be  $\Gamma_{\eta'} = (0.226 \pm 0.017(\text{stat}) \pm 0.014(\text{syst}))$  MeV/ $c^2$  [177]. This direct measurement is to be compared with the PDG fit value of  $(0.198 \pm 0.009)$  MeV/ $c^2$ , which was obtained by summing the partial cross sections and normalizing on the  $\gamma\gamma \rightarrow \eta'$  production rate. The agreement is very reassuring.

## 5 Two-pion production in nucleon-nucleon collisions

### 5.1 Two-pion production in proton-proton collisions

Although much of the excitement in recent years has been connected with two-pion production in neutron-proton collisions, COSY has also made some useful contributions in proton-proton collisions. The simplest of these to discuss is the ANKE experiment where, in an inclusive measurement, only two protons from the  $pp \rightarrow ppX$  reaction were detected at  $pp$  excitation energies  $E_{pp} < 3$  MeV [156]. This was already mentioned in connection with  $\eta$  production in sect. 4.4, where it was stressed that, under these conditions, the diproton acts kinematically like a single particle. The acceptance at ANKE is restricted to very small angles and the raw data shown in Fig. 52 were obtained for the cosine of the c.m. diproton angle bigger than 0.95.

There is a region of missing masses  $270 \lesssim M_X \lesssim 420$  MeV/ $c^2$  where the data in Fig. 52 must correspond to two-pion production and it was argued [156] that even at higher  $M_X$  two-pion production probably dominates. Even if this were true, one has no way of knowing the relative weights of  $\pi^+\pi^-$  and  $\pi^0\pi^0$  in the final state. Nevertheless, there is one intriguing feature to note in the data. At 1.1 GeV and possibly also at 1.4 GeV there is a strong enhancement compared to phase space at low dipion masses. This is the so-called ABC effect [178] that will be described in some detail in sect. 9.3. On the other hand, at 0.8 GeV, i.e.,  $Q \approx 80$  MeV, there is a kind of anti-ABC effect where the enhancement comes at the largest

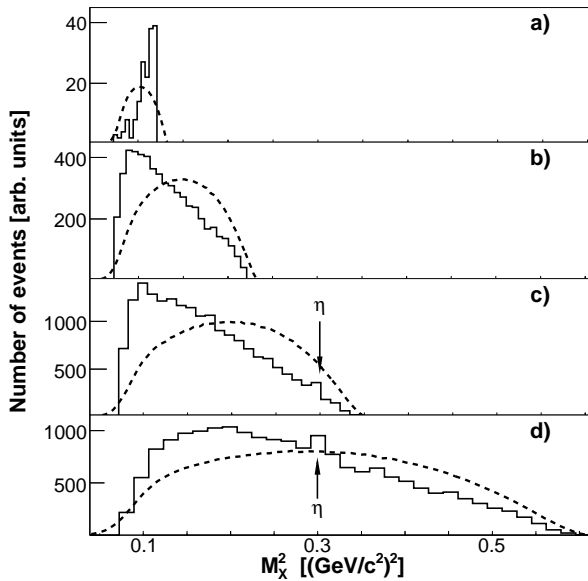


**Fig. 52.** Distribution in missing-mass squared for the  $pp \rightarrow \{pp\}_s X$  reaction for  $E_{pp} < 3$  MeV and  $\cos \theta_{pp} > 0.95$  at a) 0.8, b) 1.1, c) 1.4, and d) 2.0 GeV [156]. The  $\eta$  signal seen at the two higher energies was already mentioned in sect. 4.4. The curves represent normalized simulations within a phase-space model.

dipion masses. Exactly the same behaviour is observed in the  $pd \rightarrow {}^3\text{He} \pi^+ \pi^-$  reaction by the MOMO collaboration [32], as discussed in sect. 9.3. This striking behaviour should be reproduced in any modeling of the ABC phenomenon.

Whereas the ANKE measurements [156] covered only a tiny region of phase space, much more global studies were undertaken in experiments carried out at COSY-WASA and COSY-TOF. The TOF measurements of  $pp \rightarrow pp\pi^+\pi^-$  were carried out at 747 and 793 MeV using a polarized proton beam [179]. Although both protons fell within the geometric acceptance of TOF, the same was not true for the pions. However, since the detection of two protons and one pion was sufficient to reconstruct the event in TOF, most of the reaction phase space was covered, especially for the unpolarized cross section, which is symmetric in the c.m. frame.

The fully reconstructed events allowed the authors to extract a wide variety of one-dimensional distributions in invariant masses and proton and pion angles and in Fig. 53 we show the differential cross section at 793 MeV in terms of the  $\pi^+\pi^-$  and  $pp$  masses. The ANKE data [156] would correspond to just the first point in the  $pp$  distribution and, if we make simple assumptions on the angular distributions, it is clear that the normalizations of the ANKE and TOF data are at least broadly consistent at 800 MeV. On the other hand, the shapes of the  $\pi\pi$  distributions in Figs. 52 and 53 at this energy look very different and so any anti-ABC behaviour is only apparent for very low values of  $E_{pp}$ .

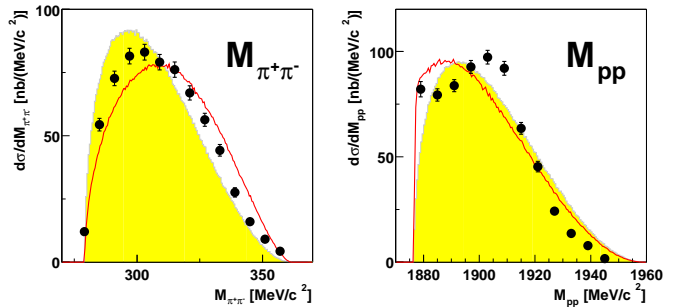


**Fig. 53.** COSY-TOF measurements of the differential distributions of the invariant masses  $M_{\pi\pi}$  and  $M_{pp}$  in the  $pp \rightarrow pp\pi^+\pi^-$  reaction at  $T_p = 793$  MeV [179]. They are compared to phase-space distributions (shaded areas) as well as to an  $N^*$ -Roper-inspired model (solid lines).

Having a good absolute normalization is, of course, critical when one is looking at the energy dependence of the total cross section measured at different facilities. Shown in Fig. 54 are the points obtained by the COSY-TOF collaboration [179] and values from an early version of WASA at CELSIUS [180]. These data seem to behave more or less like phase space, whose dependence is shown by the shaded area. On the other hand, these points are low compared to other data in the literature [181], which are also shown. Two calculations by the Valencia group [182], one with and one without the  $pp$  final state interaction, are also illustrated. Since the  $pp$  FSI must exist, it is clear that more work is required on the theoretical modeling of this reaction.

For a four-body final state the analyzing power  $A_y$  can be measured with respect to several different planes. Thus the values of  $A_y$  for the final pion and dipion directions in the c.m. frame showed some small non-zero signals at 750 MeV and, since the associated unpolarized cross sections were fairly isotropic,  $A_y$  could be fitted directly in terms of  $\sin \theta$  and  $\sin 2\theta$  [179].

On the basis of all the differential distributions, it was claimed that the dominant mechanism involved the excitation of the Roper resonance, which decayed through the emission of an  $s$ -wave dipion. This would not, of course, describe the  $pp \rightarrow \pi^+\pi^+nn$  reaction, which was searched for at 800 MeV by the COSY-TOF collaboration [183]. Only an upper limit was found and this was over an order of magnitude less than the cross sections for producing other two-pion channels. The result did not therefore invalidate the  $N^*$ (Roper) hypothesis for  $\pi^+\pi^-$  production at low energies.

However the situation for  $pp \rightarrow pp\pi^0\pi^0$  was clarified significantly by a subsequent measurement by the COSY-WASA collaboration at 1.4 GeV, where about  $5 \times 10^5$  events were analyzed [184]. The  $\pi^0 p$  invariant mass distributions showed that at this energy the reaction was driven mainly by intermediate  $\Delta(1232)\Delta(1232)$  states. It would therefore seem that there could be two competing mechanisms involved, with the Roper  $N^*$  being dominant only close to threshold.



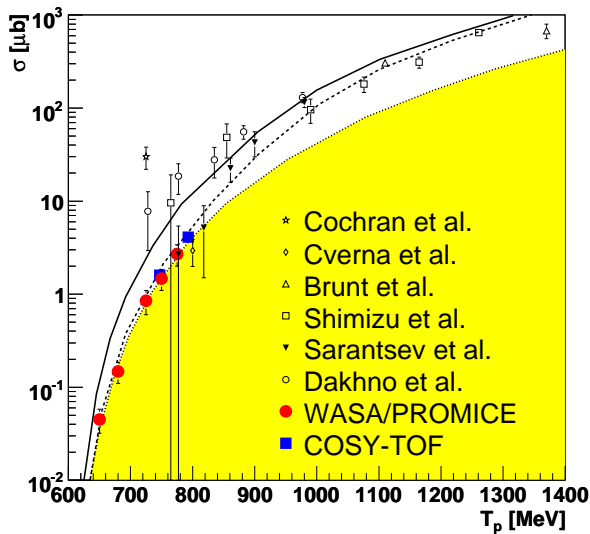


Fig. 54. Total cross section for the  $pp \rightarrow pp\pi^+\pi^-$  reaction as a function of the proton beam energy. Closed (red) circles are WASA data taken at CELSIUS [180] whereas the (blue) squares were obtained by the collaboration at COSY. A collection of older data is also shown [181]. Solid and dashed curves correspond to theoretical calculations of Ref. [182] with and without the  $pp$  FSI. The shaded area represents the phase space dependence adjusted arbitrarily to the value at  $T_p = 750$  MeV.

## 5.2 Two-pion production in neutron-proton collisions

One of the most exciting measurements in medium energy nuclear physics in recent decades was that of the differential cross section for the  $pn \rightarrow d\pi^0\pi^0$  reaction carried out by the WASA collaboration, first at CELSIUS [185] and then more extensively at COSY [186,187]. In quasi-free production on a deuterium target, the centre-of-mass energy  $W$  in the  $pn$  system has to be reconstructed from the measurements in WASA of the deuteron and the photons arising from the decays of the two  $\pi^0$ . On the other hand, the deuterium target allowed the measurement to be carried out at a range of values of  $W$  while keeping the proton beam energy fixed. The results were later confirmed at COSY by using a (polarized) deuteron beam, where the fast spectator proton could be measured explicitly [188].

Figure 55 shows the WASA measurements of the total cross section for the quasi-free  $pn \rightarrow d\pi^0\pi^0$  reaction [186, 187] and the  $np \rightarrow d\pi^0\pi^0$  reaction [188]. All these data are consistent and indicate a sharp peak at a mass of  $2.38$  GeV/ $c^2$  and a width of about  $70$  MeV/ $c^2$ . It should be noted at this point that, in order to avoid using events corresponding to very large Fermi momenta in the deuteron, the full width of the peak in Fig. 55 was scanned by using more than one setting of the proton beam momentum.

It was suggested by the WASA authors that this peak corresponded to a resonance with baryon number equal to two, i.e., that it was a dibaryon, which they denoted

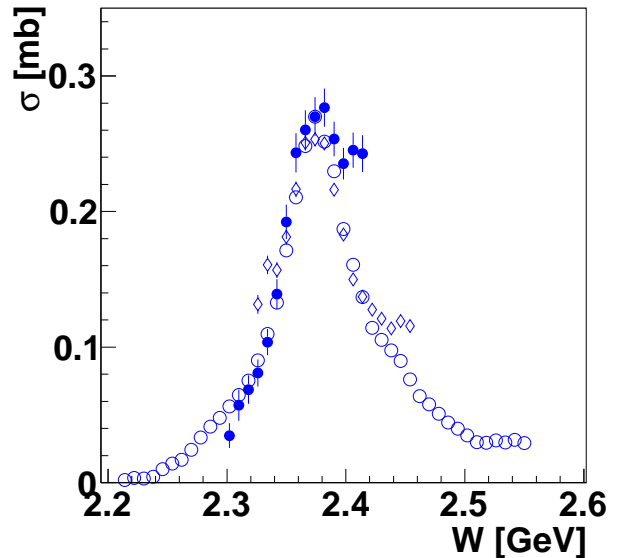


Fig. 55. Total cross section for the quasi-free  $pn \rightarrow d\pi^0\pi^0$  reaction as a function of the total energy  $W$  in the c.m. frame. The data with a deuteron target are taken from Refs. [186] (open circles) and [187] (open diamonds). Results obtained with a deuteron beam come from Ref. [188] (closed circles). The data from the two other sets were normalized to those of Ref. [187] at the maximum of the peak..

by  $d^*(2380)$ . The other interesting piece of experimental information is that the two-pion spectrum associated with this peak seems to display the ABC effect, which shows up as an enhancement in the  $\pi^0\pi^0$  mass distribution that is strongest around  $310$  MeV/ $c^2$  [178]. At such a low mass the pions must be dominantly in a relative  $s$ -wave so that the dipion has then quantum numbers<sup>4</sup>  $(J^P, I) = (0^+, 0)$ , which means that the peak in Fig. 55 must also be in the isospin  $I = 0$  channel. If, as seems likely, the dynamics of two-pion production are driven by an intermediate  $\Delta(1232)\Delta(1232)$  state then the Pauli principle requires them to be antisymmetric so that the peak must correspond to either the  $J^P = 1^+$  or  $3^+$  wave. It was argued that the angular distributions strongly favoured the  $J^P = 3^+$  assignment [186]. A similar conclusion was also reached using very different reasoning, to which we now turn.

In sect. 4.1 a method was presented to make simple estimates of the cross section for the production of  $S$ -wave isoscalar  $np$  states in the reaction  $pp \rightarrow \{pn\}\pi^+$  in terms of that for  $pp \rightarrow d\pi^+$ . This can be extended to estimate the rate for  $pn \rightarrow \{pn\}\pi\pi$  in terms of that for  $pn \rightarrow d\pi\pi$  [189,190]. Due to the different kinematic factors, these estimates have to be made separately for the two spin hypotheses but, when this is done for the  $J^P = 1^+$  case, it is seen that the sums of the  $d\pi\pi$  and

<sup>4</sup> Isospin-two pion pairs are ruled out for the  $d\pi^0\pi^0$  final state by overall isospin conservation.

$\{pn\}\pi\pi$  productions significantly exceeds the total inelastic cross section in the SAID SP07 solution [65] in the combined  ${}^3D_1 + {}^3S_1$  states. This argument is, of course, not watertight because the neutron-proton input to the SAID solution is rather incomplete above 1 GeV. Nevertheless, it does suggest that, if there is a dibaryon resonance, then it is more likely to be in the  $3^+$  wave, where the inelasticity constraints are much less severe.

The use of the deuteron beam at COSY allowed the WASA group to measure the quasi-free  $dp \rightarrow p_{\text{sp}}pn\pi^0\pi^0$  cross section in the vicinity of the  $d^*(2380)$  [191]. Only six values close to the resonance peak were obtained and the maximum in the  $pn \rightarrow pn\pi^0\pi^0$  total cross section was found to be  $295 \pm 14 \pm 29 \mu\text{b}$  compared to the  $275 \mu\text{b}$  for  $np \rightarrow d\pi^0\pi^0$  shown in Fig. 55. Of course the  $pn \rightarrow pn\pi^0\pi^0$  reaction also has contributions associated with isovector  $np$  pairs. Since there is also production of isospin-two  $\pi^0\pi^0$  pairs in the  $pn \rightarrow pn\pi^0\pi^0$  reaction, it is not possible to make model-independent estimates of the extra  $I = 1$   $np$  contributions.

The WASA authors [191] presented results based upon a modified Valencia model that had been tuned to fit the  $pp \rightarrow pp\pi^0\pi^0$  data [182]. This predicts about  $100 \mu\text{b}$  for the  $I = 1$   $np \rightarrow np\pi^0\pi^0$  cross section at the  $d^*(2380)$  peak but is impossible to quantify the associated theoretical uncertainty. Nevertheless, if we accept this value, it means that  $\sigma(np \rightarrow \{np\}_{I=0}\pi^0\pi^0)/\sigma(np \rightarrow d\pi^0\pi^0) \approx 0.7$  compared to the 0.8–0.9 predicted in the simplest FSI model [189]. Though this does not prove the dibaryon assertion, it clearly does not invalidate it.

In the search for extra data to test the  $d^*(2380)$  hypothesis, the WASA collaboration also extracted analyzing powers  $A_y$  of the quasi-free  $\bar{n}p \rightarrow d\pi^0\pi^0$  from the polarized deuteron beam data [188]. It is expected that a non-zero value of  $A_y$  would arise from an interference of the  $d^*$  with the non-resonant background. However, the data are hard to interpret, in part due to the limited range of masses covered. Below resonance the analyzing powers with respect to the final deuteron direction are small. They do increase with  $W$ , but it is difficult to see in these data the rapid phase variation associated with the  $d^*(2380)$  pole.

The group also made measurements at COSY of the closely related  $pn \rightarrow d\pi^+\pi^-$  and  $pp \rightarrow d\pi^+\pi^0$  reactions in the  $d^*(2380)$  region [187]. In the first reaction the  $pn$ , and hence the  $\pi^+\pi^-$  system, is a mixture of isospin  $I = 0$  and  $I = 1$ , whereas the  $\pi^+\pi^0$  system must be purely  $I = 1$ . Since these amplitudes do not interfere in the expression for the total cross section, they can be subtracted to give the pure  $I = 0$  cross section and this has been done in Fig. 56. Within experimental uncertainties the directly measured  $I = 0$  total cross section shown in Fig. 55 is consistent with the one measured indirectly and presented in Fig. 56. Both data sets show the very strong peaking for  $W \approx 2380$  MeV.

The  $d^*(2380)$  interpretation has been questioned [190] on the basis of the comparison of  $pn \rightarrow d\pi^+\pi^-$  and  $pn \rightarrow pn\pi^+\pi^-$  data but, as discussed in the context of a higher energy experiment [192], any apparent discrepancy might

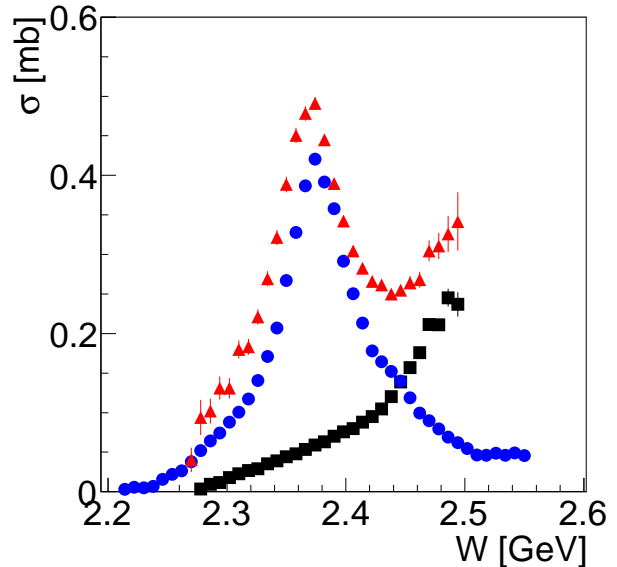


**Fig. 56.** Dependence of the total cross section for the  $pn \rightarrow d\pi^+\pi^-$  reaction (red triangles) and its isospin decomposition into an isoscalar part that should be compared to  $2\sigma(pn \rightarrow d\pi^0\pi^0)$  (blue circles) and an isovector part corresponding to  $\frac{1}{2}\sigma(pp \rightarrow d\pi^+\pi^0)$  (black squares) as functions of the centre-of-mass energy  $W$  [187].

be connected with the limited  $pn \rightarrow pn\pi^+\pi^-$  database in the vicinity of the resonance peak.

Although the original idea [193] that the  $\Delta\Delta$  channel might serve as the entrance channel for the  $np \rightarrow d\pi^0\pi^0$  reaction, and hence for the ABC effect, might be valid, no realistic calculations have yet reproduced the striking behaviour seen in Fig. 55. One obvious problem is that the width of the structure is of the order of 70 MeV compared to the 120 MeV that one normally associates with the  $\Delta(1232)$ . In part this difference may be connected with the reduction in the average  $\Delta$  mass to  $1190 \text{ MeV}/c^2$ , which would certainly have an influence on the  $p$ -wave decays. Pauli blocking may also have some effect but this might be compensated by the extra width coming from the  $\Delta\Delta \rightarrow np$  decay.

Even if the dibaryon exists, the interesting question is, of course, whether the relevant degrees of freedom are those of six quarks or those of  $\Delta\Delta$ , i.e., pions and nucleons. The nucleon-nucleon force that gives rise to the only stable dibaryon, the deuteron, is conventionally described in terms of nucleons and mesons with the binding depending critically on many refinements, such as the  $S$ - $D$  coupling driven by the tensor force of the one-pion-exchange. The coupled  $NN:\Delta\Delta$  force is likely to be even more complicated. Even if such a force could generate a  $d^*(2380)$  pole it will not necessarily describe quantitatively the  $pn \rightarrow d\pi^0\pi^0$  reaction; all the many angular and Dalitz plot distributions extracted by the WASA collaboration must also be explored.

The  $d^*(2380)$  peak in the  $pn \rightarrow d\pi^0\pi^0$  reaction seems to be associated with the ABC effect in the  $\pi^0\pi^0$  system. This is not unexpected if both are driven by the  $\Delta\Delta$  intermediate state. The ABC effect is seen also in  $pd \rightarrow {}^3\text{He}\pi^0\pi^0$  and, most spectacularly, in  $dd \rightarrow {}^4\text{He}\pi^0\pi^0$  [194, 195]. However, in the  $dd$  case the cross section and deuteron tensor analyzing power have been described using conventional physics without the need for the  $d^*(2380)$  [196]. It may therefore be that there is no one single mechanism that is responsible for generating the ABC effect for all reactions. More evidence is certainly required before it is safe to assume that the existence of an ABC effect must be a signal for the importance of the  $d^*(2380)$  in a particular reaction.

In summary, the WASA collaboration have found a very striking peak in the  $pn \rightarrow d\pi^0\pi^0$  reaction and all the data, including the energy dependence of the neutron analyzing power in  $np$  elastic scattering, seem to be consistent with the  $d^*(2380)$  dibaryon hypothesis. Even if it is later shown that the dibaryon assumption is untenable, the group will still have made a remarkable and most unexpected discovery in the domain of hadron physics.

## 6 Inclusive strangeness production

### 6.1 The $pp \rightarrow K^+X^+$ reaction

If the momentum of a well-identified  $K^+$  emerging from proton-proton collisions is measured then this will provide information on the recoiling system,  $X^+$ , which has baryon number +2 and strangeness -1. For missing masses below the  $\Sigma N$  threshold,  $m_X < m_\Sigma + m_N$ , the only strong interaction channel that is allowed is  $pp \rightarrow K^+\{Ap\}$  so that these measurements provide a simple way to investigate the  $Ap$  interaction. The situation is far more complicated at higher  $m_X$  because, in addition to real  $\Sigma$  production, there is strong channel coupling between  $Ap$  and  $\Sigma N$  final states. This problem will be discussed in connection with the cusp phenomenon in sect. 7.4 and  $\Sigma^+$  production in sect. 7.5.

The first high-resolution measurement of the  $pp \rightarrow K^+X^+$  reaction was carried out at SATURNE II with proton beam energies of 2.3 and 2.7 GeV at four fixed laboratory angles at each energy [197]. The outgoing kaons were detected at small angles in the focal plane of the SPES4 spectrometer. Decay corrections were important because of the length of this spectrometer.

Characteristic structures were seen at both the  $Ap$  and  $\Sigma N$  thresholds and the first of these could be unambiguously associated with the strong and attractive  $Ap$  final state interaction. These data were therefore used to extract estimates for the scattering length and effective range from the low energy  $Ap$  data. A major difficulty in the determination of low energy  $Ap$  parameters from these data within a final state interaction model was the resolution in the missing-mass, which was typically about 4 MeV/ $c^2$ . An attempt was made by Laget [198] to describe the whole data set, though one must recognize the ambiguities inherent in such an inclusive measurement. It

is also important to note that the  $S$ -wave  $Ap$  system can be in either the spin-triplet or spin-singlet state and the  $pp \rightarrow K^+Ap$  reaction produces some mixture of these that need not follow a statistical population rule.

In addition to the  $\Lambda$  and  $\Sigma$  threshold phenomena, the SPES4 group found suspicions of a peak in the vicinity of 2097 MeV/ $c^2$ , though its statistical significance was far from convincing [197]. The experiment was therefore repeated at beam energies of 1.953 and 2.097 GeV by the HIRES collaboration using the Big Karl spectrometer, where a missing-mass resolution of  $\sigma_M \approx 0.84$  MeV/ $c^2$  was achieved [199, 200].

In order to cover the range 2050 – 2110 MeV/ $c^2$  in missing mass, data were taken using three overlapping settings of the spectrometer, with enhanced luminosity in the highest mass interval. As shown in Fig. 57, no structure was evident in the 2097 MeV/ $c^2$  region and upper limits were determined on the production cross sections of narrow strange dibaryons over the whole missing-mass range [200].

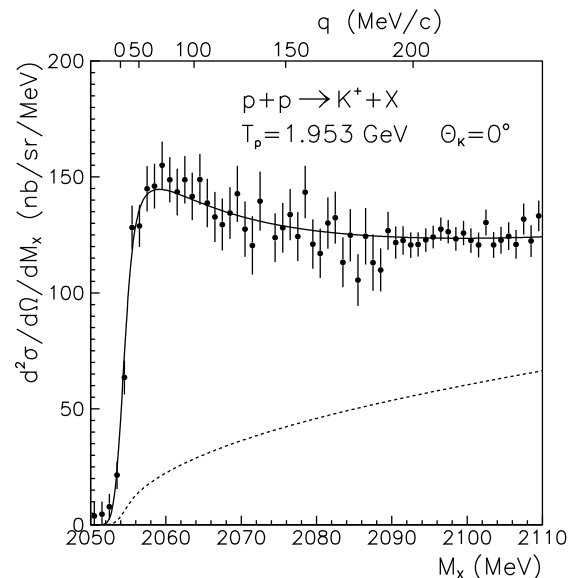


**Fig. 57.** Missing-mass spectrum of the reaction  $pp \rightarrow K^+\{Ap\}$  measured at  $T_p = 1.953$  GeV with the Big Karl spectrometer placed at  $\theta_K = 0^\circ$  [199]. The upper axis indicates the c.m. momentum  $q$  of the  $Ap$  system. Solid line: Fit including the  $Ap$  FSI. Dashed line:  $pp \rightarrow K^+Ap$  phase space distribution.

Also clearly seen in Fig. 57 is the rapid rise from the  $Ap$  threshold, which is very unlike the shape of the three-body phase space that is also shown (with arbitrary normalization). The HIRES authors tried to fit simultaneously this spectrum together with the limited data on  $Ap$  elastic scattering assuming that the final state interaction could be parameterized by the Jost function in the form of  $(q - i\alpha)/(q + i\beta)$  for both the singlet and triplet  $Ap$  states [199]. However, it was difficult to reconcile the two data sets and they found a best fit to the two sets

where spin-singlet production completely dominated the  $pp \rightarrow K^+ \Lambda p$  reaction. If the  $\Lambda p$  system is indeed in a pure singlet state then the analyzing power measured with polarized protons should be antisymmetric around  $\theta_K = 90^\circ$ . The COSY-TOF data discussed in sect. 7.3 do not support such a conclusion.

By considering only the HIRES production data they found scattering length and effective range of  $\bar{a} = -2.43 \pm 0.16$  fm and  $\bar{r}_0 = 2.21 \pm 0.16$  fm, but these values represent some unknown averages for singlet and triplet production [199]. In terms of the Jost function parameters,  $\alpha = -0.31$  fm $^{-1}$  and  $\beta = 1.215$  fm $^{-1}$ , so that there is a virtual state of the  $\Lambda p$  system with a “binding energy” of about 3.6 MeV. We will return later to attempts to determine the scattering length in the context of the exclusive COSY-TOF measurements.

## 6.2 Hypernuclei lifetime measurements

In free space the  $\Lambda$  hyperon decays principally through the channels  $\Lambda \rightarrow p\pi^-$  or  $\Lambda \rightarrow n\pi^0$  with a mean lifetime of  $\tau_{\text{free}} = 263 \pm 2$  ps [164]. The energy release in such a decay is about 38 MeV so that, when a  $\Lambda$  is bound deep inside a heavy hypernucleus, these decays are strongly suppressed by the Pauli blocking of the recoil neutron or proton. On the other hand, this reduction might be compensated by the non-mesonic decays  $\Lambda p \rightarrow np$  or  $\Lambda n \rightarrow nn$ . The nucleons from such decays have typically energies of about 80 MeV, so that they are largely unaffected by nuclear effects. It is therefore suggested that the study of the lifetimes of heavy hypernuclei might be a useful way of investigating non-mesonic decays.

The lifetimes of heavy hypernuclei have been investigated through the interaction of antiprotons with Bismuth and Uranium, but the resulting error bars are quite large [201]. The COSY-13 collaboration [202] measured the decay of hypernuclei produced in the interaction of  $\approx 1.9$  GeV protons with Bi, Au, and U targets using the recoil shadow method. The principle of the technique is illustrated schematically in Fig. 58.

After the proton beam hits a thin ribbon target, any particle emerging directly from the intersection region is blocked by the target holder so that it is not detected on the left hand side of the multiwire proportional chambers. When a produced hypernucleus travels along the beam direction, the products of its delayed decay may indeed reach the shadowed region, as indicated by the idealized trajectory shown in the figure. The obvious difficulty with this approach arises from the low production rate of hypernuclei, such that the background from fragments of non- $\Lambda$  delayed fission of recoil nuclei populates significantly the shadowed region. This was estimated using data taken at a lower proton beam energy, where hypernucleus formation is negligible.

The distribution of events in the shadowed region will reflect the hypernucleus lifetime but significant modeling is required because the recoils do not emerge from the target with a unique speed and, moreover, they do not represent a unique hypernuclear species. Nevertheless, the

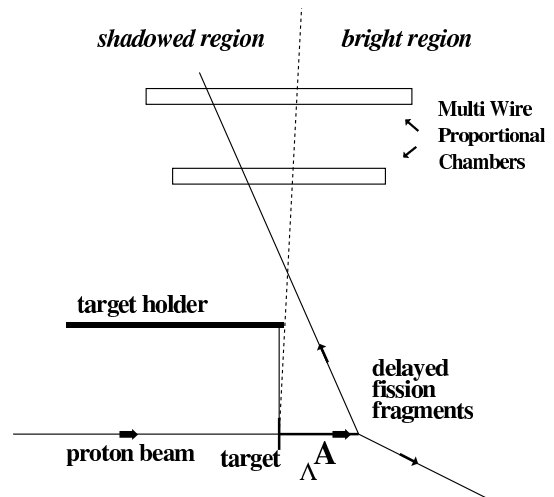


**Fig. 58.** Schematic view of the COSY-13 experimental setup illustrating the recoil shadow method. An idealized trajectory of a decay product from a produced hypernucleus is shown arriving in the region of the shadow. A particle coming directly from the target region is allowed in the forward hemisphere but is blocked by the target holder in the backward hemisphere.

lifetimes deduced from all three targets are consistent and give a mean average of  $\tau = (145 \pm 11)$  ps. This is also compatible with the value of  $(143 \pm 36)$  ps obtained from antiproton interactions in Bi and U targets [201].

In terms of the free  $\Lambda$  decay time, the COSY-13 result may be written as  $\tau = (0.55 \pm 0.04) \tau_{\text{free}}$ . Such a value is hard to explain theoretically but could be understood if the  $\Lambda N \rightarrow NN$  transition were much stronger on neutrons than protons, but this would imply a violation of the  $\Delta I = \frac{1}{2}$  rule [202]. However, this is in conflict with the neutron/proton transition ratio of  $0.51 \pm 0.14$  found for  $^{12}\text{C}$  [203]. Another alternative might be that the systematic effects were underestimated in the COSY-13 experiment. The COSY-13 result was criticized by the authors of an electroproduction experiment [204] but that paper was subsequently withdrawn from the arXiv!

It has been stressed that “COSY-13 was a simple experiment while we were waiting for ANKE to be ready” [205].

## 6.3 Inclusive $K^+$ production on nuclei

The threshold for producing a  $K^+$  in proton-proton collisions is at  $T_p = 1.58$  GeV but the meson might be produced at much lower energies in collisions with a nuclear target due to a variety of effects, including Fermi motion, two-step contributions, clustering, and kaon-nucleus potentials. These are all phenomena that are exciting to investigate.

The inclusive momentum spectrum of  $K^+$  emitted at laboratory angles  $\theta_K < 12^\circ$  was measured for 1.0 GeV protons hitting C, Cu, and Au targets [206]. The experiment was carried out at ANKE using the delayed-veto technique on the range telescopes [19]. Each telescope covered a well-defined interval of  $K^+$  momentum  $p_K$  so that

the 15 elements spanned the momentum range from 200 to 520 MeV/c [206]. There were typically 100  $K^+$  counts per telescope from a four-day run with a carbon target. Interpreted naively, the resulting cross section spectrum would suggest that of the order of 5-6 target nucleons were involved in the production process.

Many of the experimental uncertainties cancel when evaluating ratios of cross sections for different nuclear targets and the average values measured were  $R(\text{Cu}/\text{C}) = 4.0 \pm 0.3$  and  $R(\text{Au}/\text{C}) = 6.8 \pm 0.38$ , but with a slight indication that these values might increase with  $K^+$  momentum.

Though it is difficult to get a clear message from the 1.0 GeV data, the group also made similar measurements with the same strip targets plus Ag below and above the free  $pp$  threshold, where the cross sections are naturally much higher [207]. They measured the production cross sections relative to C as a function of the  $K^+$  momentum for 1.5, 1.75, and 2.3 GeV protons. What is striking is the rapid decrease in the ratios for all targets and energies for  $p_K \lesssim 200$  MeV/c. This is illustrated for the 2.3 GeV data in Fig. 59.

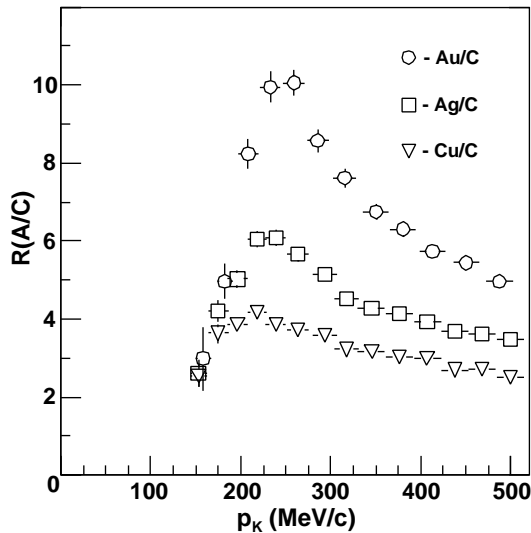


**Fig. 59.** Ratios of the  $K^+$  production cross sections on Cu, Ag, and Au to C measured at a proton beam energy of  $T_p = 2.3$  GeV as a function of the laboratory kaon momentum [207].

A large part of the suppression is due to the repulsive Coulomb potential  $V_C(r)$  between the  $K^+$  and the residual nucleus. The situation has a parallel in the well-known suppression of  $\beta^+$  emission in heavy nuclei at low positron momenta. Thus a  $K^+$  produced at rest at some radius  $R$  in the nucleus would, in the absence of all other interactions, acquire a momentum of  $p_{\min} = \sqrt{2m_K V_C(R)}$ . Taking  $R$  to be the nuclear edge, this purely classical argument leads to a minimum  $K^+$  momentum for Au of about 130 MeV/c. It is thought that, in addition, the strong interaction  $K^+$ -nucleus potential is itself mildly repulsive. A fit to the data within a transport calculation suggests that this is

about +20 MeV at normal nuclear matter density,  $\rho_0 \approx 0.16 \text{ fm}^{-3}$  [207].

Later experiments by that group involved also a deuterium target with the aim of investigating the production on the neutron [208], but the resulting uncertainties were very large.

## 7 Hyperon production

Almost all measurements in hyperon production in proton-proton collisions close to threshold were carried out at COSY. This dominance is well illustrated by the summary presented in Fig. 60, where the only non-COSY point is derived from the 11 bubble chamber events corresponding to the  $pp \rightarrow K^+ p \Lambda$  reaction [209].

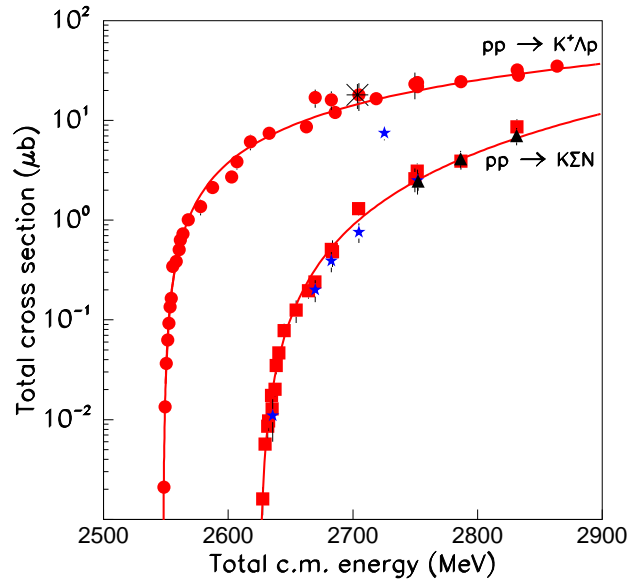


**Fig. 60.** Total cross sections for  $\Lambda$  and  $\Sigma$  production in proton-proton collisions near threshold as functions of the total energy in the c.m. system. Since the values for the various  $\Sigma$  channels overlap, the  $pp \rightarrow K^+ p \Sigma^0$  data are denoted by (red) inverted triangles, the  $pp \rightarrow K^+ n \Sigma^+$  by (blue) stars, and the  $pp \rightarrow K^0 p \Sigma^+$  by (black) triangles. All the data were obtained at COSY with the exception of a bubble chamber measurement of  $\Lambda$  production [209] that is shown by the (black) cross. The phenomenological curves are discussed in the text.

### 7.1 The $pp \rightarrow K^+ p \Lambda$ and $pp \rightarrow K^+ p \Sigma^0$ reactions

Away from the threshold region the acceptance of the COSY-11 spectrometer decreases rapidly and the extrapolation to the whole of phase space that is necessary in order to evaluate a  $pp \rightarrow K^+ p \Lambda$  or  $pp \rightarrow K^+ p \Sigma^0$  total

cross section becomes more model dependent. Nevertheless several pioneering measurements of the total cross sections near threshold were made at this facility [210,211,212]. Though the acceptance of the ANKE spectrometer is somewhat larger than that of COSY-11, it has rather similar limitations and this also restricted its use at the higher COSY energies [213,214].

In contrast, COSY-TOF has a much larger geometric acceptance and this enabled reliable measurements to be made up to higher energies and also yielded differential distributions that are so valuable for understanding the underlying physics [215,216,217,218,219,220]. Results on hyperon production were obtained at COSY-TOF at beam momenta of 2.5, 2.59, 2.68, 2.7, 2.75, 2.85, 2.95, 3.06, 3.2, and 3.3 GeV/c, though the data in later years were much more detailed as the equipment was refined through the addition of the straw tubes mentioned in sect. 2.2.4. However, some of the COSY-TOF results are only available in theses and should be treated as preliminary until appearing in regular publications.

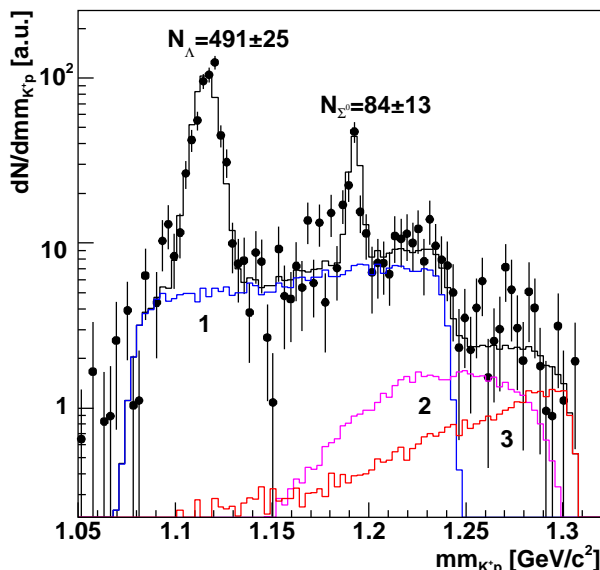


**Fig. 61.** Missing-mass distribution of  $K^+p$  pairs from  $pp$  collisions at 2.16 GeV [213]. The two peaks correspond to direct protons from the  $pp \rightarrow K^+p\Lambda/\Sigma^0$  reactions. The continua, evaluated in Monte Carlo simulation, arise from secondary protons from the  $pp \rightarrow K^+p(\Lambda \rightarrow \pi^-p)$  (histogram 1),  $pp \rightarrow K^+p(\Sigma^0 \rightarrow \gamma\Lambda \rightarrow \gamma\pi^-p)$  (2), and  $pp \rightarrow K^+n(\Sigma^+ \rightarrow \pi^0p)$  (3). The black line shows the sum of all contributions.

It must be recognized that COSY-TOF is not well suited to the measurement of small cross sections at low excess energies so that most of the data below about  $Q \approx 100$  MeV come from COSY-11 whereas at higher excess energies COSY-TOF measurements are dominant.

The principle of the COSY-11 and ANKE experiments looks simple — identify and measure a  $K^+$  and proton from a  $pp \rightarrow K^+pX$  reaction and then isolate the  $\Lambda$  and  $\Sigma^0$  from the missing-mass peaks. This is not completely

straightforward, especially at the higher energies. In the COSY-11 case there was a non-physical background from misidentified kaons, which was estimated from sideband contributions around the  $K^+$  mass. However, even if the  $K^+$  is unambiguously identified, there remains a physical source of coincident protons coming from the decays  $\Lambda \rightarrow p\pi^-$  and  $\Sigma^0 \rightarrow \gamma\Lambda \rightarrow \gamma\pi^-p$ . This is illustrated by the data in Fig. 61, obtained at ANKE at 2.16 GeV with well-identified  $K^+$  mesons [213].

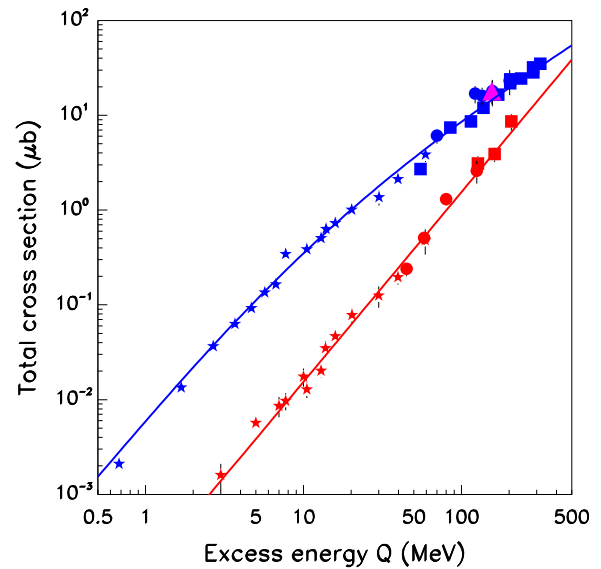


**Fig. 62.** Upper (blue) points are experimental measurements of the  $pp \rightarrow K^+p\Lambda$  total cross section whereas the lower (red) points represent data from the  $pp \rightarrow K^+p\Sigma^0$  reaction. Stars are COSY-11 values [210,211,212], squares are from COSY-TOF [215,216,217,218], and circles from ANKE [213,214]. Note that not all systematic uncertainties have been included. The solitary bubble chamber point for  $\Lambda$  production [209] is shown by the (magenta) triangle.  $\Sigma^0$  production seems to follow the indicated  $Q^2$  behaviour that is expected from three-body phase space but there is evidence for a  $\Lambda p$  final state interaction and the (blue) curve is evaluated from Eq. (4.4) with  $B_0 = 5.20$  MeV [218].

The total cross sections for  $\Lambda$  and  $\Sigma^0$  production obtained at the different COSY facilities are illustrated in Fig. 62. It is obvious from this presentation that there has been a truly impressive amount of work done in this field at COSY. The only previous data came from bubble chamber work, where 11  $K^+p\Lambda$  events were found at  $Q \approx 156$  MeV [209]. These data did at least show that the cross section was small! The total cross section for  $\Sigma^0$  production seems to follow closely the  $Q^2$  behaviour expected from undistorted three-body phase space and, as will be shown later in this section, such a behaviour is consistent with data on other  $\Sigma$  production reactions.

If one considers only the effects of an  $S$ -wave  $\Lambda p$  final state interaction then the expected energy variation is that given by Eq. (4.4) [103]. The  $\Lambda$  data are well fit with the position in energy of the antibound state  $B_0 = 5.20$  MeV ( $\alpha \approx -0.37$  fm $^{-1}$ ) [218], though it must be noted that this is an effective parameter that will depend on the relative production of spin-singlet and spin-triplet  $S$ -wave  $\Lambda p$  states.

Deviations from Eq. (4.4) are, however, easier to see on the linear scale of Fig. 63. Here is shown the ratio  $R$  of measured  $pp \rightarrow K^+ p \Lambda$  and  $pp \rightarrow K^+ p \Sigma^0$  total cross sections compared to the predictions that follow from Eq. (4.4);

$$R = C' / \left(1 + \sqrt{1 + Q/B_0}\right)^2. \quad (7.1)$$

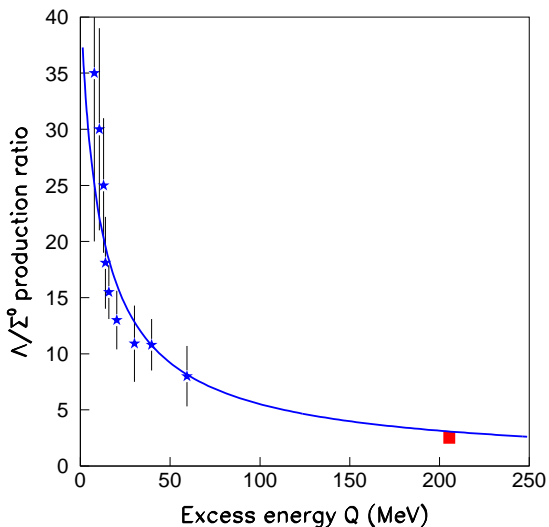


**Fig. 63.** Ratio of the total cross sections for the  $pp \rightarrow K^+ p \Lambda$  and  $pp \rightarrow K^+ p \Sigma^0$  reactions at the same values of excess energy. The (blue) stars are from COSY-11 work [211,212] and the (red) square from COSY-TOF [218]. Only data measured for the two hyperons at similar values of  $Q$  are shown here. The curve of Eq. (7.1) assumes that there is a final state interaction purely in the  $\Lambda p$  system.

## 7.2 Differential distributions

Most phenomenological descriptions of the  $pp \rightarrow K^+ p \Lambda$  reaction are based upon some form of a one-boson-exchange model and there has been considerable controversy among theorists as to whether the data are dominated by the exchange of strange (e.g.  $\bar{K}$ ) or non-strange mesons (e.g.  $\pi$ ). This problem was brought to the fore by the DISTO measurement of the spin-transfer parameter  $D_{NN}$  between

the incident proton and final  $\Lambda$  in the  $pp \rightarrow K^+ p \Lambda$  reaction [221]. The negative value of  $D_{NN}$  found was taken as evidence for the dominance of kaon compared to pion exchange [198], but it is important to stress that the possibility of  $\rho$  exchange was not considered in this discussion.

In contrast, the early COSY-TOF differential cross section results came down in favour of non-strange meson exchange by showing that the  $pp \rightarrow K^+ p \Lambda$  data have evidence for the excitation of  $N^*$  isobars in the final  $K^+ \Lambda$  channel [216,217]. This approach has far less model dependence than the  $D_{NN}$  studies. The COSY-TOF collaboration found that the  $S_{11}(1650)$  plays a prominent role near threshold and there are certainly similarities with the  $pp \rightarrow pp\eta$  reaction, which is dominated by the analogous  $S_{11}(1535)$  near threshold. Away from the threshold region the group also found evidence from the Dalitz plots for the importance of the  $P_{11}(1710)$  and/or the  $P_{13}(1710)$  isobars in  $\Lambda$  production [216,217].

Of great importance for theoretical modeling are the angular distributions measured by the COSY-TOF collaboration, only a small fraction of which are shown for  $pp \rightarrow K^+ p \Lambda$  at 2.95 GeV/c in Fig. 64 and  $pp \rightarrow K^+ p \Sigma^0$  at 3.06 GeV/c in Fig. 66. The resulting differential cross sections in the overall c.m. frame with respect to the incident proton direction should be symmetric about  $90^\circ$  because of the identical particles in the initial state. In order to check for instrumental bias, this has not been imposed for the  $p$  and  $K^+$  in the fits shown but the coefficients of the terms that are odd in  $\cos\theta$  are small and often consistent with zero [218]. Tables of preliminary values with finer binning are to be found in some COSY-TOF theses, e.g., at 2.7 GeV/c [26].

There has been a remarkable advance in both the quantity and quality of the COSY-TOF  $pp \rightarrow K^+ p \Lambda$  data in recent years and this is most evident in Fig. 64 which shows data on this reaction published in 2010 [218] and 2015 [27]. Though the two data sets are clearly consistent, the newer one allows the fit parameters to be determined much more precisely. On the other hand, the quality of the data shows more clearly the limitations of COSY-TOF in the forward direction.

Apart from providing invaluable data for models, the results are also useful in checking some of the assumptions made at other COSY facilities that do not have the advantage of TOF's extensive angular coverage. It is, for example, very helpful to see that the  $K^+$  distribution in Fig. 64 is essentially consistent with isotropy, though the proton and  $\Lambda$  distributions are forward-peaked.

In addition to the distributions in the c.m. angle shown in Figs. 64, the collaboration also evaluated distributions in the Jackson and helicity angles [218,26,27]. By fitting simultaneously the angular distributions in all three frames of reference, it was possible to confirm the importance of  $P_{11}(1710)$  and/or the  $P_{13}(1720)$  isobars away from threshold [218].

The azimuthal symmetry of the COSY-TOF detector minimizes many systematic uncertainties in measurements involving polarized particles. Figure 65 shows several measurements carried out at 2.7 and 2.95 GeV/c in

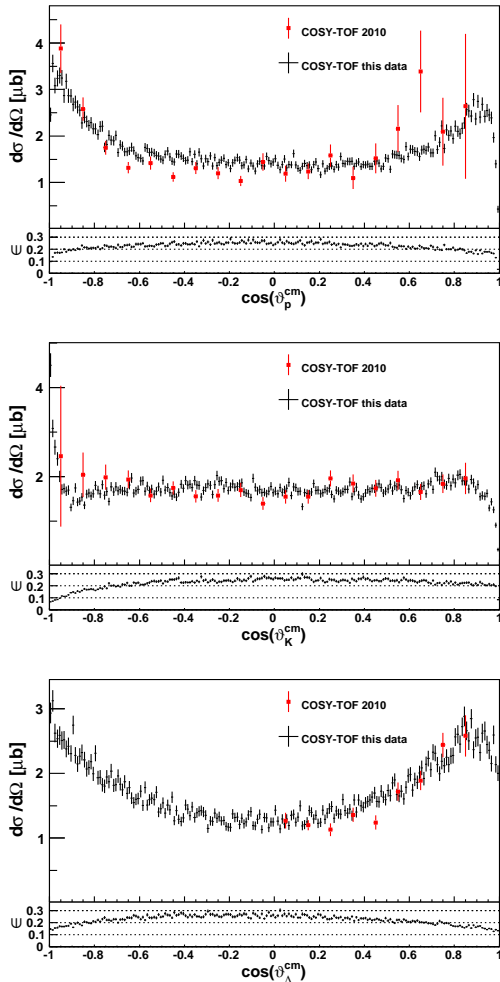


**Fig. 64.** Differential cross section for the  $pp \rightarrow K^+p\Lambda$  reaction at 2.95 GeV/c in the overall c.m. frame. The (black) crosses are recent COSY-TOF results [27] and these are to be compared to the collaboration's earlier data shown as (red) circles [218]. The distributions are for the proton (top panel), kaon (middle panel), and  $\Lambda$  (bottom panel). Beneath each distribution is shown the value of the detector acceptance and efficiency.

the  $pp \rightarrow K^+p\Lambda$  reaction [222]. Though all the events were fully reconstructed, only observables associated with the direction of the  $\Lambda$  are shown here. The first thing to notice is the change of sign in the  $\Lambda$  polarization as the beam momentum is increased by 250 MeV/c. The proton analyzing power also changes, but not as dramatically and only in the forward hemisphere. Both these quantities are sensitive to interferences between partial waves but the transverse spin-transfer parameter  $D_{NN}$  is a much more robust observable that lends itself to more direct interpretation. As already noted in connection with the DISTO data, Laget [198] has shown that a positive value of  $D_{NN}$  generally favours pion exchange whereas kaon exchange would generally lead to negative values. This argument may have little real relevance since it is believed that,

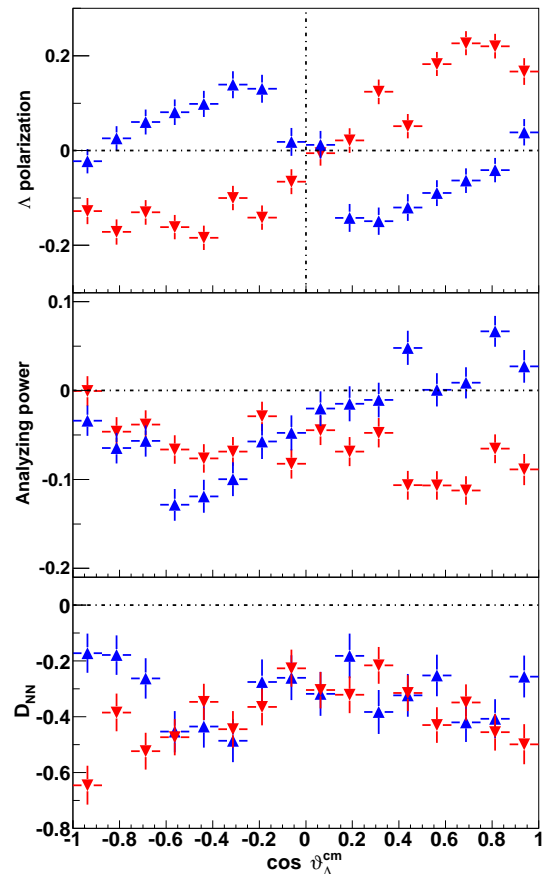


**Fig. 65.** COSY-TOF measurements of the  $pp \rightarrow K^+p\Lambda$  reaction at a beam momentum of 2.7 GeV/c (red downward-pointing triangles) and 2.95 GeV/c (blue upward-pointing triangles) [222]. Shown are the  $\Lambda$  polarization, the proton analyzing power with respect to the  $\Lambda$  direction, and the transverse spin-transfer coefficient  $D_{NN}$  between the incident polarized proton and the produced  $\Lambda$ .

even for  $\eta$  production,  $\rho$ -meson exchange is more important than pion [223] and this trend is likely to be reinforced for the production of even heavier systems.

Although one sees from Fig. 64 that the differential cross section depends strongly on the  $\Lambda$  c.m. angle, in most of the analyzes it has nevertheless been assumed that one can expand the polarization as a series in associated Legendre polynomials. This makes it even harder to identify contributions from individual partial waves.

The corresponding cross section data for the  $pp \rightarrow K^+p\Sigma^0$  reaction are shown in Fig. 66 at a beam momentum of 3.06 GeV/c. Because of the much smaller cross sections the data have been put into wider bins. Nevertheless one can see qualitative differences with  $\Lambda$  production; the  $K^+$  distribution is more bowed though the  $\Sigma^0$  looks flatter than the  $\Lambda$ . These differences might arise from the possibilities of kaon exchange or  $\Delta^*$  excitation in  $\Sigma$  production [218].



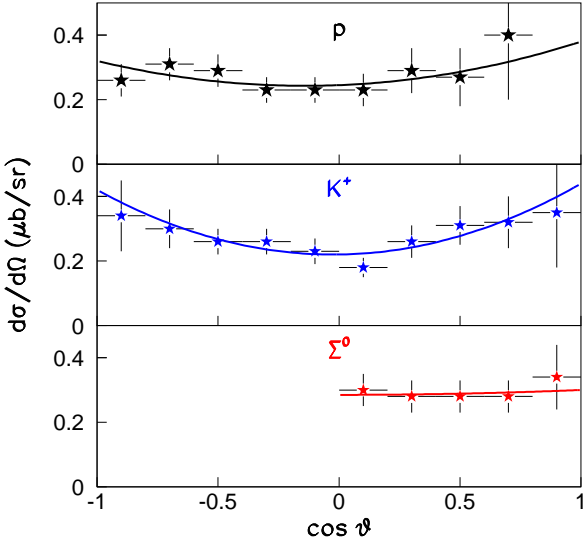


**Fig. 66.** Differential cross section for the  $pp \rightarrow K^+ p \Sigma^0$  reaction at 3.06 GeV/c in the overall c.m. frame [218]. The distributions are shown separately for the three particles in the final state, though symmetry around  $90^\circ$  has not been imposed in the fits shown. Although the beam momentum is higher than that shown in Fig. 64, the excess energy for  $\Sigma^0$  production is somewhat less than that for the  $\Lambda$ .

### 7.3 Polarization and the $\Lambda p$ scattering length

Data with a polarized proton beam were taken by the COSY-TOF collaboration at 2.95 GeV/c [220] and at 2.7 GeV/c [26]. Although one should expand  $A_y^p d\sigma/d\Omega_K$  in terms of associated Legendre polynomials, the fact that the cross section in Fig. 64 is almost independent of the kaon angle means that a direct expansion of  $A_y^p$  for the kaon asymmetry is not unreasonable. The fit

$$A_y^p = (-0.145 \pm 0.013) P_1^1(\cos \theta) + (0.065 \pm 0.010) P_2^1(\cos \theta)$$

is shown in Fig. 67. At least two terms are required in this description, suggesting that kaon  $d$ -waves are important, despite there being no sign of their presence in the differential cross section.

The results at 2.7 GeV/c are broadly similar [26] and they both show that the component that is symmetric about  $\theta_K = 90^\circ$  is as important as the one that is anti-symmetric. This proves that, in conflict with the HIREs fit [199], there must be significant amount of  $\Lambda p$  spin-triplet production, the argument being very similar to that for pion production in the  $pp \rightarrow \{pp\}_s \pi^0$  reaction discussed in sect. 4.3. Of course, since the analyzing power represents interference between amplitudes, it is not possible from this picture to determine the relative magnitudes of the singlet and triplet contributions, though some weak limits might be established, depending upon the phase assumptions.

Since the  $\Lambda p$  spin-singlet contribution to the analyzing power with respect to the kaon direction must vanish at  $\theta_K = 90^\circ$ , the product  $A_y^p d\sigma/d\Omega|_{\theta_K=90^\circ}$  is sensitive to

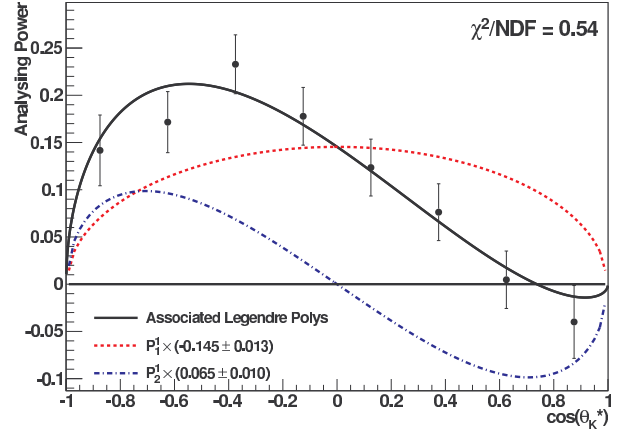


**Fig. 67.** The proton analyzing power  $A_y^K$  with respect to the kaon direction for the full range of data taken on the  $\bar{p}p \rightarrow K^+ p \Lambda$  reaction at 2.95 GeV/c [220]. Since it is seen in Fig. 64 that the  $K^+$  angular distribution is essentially isotropic, it is useful to expand  $A_y^K$  in a series of associated Legendre polynomials to give the fits shown.

the spin-triplet scattering length. However, to study this quantity in fine steps in the  $\Lambda p$  invariant mass would require very high statistics. The IKP theory group proposed an alternative procedure that exploits more seriously the analyticity properties of the production amplitudes [224, 225]. This involves the evaluation of a dispersion integral which, it is claimed, is less sensitive to the mass resolution and can lead to a robust estimate of the error associated with the theory.

In the dispersion approach,  $a = \lim_{m \rightarrow m_0} \{a(m)\}$ , where

$$a(m) = \frac{1}{2\pi} \sqrt{\frac{m_0}{m_{\text{red}}}} \mathbf{P} \int_{m_0^2}^{m_{\text{max}}^2} d\mu^2 \sqrt{\frac{m_{\text{max}}^2 - m^2}{m_{\text{max}}^2 - \mu^2}} \times \frac{1}{\sqrt{\mu^2 - m_0^2} (\mu^2 - m^2)} \log \left\{ \frac{1}{p} \left( \frac{d^2\sigma}{d\mu^2 dt} \right) \right\}. \quad (7.2)$$

Here  $m_{\text{red}}$  is the reduced  $\Lambda$  and proton mass and  $m_0 = m_p + m_\Lambda$ . The bracket contains the double-differential cross section for producing a  $\Lambda p$  pair of invariant mass  $\mu$ ,  $p$  is the relative momentum between that pair, and  $t$  is the four-momentum transfer between the incident proton and final kaon. The choice of the cut-off parameter  $m_{\text{max}}$  is rather subjective. It should be as large as possible, subject to the  $\Lambda p$  system still being in an  $S$ -wave and, in the ideal world, the theoretical corrections would be minimized if one could let  $m_{\text{max}} \rightarrow \infty$ . The authors argued that it would be sufficient to take  $m_{\text{max}} = m_0 + 40 \text{ MeV}/c^2$  [224, 225].

In the evaluation of Eq. (7.2) it is very convenient to parameterize the production cross section in order to provide a simple estimate of the principal value ( $\mathbf{P}$ ) integral. A particular choice of fit function even allows the integral to be evaluated analytically [224, 225]. The approach was tested on the Saclay inclusive  $K^+$  production data at 2.3 GeV. A spin-average scattering length of  $\bar{a} = (-1.5 \pm 0.15 \pm 0.3) \text{ fm}$  was obtained, where the

first error corresponds to the uncertainty from the data and the second from the theory. Already in this case it was found that the experimental error is smaller than the theoretical one [224,225].

Since the statistics are so much higher for the unpolarized distributions, the dispersion integral method [224,225] was first used to determine a spin-average scattering length from the COSY-TOF data [226]. This led to values for  $\bar{a}$  of

$$\begin{aligned} &(-1.25 \pm 0.08 \pm 0.3) \text{ fm at } 2.95 \text{ GeV}/c, \\ &(-1.38_{-0.05\text{stat}}^{+0.04} \pm 0.22_{\text{syst}} \pm 0.3_{\text{theo}}) \text{ fm at } 2.7 \text{ GeV}/c. \end{aligned}$$

for Refs. [220] and [26], respectively. The uncertainty in the 2.95 GeV/c value should be increased to include the systematic effects of distortions due to the  $N^*$  isobars [220], which seem to be far less important at 2.7 GeV/c, giving there perhaps an uncertainty of only  $\pm 0.1$  fm [26].

The average scattering lengths from the COSY-TOF data [220,226] are not inconsistent with the value  $(-1.5 \pm 0.15 \pm 0.3)$  fm obtained from the SPES4 data [197] using the same analysis technique. However, they are in conflict with the  $(-2.43 \pm 0.16)$  fm quoted by the HIRES collaboration [199]. In this context one should note that the HIRES data were obtained at a similar momentum (2.735 GeV/c) to those of COSY-TOF [226], but with the Big Karl spectrometer being set to take data around the forward direction. It seems likely that most of the discrepancy in the scattering length determinations arises from relatively small differences in the input in the logarithm of Eq. (7.2) near the kinematic threshold of  $m_p + m_\Lambda$ .

The COSY-TOF data at 2.95 GeV/c were not precise enough to extract a useful value for the spin-triplet scattering length by weighting the data with the  $K^+$  analyzing power [220]. The conditions are far more favourable at 2.7 GeV/c and a value of

$$a_t = (-2.55_{-1.39\text{stat}}^{+0.72} \pm 0.6_{\text{syst}} \pm 0.3_{\text{theo}}) \text{ fm}$$

was obtained, where the error bar includes an estimate of the possible  $N^*$  distortion [26]. The value found for the triplet scattering length is not inconsistent with the spin-average result and, in view of the large error bars, it is clearly going to be very hard to separate the singlet value from the triplet with this method.

It has recently been pointed out that, although the scattering length changes significantly when the maximum energy in the dispersion integral of Ref. [224,225] is reduced, the position of the  $\Lambda p$  virtual bound state at  $k = i\alpha$  hardly moves at all [227]. In fact, for the Jost parametrization used by the HIRES collaboration [200], the position of the virtual bound state is completely independent of the cut-off energy in the dispersion relation. The COSY-TOF spin-average value of  $\alpha(\text{TOF}) = -0.42 \text{ fm}^{-1}$  should be compared to the COSY-HIRES result of  $\alpha(\text{HIRES}) = -0.31 \text{ fm}^{-1}$  and  $\alpha(\sigma_T) = -0.37 \text{ fm}^{-1}$  deduced from the energy dependence of the  $pp \rightarrow K^+\Lambda p$  total cross sections shown in Fig. 62. In order to assess the significance of the deviations between these values, careful studies of

the systematic and statistical uncertainties in the different experiments are required. All the  $\Lambda p$  potentials discussed in a recent review [228] generate virtual bound states and these are typically at  $\alpha(\text{singlet}) \approx -0.28 \text{ fm}^{-1}$  and  $\alpha(\text{triplet}) \approx -0.38 \text{ fm}^{-1}$ . These are not very different from the values derived from the HIRES and TOF data but the COSY experimental results correspond to unknown spin averages.

#### 7.4 The $\Lambda : \Sigma$ cusp effect

It was already suspected from earlier COSY-TOF work that there was some kind of anomaly in the differential distribution of the  $pp \rightarrow K^+p\Lambda$  reaction at a  $\Lambda p$  invariant mass corresponding to the  $\Sigma N$  threshold [216,217]. However, by far the most detailed study of this region is to be found in their Refs. [219,220], where the effect is ascribed to a cusp associated with the very strong  $S$ -wave  $\Lambda p \rightleftharpoons \Sigma N$  transitions. As shown in Fig. 68, there is a sharp but asymmetric peak in well-identified  $pp \rightarrow K^+p\Lambda$  events. These data resulted from the high resolution COSY-TOF experiment at 2.95 GeV/c, where the invariant mass resolution of  $2.6 \text{ MeV}/c^2$  was much narrower than the cusp peak.

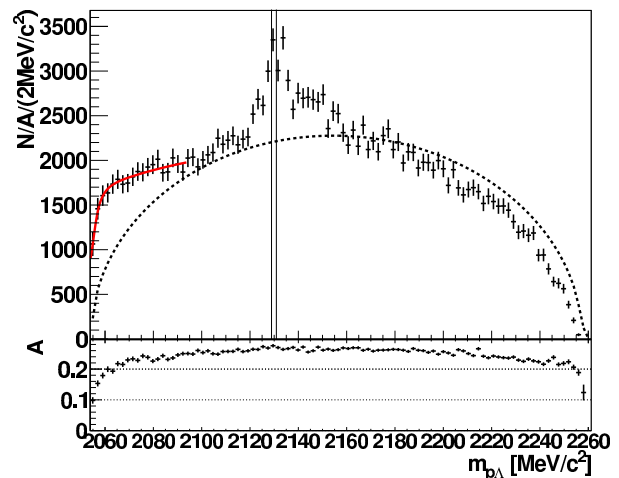


**Fig. 68.** The spectrum of  $p\Lambda$  invariant mass taken from the high resolution  $pp \rightarrow K^+p\Lambda$  COSY-TOF data at 2.95 GeV/c in  $2 \text{ MeV}/c^2$  bins [220]. The data have been corrected for the acceptance ( $A$ ) that is shown at the bottom of the figure. The vertical lines indicate the positions of the two  $\Sigma N$  thresholds. An arbitrarily scaled phase space distribution (dashed line) is shown to guide the eye. The solid (red) line at low invariant masses represents the data used in the scattering length determination discussed in the previous subsection.

There is a long history of cusps in nuclear and particle physics, especially in connection with the production of strange particles [229]. In lowest order of the transitions, the peak in Fig. 68 can be understood as being caused by an interference between a direct  $pp \rightarrow K^+\Lambda p$  amplitude and one arising from  $pp \rightarrow K^+\Sigma N$  followed by the conversion  $\Sigma N \rightarrow \Lambda p$ . The on-shell part of this second term

is proportional to the c.m. momentum in the  $\Sigma N$  system,  $q_{\Sigma N}$ . But this variable changes from being purely imaginary below the  $\Sigma N$  threshold to purely real above, which means that the interference between the direct and conversion terms changes very abruptly at the  $\Sigma N$  threshold, often giving rise to a cusp shape.

The on-shell contribution, which is really a reflection of unitarity, could be calculated using the physical  $\Sigma N \rightarrow \Lambda p$  amplitudes (if we knew them) but the off-shell ones would require a model for the coupled channel  $\Sigma N : \Lambda p$  potential. Since the cusp manifests itself largely as an interference term, there is no reason for it to be symmetric or to be Breit-Wigner in shape [219]. A full simulation of the effect would depend on knowing both the  $pp \rightarrow K^+ \Lambda p$  and  $pp \rightarrow K^+ \Sigma N$  amplitudes as well as the  $\Sigma N : \Lambda p$  potential, or at the very least the  $\Sigma N \rightarrow \Lambda p$  amplitude. The situation is further complicated by the fact that one has also to consider total spin-one and -zero in the  $\Sigma N : \Lambda p$  channels.

It is clear that it will take considerable effort to extract the full information from the data shown in Fig. 68. The peak structure in fact looks very similar to the very strong cusp effect observed with stopping kaons in the  $K^- d \rightarrow \pi^- \Lambda p$  reaction [230]. Just as in Fig. 68, there is also an unexplained enhancement on the high mass side of the  $\Lambda p$  peak. However, there is no reason for the cusp structure to look identical for the two reactions. Of course, if much higher statistics were available, then one might expect the angular distribution to change through the cusp region but it seems that in any case the cusp peak is less than 20% of the total events in the threshold region of Fig. 68 and this will limit the size of any angular change.

It could be argued that such a strong peak as that seen in Fig. 68 would only occur if the interaction had given rise to a virtual state in the  $\Sigma N$  system but there is no obvious evidence for a significant final state interaction from the energy dependence of the  $pp \rightarrow K^+ \Sigma^0 p$  reaction in Fig. 62.

Since there is a mass splitting between the  $\Sigma^0 p$  and  $\Sigma^+ n$  thresholds, one might hope to see a double cusp [229] but this would require mass resolutions that better than the 2 MeV/ $c^2$  threshold difference. Only the HIRES inclusive  $K^+$  production data achieves this, but even here it is hard to be sure if there is a two-peak structure in the data [199].

## 7.5 $pp \rightarrow K^+ n \Sigma^+$

There are many reliable measurements of the  $pp \rightarrow K^+ p \Lambda$  and  $pp \rightarrow K^+ p \Sigma^0$  total cross sections presented earlier in this section that were achieved by detecting the  $K^+$  and proton in coincidence and identifying the neutral hyperons through peaks in the missing-mass distributions. It is far harder to extend such a method to  $\Sigma^+$  production.

The most direct approach to the study of the  $pp \rightarrow K^+ n \Sigma^+$  reaction was attempted at  $Q = 13$  and 60 MeV at COSY-11 [231], where the momenta of the  $K^+$  and neutron were measured and the corresponding missing mass evaluated. For this purpose the standard COSY-11 facility

was supplemented through the introduction of a neutron detector. The total cross sections thus obtained were extraordinarily large, being about two orders of magnitude higher than those for  $\Sigma^0$  production at similar values of  $Q$  and also much larger than the results reported from later COSY experiments [213, 214, 232, 233].

In order to avoid problems associated with the detection of neutrons, a different three-prong approach was undertaken at ANKE at five beam energies, corresponding to  $Q = 13, 47, 60, 82,$  and 128 MeV [213, 214]. All three methods used the delayed-veto technique [19], that was already mentioned in connection with sub-threshold  $K^+$  production in nuclei in sect. 6.3. The approaches followed were:

- (a) A conservative upper limit on  $\Sigma^+$  production was deduced through the study of inclusive  $K^+$  production in the  $pp \rightarrow K^+ X$  reaction. This method suggested that the cross section for  $\Sigma^+$  production was broadly similar to that for the  $\Sigma^0$ . This limit was already in severe conflict with the COSY-11 claim [231].
- (b) As discussed with respect to Fig. 61, there are two significant contributions to the  $K^+ p$  missing-mass distribution in  $pp \rightarrow K^+ p X$  near the highest values of  $m_X$ . These are  $pp \rightarrow K^+ p (\Sigma^0 \rightarrow \gamma \Lambda \rightarrow \gamma \pi^- p)$  and  $pp \rightarrow K^+ n (\Sigma^+ \rightarrow \pi^0 p)$ . The first of these could be estimated from the measured  $\Sigma^0$  production rate. After taking this into account, the measurement gave values for the  $\Sigma^+$  cross section that were below the upper limits set in (a). However, it is hard to estimate quantitatively the systematic uncertainties involved.
- (c) Although the statistics were not high, the cleanest signal for  $\Sigma^+$  production was found from the  $K^+ \pi^+$  correlations that arise from the  $pp \rightarrow K^+ n (\Sigma^+ \rightarrow \pi^+ n)$  reaction. Even at the highest excess energy the background from the direct  $pp \rightarrow K^+ n \Lambda \pi^+$  is believed to be less than of the order of 2%.

All three methods gave consistent results. The ratio  $R(\Sigma^+/\Sigma^0)$  of  $\Sigma^+$  to  $\Sigma^0$  production was found to be  $0.7 \pm 0.1$  [214]. As a cross check, the cross sections derived for the  $\Sigma^0$  and  $\Lambda$  production cross sections from the missing-mass peaks were found to be consistent with other results shown in Fig. 62, though there were more uncertainties in the  $\Lambda$  case because of the higher excess energies and the limited ANKE acceptance.

The COSY-11 total cross sections for  $\Sigma^+$  production [231] are compared with those obtained at ANKE [213, 214] in Fig. 69. Also shown is the  $Q^2$  dependence expected on the basis of pure three-body phase space.

The HIRES collaboration [199], whose results were discussed extensively in sect. 6, measured the inclusive  $pp \rightarrow K^+ X$  cross section in fine steps in kaon momentum using the high resolution Big Karl spectrometer. The data taken at 2.87 GeV/ $c$  show a big jump in the missing-mass spectrum around the threshold for  $\Sigma$  production and it was assumed that this was mainly associated with the  $pp \rightarrow K^+ p \Sigma^0$  and  $pp \rightarrow K^+ n \Sigma^+$  reactions, with some localized effect coming from  $\Lambda/\Sigma$  channel coupling. Using techniques developed earlier [235], and knowing the

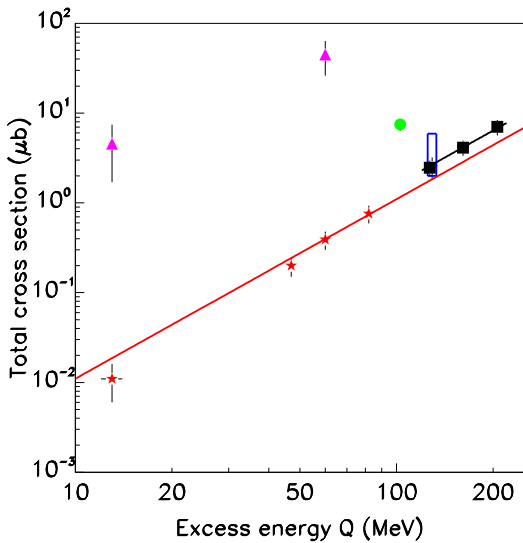


**Fig. 69.** Values of the total cross section for the  $pp \rightarrow K^+\Sigma^+n$  reaction extracted from COSY experiments. The (magenta) triangles are the original COSY-11 measurements [231]; (red) stars were obtained at ANKE [213,214]; the (green) circle was deduced from the HIRES inclusive  $K^+$  data [199]; the (blue) open rectangle is the range of values allowed by the TOF measurement at the 68% confidence level [233]. In all cases the systematic and statistical errors have been added in quadrature. Also shown by (black) squares are three points corresponding to the  $pp \rightarrow K^0p\Sigma^+$  total cross section measured by the COSY-TOF collaboration [234]. Note that one of these partially obscures the highest ANKE point. The curves represent the  $Q^2$  three-body phase-space behaviour normalized arbitrarily to the ANKE 82 MeV point and the COSY-TOF 161 MeV point.

value of the  $\Sigma^0$  production cross section, they claimed that  $R(\Sigma^+/\Sigma^0) \approx 5 \pm 1$  at  $Q = 129$  MeV [232].

Although the HIRES result casts significant doubts on the COSY-11 values in Fig. 69, there remains a very serious disagreement with the ANKE data. It has been argued [236] that the HIRES analysis should really be considered as an upper limit, principally because it underestimates the significance of the coupling between the  $pp \rightarrow K^+p\Lambda$  and  $pp \rightarrow K^+N\Sigma$  channels. The very robust measurements of the exclusive  $pp \rightarrow K^+p\Lambda$  reaction by the COSY-TOF collaboration displayed in Fig. 68 show a very strong cusp effect in the  $\Sigma$  threshold region [216,217] associated with  $\Lambda p \rightleftharpoons \Sigma N$  transitions. As a consequence, some of what had been assumed by the HIRES group to have been  $\Sigma$  production [232] could, instead, be due to  $\Lambda$  production, where the  $K^+$  missing-mass distribution is far from smooth [216,217].

The geometric acceptance of the COSY-TOF detector is much larger than that of ANKE but, as discussed in sect. 2.2.4, it was designed mainly for the detection of charged particles. In order to study the  $pp \rightarrow K^+n\Sigma^+$  reaction, the standard COSY-TOF design was extended

through the addition of a large neutron detector that was placed outside the TOF barrel, some 5.17 m downstream of the target. An unambiguous signature of the  $pp \rightarrow K^+n\Sigma^+$  reaction was a primary track due to a charged kaon, a hit in the neutron detector, and a decay of the  $\Sigma^+$  hyperon, which resulted in a kinked track [233].

Although the COSY-TOF events are very clean, the statistics achieved at  $Q = 129$  MeV were extremely limited. Of the 9 identified events, it was estimated that perhaps 2 were due to background and the rest to  $\Sigma^+$  production. Applying Poisson statistics, the authors concluded that  $(2.0 \pm 0.8) < \sigma(pp \rightarrow K^+n\Sigma^+) < (5.9 \pm 1.2) \mu\text{b}$  at the 68% confidence level [233] and this limit is shown in Fig. 69 by the open (blue) box. The ANKE value at 129 MeV [213] clearly falls within this range but, if one assumes a reasonable energy dependence, the HIRES point at 103 MeV seems very high.

Limits on the  $pp \rightarrow K^+n\Sigma^+$  cross section can also be derived by combining data on the  $pp \rightarrow K^+\Sigma^+n$  and  $pp \rightarrow K^0\Sigma^+p$  channels. However, as will be discussed in the following subsection, these are comparatively weak limits and merely suggest that the COSY-11 point at 60 MeV is likely to be in error. There are also bubble chamber data that are shown in some of the publications cited but these were taken at much higher excess energies, where the underlying Physics might be significantly different

## 7.6 $pp \rightarrow K^0p\Sigma^+$

The  $pp \rightarrow K^0p\Sigma^+$  reaction is much more closely matched to the capabilities of the COSY-TOF detector than  $pp \rightarrow K^+\Sigma^+n$  because the  $K_s^0$  decay into two charged pions occurs mainly within the barrel [234]. Since the decay  $\Sigma^+ \rightarrow p\pi^0/n\pi^+$  largely happens after the start counter, this means that there is the excellent trigger of two charged tracks turning into four tracks within the volume of the detector. Kinematic fitting procedures could then be applied with confidence because there is relatively little background. This channel was the basis of the COSY-TOF pentaquark search that is described in sect. 7.8.

Extensive angular and mass distributions were obtained at three excess energies,  $Q = 126, 161,$  and  $206$  MeV [234] and the resulting total cross sections are also shown in Fig. 69. Over the small range in excess energy, these behave like three-body phase space, i.e.,  $\sigma \propto Q^2$ , which is also indicated. This variation, which is similar to that observed in  $pp \rightarrow K^+p\Sigma^0$  and  $pp \rightarrow K^+n\Sigma^+$ , suggests that any  $\Sigma N$  FSI is quite weak. Just as for  $\Lambda$  production [218], the angular distributions were analyzed in the three frames of reference and it was found that one nucleon isobar with a mass  $\approx 1720$  MeV/ $c^2$  and width  $\approx 150$  MeV/ $c^2$  could describe the bulk of these data.

Isospin invariance allows one to put limits on the  $pp \rightarrow K^+n\Sigma^+$  cross section in terms those for  $pp \rightarrow K^+\Sigma^+n$

and  $pp \rightarrow K^0 \Sigma^+ p$ :

$$\begin{aligned} & \left[ \sqrt{2\sigma(pp \rightarrow K^+ p \Sigma^0)} - \sqrt{\sigma(pp \rightarrow K^0 p \Sigma^+)} \right]^2 \\ & \leq \sigma(pp \rightarrow K^+ n \Sigma^+) \\ & \leq \left[ \sqrt{2\sigma(pp \rightarrow K^+ p \Sigma^0)} + \sqrt{\sigma(pp \rightarrow K^0 p \Sigma^+)} \right]^2. \end{aligned} \quad (7.3)$$

Using the COSY-TOF values [218,234] as input, this results in the rather wide limits [233]

$$(0.9 \pm 0.8) \mu\text{b} \leq \sigma(pp \rightarrow K^+ n \Sigma^+) \leq (16.8 \pm 0.8) \mu\text{b}, \quad (7.4)$$

which provide little constraint in Fig. 69. The triangle constraint of Eq. (7.3) is also valid for differential distributions but the available data do not suggest that this would currently offer a very profitable approach.

### 7.7 The production of heavy hyperons

Of the heavier hyperons, there is great interest in the production of the  $\Lambda(1405)$  because models based on unitary chiral perturbation theory find two poles in the neighborhood of the  $\Lambda(1405)$  that evolve from a singlet and an octet in the exact SU(3) limit [237]. The existence of two poles means that the lineshape measured in an experiment will depend upon the particular reaction being studied [238]. This unusual situation is discussed clearly in Ref. [239].

Naively one might hope to carry out the same type of missing-mass experiment that was so successfully used for  $\Lambda$  and  $\Sigma^0$  production. This is in fact not possible because of the presence of a nearby isospin-one resonance, the  $\Sigma(1385)$ . Due to their finite widths, the two states overlap and cannot be separated in a simple  $pp \rightarrow K^+ p X$  experiment. Secondary protons are also more troublesome when the peaks are not narrow. Extra particles have therefore to be detected and, in a spectrometer such as ANKE, this leads to reduced acceptance and much greater ambiguity in the evaluation of cross sections.

The suppression of the  $\Sigma(1385)$  in the ANKE experiment [240] was achieved by looking for neutral decays because isospin forbids the reaction  $\Sigma^0(1385) \rightarrow \Sigma^0 \pi^0$ . The basic principle of the experiment was the search for the four-fold coincidence of two protons, one positively charged kaon and one negatively charged pion, i.e.,  $pp \rightarrow pK^+ p\pi^- X$ . These could correspond to the reaction chains

- (i)  $pp \rightarrow pK^+ \Sigma^0(1385) \rightarrow pK^+ \Lambda \pi^0 \rightarrow pK^+ p\pi^- \pi^0$
- (ii)  $pp \rightarrow pK^+ \Lambda(1405) \rightarrow pK^+ \Sigma^0 \pi^0 \rightarrow pK^+ \Lambda \gamma \pi^0 \rightarrow pK^+ p\pi^- \gamma \pi^0$ .

Having identified the  $\Lambda$  from its  $\pi^- p$  decay, the final piece in the jigsaw is to separate the missing masses corresponding to the  $\pi^0$  (the  $\Sigma(1385)$  case) and  $\pi^0 \gamma$  (the  $\Lambda(1405)$  case). This is illustrated in Fig. 70 for the ANKE data taken at 2.83 GeV [240]. The experimental points are compared to the simulation of the  $\Lambda(1405)$  channel, where the  $X = \pi^0 \gamma$  distribution should be little affected by any uncertainties in the experimental resolution. The remainder is a Gaussian fit to the  $\pi^0$  peak, which arises from the  $\Sigma^0(1385)$  contribution. This fit shows that only

about 4 of the  $\Sigma^0(1385)$  events lie above the experimental cut of  $190 \text{ MeV}/c^2$  that was chosen to select the  $\Lambda(1405)$  signal [240].

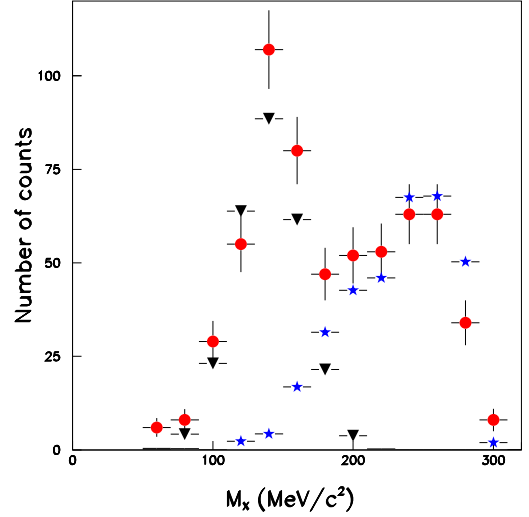


**Fig. 70.** Missing-mass distribution from the  $pp \rightarrow K^+ p \Lambda X$  reaction at 2.83 GeV [240]. The (red) circles are experimental data whereas the (blue) stars are simulations of the reaction chain leading to  $X = \pi^0 \gamma$  normalized to the large  $M_X$  data. After subtracting this contribution, the (black) inverted triangles are a fitted Gaussian representation of the  $X = \pi^0$  signal.

The biggest uncertainty in the quoted cross section,

$$\sigma_{\text{tot}}(pp \rightarrow pK^+ \Lambda(1405)) = (4.5 \pm 0.6_{\text{stat}} \pm 1.8_{\text{sys}}) \mu\text{b},$$

comes from the extrapolation from the miniscule ANKE acceptance to the whole of phase space, which is certainly a leap of faith. The rather complex analysis reported in Ref. [240] is typical of the approaches that have to be undertaken in the study of heavy hyperon production at ANKE. The acceptance at COSY-TOF is much larger but this spectrometer was not designed for events with two neutral particles.

The  $\Lambda(1405)$  mass spectrum produced in a single reaction [240] sheds little light on the two-pole hypothesis [238], though it is informative regarding the interpretation of kaon pair production presented in sect. 8.1.

A similar but more detailed experiment was carried out at the higher energy of 3.5 GeV using the HADES spectrometer at GSI [241]. Within the uncertainties of the two ANKE and HADES points, it seems that the  $Q$  dependence of  $\sigma_{\text{tot}}(pp \rightarrow pK^+ \Lambda(1405))$  could be similar to that for  $\sigma_{\text{tot}}(pp \rightarrow pK^+ \Lambda)$ .

An earlier experiment at ANKE [242] investigated the three-particle correlations in  $pp \rightarrow K^+ p\pi^- X^+$  and  $pp \rightarrow K^+ p\pi^+ X^-$ , also at 2.83 GeV. For both reaction channels evidence was found for bumps that could correspond to a heavy hyperon with mass  $M(Y^{0*}) = (1480 \pm 15) \text{ MeV}/c^2$

and width  $\Gamma(Y^{0*}) = (60 \pm 15) \text{ MeV}/c^2$ . The isospin dependence of this effect was not established and there is little supporting evidence for either a  $\Lambda$  or a  $\Sigma$  state in this region in the current PDG tables [164].

## 7.8 Pentaquarks

Following the introduction of the quark model, mesons were generally categorized as  $q\bar{q}$  pairs and baryons as  $qqq$  triplets; any state that did not fit into this scheme was classed as being *exotic*. A prime example of this was the  $Z_0^*$  baryon, which has isospin-zero and strangeness +1. Searches were made for such a state in the nineteen sixties through the comparison of total cross sections of  $K^+$  interactions with hydrogen and deuterium but, because of decay losses in the kaon beams of low momenta, the data were not sensitive to low mass states [243,244].

The subject was opened again towards the end of the century with the proposal for a narrow ( $\Gamma < 15 \text{ MeV}/c^2$ )  $Z_0^*$  baryon with a mass of  $\approx 1530 \text{ MeV}/c^2$  [245], which fell below the energy region of the total cross section experiments [243,244]. This suggestion inspired numerous enthusiastic searches for such a state, which had been renamed  $\Theta^+$  by the theorists involved. Unlike some of the other members of the proposed antidecuplet of states, there could be no doubt that one in the  $K^+n$  or  $K^0p$  channel would be *exotic* and so had, in the quark model, to be of the form  $qqqqq$ , i.e., be a *pentaquark*.

In view of the mixed results achieved at other laboratories, the search carried out at COSY-TOF looked very clean and promising because it was well adapted to the unique characteristics of the spectrometer [246]. The experiment consisted of a measurement of the  $pp \rightarrow K^0p\Sigma^+$  reaction, which was already described in sect. 7.6. At a beam momentum of  $2.95 \text{ GeV}/c$ , the excess energy was only  $Q = 126 \text{ MeV}$ , which limited the  $K^0p$  invariant mass to lie below about  $1562 \text{ MeV}/c^2$ .

Immediately after the TOF start counter there were two tracks from the proton and the  $\Sigma^+$  but, after a  $K_s^0 \rightarrow \pi^+\pi^-$  decay, these become four tracks within the TOF barrel. Also within the barrel the  $\Sigma^+$  decays into either  $\pi^0p$  or  $\pi^+n$ , and events were retained that showed the resulting kink in the track. The decay kinematics and angular distributions allow a clear suppression of the main background arising from the  $pp \rightarrow K^+p\Lambda$  reaction. Clear peaks were seen in the reconstruction corresponding to the  $\Sigma^+$  and  $K^0$  and the resolution in these masses was consistent with the simulations, which showed that the resolution in  $m(K^0p)$  should be  $18 \pm 3 \text{ MeV}/c^2$ . There were some 939 events that passed all the required cuts.

The initial data shown in Fig. 71 display a peak at  $1530 \pm 5 \text{ MeV}/c^2$  with a width of  $18 \pm 4 \text{ MeV}/c^2$  (FWHM), which is completely consistent with the expected mass resolution. This seemed to present strong evidence for the existence of the  $\Theta^+$  with the expected properties.

The definitive COSY-TOF experiment was carried out at the slightly higher momentum of  $3.059 \text{ GeV}/c$  [247], so that the upper bound of the  $K^0p$  invariant mass was increased to  $1.597 \text{ GeV}/c^2$ , which is further away from

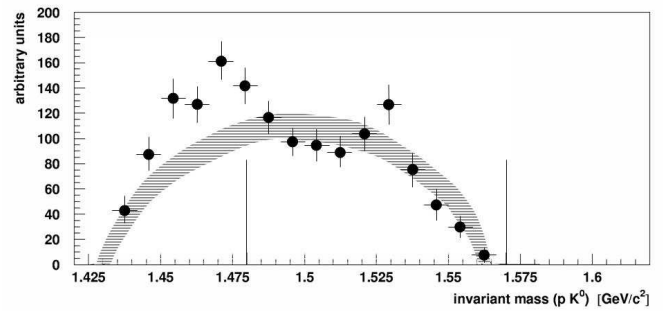


**Fig. 71.** Invariant  $K^0p$  mass distribution from the  $pp \rightarrow K^0p\Sigma^+$  reaction. The points represent the results of the initial COSY-TOF experiment at  $Q = 126 \text{ MeV}$  [246]. The shaded band corresponds to the spectrum evaluated in the second experiment at  $Q = 161 \text{ MeV}$  [247]. To account for the different values of  $Q$ , the invariant mass axis has been scaled according to the kinematically allowed range and the height of the band adjusted so that the averages agreed for data between the two vertical lines, i.e.,  $m(K^0p) > 1480 \text{ MeV}/c^2$ .

the suggested pentaquark peak. The experimental method was similar to the previous one [246] but with the much higher statistics of more than 12,000 independent events. In addition, three different approaches were used in the analysis, depending largely on how the information regarding the  $\Sigma^+$  track was included. All three results agreed within statistical uncertainties.

No evidence was found for any peak, especially one in the  $1530 \text{ MeV}/c^2$  region, and an upper limit of the  $pp \rightarrow \Sigma^+\Theta^+$  production cross section of  $150 \text{ nb}$  was found at the 95% confidence level. It should be noted here that systematic studies of the instrumental background allowed corrections to be made to the second data set [247] that were not available for the earlier results [246]. An even lower limit was found in a subsequent analysis [248], depending upon the assumed  $\Theta^+$  mass.

To give a *qualitative* illustration of the difference between the two sets of COSY-TOF results, we show in Fig. 71 the original COSY-TOF points [246] together with a grey band corresponding to the newer COSY-TOF results [247]. To account for the different beam energies, the  $K^0p$  invariant mass axis has been scaled according to the kinematically allowed range.

A very different approach was undertaken at ANKE, where the four-body final state in the  $pp \rightarrow K^0p\pi^+\Lambda$  reaction was investigated at  $2.83 \text{ GeV}$  [249]. Here the  $\Lambda$  was identified through its  $\pi^-p$  decay so that the actual final state was  $K^0pp\pi^+\pi^-$ . Rather than measuring the  $K^0$  through its  $\pi^+\pi^-$  decay, as was done at COSY-TOF [246,247], it was deduced from the missing mass of the other four particles, viz.  $pp\pi^+\pi^-$ . With this selection procedure, 1041 events were found corresponding to the  $pp \rightarrow K^0p\pi^+\Lambda$  reaction. Assuming a phase-space dependence this led to a total cross section of  $\sigma(pp \rightarrow K^0p\pi^+\Lambda) = 1.41 \pm 0.05 \pm 0.33 \mu\text{b}$ .

No peak was found that could correspond to the  $\Theta^+$  and the upper limit for producing this state

$$\sigma(pp \rightarrow \Lambda\pi^+\Theta^+) < 58 \text{ nb}$$

at the 95% confidence level depended weakly on the assumed position and width of the state. Without a reaction model for the production of this non-existent state, it is not useful to try to compare this limit with that obtained at COSY-TOF for the  $pp \rightarrow \Theta^+\Sigma^+$  reaction [247], though the order of magnitude larger statistics in the COSY-TOF case should certainly be noted.

Despite the negative results of the COSY-TOF experiment, pentaquarks are far from being dead since the LHCb collaboration at CERN have recently claimed two peaks in the  $J/\Psi p$  system with high statistical significance but with masses over  $4 \text{ GeV}/c^2$  [250].

### 7.9 Hyperon production in proton-neutron collisions

There is relatively little information available on hyperon production in proton-neutron collisions and what does exist is rarely very systematic. The first indications of the strength of production on the neutron came from a comparison of inclusive  $K^+$  production by protons on hydrogen and deuterium targets [251]. Below the threshold for  $\Sigma$  production, the  $K^+$  rates are dominated by quasi-free  $pp \rightarrow K^+p\Lambda$  and  $pn \rightarrow K^+n\Lambda$  reactions but, at higher energies,  $\Sigma$  production and even the formation of kaon pairs must also be considered.

The obvious disadvantage of this approach is that the centre-of-mass energy is not well determined, due to the Fermi motion in the deuteron target, and some modeling is required. After doing this, it was found that the weighted average of the production ratio over the three lowest beam energies was  $\sigma_{pd}^{K^+}/\sigma_{pp}^{K^+} = 1.4 \pm 0.2$  which, after taking shadowing into account, means that the ratio of  $K^+$  production cross sections in  $pn$  and  $pp$  collisions

$$R = \sigma_{pn}^{K^+}/\sigma_{pp}^{K^+} = 0.5 \pm 0.2. \quad (7.5)$$

At low energies, where only  $\Lambda$  production is possible, the  $0.5 \pm 0.2$  is comfortably above the isospin lower bound  $R \geq 0.25$ . The result in this region for the ratio of cross sections of definite isospin becomes

$$\sigma^{I=0}(NN \rightarrow KNA)/\sigma^{I=1}(NN \rightarrow KNA) = 1.0 \pm 0.8. \quad (7.6)$$

It should, of course, be noted in this context that, for a neutron target, half of the  $I = 0$  signal would be associated with  $K^0$  production.

The inclusive approach was later refined by detecting a *spectator* proton in an STT in coincidence with the  $K^+$  measured in ANKE [252]. Apart from being more selective, the spectator proton allowed the reconstruction of the c.m. energy on an event-by-event basis. Although extensive data were taken below the  $\Sigma$  threshold, definitive results on the quasi-free  $pn \rightarrow K^+\Lambda n$  cross section are still not available.

A similar use of the STT was made in the study of the quasi-free measurement of the  $pd \rightarrow p_{\text{sp}}K^+p\Sigma^-$  reaction at ANKE [253]. By measuring the spectator proton  $p_{\text{sp}}$  in a silicon tracking telescope, a scan over a wide range of centre-of-mass energies was achieved while keeping the beam energy fixed. The  $K^+$  and primary proton could then be detected in ANKE and the  $\Sigma^-$  identified through the missing-mass peak. The experiments were carried out at beam momenta of 2.915 and 3.015 GeV/c. If these had been undertaken on a free neutron target they would have corresponded to excess energies of about 110 and 140 MeV, respectively. These values are reduced by the deuteron binding energy and the energy taken by the spectator proton in the STT. However, the biggest effect comes from the placing of the STT towards the backward hemisphere so that the useful coverage shown for the total cross sections of Fig. 72 is  $30 \leq Q \leq 130 \text{ MeV}$ .

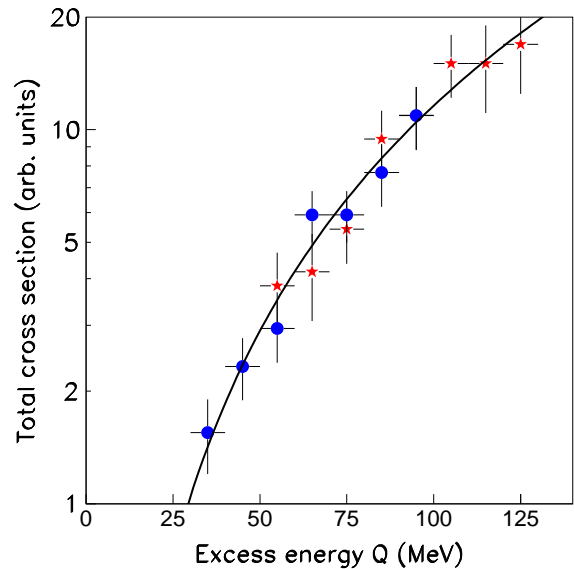


**Fig. 72.** The total cross section for the quasi-free  $pn \rightarrow K^+p\Sigma^-$  reaction extracted from proton-deuteron collisions at 2.915 GeV/c (blue circles) and 3.015 GeV/c (red stars) [253]. Due to difficulties in evaluating the acceptance involving the STT, these preliminary values are not normalized and the 3.015 GeV/c results have been multiplied by a factor of 1.3 compared to Ref. [253] in order to ensure good relative normalization between the two data sets. The curve,  $\sigma \propto Q^2$ , represents undistorted three-body phase space.

Due to complications in evaluating the acceptance involving the STT, the total quasi-free  $pn \rightarrow K^+p\Sigma^-$  cross sections of Fig. 72 have not yet been reliably normalized and they are displayed in arbitrary units. Nevertheless, over the range of energies shown, the cross section seems to follow the  $Q^2$  behaviour expected from three-body phase space. This is seen in other  $\Sigma$  production reactions but, of course, the effects of a strong  $\Sigma N$  final state interaction might well only show up closer to threshold.

By charge symmetry, the cross sections for  $pn \rightarrow K^0 \Lambda p$  should be identical to that for  $pn \rightarrow K^+ \Lambda n$ . The reaction  $pd \rightarrow p_{\text{sp}} K^0 p \Lambda$  was studied in the COSY-TOF detector [254]. Immediately after the target, only the track of the fast proton is seen, the *spectator* proton  $p_{\text{sp}}$  being undetectable. However, after  $\Lambda \rightarrow p\pi^-$  and  $K^0 \rightarrow \pi^+\pi^-$  decays, five tracks are present, which is an excellent signal for a good event. The main difficulty is identifying the two decay vertices from the four tracks with their measurement errors – the combinatorial background. In practice, this combinatorial background can be much more of a problem than the physical background.

In the data taken at 2.261 GeV, fewer than one in  $10^5$  events corresponded to the  $pd \rightarrow p_{\text{sp}} K^0 p \Lambda$  reaction and so the robust trigger was crucial [254]. Nevertheless, the preliminary cross section ratio of Eq. (7.5) seems to be only just above the isospin limit of  $R = 0.25$ , though this value depends sensitively upon the detector efficiencies. In stark contrast to the ANKE result [251], this would imply very little isospin  $I = 0$  production. However, a more detailed COSY-TOF data set is currently under analysis [255].

## 8 Kaon pair production

Since strangeness is conserved in strong interactions, the production of a  $K^+$  must be associated with that of particles with a net strangeness  $-1$ . In the previous section these were hyperons but now we turn to  $K^+K^-$  production. However, the specific case of  $pd \rightarrow {}^3\text{He} K^+K^-$  will be deferred until sect. 9.4, where it will be treated along with other  $pd \rightarrow {}^3\text{He} X$  reactions.

### 8.1 Kaon pair production in nucleon-nucleon collisions

Well above the threshold for hyperon production in proton-proton collisions it is possible to produce kaon pairs through the  $pp \rightarrow ppK^+K^-$  reaction. The early COSY experiments in this area were carried out by the COSY-11 collaboration [256, 257, 258, 259] and these results are crucial in the determination of the energy dependence of the total cross section near threshold. The larger acceptance available at the ANKE spectrometer allowed experiments to be carried out at higher excess energies, including above the  $\phi$  threshold. The higher statistics also meant that more differential observables could be usefully measured [260, 261, 262, 263].

In the COSY-11 experiments the two protons were first identified and measured using the time-of-flight information in combination with the momentum analysis [256, 257, 258]. Due to the decay of the  $K^+$ , the probability that it reached the second stop counter is of the order of a few percent and so its four-momentum was evaluated using the time difference from the target to the first stop counter, using start information derived from the proton measurements. Though  $K^-$  were also detected by a combination of scintillator and silicon pads, the reaction was confirmed through the evaluation of the missing mass with respect to the two protons and the  $K^+$  candidate, which showed a

peak at the  $K^-$  mass. The value of the overall luminosity was reliably derived by measuring proton-proton elastic scattering in parallel. More problematic was the  $\approx 10\%$  uncertainty in the efficiency, which was estimated by including only the  $pp$  final state interaction in the four-body phase space. Distortions due to the  $K^-p$  and  $K^+K^-$  final state interactions were not considered for this purpose.

The experimental procedure was somewhat different at ANKE [260, 261, 262, 263], where the  $K^+$  candidate was first selected using time-of-flight information<sup>5</sup>. The signal from the  $K^+$  stop counter was then used in the determination of the momenta of the  $K^-$  and one of the protons. The reaction was finally identified by looking for the proton peak in the missing mass with respect to the  $pK^+K^-$  recoiling system. The uncertainties in the overall acceptance are slightly less than those at COSY-11 but, for data taken above the  $\phi$  threshold, there is an additional uncertainty associated with the separation of  $\phi$  and non- $\phi$  events. The resulting  $\phi$  data will be reviewed in the next subsection. Proton-proton elastic scattering was also used as the basis for the luminosity determination, though there was greater ambiguity in the  $pp$  database at the small angles used at ANKE, which has only recently been clarified [78].

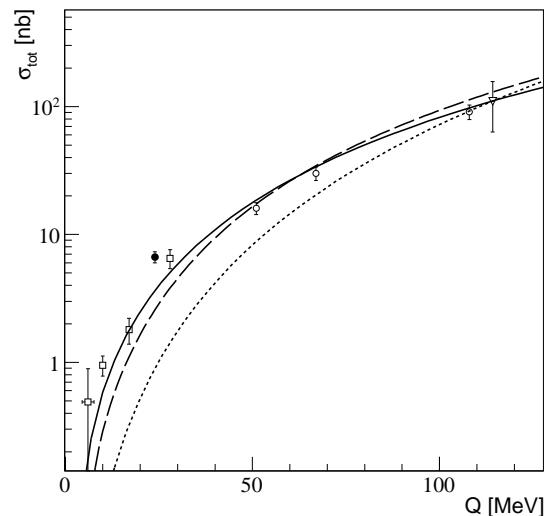


**Fig. 73.** Total cross section for the non- $\phi$  contribution to the  $pp \rightarrow ppK^+K^-$  reaction as a function of the excess energy  $Q$ . The data are taken from DISTO (triangle) [168], COSY-11 (squares) [256, 257, 258], and ANKE (open and closed circles) [260, 261, 262, 263]. The dotted line shows the four-body phase space simulation, whereas the solid line represents the simulations of Eq. (8.2) with  $a_{K-p} = 1.5i$  fm. The predictions of a one-boson exchange model are shown by the dashed line [264].

<sup>5</sup> A use of the delayed-veto trigger for the  $K^+$  would have reduced the acceptance by almost an order of magnitude.



The total cross sections measured at COSY for the non- $\phi$  contribution to the  $pp \rightarrow ppK^+K^-$  reaction are shown in Fig. 73 along with one point measured earlier by the DISTO collaboration [168]. These show a steady rise with excess energy  $Q$  but the four-body phase space normalized in the 100 MeV region seriously underestimates the low energy data<sup>6</sup>. Part of this can be compensated through the introduction of a  $pp$  final state interaction but, in order to get a reasonable description near threshold, some attraction is required between the  $K^-$  and each of the final protons. Clear evidence for this is to be found in the differential distributions, to which we now turn.

It was first apparent in the COSY-11 data at  $Q = 10$  and 28 MeV [258] that the  $K^-p$  interaction was strongly attractive because the measured events clustered around low  $K^-p$  or even low  $K^-pp$  invariant masses. This observation was taken up by the ANKE collaboration [261, 262, 263] which, following COSY-11, constructed the ratios of cross sections with respect to the  $K^\pm p$  and  $K^\pm pp$  invariant masses:

$$R_{Kp} = \frac{d\sigma/dM_{K^-p}}{d\sigma/dM_{K^+p}}, \quad R_{Kpp} = \frac{d\sigma/dM_{K^-pp}}{d\sigma/dM_{K^+pp}}. \quad (8.1)$$

The  $R_{Kp}$  and  $R_{Kpp}$  ratios at  $Q = 24$  MeV are shown in Fig. 74 [263].

It is well known that there can be no rigorous estimation of an enhancement factor  $F$  when three or more particles interact in the final state. Nevertheless, in the case of  $pp \rightarrow pp\eta$ , where there are strong interactions between all three pairs of particles, the data can be well described by taking the overall enhancement as the product of the three two-body enhancements [267]. This ansatz was also adopted in the analysis of the ANKE data, where it was assumed that

$$F = F_{pp}(q_{pp}) \times F_{Kp}(q_{Kp_1}) \times F_{Kp}(q_{Kp_2}) \times F_{KK}(q_{KK}), \quad (8.2)$$

where  $q_{pp}$ ,  $q_{Kp_1}$ ,  $q_{Kp_2}$ , and  $q_{KK}$  are the magnitudes of the relative momenta in the  $pp$ , the two  $K^-p$ , and the  $K^+K^-$  systems, respectively. It is believed that the  $K^+p$  interaction is weakly repulsive and may be neglected compared to the uncertainties in the other effects.

The critical interaction in the  $R_{Kp}$  ratio of Fig. 74 is that between the  $K^-$  and each of the protons. A good description of the data is achieved by assuming a simple  $K^-p$  scattering length formula with  $a_{K^-p} = 2.45i$  fm [263]. What is more surprising is that the ansatz of Eq. (8.2) gives an equally good description of the  $Kpp$  data at  $Q = 24$  MeV. However, it must be admitted that  $a_{K^-p}$  is an effective parameter and should not necessarily be equated to the free  $K^-p$  scattering length because the factorization assumption clearly does not contain all of the relevant

<sup>6</sup> Unpublished COSY-11 data suggest that the cross section is below 0.1 nb at  $Q \approx 4.5$  MeV [265], which is more restrictive than the previous COSY-11 upper limit of 0.16 nb at  $Q = 3$  MeV [266]. This departure from the trend shown by the higher energy data might be due to the Coulomb repulsion between the  $K^+$  and the two protons, which must be critical so close to threshold.

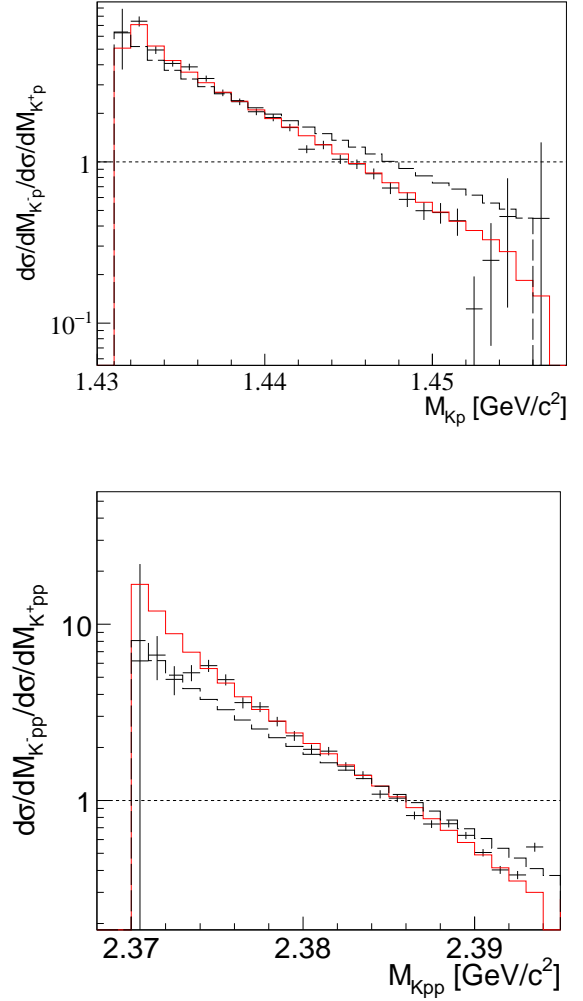


**Fig. 74.** The ratios  $R_{Kp}$  and  $R_{Kpp}$  of Eq. (8.1) at  $Q = 24$  MeV [263]. The red solid and broken black histograms represent estimations based on Eq. (8.2) that take into account  $K^-p$ ,  $pp$  and  $K^+K^-$  final state interactions with  $a_{K^-p} = 2.45i$  fm and  $a_{K^-p} = 1.5i$  fm, respectively.

physics. In fact the ANKE data above the  $\phi$  threshold are better fit with  $a_{K^-p} = 1.5i$  fm, though it should be noted that the data are not very sensitive to the phase of  $a_{K^-p}$  [261, 262].

Interesting effects also arise from mass differences. For example,  $2m_{K^0} - 2m_{K^\pm} \approx 8$  MeV/ $c^2$  and a change in behaviour might be seen at the  $K^0\bar{K}^0$  threshold in the  $pp \rightarrow ppK^+K^-$  data as a function of  $m_{K^+K^-}$  shown in Fig. 75. The inclusion of final state interactions through  $K^0\bar{K}^0 \rightleftharpoons K^+K^-$  in a coupled-channel formalism was explored in Ref. [268] though even these high statistics data were not sufficient to identify unambiguously a cusp at the  $K^0\bar{K}^0$  threshold. On the other hand, there is no evidence for the production of the  $a_0/f_0$  scalar mesons in this reaction, which was one of the motivations for measuring  $pp \rightarrow ppK^+K^-$ .

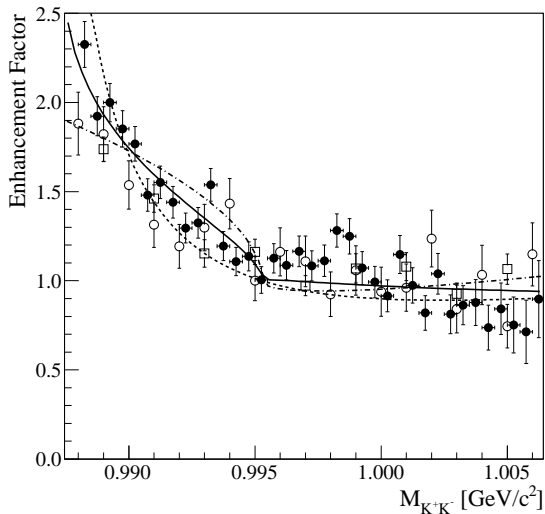


**Fig. 75.** Ratio of  $K^+K^-$  invariant mass distributions measured at different energies at ANKE in the  $pp \rightarrow ppK^+K^-$  reaction [261,262,263] to a simulation that includes only  $K^-p$  and  $pp$  final state interactions. The solid curve represents the best fit in a model that includes elastic  $K^+K^-$  FSI and  $K^0\bar{K}^0 \Rightarrow K^+K^-$  charge-exchange [268]. The best fits neglecting charge exchange or neglecting the elastic  $K^+K^-$  FSI are shown by the dashed and dot-dashed curves, respectively.

Another mass difference that might be significant is  $m_{K^0} + m_n - m_{K^-} - m_p \approx 5.3 \text{ MeV}/c^2$ , which means that there might be some kind of anomaly in the  $K^-p$  mass distribution of Fig. 74 at  $m_{K^-p} \approx 1437 \text{ MeV}/c^2$ , though there is little sign of this in the data.

The inclusion of the  $pp$ ,  $K^-p$ , and  $K^+K^-$  final state interactions improves significantly the prediction of the energy dependence of the  $pp \rightarrow ppK^+K^-$  total cross section shown in Fig. 73.

The ANKE data on  $\Lambda(1405)$  production in the reaction  $pp \rightarrow K^+p(\Lambda(1405) \rightarrow \Sigma^0\pi^0)$  were discussed in sect. 7.7. Although the centre of this hyperon lies just below the  $K^-p$  threshold, it has a finite width and the high mass tail can decay into the  $K^-p$  channel. There is therefore a strong possibility that some of the kaon pair production observed at COSY might be proceeding through this doorway state, i.e.,  $pp \rightarrow K^+p(\Lambda(1405) \rightarrow K^-p)$ . This would account for the strong enhancements that are observed for low  $K^-p$  invariant masses. This idea has been tested in a specific Lagrangian model [269] and the results are shown in Fig. 76.

The shapes of both mass distributions shown in Fig. 76 are very encouraging and the normalization factor of 0.4 may be within the combined experimental and theoretical uncertainties. Though the predictions were based upon a specific model whose normalization was tuned to fit the  $pp \rightarrow pK^+K^-p$  data, it is quite likely that the results and normalization for the  $pp \rightarrow pK^+\pi^0\Sigma^0$  reaction are more general than the particular model used in Ref. [269]. It is clear that, if the  $\Lambda(1405)$  plays an important role

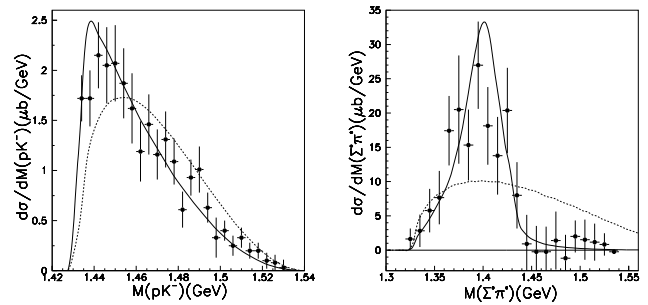


**Fig. 76.** Left: Differential cross section for the  $pp \rightarrow pK^+K^-p$  reaction at  $T_p = 2.83 \text{ GeV}$  as a function of the  $K^-p$  invariant mass [261]. The predictions of the Lagrangian model are shown by the solid line [269]. Right: Differential cross section for the  $pp \rightarrow pK^+\pi^0\Sigma^0$  reaction also at 2.83 GeV. The predictions of the Lagrangian model (solid line) have been scaled by a factor of 0.4 before being compared to the ANKE data [240]. In both cases the dashed line represents normalized four-body phase space [269].

in kaon pair production, one will find it very hard to identify a signal for the production of the scalar bosons  $a_0(980)/f_0(980)$ .

The background for the  $a_0(980)$  could be smaller in the  $K^+\bar{K}^0$  charged channel and searches were undertaken at ANKE for scalar meson production in the  $pp \rightarrow K^+\bar{K}^0d$  reaction at proton beam energies of 2.65 GeV [270] and 2.83 GeV [271]. Selection rules play a very important role here because the combination of the Pauli principle and angular momentum and parity conservation do not allow all three final particles to be in relative  $s$ -waves. An analysis of the two data sets suggests that it is the  $\bar{K}^0d$  system that is dominantly in the  $s$  wave, being driven by the attraction of the antikaon to nucleons and nuclei [272]. There is only very weak evidence for the possible production of the  $a_0^+(980)$  but the two final state interactions together do reproduce a little better the energy dependence of the total cross section.

A closely allied reaction is  $pn \rightarrow K^+K^-d$ , which was studied at ANKE in quasi-free kinematics using a deuterium target [273]. The effective luminosity was determined using the Schottky technique that was discussed in sect. 2.4 [52]. Though the beam energy was fixed at 2.65 GeV, the reconstruction of the  $K^+K^-d$  centre-of-mass energy allowed the reaction to be studied up to excess energies of around 100 MeV. Above  $Q = 32.1 \text{ MeV}$  there was also the problem of separating direct  $K\bar{K}$  production from that of the  $\phi$ , whose results are discussed in sect. 8.2. The resulting total cross sections are shown in Fig. 77 along with those for  $pp \rightarrow dK^+\bar{K}^0$  [270,271].

The relationship between the two reactions is seen more clearly in the isospin basis of Eq. (8.3):

$$\sigma(pp \rightarrow dK^+\bar{K}^0) = \sigma_1, \quad \sigma(pn \rightarrow dK^+K^-) = \frac{1}{4}(\sigma_1 + \sigma_0) \quad (8.3)$$

An interpolation of the  $pn$  results to energies where  $pp \rightarrow dK^+\bar{K}^0$  was measured [270,271] gives isospin ratios of  $\sigma_0/\sigma_1 = 0.9 \pm 0.9$  at  $Q = 47 \text{ MeV}$  and  $0.5 \pm 0.5$  at 105 MeV,

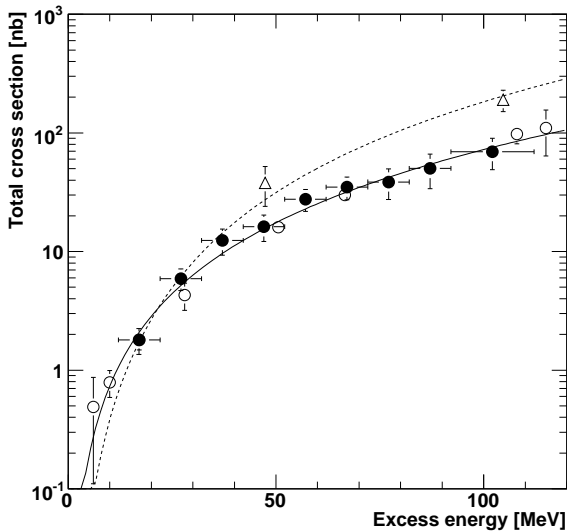


**Fig. 77.** Total cross section for non- $\phi$   $K\bar{K}$  production in nucleon-nucleon collisions near threshold. The closed circles denote  $pn \rightarrow dK^+K^-$  data [273] and the open triangles  $pp \rightarrow dK^+\bar{K}^0$  [270,271], whereas the open circles show the results for  $pp \rightarrow ppK^+K^-$  up to 2008 [256,257,258,261,168]. The dotted curve is the best fit to the  $pp \rightarrow dK^+\bar{K}^0$  data within a simple final state interaction model [103], whereas the solid curve includes also the isospin-zero contribution needed to describe the energy dependence of the  $pn \rightarrow dK^+K^-$  total cross section.

where the large error bars arise from the subtraction implicit in Eq. (8.3). All that one can reasonably conclude from this is that  $\sigma_0$  cannot be much larger than  $\sigma_1$ , despite the necessity for having a  $p$ -wave in the final state in the  $I = 1$  case.

Also shown in Fig. 77 are values of the  $pp \rightarrow ppK^+K^-$  total cross sections [256,257,258,261,168], which are very similar in magnitude to those for  $pn \rightarrow dK^+K^-$  [273]. However, some account must be taken of the difference between the 3-body and 4-body final states but, when this is done, one sees that

$$\sigma(pp \rightarrow ppK^+K^-)/\sigma(pn \rightarrow \{pn\}_{I=0}K^+K^-) \approx 1.5, \quad (8.4)$$

though this estimate is rather model-dependent.

The  $K^-d/K^+d$  cross section ratio, i.e., the analogue of Eq. (8.1), shows the usual preference for the  $K^-$  to be attracted to the deuteron. A reasonable agreement with the data was achieved with a scattering length of  $a_{K^-d} = (-1.0 + i1.2)$  fm, which would be in line with theoretical expectations [274].

## 8.2 $pp \rightarrow pp\phi$ and $pn \rightarrow d\phi$ reactions

The ANKE experiments on  $K^+K^-$  production in both  $pp$  [260,261,262] and  $np$  [275] collisions were primarily motivated by the study of  $\phi$  production, where the meson was detected through its decay  $\phi \rightarrow K^+K^-$ . Since

the cross sections are low, and the multipion backgrounds are high, it is hard to isolate the  $\phi$  in  $pp$  collisions just by detecting the final protons. Even by reducing the background by several orders of magnitude by demanding the presence of a  $K^+K^-$  pair in the final state, the separation of the  $\phi$  from direct  $K^+K^-$  production is non-trivial, as illustrated in Fig. 78.

Of immediate interest here is the ratio  $R_{\phi/\omega}$  of the production of the  $\phi$  and  $\omega$  vector mesons in reactions where there are no strange particles in the initial state. According to the Okubo-Zweig-Iizuka (OZI) rule [276], one expects  $R_{\phi/\omega}$  to be on the order of  $R_{OZI} = 4 \times 10^{-3}$ . Using  $\omega$  production data from Refs. [165,169] it was found that in  $pp$  collisions  $R_{\phi/\omega} \approx 6-8 \times R_{OZI}$  [260] and a similar conclusion was reached using later COSY-TOF data [170]. This is consistent with the result obtained in the  $pn$  case [275] on the basis of  $pn \rightarrow d\omega$  data taken at COSY [175]. These values are to be contrasted with the  $1-2.4 \times R_{OZI}$  found in high energy  $pp \rightarrow ppV$  data [277].

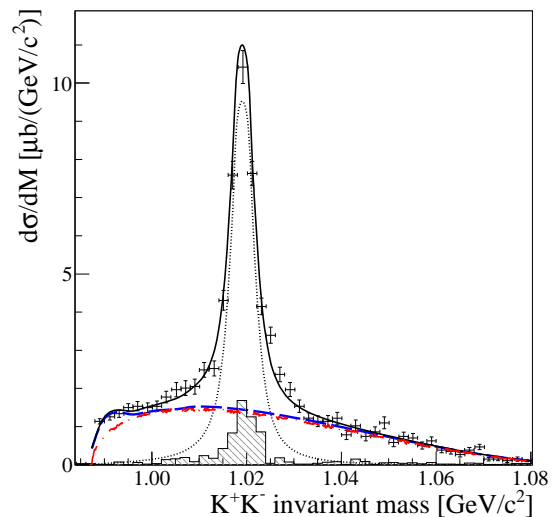


**Fig. 78.** The  $pp \rightarrow ppK^+K^-$  differential cross section at 2.83 GeV as a function of the  $K^+K^-$  invariant mass [262]. The error bars are statistical; systematic uncertainties are shown by the hatched histogram. The dashed-dotted (red) curve represents four-body phase-space that is distorted slightly by the FSI to give the dashed (blue) curve. The dotted curve is the fit to the  $\phi$  contribution, whereas the solid line is the incoherent sum of the  $\phi$  and non- $\phi$  contributions.

Close to threshold, the two final-state protons in the  $pp \rightarrow pp\phi$  reaction must be in the  $^1S_0$  wave, and the  $\phi$  in an  $s$  wave relative to this pair. The  $\phi$  is then aligned with polarizations  $m = \pm 1$  along the beam direction. The polar angular distribution of the decay kaons in the  $\phi$  meson rest frame must then display a  $\sin^2\theta_\phi^K$  shape, which is consistent with the  $Q = 18.5$  MeV data [260]. On the other hand, at  $Q = 76$  MeV the kaon angular distribution is almost isotropic, which means that the  $\phi$  is essen-

tially unpolarized [263]. This is an unambiguous proof of the importance of higher partial waves in  $\phi$  production at 76 MeV.

A similar conclusion can be drawn from the study of the  $pn \rightarrow d\phi$  data [275]. At threshold a pure  $\sin^2 \theta_\phi^K$  is required but, if the data are parameterized as

$$d\sigma/d\Omega_\phi^K = 3(a \sin^2 \theta_\phi^K + 2b \cos^2 \theta_\phi^K)/8\pi, \quad (8.5)$$

then the best fit gives  $b/a \approx 0.012 (Q/\text{MeV})$ . The  $\phi$  are therefore produced unpolarized for  $Q \approx 40$  MeV.

Despite the evidence for higher partial waves coming from the angular distributions, there is no sign of their effect in the total cross section. Thus the total cross section for the quasi-free  $pn \rightarrow d\phi$  reaction shown in Fig. 79 is well described by the curve representing  $48\sqrt{Q}/\text{MeV}$ . The figure also shows that, over the range in  $Q$  measured, the  $pn \rightarrow d\phi$  cross section is much bigger than that of  $pp \rightarrow pp\phi$ , though one has to bear in mind the difference between a two-body and a three-body final state.

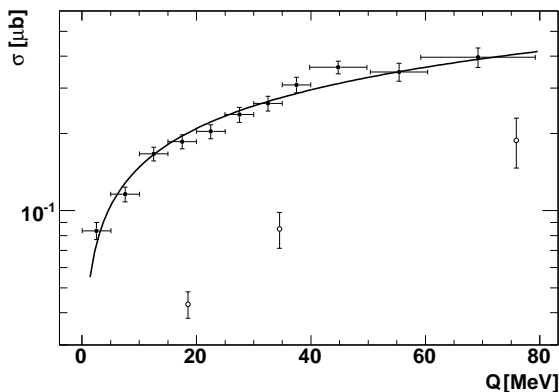


**Fig. 79.** Total cross section for the quasi-free  $pn \rightarrow d\phi$  reaction as a function of the excess energy (filled circles) [275]. The curve represents a phase-space  $\sqrt{Q}$  behaviour. For comparison, also shown by open circles are the values obtained for  $pp \rightarrow pp\phi$  in the first ANKE experiment [260].

### 8.3 $pA \rightarrow K^+K^-X$ and $pA \rightarrow \phi X$

In the experiments described so far, and those that will be discussed in sec 9.4, only exclusive  $\phi$  production was studied. In such hard processes the interaction of the  $\phi$  with nucleons plays only a minor role compared to the uncertainty of the reaction mechanism itself. In order to investigate how the  $\phi$  interacts with the nuclear medium, its inclusive production was studied with 2.83 GeV protons incident on C, Cu, Ag, and Au nuclear targets [278, 279]. Only the  $K^+K^-$  pair was detected in the ANKE facility but, unlike the  $pp \rightarrow ppK^+K^-$  experiments that were the subject of sects. 8.1 and 8.2, the delayed-veto technique [19] was employed to identify the  $K^+$  unambiguously.

The  $K^+K^-$  peak corresponding to the  $\phi$  meson was clearly seen for all four nuclear targets, the carbon example being shown in Fig. 80. The background, which was dominantly due to direct pair production, was parameterized by a quadratic function in  $m_{K^+K^-}$  in order to make subtractions under the invariant mass peak. The resulting number of reconstructed  $\phi$  mesons for each target was between 7000 and 10000. It has, of course, to be recognized that these numbers depended sensitively upon the ANKE acceptance for the positive and negative kaons.

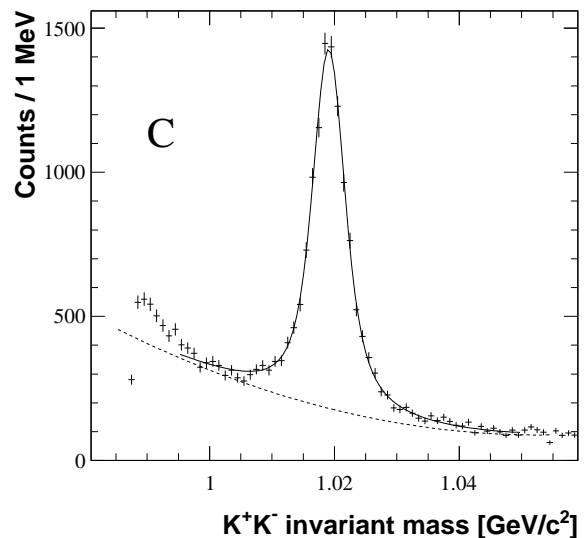


**Fig. 80.** Invariant mass distributions for  $K^+K^-$  pairs produced in  $pC$  collisions at 2.83 GeV [278]. The experimental data are not acceptance-corrected. The dashed line is a second-order polynomial representation of the background in the region of the  $\phi$  peak.

The standard way of describing such data is through the evaluation of the so-called transparency ratios

$$R = \frac{12 \sigma_{pA \rightarrow \phi X'}}{A \sigma_{pC \rightarrow \phi X}} \quad (8.6)$$

normalized to carbon. Here  $\sigma_{pA \rightarrow \phi X'}$  and  $\sigma_{pC \rightarrow \phi X}$  are inclusive cross sections for  $\phi$  production in  $pA$  and  $pC$  collisions, respectively. By dividing by the carbon data one takes into account production on neutrons as well as protons, though it must be noted that there is a significant neutron excess in the heavier targets.

The values obtained for the transparency ratios are shown in Fig. 81. Any interpretation of these data has to rely on a detailed theoretical treatment and the curves shown in the figure are the predictions of one specific model [280] for various values of the  $\phi$  width  $\Gamma_\phi$  in nuclear matter, taking into account the effects of the ANKE cuts on the distributions in the laboratory  $\phi$  momenta and production angles. It should be noted that in the low density limit the medium contribution to  $\Gamma_\phi$  is proportional to the  $\phi$ -nucleon total cross section.

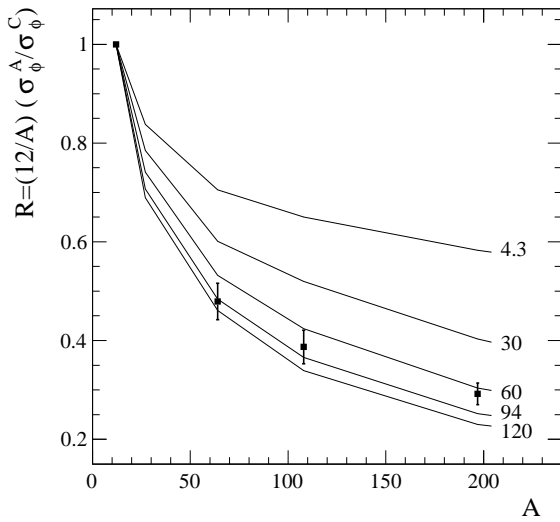


**Fig. 81.** Comparison of the measured transparency ratio  $R$  with the predictions of the Paryev model [280] for various values of the  $\phi$  width in the nuclear medium (in  $\text{MeV}/c^2$ ) [278].

The best fit for the in-medium width within this model is achieved with  $\Gamma_\phi = 73_{-10}^{+14} \text{ MeV}/c^2$ . Since the average  $\phi$  momentum at ANKE is around  $1.1 \text{ GeV}/c$ , this corresponds to  $\Gamma_\phi \approx 50 \text{ MeV}/c^2$  in the nuclear rest frame. However, there is significant model dependence, especially regarding the relative production rates on protons and neutrons, but also on the importance of two-step processes induced, e.g., by intermediate pions. Independent of any particular model, the results suggest a substantial increase in the total  $\phi$  width in the nuclear environment.

In a subsequent analysis [279], the dependence of the transparency ratio on the  $\phi$  momentum was investigated over the range  $0.6 < p_\phi < 1.6 \text{ GeV}/c$ . In all the models tested, the experimental results show evidence for an increase of  $\Gamma_\phi$  with the  $\phi$  momentum. However, these models do not reproduce satisfactorily the large numbers of  $\phi$  mesons produced with momenta below  $1 \text{ GeV}/c$ .

Figure 80 shows, in addition to the  $\phi$  peak, a large number of  $K^+K^-$  pairs produced “directly” in the  $pA \rightarrow K^+K^-X$  reaction. These have been used to investigate the interaction of the  $K^-$  with nuclear matter [281]. In the framework of a specific reaction model [282], the data are best described by a moderately attractive  $K^-$ -nucleus potential of depth  $\approx 60 \text{ MeV}$  for an average kaon momentum  $\approx 0.5 \text{ GeV}/c$ .

## 9 The $pd \rightarrow {}^3\text{He} X ({}^3\text{H} X')$ family of reactions

Despite the  $pd \rightarrow {}^3\text{He} X ({}^3\text{H} X')$  reactions generally involving large momentum transfers, they have the big experimental advantage of requiring the measurement of only one charged particle,  ${}^3\text{He}$  or  ${}^3\text{H}$ , in the final state in order

to reconstruct  $X$  through the missing mass in the reaction. For this reason there have been numerous studies of such reactions over the years. At COSY there were important measurements of single and two-pion production as well as the formation of  $K^+K^-$  pairs, including  $\phi$  production. However, the most fascinating data are associated with  $\eta$  production, which has proved to be a very rich field to explore at COSY. Data taken at WASA on the combined measurement of the production of  $\eta$  mesons and single and multiple pions above the  $\eta$  threshold are currently being analyzed but definitive results with absolute normalizations are not yet available [283].

### 9.1 $pd \rightarrow {}^3\text{He} \pi^0$ and $pd \rightarrow {}^3\text{H} \pi^+$

The most extensive published measurements of the differential cross section of the  $pd \rightarrow {}^3\text{He} \pi^0$  and  $pd \rightarrow {}^3\text{H} \pi^+$  reactions was undertaken by the GEM collaboration, where the final  ${}^3\text{He}$  or  ${}^3\text{H}$  was detected [284,285]<sup>7</sup>. Isospin invariance predicts that there should be a factor of two difference in the cross sections, though the spin dependence of the observables should be identical in the two channels.

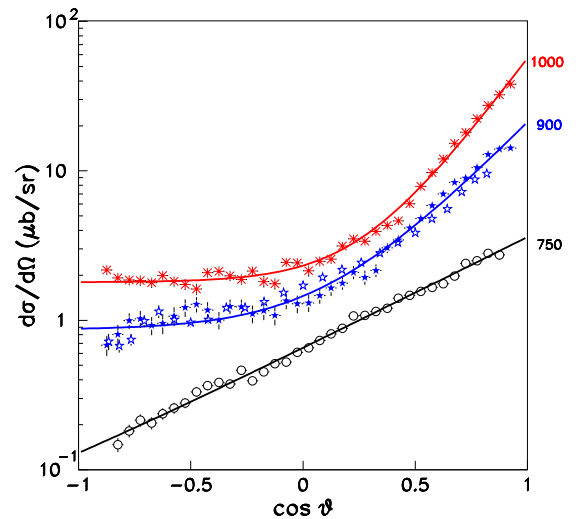


**Fig. 82.** Differential cross sections for the  $pd \rightarrow {}^3\text{He} \pi^0$  reaction measured by the GEM collaboration at the three beam momenta indicated [284,285]. For presentational purposes, the data at  $900 \text{ MeV}/c$  have been scaled by a factor of 2.25 and at  $1000 \text{ MeV}/c$  by  $(2.25)^2$ . The (blue) open stars represent the results of the TRIUMF measurement at  $883 \text{ MeV}/c$  [286] using the  $900 \text{ MeV}/c$  scaling factor. Also shown are the fits based upon Eq. (9.1).

Data were taken over the whole angular range for both  $\pi^0$  and  $\pi^+$  production for laboratory momenta between

<sup>7</sup> Data on the  $pd \rightarrow {}^3\text{He} \pi^0$  reaction taken by the WASA collaboration at a variety of energies are currently under analysis [283]

750 and 1000 or 1050 MeV/c. Samples of the  $\pi^0$  data are plotted in Fig. 82. Also shown are data obtained at TRIUMF at a beam momentum of 883 MeV/c [286], which are broadly in line with the GEM results at 900 MeV/c.

The shape of the data changes with beam momentum and the results are well fit with:

$$\frac{d\sigma}{d\Omega} = a + \exp\{b + c(\cos\theta - 1)\}. \quad (9.1)$$

The GEM authors [284,285] argue that the change in the slope parameter  $c$  is mainly kinematic; at larger beam momenta the momentum transfer between the deuteron and  ${}^3\text{He}$  increases faster with angle. As a consequence, the slope parameter should vary like  $pk$ , where  $p$  and  $k$  are the proton and pion momenta in the c.m. frame. This behaviour is clearly seen in the values of the fit parameters shown in Fig. 83.

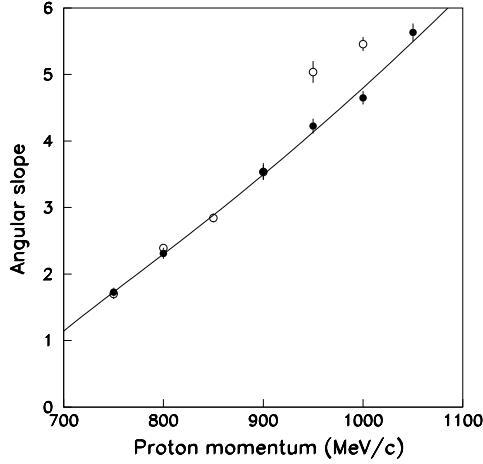


**Fig. 83.** Slope parameter  $c$  of Eq. (9.1) deduced from fits to the GEM data on  $pd \rightarrow {}^3\text{He}\pi^0$  (closed circles) and  $pd \rightarrow {}^3\text{H}\pi^+$  (open circles) differential cross sections [284,285]. Since the slope parameters should be similar for the two channels, the values of  $c$  for the  $\pi^+$  case may be questioned at the two highest momenta. Also shown is the arbitrarily normalized curve  $1.31pk$ , where the proton ( $p$ ) and pion ( $k$ ) c.m. momenta are measured in  $\text{fm}^{-1}$ .

Equation (9.1) also suggests that there are at least two mechanisms that play important roles here. At small angles the reaction might involve a spectator nucleon but at large angles all nucleons seem to be involved [287].

As by-products of studying other reactions at ANKE, data were taken on the proton analyzing powers in  $pd \rightarrow {}^3\text{He}\pi^0$  and  $pd \rightarrow {}^3\text{H}\pi^+$  and also the deuteron and proton analyzing powers in  $\vec{d}\vec{p} \rightarrow {}^3\text{He}\pi^0$  and  $\vec{d}\vec{p} \rightarrow {}^3\text{H}\pi^+$  [288]. The proton analyzing power data shown in Fig. 84 complement the earlier TRIUMF measurements at 350 MeV [286] and show much structure from the higher partial waves than is apparent in the differential cross section shown in Fig. 82.

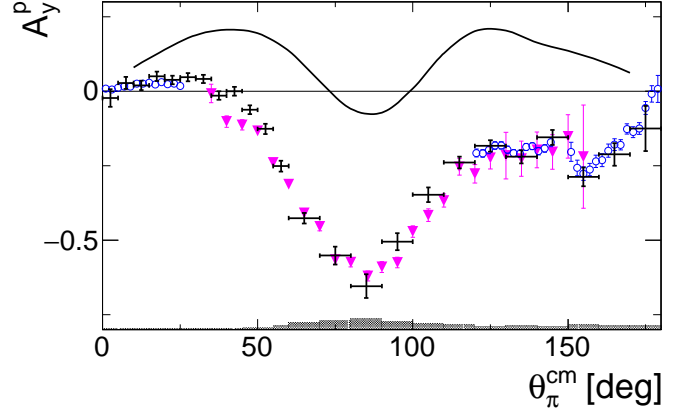


**Fig. 84.** TRIUMF data on the proton analyzing power  $A_y^p$  in the  $\vec{p}d \rightarrow {}^3\text{He}\pi^0$  reaction at 350 MeV [286] (magenta triangles) are compared to ANKE results obtained at 353 MeV (blue open circles) and at 363 MeV per nucleon with a polarized hydrogen target (black crosses) [288]. The curve corresponds to the predictions by Falk in a cluster-model approach [289].

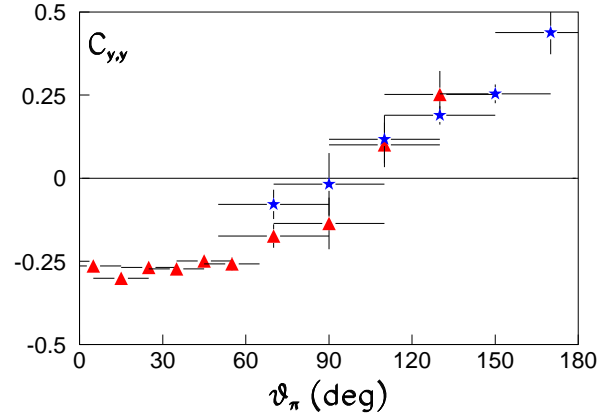


**Fig. 85.** Transverse spin correlation coefficient  $C_{y,y}$  measured in the  $\vec{d}\vec{p} \rightarrow {}^3\text{He}\pi^0$  and  $\vec{d}\vec{p} \rightarrow {}^3\text{H}\pi^+$  reactions at 363 MeV per nucleon [288]. The (red) triangles were obtained through  ${}^3\text{He}$  detection and the (blue) stars through  ${}^3\text{H}$  detection. Only statistical errors are shown. The systematic ones are about 11% for  ${}^3\text{He}$  detection and a little bit larger in the  ${}^3\text{H}$  case.

The deuteron beam measurements also allowed transverse spin correlations to be studied for the first time and values obtained for  $C_{y,y}$  and  $C_{x,x}$  at 363 MeV per nucleon are shown in Fig. 85 [288]. In the forward and backward directions the the number of independent amplitudes reduces from six to two,  $A$  and  $B$ , and their values can be determined through measurements of the cross section, spin correlation, and deuteron tensor analyzing power,

$T_{20}$ , which was measured at Saclay [290]:

$$\begin{aligned} \frac{d\sigma}{d\Omega} &= \frac{kp}{3}(|A|^2 + 2|B|^2), \\ T_{20} &= \sqrt{2} \frac{|B|^2 - |A|^2}{|A|^2 + 2|B|^2}, \\ C_{y,y} = C_{x,x} &= -\frac{2\text{Re}(A^*B)}{|A|^2 + 2|B|^2}, \end{aligned} \quad (9.2)$$

where  $k$  and  $p$  are the pion and proton c.m. momenta. Thus the ANKE measurements of  $C_{x,x} = C_{y,y}$  in collinear kinematics determines the relative phase of the  $A$  and  $B$  amplitudes. Whereas at 363 MeV per nucleon there is strong interference between  $A$  and  $B$ , at 600 MeV per nucleon the two amplitudes are almost out of phase in the forward direction [288].

## 9.2 $pd \rightarrow {}^3\text{He}\eta$

There have been numerous missing-mass measurements of the differential cross section for the  $pd \rightarrow {}^3\text{He}\eta$  reaction away from threshold at COSY [291,292,293,294] and these have confirmed the striking angular dependence illustrated at two energies by the WASA data shown in Fig. 86.

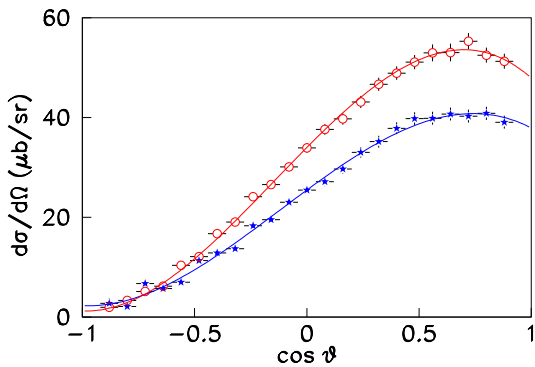


**Fig. 86.** Differential cross section for the unpolarized  $pd \rightarrow {}^3\text{He}\eta$  reaction obtained at WASA-at-COSY [294] at  $Q = 49$  MeV (blue filled stars) and 60 MeV (red open circles), respectively. The curves are cubic fits in  $\cos\theta$ , where  $\theta$  is the c.m. angle between the initial proton and final  $\eta$ . The relative normalization between the two data sets was established through a comparison with the  $pd \rightarrow {}^3\text{He}\pi^0$  results. The reliability of this procedure is currently being checked on a larger data sample [283].

Although the cross section in the backward hemisphere, where the momentum transfer between the deuteron and the  ${}^3\text{He}$  is very large, is strongly suppressed, the data seem to turn over well before reaching  $\theta = 0^\circ$ . This is in sharp contrast to the corresponding pion production

data discussed in sect. 9.1 and is an indication that the impulse approximation might not be the dominant driving mechanism for  $\eta$  production, even at small angles. Three-nucleon mechanisms, involving intermediate pions, have been suggested to describe these large momentum transfer reactions. Though classical [295] and quantum mechanical [296] calculations have had some success near threshold, they have not provided any real insight away from the small  $Q$  region.

The values of the total cross sections, which are summarized in Ref. [294], have a wide scatter, due in part to the different techniques used to obtain the absolute normalizations. An observable that is independent of such uncertainties is the logarithmic slope at the mid-point, defined by

$$\alpha = \frac{d}{d(\cos\theta_\eta)} \ln \left( \frac{d\sigma}{d\Omega} \right) \Big|_{\cos\theta_\eta=0}. \quad (9.3)$$

Apart from one exceptional point at  $Q = 59.4$  MeV [293], the values of  $\alpha$  shown in Fig. 87 seem to display a steady rise with  $Q$ . However, it is clear from the disparity between the different experimental results, which are much larger than the statistical errors, that there must be significant systematic uncertainties. These could originate from the understanding of the acceptance of the various spectrometers used. The conflicts are likely to be underscored when the new WASA data are published [283].

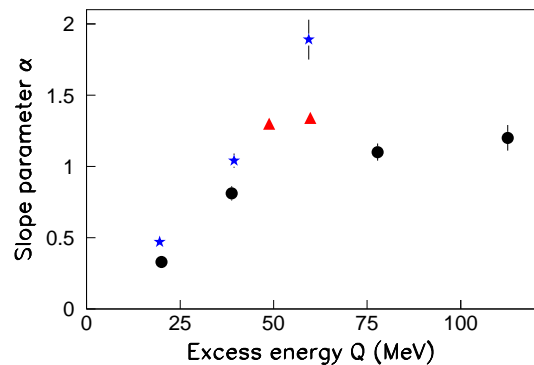


**Fig. 87.** Values of the symmetry parameter  $\alpha$ , defined by Eq. (9.3), deduced from measurements of the  $pd \rightarrow {}^3\text{He}\eta$  differential cross section. These are shown as (black) circles [297], (blue) stars [293], and (red) triangles [294]. Only statistical errors are shown.

The general physics interest is much greater in the two near-threshold measurements, carried out simultaneously at COSY-11 [172] and ANKE [173], where values of the  $dp \rightarrow {}^3\text{He}\eta$  cross section were extracted at many energies with robust relative normalizations. In both experiments, only the recoiling  ${}^3\text{He}$  was detected and the  $\eta$ -meson identified through the peak in the missing-mass distribution.

The first point to note is that the missing-mass  $m_X$  resolution gets better as the threshold is approached. The reason for this is most easily seen by using non-relativistic kinematics in the c.m. frame, where

$$m_X = W - m_\tau - k^2/2m_{\text{red}}. \quad (9.4)$$

Here  $W$  is the total c.m. energy,  $m_\tau$  the mass of  ${}^3\text{He}$ ,  $k$  the momentum of the  ${}^3\text{He}$ , and  $m_{\text{red}}$  the reduced mass of  $m_\tau$  and  $m_X$ . The  $\eta$  threshold corresponds to  $m_X = m_\eta$  and  $k = 0$ , so that

$$|\partial m_X/\partial k| = k/m_{\text{red}} \rightarrow 0 \text{ as } k \rightarrow 0. \quad (9.5)$$

The value of  $m_X$  is therefore stationary at threshold in the c.m. frame and this is also true for small changes of the  ${}^3\text{He}$  momentum from threshold in the laboratory frame.

The improvement in resolution near threshold is, of course, more general than this particular reaction and a similar improvement in the missing-mass resolution is to be expected in, for example, the  $pp \rightarrow pp\eta'$  reaction near its threshold. The power of this result is, however, diluted by the smearing arising from the finite momentum bite of the COSY beam.

The early Saclay experiments [298,299] showed that the  $dp(pd) \rightarrow {}^3\text{He}\eta$  total cross section jumped very rapidly in the  $\eta$  threshold region and it was suggested that this is likely to be the consequence of a strong  $\eta$ - ${}^3\text{He}$   $s$ -wave final state interaction, that might even lead to the  $\eta$  being quasi-bound to the nucleus [300]. Such states had been predicted previously [301,302], but their positions were rather ambiguous due to uncertainties in the parameters of the  $\eta$ -nucleon interaction. More detailed experiments were needed to investigate the possible existence of  ${}^3\text{He}$ .

The COSY-11 and ANKE experiments were carried out in very similar ways, using a deuteron beam that was steadily accelerated through each cycle. The binning in beam energy of events taken in this ramping mode could be chosen at will at the analysis stage and, as will be shown shortly, the two groups did make very different choices here. The background to the  $dp \rightarrow {}^3\text{He}\eta$  data was, in both cases, estimated from data taken below the  $\eta$  threshold. These were shifted so that the kinematic limits coincided and scaled to give consistency outside the  $\eta$ -peak region. As can be seen from the COSY-11 data shown in Fig. 88, this procedure gives a very plausible description of the data.

The absolute normalizations of the cross sections were achieved by measuring deuteron-proton elastic scattering in parallel, though in different kinematic regions in the two experiments. This gave overall systematic errors of  $\approx 15\%$  [173] and  $\approx 10\%$  [172] and these uncertainties are not included in the results presented in Fig. 89. Only the small  $Q$  region is shown because the total cross sections at higher energies are almost constant, up to the limits of the two experiments [172,173]. The larger acceptance for single particles at ANKE allowed a somewhat larger range in  $Q$  to be studied but this is not crucial here because the important Physics is contained in the first few MeV of excess energy.

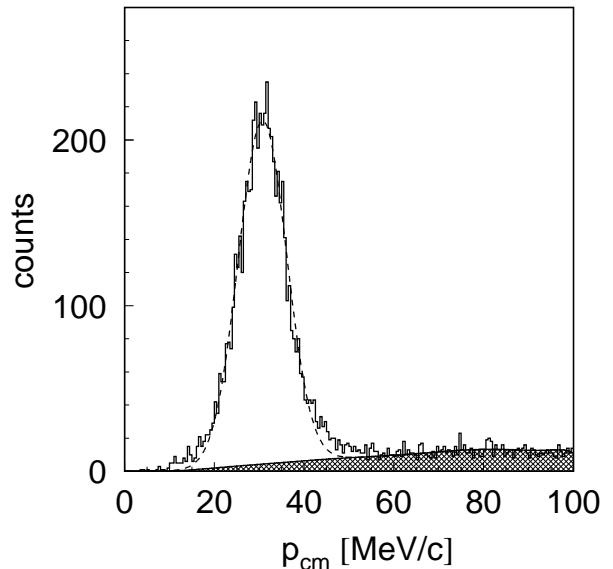


**Fig. 88.** Distribution of  ${}^3\text{He}$  momenta in the c.m. frame at  $Q \approx 1.88$  MeV [172]. The dashed line represents a Gaussian fit to the  $\eta$  peak and the shaded region corresponds to the background estimated from below-threshold measurements.

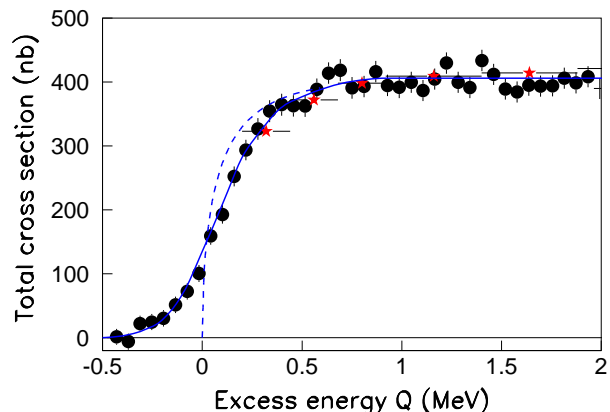


**Fig. 89.** Near-threshold  $dp \rightarrow {}^3\text{He}\eta$  total cross sections measured by ANKE (black circles) [173] and COSY-11 (red stars) [172]. Only statistical errors are shown. The solid curve is the fit of Eq. (9.7) to the ANKE data, where a 171 keV smearing in  $Q$ , arising mainly from the deuteron beam profile, is taken into account. The dashed curve shows what the data should look like if the deuteron beam were truly monochromatic and other sources of smearing were neglected.

It is important to note that the values of the COSY-11 and ANKE total cross sections shown in Fig. 89 are completely consistent, especially in view of the overall luminosity uncertainties. The COSY-11 group omitted effects associated with smearing in  $Q$  and, by fitting their data with an  $\eta$ - ${}^3\text{He}$  scattering length formula, obtained a



relatively modest value of the magnitude of the scattering length. This can easily be understood because the energy smearing softens the jump to the cross section plateau.

In the alternative approach, it was noted in the ANKE data of Fig. 89 that there were many  $\eta$  events produced below the nominal threshold and these must have arisen from the spread in momentum of the COSY deuteron beam. The existence of such a spread of the right order of magnitude was confirmed independently from the spin depolarizing measurements described in sect. 2.4.2 [53].

After defining an average production amplitude in terms of the cross section by dividing by the ratio of the  $\eta$  and deuteron momenta in the c.m. frame,

$$|f|^2 = \frac{p_d}{p_\eta} \frac{d\sigma}{d\Omega}, \quad (9.6)$$

the ANKE total cross section data were fitted with a two-pole final state interaction factor,

$$f = \frac{f_B}{(1 - p_\eta/p_1)(1 - p_\eta/p_2)}, \quad (9.7)$$

smearing with a Gaussian distribution in  $Q$  and put into finite energy bins. Here  $f_B$  is assumed to be constant over the energy range where the FSI is important. The fit parameters obtained were [173]

$$p_1 = [(-5.2 \pm 7.0_{-0.8}^{+1.5}) \pm i(18.7 \pm 2.4_{-0.8}^{+0.7})] \text{ MeV}/c \quad (9.8)$$

$$p_2 = [(106.3 \pm 4.5_{-0.3}^{+0.2}) \pm i(75.6 \pm 12.5_{-1.8}^{+0.7})] \text{ MeV}/c$$

and a smearing that could arise from a beam spread of  $\delta p_d/p_d \approx 2.2 \times 10^{-4}$ . Here the first errors are statistical and the second systematic. It is important to note here that the error bars quoted refer to the specific form of Eq.(9.7) and the nearby pole may move by more than these if one assumed a different fit function.

It is possible to deduce scattering length and effective range parameters from the numbers given in Eq. (9.8), but it must be realized that  $p_2$  is really an effective parameter that might be hiding some of the energy dependence of  $f_B$ . The real physics is contained in the value of  $p_1$ , which shows that there is a pole in the  $\eta^3\text{He}$  scattering amplitude at  $Q_{\text{pole}} = [(-0.30 \pm 0.15 \pm 0.04) \pm i(0.21 \pm 0.29 \pm 0.06)] \text{ MeV}$ . The sign of the imaginary part of  $Q_{\text{pole}}$ , i.e., whether the state is “bound” or “antibound” cannot be determined from above-threshold measurements but, nevertheless, the proximity of the pole to the origin and the associated large scattering length have excited a lot of interest in the mesic nuclei community.

It is important to check that the pole really is due to an interaction in the  $s$ -wave  $\eta^3\text{He}$  final state. This state can be accessed from either the total spin  $S = \frac{3}{2}$  or the  $S = \frac{1}{2}$  deuteron-proton initial system and the differences will influence the deuteron tensor analyzing power  $T_{20}$ . The pure  $s$ -wave FSI hypothesis requires that  $T_{20}$  should remain constant, despite the strange behaviour of the unpolarized cross section.

The tensor analyzing power of the  $\vec{d}p \rightarrow ^3\text{He}\eta$  total cross section was measured at ANKE for  $Q \lesssim 11 \text{ MeV}$  [303]

using a similar system to that employed earlier for the unpolarized cross section [173]. The results are indeed consistent with a constant value of  $T_{20}$ , which offers strong support to the FSI interpretation of the near-threshold energy dependence. It is important to note here that the detection system was independent of the deuteron beam polarization so that many of the systematic effects cancel. The result is not totally unexpected because, if the poles in the two threshold amplitudes had been significantly separated, the single pole fit of Eq. (9.8) would not have resulted in such a small value of the imaginary part of  $Q_{\text{pole}}$ .

Further evidence in support of the FSI hypothesis is to be found from studying the  $Q$  dependence of the slope parameter  $\alpha$  of Eq. (9.3) in the near-threshold region. At high  $Q$  the cross sections are forward peaked and the  $\alpha$  of Fig. 87 are all positive. However, there were already suspicions from the Saclay data [299] that  $\alpha$  might be slightly negative near threshold and this was confirmed by the ANKE data [173]. It was argued in Ref. [304] that this behaviour could only occur if the interference between the  $s$ - and  $p$ -wave production amplitudes changed significantly near threshold. This is precisely what would be expected if there were a complex pole in the  $\eta^3\text{He}$  amplitude.

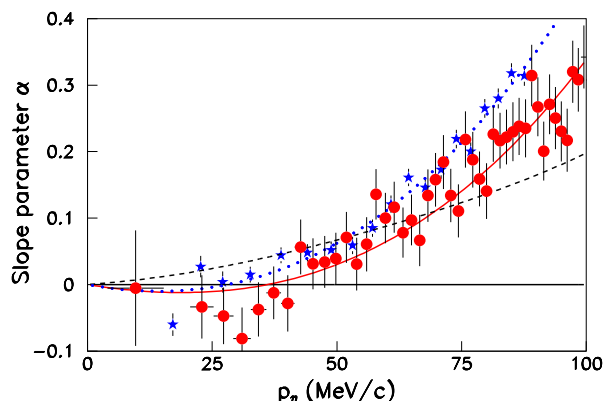


**Fig. 90.** Slope parameter  $\alpha$  of the  $dp \rightarrow ^3\text{He}\eta$  reaction as a function of the  $\eta$  c.m. momentum. The experimental data from COSY-ANKE (red closed circles) [173] and COSY-11 (blue stars) [172] are compared to fits (solid red curve and blue dots) where the phase variation of the  $s$ -wave amplitude is taken into account. If the phase variation is neglected, the best fit (black dashed curve) fails to describe the data.

Figure 90 shows the results for  $\alpha$  obtained by the ANKE [173] and COSY-11 [172] collaborations and the best fits to these data achieved when taking the phase variation from the  $s$ -wave pole into account [304]. For comparison, the best fit obtained when the phase variation is neglected is also shown. It seems clear that these data are better described by including the phase variation. It is interesting to note that an analogous reversal

of the slope parameter near threshold is also observed in the  $\gamma^3\text{He} \rightarrow \eta^3\text{He}$  photoproduction data [305], though the details will depend on the phase of the  $p$ -wave amplitude in any particular reaction.

However, one must be cautious because data or their interpretation may change. Thus it could well be argued that, instead of using Eq. (9.7), one would be on slightly firmer ground by assuming that

$$f = f_B \times (1 - p_\eta/p_2)/(1 - p_\eta/p_1). \quad (9.9)$$

As expected, by fitting the ANKE  $dp \rightarrow ^3\text{He}\eta$  total cross section data [173] with Eq. (9.9) it is seen that the nearby pole is still in the region where  $|Q| < 1$  MeV, but it is now on an unphysical sheet with  $p_1 = -28 \pm 2$  MeV/ $c$ , with a relatively small imaginary part [306]. Since the extracted value of  $p_2$  is also large and real, the phase of the  $s$ -wave amplitude changes little with momentum and so the value of the slope parameter  $\alpha$  could never change sign and so the data shown in Fig. 90 would not be reproduced in this model.

However, very precise  $dp \rightarrow ^3\text{He}\eta$  differential cross section data were taken in connection with the measurement of the mass of the  $\eta$  meson [307] that is discussed in the next section. Unlike the ramping mode used in the initial ANKE experiment [173], these consisted of a series of 14 flat tops with  $p_\eta < 100$  MeV/ $c$ . In contrast to the data shown in Fig. 90, the *preliminary* results from this analysis show little indication of  $\alpha$  going negative close to threshold [308] and this is precisely what one would expect if the  $s$ -wave amplitude did not show a rapid phase variation.

### 9.2.1 Measurements of the mass of the $\eta$ meson

The first measurement of the mass of the  $\eta$  meson at COSY by the GEM collaboration [309] yielded a value that was about  $0.5$  MeV/ $c^2$  lower than the results of other modern determinations that were reported by the PDG group [164]. In contrast, the later experiment, carried out with a circulating deuteron beam using the ANKE spectrometer [307], is completely consistent with the PDG recommended value and the error bars are among (or possibly are) the best in the World.

The GEM experiment used a proton beam that was electron-cooled at injection energy and then stochastically extracted. This was incident on a thin liquid target, with the charged particles produced being detected in the Big Karl spectrometer, described in sect. 2.2.5. Big Karl was calibrated by measuring separately the proton and positive pion from the  $pp \rightarrow d\pi^+$  reaction [309].

In order to extract a value for the  $\eta$  mass, the beam momentum must be well measured and the kinematics of a reaction where the  $\eta$  meson is produced fully determined. These requirements were met in the Big Karl experiment by measuring simultaneously the  $\pi^+$  and  $^3\text{H}$  from one branch of the  $pd \rightarrow ^3\text{H}\pi^+$  reaction and the  $^3\text{He}$  from one branch of  $pd \rightarrow ^3\text{He}X$  at an excess energy  $Q \approx 34$  MeV

with respect to the threshold for  $\eta$  production. At this energy the relevant  $\pi^+$ ,  $^3\text{H}$ , and  $^3\text{He}$  all have similar rigidities and can be detected in parallel in the Big Karl focal plane. Though different in detail, there are some similarities with the SATURNE experiment [310], where the same  $\eta$ -production reaction was studied and pion production was also used to determine the beam momentum.

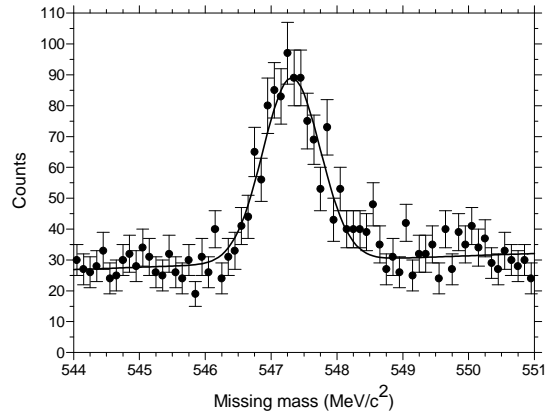


**Fig. 91.** Missing-mass distribution from the  $pd \rightarrow ^3\text{He}\eta$  distribution at Big Karl, where the beam momentum was determined through the simultaneous study of the  $pd \rightarrow ^3\text{H}\pi^+$  reaction [309].

It is clear from the missing-mass distribution shown in Fig. 91 that there is little difficulty in separating the  $\eta$  peak (with  $\text{FWHM} \approx 1$  MeV/ $c^2$ ) from the slowly varying background. The mass scale shown here was fixed using the measurements in parallel of the  $pd \rightarrow ^3\text{H}\pi^+$  reaction. The problem is that the central value of  $m_\eta = 547.31$  MeV/ $c^2$  is lower than the PDG recommended mean by of the order of  $0.5$  MeV/ $c^2$ . This disagreement is very large compared to the  $\pm 0.03(\text{stat}) \pm 0.03(\text{syst})$  MeV/ $c^2$  errors quoted in the GEM paper [309]. To put the deviation into some kind of context, the  $0.5$  MeV/ $c^2$  off-set would correspond to about twice the energy loss of the  $^3\text{He}$  in the  $1 \mu\text{m}$  mylar window.

Rather than repeating the Big Karl experiment and analysis, it was decided to carry out an  $\eta$  mass measurement using the circulating deuteron beam in COSY [307], with the aim of reducing the error bars to below those quoted in the literature [164]. Such a  $dp \rightarrow ^3\text{He}\eta$  experiment offered distinct advantages over the Big Karl measurement. As shown in sect. 2.4.2, the momentum of the deuteron beam could be determined to better than  $3 \times 10^{-5}$  by inducing an artificial depolarizing resonance [53]. The energy loss of the  $^3\text{He}$  in the hydrogen cluster-jet target is negligible and, by working very close to threshold, good missing-mass resolution and low backgrounds could be achieved [307]. Furthermore, as will be shown later, this allowed the data to be extrapolated to threshold, which reduced the systematic uncertainties.

As discussed earlier, the background under the  $\eta$  peak in the missing-mass distribution could be reliably estimated using data taken a little below the  $\eta$  threshold.

The  ${}^3\text{He}$  were measured in the Forward Detector of the ANKE spectrometer and this has full geometric acceptance for the  $dp \rightarrow {}^3\text{He}\eta$  reaction for  $Q \lesssim 11$  MeV. This was of crucial importance because it allowed the study of the effects of the finite momentum resolution in the three different directions in space. If this had not been done, the value obtained for  $m_\eta$  would have depended on the production angle, with differences of up to  $0.5$  MeV/ $c^2$  between  $\cos\theta_\tau = \pm 1$  and  $\cos\theta_\tau = 0$ . It may be interesting to note that the Big Karl data were taken only in the forward direction [309]. The careful corrections to the measurements of the  ${}^3\text{He}$  momenta to compensate for the spectrometer resolution are thoroughly described in Ref. [307].

Figure 92 shows the squares of the resolution-corrected  ${}^3\text{He}$  momentum  $p_\tau$ , as measured in the ANKE Forward Detector at twelve incident deuteron momenta  $p_d$ . It is important to note that, for the kinematics of the  $dp \rightarrow {}^3\text{He}\eta$  reaction, the only free parameter is  $m_\eta$  so that, once the intercept is fixed, the form of the fit function in Fig. 92 is completely determined *a priori*. These considerations show that the fit should deviate slightly from a straight line and this must be taken into account when extracting the best value for  $m_\eta$ .

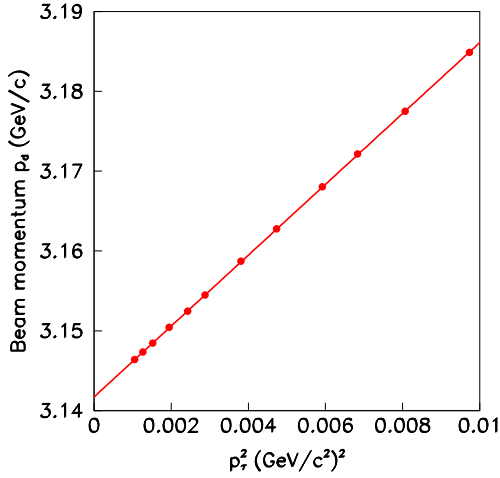


**Fig. 92.** The momentum of the circulating deuteron beam  $p_d$  compared to the square of the corresponding  ${}^3\text{He}$  momentum  $p_\tau$  for the 12 points  $dp \rightarrow {}^3\text{He}\eta$  points measured at COSY [307]. The shape of the function  $p_d = f(p_\tau)$  and its value at  $p_\tau = 0$  are governed by the single parameter  $m_\eta$  but to a good approximation the data are well described by the straight line shown, viz.  $p_d = 3.14171 + 4.44 p_\tau^2$ .

It is, however, sufficient for the discussion here to consider the free linear fit shown in the figure,  $p_d = 3.14171 + 4.44 p_\tau^2$ . With a perfectly tuned spectrometer, the slope of this line should be

$$\text{slope} = \frac{(m_\tau + m_\eta)^2}{m_\tau m_\eta} \frac{E_d}{2m_p p_d} = 4.54 (\text{GeV}/c)^{-1}, \quad (9.10)$$

where  $p_d$  and  $E_d$  are, respectively, the deuteron momentum and total energy evaluated at the  $\eta$  threshold. The 1.1% correction to the momentum that this exhibits, compared to the 0.8% in the refined fit [307], is of no real importance because it does not affect the extrapolation to threshold. On the other hand it would be relevant if the experiment were conducted at an isolated energy above threshold. Thus the extrapolation to  $p_\tau = 0$  reduces the systematic uncertainties in the mass determination.

The value of the  $\eta$  mass given in Ref. [307] is

$$m_\eta = (547.873 \pm 0.005_{\text{stat}} \pm 0.023_{\text{syst}}) \text{ MeV}/c^2, \quad (9.11)$$

where the systematic error is dominated by that associated with the determination of the beam momentum through the induced depolarizing resonance technique. This might be improved but there seems to be currently no pressing need to know the value of the  $\eta$  mass to better than  $23$  keV/ $c^2$ . The statistical and systematic errors are both marginally better than those of other modern measurements quoted in the PDG compilation [164]. With a relative uncertainty of about  $4 \times 10^{-5}$ , this is certainly the most precise measurement carried out within the hadron physics programme at COSY.

### 9.3 The $pd \rightarrow {}^3\text{He}\pi^+\pi^-$ reaction

At the height of the meson hunt, Abashian, Booth, and Crowe [178] measured the inclusive cross sections for  $pd \rightarrow {}^3\text{He}X^0$  and  $pd \rightarrow {}^3\text{H}X^+$  at a beam energy of  $T_p = 743$  MeV. This corresponds to an excess energy with respect to the  $\pi^+\pi^-$  threshold of  $Q = W - M_{{}^3\text{He}} - 2M_{\pi^+} = 184$  MeV, where  $W$  is the total energy in the centre-of-mass system. In addition to the expected single-pion peaks, a striking enhancement was seen in the  ${}^3\text{He}$  case at a missing mass of about  $310$  MeV/ $c^2$ , with a width  $\approx 50$  MeV/ $c^2$ . Being so close to the  $\pi^+\pi^-$  threshold, it could be assumed that the pions were in a relative  $s$ -wave and hence had an overall isospin of  $I = 0$ . This is consistent with the lack of a similar signal in the  $pd \rightarrow {}^3\text{H}X^+$  data. This behaviour has since become known as the ABC effect or enhancement. However, the ABC parameters change with the experimental conditions and it is believed that the ABC is a kinematic effect, related to the presence of nucleons, rather than the hoped-for  $s$ -wave isoscalar  $\pi\pi$  resonance [311].

A similar inclusive measurement could have been carried out using the high resolution Big Karl spectrometer described in sect. 2.2.5. However, to investigate the  $pd \rightarrow {}^3\text{He}X^+X^-$  reaction in greater depth, one needs more information on the distributions of the mesons  $X$  produced. For this purpose Big Karl was used in conjunction with the MOMO vertex detector that was described in sect. 2.2.7. In a low energy run, an event with two charged particles in the vertex detector and a  ${}^3\text{He}$  in Big Karl was considered to be a candidate for the  $pd \rightarrow {}^3\text{He}\pi^+\pi^-$  reaction. Its identification and complete reconstruction involved a two-constraint kinematic fit. About 15,000 unambiguous events were obtained at a beam energy of  $546$  MeV ( $Q = 70$  MeV).

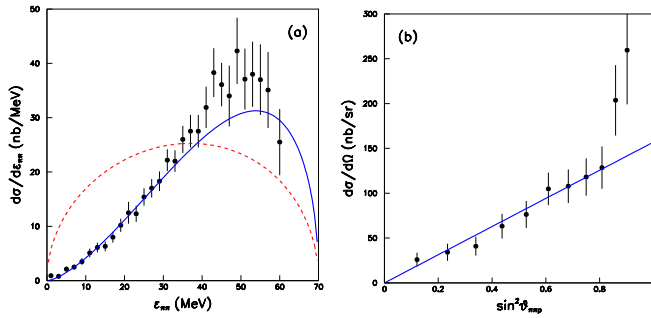


**Fig. 93.** Differential cross sections for the  $pd \rightarrow {}^3\text{He}\pi^+\pi^-$  reaction at  $T_p = 546$  MeV [32] as a function of (a) the pion-pion excitation energy  $\varepsilon_{\pi\pi}$  and (b) the angle  $\theta_{\pi\pi p}$  between the two-pion relative momentum and the beam axis in the  $\pi^+\pi^-$  rest frame. The dashed curve represents phase space normalized to the data whereas the solid ones are predictions assuming that the pion pair emerges in a relative  $p$ -wave with spin projection  $m = \pm 1$ .

The only variable accessible in a single-arm experiment [178] is the pion-pion excitation energy  $\varepsilon_{\pi\pi} = (m_{\pi\pi} - 2m_\pi)c^2$ , where  $m_{\pi\pi}$  is the two-pion invariant mass. This distribution, which is shown in Fig. 93a, could have been studied using just the Big Karl measurement, but it would then have summed the charged and neutral pion data. In marked contrast to the original ABC experiments [178], which showed an enhancement over phase space in the region of  $\varepsilon_{\pi\pi} \approx 30$  MeV, the MOMO data were pushed towards maximum  $\varepsilon_{\pi\pi}$ . The MOMO authors suggested that this distortion might be due to the  $\pi^+\pi^-$  pair emerging in a relative  $p$ -wave and the solid curve in Fig. 93a represents phase space multiplied by a kinematic factor of  $\varepsilon_{\pi\pi}$ .

Further evidence in support of the  $p$ -wave *ansatz* is given in Fig. 93b, which shows the distribution in the angle between the  $\pi^+\pi^-$  relative momentum in the dipion rest frame relative to the beam direction. If the  $\pi^+\pi^-$  pair had been in an  $s$ -wave, as was expected for the ABC, the distribution would be isotropic. This is far from being the case and the MOMO authors argued that the observed  $\sin^2 \theta_{\pi\pi p}$  behaviour was consistent with the production of a  $p$ -wave dipion with angular momentum projection  $m = \pm 1$  along the beam direction. Other distributions presented by the MOMO collaboration [32] did not disagree with this  $p$ -wave hypothesis.

Although the angular distribution in Fig. 93b clearly demonstrates the presence of higher partial waves in the  $\pi^+\pi^-$  system, the MOMO interpretation is not unambiguous. Similar effects could arise from  $s$ - $d$  interference in the  $I = 0$  channel and, in a two-step model [312], the shape of the  $\varepsilon_{\pi\pi}$  distribution was described in terms of  $\pi^-p \rightarrow \pi^0\pi^0p$  amplitudes. However, the uncertainty in the normalization in such a model means that a significant  $p$ -wave component cannot be excluded.

The anti-ABC behaviour near threshold was also seen in subsequent MOMO data taken with proton and deuteron beams at  $Q = 92, 28,$  and  $8$  MeV [313]. The clearest proof for the importance of higher partial waves in the  $\pi^+\pi^-$  system produced in the  $dp \rightarrow {}^3\text{He}\pi^+\pi^-$  reaction

at  $Q = 28$  MeV is provided by the distribution in the Gottfried-Jackson angle  $\theta_{GJ}$ . This is the angle between the relative momentum between the two pions and the direction of the deuteron beam, evaluated in the dipion rest frame. The MOMO data shown in Fig. 94 are symmetric about  $90^\circ$  because the  $\pi^+$  and  $\pi^-$  are not distinguished in this detector. The deviation from isotropy could be a signal for a superposition of  $s$ - and  $p$ -wave pion pairs but even higher partial waves are not definitively excluded.

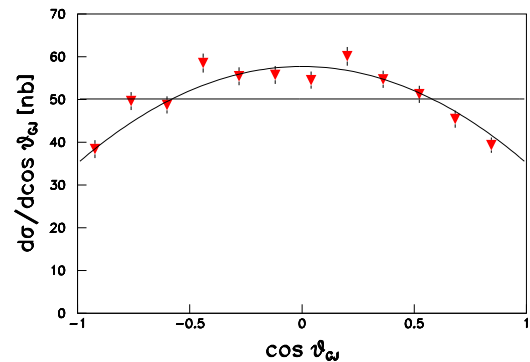


**Fig. 94.** Distribution of the MOMO  $dp \rightarrow {}^3\text{He}\pi^+\pi^-$  data at  $Q = 28$  MeV in the Gottfried-Jackson angle [313]. The data are symmetric about  $90^\circ$  because the sign of the charges on the pions was not measured. The solid curve is a linear fit to the data in  $\cos^2 \theta_{GJ}$ .

A different behaviour for the  $pd \rightarrow {}^3\text{He}\pi^+\pi^-$  reaction at low energies is also suggested by the simple  $\Delta(1232)$  decay model used to evaluate the acceptance for this process at ANKE at  $Q = 265$  MeV, and which is discussed later in this section. Though this does not predict the anti-ABC shape shown by the MOMO data in Fig. 93a, it does suggest that the ABC effect might have largely vanished when the energy is reduced to  $Q \approx 70$  MeV.

Values of the  $pd \rightarrow {}^3\text{He}\pi^0\pi^0$  cross section could be derived by subtracting the exclusive  $pd \rightarrow {}^3\text{He}\pi^+\pi^-$  cross section measured using MOMO plus Big Karl from the inclusive  $pd \rightarrow {}^3\text{He}X^0$  data obtained using Big Karl alone [313]. However, it is hard to quantify the systematic errors associated with this procedure.

A first fully exclusive measurement of the  $pd \rightarrow {}^3\text{He}\pi\pi$  reaction well away from threshold was undertaken by the WASA collaboration working close to the  $\eta$  threshold at CELSIUS [314]. In addition to seeing ABC peaks in both the  $\pi^0\pi^0$  and  $\pi^+\pi^-$  invariant mass distributions, the fully reconstructed events and the large WASA acceptance allowed the group to study also the individual  ${}^3\text{He}\pi^+$  and  ${}^3\text{He}\pi^-$  mass distributions. The measurements of  $pd \rightarrow {}^3\text{He}\pi^0\pi^0$  were continued by the group working at COSY at a higher energy, corresponding to  $Q = 338$  MeV [315].

Of greater interest for the low energy discussion is the fact that data were also taken with a 1.7 GeV deuteron

beam and the results analyzed in terms of quasi-free  $dd \rightarrow {}^3\text{He}\pi^0\pi^0n_{\text{sp}}$ . For this purpose the photons from the  $\pi^0$  decays were detected in coincidence with the  ${}^3\text{He}$  and the neutron spectator  $n_{\text{sp}}$  identified from the missing-mass peak. This allowed the  $pd \rightarrow {}^3\text{He}\pi^0\pi^0$  reaction to be studied simultaneously over a range of energies. It was seen there that even as low as  $Q = 172$  MeV there was evidence for some ABC enhancement at low  $\pi\pi$  masses [315]. Of course it must be realized that pion-pion  $p$ -waves are excluded in this channel and so it would really be most interesting to get data also in the  $pd \rightarrow {}^3\text{He}\pi^+\pi^-$  channel above the highest MOMO energy of 92 MeV.

The use of the ANKE magnetic spectrometer improved the resolution relative to that achieved with WASA. Furthermore, the higher beam energies available at COSY meant that the  $dp \rightarrow {}^3\text{He}\pi^+\pi^-$  differential cross section could be measured with a deuteron beam incident on a hydrogen target which, in the absence of a beam pipe hole, increases significantly the acceptance [316]. It is important to realize that, in contrast to experiments using the MOMO device, the charges on each pion could be determined. At least one pion had to be detected in coincidence with the  ${}^3\text{He}$ , the other being identified through the missing-mass peak, though in some cases all three particles were measured.

The ANKE  $dp \rightarrow {}^3\text{He}\pi^+\pi^-$  data were also taken close to the  $\eta$  threshold as background measurements in the experiment to determine the mass of the  $\eta$  meson [307]. Since the ANKE acceptance is very limited, a model was needed to estimate the necessary corrections. The one used was based loosely on the idea of the Roper resonance emitting a  $p$ -wave pion and decaying into the  $\Delta(1232)$  resonance, which also emits a  $p$ -wave pion when it decays. They therefore assumed that

$$\sigma \propto |[M_\pi^2 + B\mathbf{k}_1 \cdot \mathbf{k}_2](3\Delta^{++} + \Delta^0)|^2, \quad (9.12)$$

where the  $\mathbf{k}_i$  are the pion momenta in centre-of-mass frame, the factors 3 and 1 result from the isospin couplings of the  $\Delta$  propagators, and  $B$  is a complex fit parameter. Note that this *ansatz* neglects any dependence on the direction of the beam. Other models gave rather similar correction factors, as did that of the multidimensional matrix approach.

The model of Eq. (9.12) describe well the two  $M_{3\text{He}\pi}$  spectra of Fig. 95 and their difference but the ABC peak in the  $\pi^+\pi^-$  mass distribution is not quite sharp enough, though this might be adjusted through the introduction of a modest  $\pi^+\pi^-$  form factor. If the  $\pi^+\pi^-$  spectrum is purely isoscalar then the  $\pi^\pm{}^3\text{He}$  distributions should be identical but, as is clearly shown in Fig. 95b, the peak in the  $\pi^-{}^3\text{He}$  distribution is at a lower mass than that of  $\pi^+{}^3\text{He}$ . This is indicative of an  $I_{\pi\pi} = 1$  amplitude interfering with one for  $I_{\pi\pi} = 0$ . It is therefore a much more sensitive test of isovector pion pairs than, say, a comparison of  $\pi^+\pi^-$  and  $\pi^0\pi^0$  production rates and, moreover, there is no ambiguity accounting for the pion mass differences. The broad features of the difference spectrum in Fig. 95b are reproduced by the simple model of Eq. (9.12) and this should contribute to the understanding of the

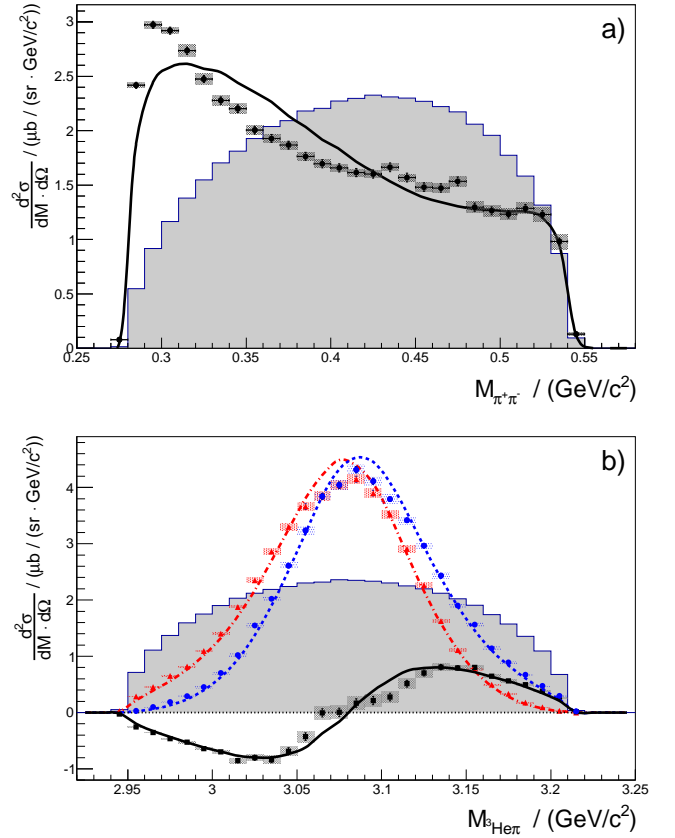


**Fig. 95.** Centre-of-mass double differential cross sections for the  $dp \rightarrow {}^3\text{He}\pi^+\pi^-$  reaction averaged over  $143^\circ < \vartheta_{3\text{He}}^{CMS} < 173^\circ$  [316] in terms of (a)  $M_{\pi^+\pi^-}$  and (b)  $M_{3\text{He}\pi^+}$  (blue circles) and  $M_{3\text{He}\pi^-}$  (red triangles). The differences between the two  $M_{3\text{He}\pi}$  distributions are plotted as black squares. There is, in addition, an overall normalization uncertainty of 6%. The curves correspond to Eq. (9.12) and the shaded areas are phase-space distributions normalized to the integrated cross section.

double-pion-production reaction. It further suggests that there must have been also some isovector two-pion production on the original ABC experiment [178]. It is unfortunate that there are no similar fully exclusive measurements closer to the MOMO domain.

#### 9.4 The $pd \rightarrow {}^3\text{He}K^+K^-$ ( $\phi$ ) reactions

The MOMO/Big Karl combination was also used to measure the  $pd \rightarrow {}^3\text{He}K^+K^-$  differential cross section [33], though the multipion background is here much larger than for two-pion production [32]. In view of this, and in order to identify the produced particles unambiguously as kaons, the detector was supplemented by a hodoscope of 16 wedge-shaped scintillators. Charged kaons could thus be detected and their production vertex measured with full azimuthal acceptance within a polar angular range of  $8^\circ < \theta_{\text{lab}} < 45^\circ$ .

The experiments were carried out at three beam momenta, corresponding to excess energies of  $Q = 35.1, 40.6,$

and 55.2 MeV with respect to the  ${}^3\text{He} K^+K^-$  threshold (i.e., 3.0, 8.5, and 23.1 MeV with respect to the nominal  ${}^3\text{He} \phi$  threshold). The separation of  $\phi$  production from direct  $K^+K^-$  production was done on the basis of the  $K^+K^-$  invariant mass distribution, an example of which is shown in Fig. 96a at  $Q = 55.2$  MeV. This is in fact the most challenging energy because, in addition to the resolution getting worse kinematically as  $Q$  increases, the beam conditions were also less favourable.

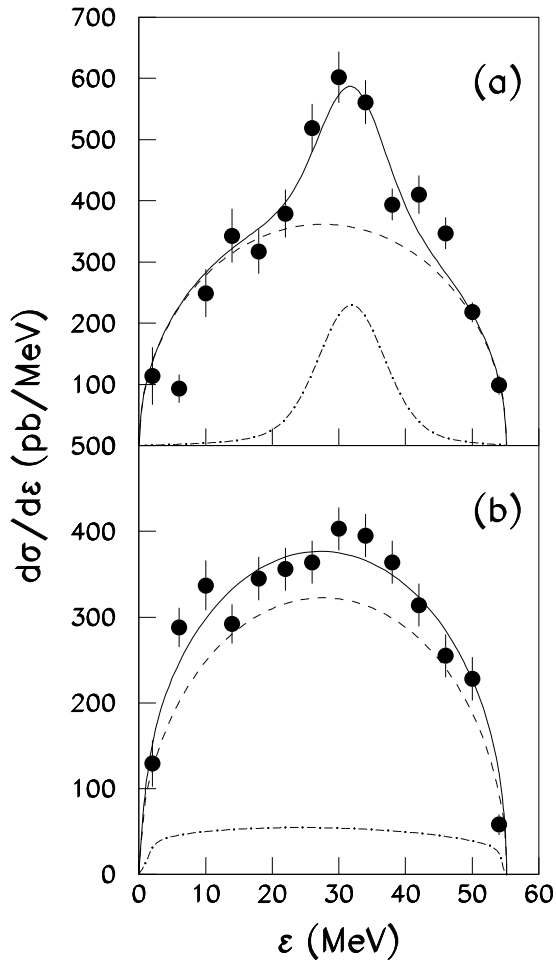


**Fig. 96.** Differential cross section for the  $pd \rightarrow {}^3\text{He} K^+K^-$  reaction at an overall excess energy of  $Q = 55.2$  MeV [33]. The curves are fits to the distributions in terms of phase space coming from prompt  $K^+K^-$  production (dashed line), proceeding via  $\phi$ -meson formation (chain), and their sum (solid line). The distributions are shown in terms of (a) the excitation energy  $\epsilon$  in the  $K^+K^-$  system and (b) that in the  $K^3\text{He}$  system.

The  $\phi$  contribution to the differential cross section was modeled in terms of a peak with a natural width of  $\Gamma = 4.2$  MeV, smeared with the expected energy resolution. In contrast, the direct  $K^+K^-$  component was taken to be proportional to three-body phase space, which is very different to the distributions found by MOMO for

$\pi^+\pi^-$  production [32]. The sum of these two elements reproduces very well the  $K^+K^-$  data at all three values of  $Q$ , an example of which is shown in Fig. 96a. This therefore gave confidence in using such a model in correcting the overall acceptance. However, the large background under the  $\phi$  made it difficult to extract separate angular distributions at this energy, though the conditions are much more favourable close to the  $\phi$  threshold.

The distribution in the  $K^3\text{He}$  invariant mass shown in Fig. 96b is little sensitive to the  $\phi/K^+K^-$  separation. There is no sign of any  $K^-p$  enhancement that was so evident in the  $pp \rightarrow ppK^+K^-$  case of sect. 8.1 because it was not possible to distinguish between  $K^-$  and  $K^+$  with the MOMO detector.

By measuring all three final particles it was possible to construct several angular distributions, the most interesting of which is the angle between the relative  $K^+K^-$  direction in its rest frame and the initial beam direction. The  $Q = 35.1$  MeV data in a region where the  $\phi$  cannot contribute ( $\epsilon < 28$  MeV) are flat. On the other hand, the  $\phi$ -rich region ( $\epsilon > 28$  MeV) has a very strong angular dependence that could only be explained by the  $\phi$  being produced almost exclusively with polarization projection along the beam direction of  $m = 0$ . This clear effect is in complete contrast to the behaviour in  $pd \rightarrow {}^3\text{He} \omega$ , where the  $\omega$  mesons are produced effectively unpolarized [317]. This is the clearest signal for a violation of the OZI rule that relates  $\omega$  and  $\phi$  production rates [276], since there is much less ambiguity in accounting for the effects of the meson mass difference.

Though the shapes of the distributions and the angular dependence are largely unaffected by the overall normalizations, these are of course important for the cross section evaluations, which have systematic uncertainties of the order of 10%. The resulting energy dependence is illustrated in Fig. 97. For  $\phi$  production, this is shown in the form of the angular average of the square of the production amplitude, as defined by Eq. (9.6). Within the experimental uncertainties,  $|f(pd \rightarrow {}^3\text{He} \phi)|^2$  is consistent with being constant, and this value agrees with the Saclay near-threshold missing-mass measurement [318].

On the other hand, it is seen in Fig. 96a that the cross section for direct  $K^+K^-$  production looks very much like phase space. This is confirmed in Fig. 97, where it is shown that the total cross section divided by a phase space factor of  $Q^2$  is effectively constant.

Whereas in the vicinity of the  $\phi$  threshold the resolution and the signal-to-background ratio allow the  $pd \rightarrow {}^3\text{He} \phi$  cross section to be measured in a missing-mass experiment, at higher excess energies this is no longer possible and the detection of a  $K^+K^-$  pair in coincidence is necessary. It is unfortunate that the MOMO detector could not determine the charges on the mesons. Otherwise it could have investigated the  $K^-{}^3\text{He}$  final state interaction in  $pd \rightarrow {}^3\text{He} K^+K^-$ .

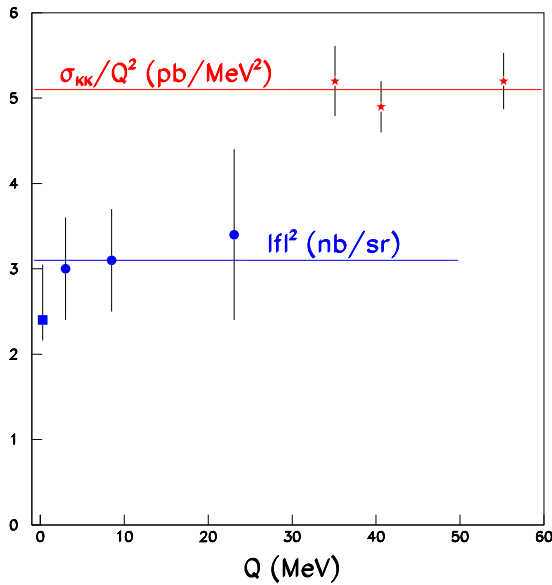


**Fig. 97.** Circles (blue) denote MOMO values of the amplitude-square for  $\phi$  production [33], as defined by Eq. (9.6); the SPES4 result at  $Q = 0.3$  MeV [318] is shown by a square. The data are consistent with  $|f|^2$  being constant, as indicated. The MOMO data for the total cross section for direct  $K^+K^-$  production divided by the phase space factor of  $Q^2$  are shown by the (red) stars [33].

## 10 The $dd \rightarrow {}^4\text{He}X^0$ family of reactions

Meson production rates in the  $dd \rightarrow {}^4\text{He}X^0$  reaction are expected to be very low because two deuterons, with mean diameters of about 4 fm, have to be squeezed to form the much smaller  $\alpha$ -particle. An exception is the  $dd \rightarrow {}^4\text{He}\pi^+\pi^-$  reaction [195], but there may be special reasons for this [196]. However, the rates are often disappointingly low as, for example, in the search for evidence for the production of the  $f_0$  meson in the  $dd \rightarrow {}^4\text{He}K^+K^-$  reaction [319]. Nevertheless, some channels have to be studied in depth because of their importance in Physics and two such examples are outlined in this section.

Evidence from COSY-11 and ANKE was presented in sect. 9.2 for the possible existence of the  ${}^3_\eta\text{He}$   $\eta$ -mesic nucleus. The interpretation of these results suggest that the  $\eta$  might bind to  ${}^4\text{He}$  but that signals could be harder to detect for heavier nuclei. Given that the final  $s$ -wave is forbidden by spin-parity constraints in the  $\gamma{}^4\text{He} \rightarrow \eta{}^4\text{He}$  reaction, and that the use of a tritium target in the  $p{}^3\text{H} \rightarrow \eta{}^4\text{He}$  reaction presents its own special problems, the attention naturally turns to  $dd \rightarrow \eta{}^4\text{He}$ , which is the subject of sect. 10.1.

Symmetry properties have been one of the cornerstones of particle and nuclear physics and, as such, have been extensively investigated for over sixty years. In modern parlance, charge symmetry corresponds to invariance under the interchange of the  $u$  and  $d$  quarks. It has even been dismissed as an *accidental* symmetry that arises because of the near equality of the  $u$  and  $d$  masses. Charge symmetry

violation associated with isospin mixing within multiplets is responsible for the well-known mixing of the  $\rho^0$  and  $\omega$  mesons but there has been far less direct evidence for such violations in nuclear reactions.

Under the charge symmetry operation, the  $\pi^0$  changes sign whereas the deuteron and  $\alpha$ -particle are unaffected. As a consequence, a non-vanishing rate for the  $dd \rightarrow \alpha\pi^0$  reaction, which is discussed in sect. 10.2, is a clear example of charge symmetry breaking (CSB). It is also the most convincing example in nuclear reactions because it is proportional to the square of a CSB amplitude, with no contribution from interference terms.

### 10.1 The $dd \rightarrow {}^4\text{He}\eta$ reaction

The first measurements of the  $dd \rightarrow {}^4\text{He}\eta$  total cross sections were carried out using the SPES4 [320] and the SPES3 [321] spectrometers at SATURNE. Figure 98 shows the data converted into averaged-squared-amplitudes  $|f_s|^2$  on the basis of the analogue of Eq. (9.6) used for the  $pd \rightarrow {}^3\text{He}\eta$  reaction. Corrections, which will be discussed later, have been made to eliminate effects of higher partial waves. The first point to notice is that the production rate at small  $p_\eta$  is about a factor of 50 lower for  ${}^4\text{He}\eta$  than for  ${}^3\text{He}\eta$ .

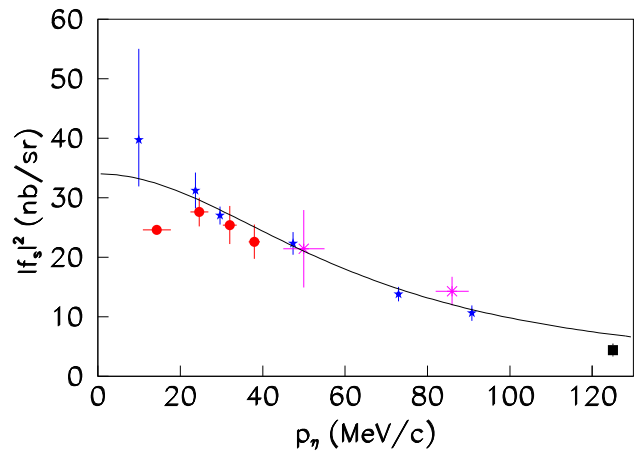


**Fig. 98.** Experimental values of the square of the  $dd \rightarrow {}^4\text{He}\eta$   $s$ -wave amplitude. The data are taken from Refs. [320] (red circles), [321] (blue stars), [322] (magenta crosses), and [323] (black closed square). The curve is a scattering-length fit:  $|f_s|^2 = 34/[1+(p_\eta/64)^2]$  nb/sr, where  $p_\eta$  is measured in MeV/c.

Though the acceptance of SPES3 was much larger than that of SPES4, its missing-mass resolution was certainly poorer and it was therefore difficult to overcome the multipion background. However, the SPES3 experiment was carried out with a polarized deuteron beam. Since  $s$ -wave  $\eta$  production is forbidden by Bose symmetry for deuterons with spin projection  $m = 0$ , the tensor analyzing power near threshold must be  $A_{xx} = -\frac{1}{2}$ . Any deviations from

this would be a signal for  $p$  or higher  $\eta$  partial waves. The SPES3 analysis assumed that this constraint was also valid for all the energies so that they studied the shape of the multipion background by forming the  $m = 0$  combination  $(1+2A_{xx}) d\sigma/d\Omega$ . Thus, if the analyzing power were small away from threshold, the SPES3 results for the total cross section would be too low by a factor of 1.5.

The unpolarized differential cross section was studied later at two excess energies  $Q$  with the ANKE spectrometer [322]. Whereas the results were consistent with isotropy at  $Q = 2.6$  MeV, there was clearly a need for a linear term in  $\cos^2\theta_\eta$  at  $Q = 7.7$  MeV. However, there is no way from these data to discover if this effect is due to the square of a large  $p$ -wave amplitude or arises from a much smaller  $d$ -wave interfering with the dominant  $s$ -wave amplitude. For that one needs well identified events obtained with a tensor polarized deuteron beam (or target).

The GEM collaboration used the high resolution Big Karl spectrometer to study the  $dd \rightarrow {}^4\text{He}\eta$  reaction with both polarized and unpolarized deuteron beams at an excess energy of  $Q = 16.6$  MeV [323]. By expanding the unpolarized differential cross section in terms of Legendre polynomials it was found that terms up to at least  $P_4(\cos\theta_\eta)$  were required to describe the data and the corresponding coefficient  $a_4$  was in fact the largest in the series. This demonstrated that the production involved significant contributions from  $d$  or higher waves.

In the second stage, data were taken with a polarized deuteron beam but, due to the side yoke in the first magnetic dipole of Big Karl, the acceptance had severe cuts in the azimuthal angle and the results were only sensitive to the  $A_{xx}$  deuteron analyzing power [323]. Nevertheless this is sufficient to separate the contributions from even and odd partial waves. An analysis of the data shows that at this energy the reaction is dominated by the  $d$ -wave in the  $\eta^4\text{He}$  system. By assuming that each of the partial waves varied with the threshold factor  $(p_\eta)^{\ell_\eta}$ , it was possible to correct all the previous data in order to extract values for the  $s$ -wave contributions, and this is precisely what is shown in Fig. 98.

It is clear that  $|f_s|^2$  falls far less rapidly than the corresponding quantity for  $dp \rightarrow {}^3\text{He}\eta$  discussed in sect. 9.2. Even if one restricts a parametrization of the data to one in terms of a scattering length, there would still be strong coupling between the real and imaginary parts. The curve shown in the figure,  $|f_s|^2 = 34/[1 + (p_\eta/64)^2]$  nb/sr, corresponds to a purely imaginary scattering length. Here  $p_\eta$  is measured in MeV/ $c$  and the pole is at  $Q \sim -4$  MeV, though there is no way of knowing from  $\eta$  production data whether this would correspond to a bound or anti-bound state.

Limits on the production of  ${}^4_\eta\text{He}$  were also obtained through the COSY-WASA measurements of the cross sections for the  $dd \rightarrow {}^3\text{He}p\pi^-$  and  $dd \rightarrow {}^3\text{He}n\pi^0$  reactions, where the exotic nucleus is expected to decay via  $\eta n \rightarrow \pi^- p$  or  $\eta n \rightarrow \pi^0 n$  [324]. These limits are, however, comparable to theoretical estimates, which themselves have a large degree of uncertainty [325].

The use of a polarized deuteron beam helped significantly in the understanding of the  $dd \rightarrow {}^4\text{He}\eta$  reaction and constrained the position of the  $s$ -wave pole by reducing the influence of higher partial waves. Unfortunately this has not proved possible for the much rarer  $dd \rightarrow {}^4\text{He}\pi^0$  reaction, to which we turn in the next section.

However, before we leave entirely the topic of  $\eta$ -mesic nuclei, mention should be made of one COSY experiment that investigated the possibility of the formation of heavier nuclei [35,36]. Here the ENSTAR detector, described in sect. 2.2.8, was used in combination with the Big Karl spectrometer. ENSTAR detected back-to-back  $\pi^- p$  pairs from the hoped-for  $\eta N$  decays, with Big Karl measuring the  ${}^3\text{He}$  in the  $p^{27}\text{Al} \rightarrow {}^3\text{He}p\pi^- X$  reaction. The kinematics were cunningly chosen such that, for a weakly bound  $\eta$ -nucleus state, the meson was produced almost at rest so that it had a higher chance of *sticking* to the residual nucleus.

It was suggested that the excess of events for  $Q \approx -13$  MeV with a FWHM of  $\approx 10$  MeV in Fig. 99 might be a signal for a  ${}^{25}_\eta\text{Mg}$  bound state. If this were indeed the case, then the production cross section for this state is estimated to be  $0.46 \pm 0.16(\text{stat}) \pm 0.06(\text{syst})$  nb. Haider and Liu [326] predicted a state in  ${}^{25}_\eta\text{Mg}$  at  $Q \approx -7$  MeV but offered an explanation for the difference of 6 MeV. However it is still possible that the structure is a statistical fluctuation and so further investigations are required.

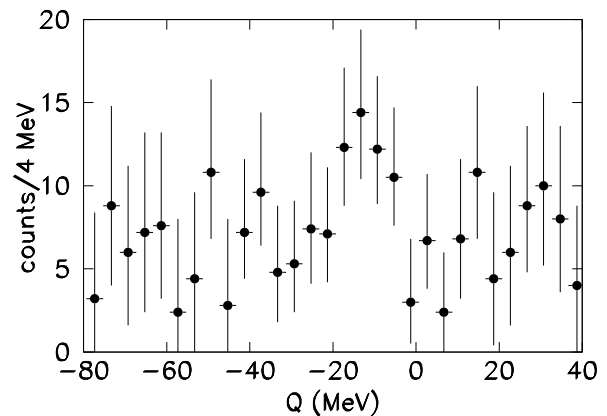


Fig. 99. Counts for the  $p^{27}\text{Al} \rightarrow {}^3\text{He}p\pi^- X$  reaction as a function of the excess energy in the  $\eta^{25}\text{Mg}$  system [35].

## 10.2 The $dd \rightarrow {}^4\text{He}\pi^0$ reaction and charge symmetry

There have been many attempts over the years to detect the  $dd \rightarrow \alpha\pi^0$  reaction but the first positive claim [327] was possibly a misidentification of the non-pionic three-body  $\alpha\gamma\gamma$  final state [328]. The first unambiguous measurement of the  $dd \rightarrow \alpha\pi^0$  reaction was made at IUCF



at two energies close to threshold [329]. The momentum of the  $\alpha$ -particle was determined by magnetic analysis and time-of-flight measurements, which allowed the missing mass in the  $dd \rightarrow \alpha X$  reaction to be evaluated reliably. Photons from the  $\pi^0$  decay were detected in lead glass arrays placed to the left and right of the gas jet target. The resulting missing-mass distribution was therefore that of  $dd \rightarrow \alpha\gamma\gamma$  with the  $\pi^0$  in the final state being recognized through the peak in the distribution with  $\text{FWHM} \approx 600 \text{ keV}/c^2$ . The three-body  $\alpha\gamma\gamma$  background was predicted to vary smoothly with  $m_{\gamma\gamma}$ , though the rates extracted were about twice those estimated in an *ab initio* model [328]. The IUCF total cross sections of  $\approx 14 \text{ pb}$  are shown in Fig. 100 divided by the phase-space factor and plotted in terms of the pion reduced momentum  $\eta = p_{\pi}^{cm}/m_{\pi}$ .

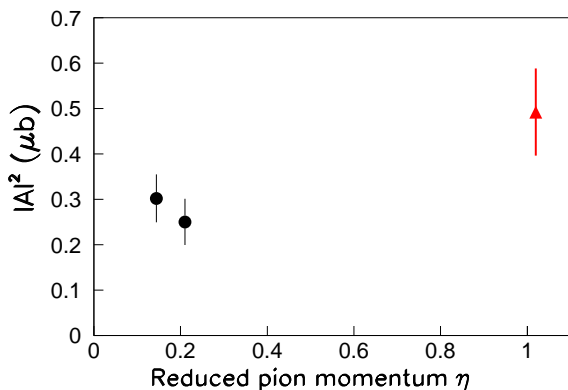


**Fig. 100.** Values of the total cross sections measured for the  $dd \rightarrow \alpha\pi^0$  reaction measured at IUCF (black circle [329]) and WASA-at-COSY (red triangle [330]). The data are multiplied by the phase-space factor of the ratio of the initial to the final c.m. momenta and plotted in terms of the reduced pion c.m. momentum  $\eta = p_{\pi}/m_{\pi}$ .

The two IUCF points shown in Fig. 100 are consistent with  $s$ -wave production but, in order to put extra constraints on the theoretical modeling, data are required away from the threshold region where higher partial waves may play a role. The decay photons are, of course, very well measured in the WASA central detector but the  ${}^4\text{He}$  identification and measurement in the WASA forward detector was less effective than in the IUCF setup and some  ${}^3\text{He}$  may have been falsely identified as  ${}^4\text{He}$ . In addition, in common with many meson production experiments, the missing-mass peaks become less pronounced as one moves away from threshold.

The WASA-at-COSY experiment was carried out at an excess energy of  $Q = 60 \text{ MeV}$  with respect to the  $\pi^0$  production threshold. The missing-mass distribution from the initial publication is shown in Fig. 101, which was evaluated on the assumption that all the remaining recoiling helium ions were  ${}^4\text{He}$  [330]. Though much suppressed by the kinematics, the most prominent peak is

that due to the charge-symmetry-allowed  $dd \rightarrow {}^3\text{He}n\pi^0$  reaction, which was actually used to establish the normalization, using data previously obtained by the group [331]. There is, in addition, the rather featureless  $dd \rightarrow {}^4\text{He}\gamma\gamma$  background, though there may also be a small contamination here from the  ${}^3\text{He}n\gamma\gamma$  final state. Nevertheless, the evidence for the  $dd \rightarrow {}^4\text{He}\pi^0$  reaction in Fig. 101 is quite clear.

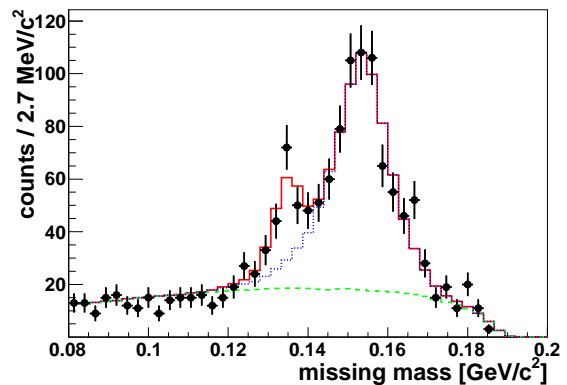


**Fig. 101.** Missing-mass distribution for the  $dd \rightarrow {}^4\text{He}X$  reaction measured by the WASA-at-COSY collaboration [330]. Fits were made that included the three-body  $dd \rightarrow {}^4\text{He}\gamma\gamma$  contribution (green dashed), plus the  $dd \rightarrow {}^3\text{He}n\pi^0$  reaction (blue dotted), plus the desired signal (red solid).

Extrapolating to the whole of phase space, including events lost down the beam pipe, a total cross section  $\sigma_{\text{tot}} = (118 \pm 24) \text{ pb}$  was obtained, which is about  $5 \times 10^{-5}$  times smaller than the allowed  $dd \rightarrow {}^3\text{He}n\pi^0$  cross section at the same beam energy [331]. The value obtained for the total  $dd \rightarrow {}^4\text{He}\gamma\gamma$  cross section ( $\approx 1 \text{ nb}$ ) contained significant model dependence and was not compared to theoretical estimates.

The phase-space-modified  $dd \rightarrow \alpha\pi^0$  total cross section is shown along with the IUCF points in Fig. 100. The increase in  $p_d^{cm}\sigma_{\text{tot}}/p_{\pi}^{cm}$  with  $\eta$  might be taken as evidence for higher partial waves but is not conclusive. Limited information was also obtained on the angular distribution, which suggests some anisotropy, which was confirmed in a more extensive later run with higher statistics [332]. An angular dependence could arise from either  $s$ - $d$  interference or from the square of a  $p$ -wave amplitude. These possibilities could only be separated through a measurement of the deuteron tensor analyzing power, as was done for the analogous but allowed  $dd \rightarrow {}^4\text{He}\eta$  reaction [323]. Such information would be very valuable for theorists trying to understand the origin of the symmetry breaking.

## 11 Rare decays of $\eta$ and $\pi^0$ mesons

The initial motivation for the study of  $\eta$  decays at hadronic machines came from the SATURNE measurement of the

$dp \rightarrow {}^3\text{He}\eta$  total cross section [298]. This showed that there was a very strong  $\eta$  signal even within a few MeV of threshold but that the multipion background under the  $\eta$  missing-mass peak was very low. Some  $\eta$  decays were studied at SATURNE using this facility but the chance to create an  $\eta$ -meson factory [333] was lost when the CsI crystals, which were the basis of the detector design, could not be delivered on time and in budget before the closure of the SATURNE accelerator. Much of the physics programme was taken up at the WASA detector installed at the CELSIUS storage ring but the full impact was only felt after the transfer of WASA to COSY.

It is important to realize that, although the tagging of the  $\eta$  is very good indeed in the  $pd \rightarrow {}^3\text{He}\eta$  reaction, the counting rates are limited and so this source cannot be used for the very rare decays. Higher counting rates can be achieved in proton-proton collisions using the  $pp \rightarrow pp\eta$  reaction, though the backgrounds may then be larger than those found at electron machines. Some WASA  $\eta$ -decay data obtained with the  $pp \rightarrow pp\eta$  reaction are still at the analysis stage [22].

The situation is more challenging for the study of the  $\eta'$ , where the production rates with proton beams are low but the multipion background high [334].

### 11.1 $\eta$ decays

The WASA detector, as installed at COSY, was introduced in sect. 2.2.3. Its first production run at COSY used  $\eta$  mesons generated in  $pp$  collisions at 1.4 GeV [335]. The  $1.2 \times 10^5$  fully reconstructed events of the  $\eta \rightarrow \pi^0\pi^0\pi^0$  decay were a sub-sample of the  $8 \times 10^5$  identified  $pp \rightarrow pp6\gamma$  events. In order to select  $\pi^0$  candidates from the six reconstructed photons, all fifteen possible combinations of the photon pairs were considered and only solutions with reasonable probabilities retained.

Since the final  $\pi^0$  are identical particles, the  $\eta \rightarrow \pi^0\pi^0\pi^0$  Dalitz plot must be symmetric under the exchange of any two of their kinetic energies  $T_i$ . For a constant matrix element the population of the Dalitz plot should be uniform but this may be distorted by, among other things, pion-pion scattering in the final state. Because of the identity of the  $\pi^0$ , one would expect the population to vary as  $1 + 2\alpha z$ , where the variable  $z$ , defined by  $z = [(T_1 - T_2)^2 + 3(T_3 - \langle T \rangle)^2] / 3\langle T \rangle^2$ , with  $\langle T \rangle = (T_1 + T_2 + T_3) / 3$ , is indeed symmetric under particle interchange.

The asymmetry found,  $\alpha = -0.027 \pm 0.008(\text{stat}) \pm 0.005(\text{syst})$ , is consistent with the other modern measurements in the PDG tabulation [164], though the KLOE and Crystal Barrel collaborations quote slightly smaller error bars. The statistical precision of the WASA data is unfortunately insufficient to investigate the cusp effect that must be present when the two-pion invariant mass is around twice the mass of the charged pion.

Later experiments at WASA used the  $pd \rightarrow {}^3\text{He}\eta$  reaction as the source of  $\eta$  mesons but a compromise had to be made between the better signal-to-background ratio close to threshold and the larger  $\eta$  counting rates achievable at a slightly higher energy. Thus, in the measurement

of the decay  $\eta \rightarrow \pi^+\pi^-\gamma$ , the data were taken at a beam momentum of 1.7 GeV/c, which corresponds to an excess energy of  $Q = 60$  MeV [336]. Cuts were required to remove unwanted backgrounds, some of which were reflections of other  $\eta$  decay modes or direct meson production. The group reconstructed  $1.4 \times 10^4$   $\eta \rightarrow \pi^+\pi^-\gamma$  events out of a total of  $1.2 \times 10^7$  candidates that contained an  $\eta$  and the resulting distribution in photon energy in the  $\eta$  rest frame is shown in Fig. 102.

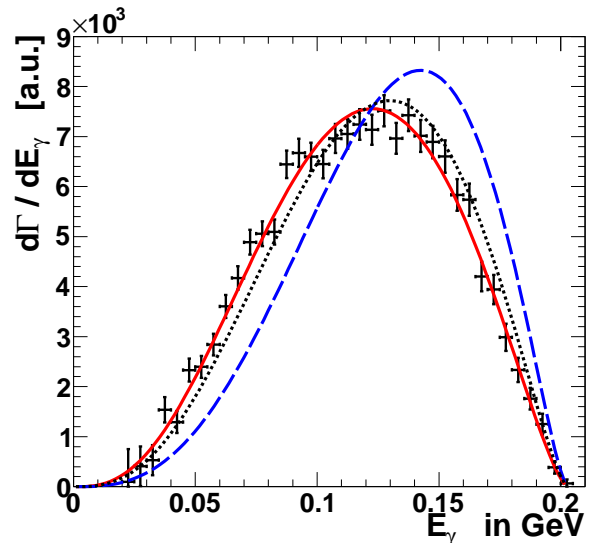


**Fig. 102.** The photon energy distribution measured in the  $\eta$  rest frame for the decay  $\eta \rightarrow \pi^+\pi^-\gamma$  [336]. The dashed (blue) curve represents the shape expected from a point interaction,  $E_\gamma^2 q^2$ , with  $q$  being the relative momentum in the pion-pion rest frame. Multiplying this by the square of the pion vector form factor leads to the dotted (black) curve. This has to be modified slightly to give the solid (red) curve that fits the WASA data. All curves are normalized to the same total number of events.

Just as for the  $\eta \rightarrow \pi^0\pi^0\pi^0$  mode, the differential distributions are strongly affected by  $\pi\pi$  final state interactions. The big difference in this case is that the  $\pi^+\pi^-$  spectrum is governed by the  $\rho$ -channel isovector  $p$ -wave form factor, which tends to favour higher  $\pi\pi$  masses. Though this explains most of the distortion apparent in Fig. 102, it needs a little “help” to give a perfect fit to the WASA data.

No attempt was made in Ref. [336] to extract an overall  $\eta \rightarrow \pi^+\pi^-\gamma$  branching ratio but the decay rates for four charged modes were extracted in a later analysis from an extended data set that started from  $3 \times 10^7$   $\eta$  events obtained from twelve weeks of runs [22]. No absolute values of the decay probabilities were extracted but the rates were measured relative to the well established  $\eta \rightarrow \pi^+\pi^-(\pi^0 \rightarrow \gamma\gamma)$  decay, which means that many of the systematic effects cancel in the ratios.

The results for the  $\eta \rightarrow \pi^+\pi^-\gamma$ ,  $\eta \rightarrow \pi^+\pi^-e^+e^-$ ,  $\eta \rightarrow e^+e^-\gamma$ , and  $\eta \rightarrow e^+e^-e^+e^-$  are shown in Table 4 [336]. The value extracted for the  $\eta \rightarrow \pi^+\pi^-\gamma$  channel is about

a factor of 1.1 larger than the PDG average [164], which is based upon the results of other modern measurements. The difference would correspond to 2.4 times the WASA systematic error but, as yet, there is no explanation for the discrepancy. The other three branching ratios reported in Table 4 are consistent with those reported by PDG [164].

Channel	Branching ratio with respect to $\eta \rightarrow \pi^+\pi^-(\pi^0 \rightarrow \gamma\gamma)$
$\eta \rightarrow \pi^+\pi^-\gamma$	$0.206 \pm 0.003_{\text{stat/fit}} \pm 0.008_{\text{sys}}$
$\eta \rightarrow \pi^+\pi^-e^+e^-$	$(1.2 \pm 0.1_{\text{stat}} \pm 0.1_{\text{sys}}) \times 10^{-3}$
$\eta \rightarrow e^+e^-\gamma$	$(2.97 \pm 0.03_{\text{stat/fit}} \pm 0.13_{\text{sys}}) \times 10^{-2}$
$\eta \rightarrow e^+e^-e^+e^-$	$(1.4 \pm 0.4_{\text{stat}} \pm 0.2_{\text{sys}}) \times 10^{-4}$

**Table 4.** Summary of WASA measurements [22] of the branching ratios for charged  $\eta$  decays relative to the  $\eta \rightarrow \pi^+\pi^-(\pi^0 \rightarrow \gamma\gamma)$  normalization channel.

One should note, however, the large statistical error bar on the double Dalitz decay  $\eta \rightarrow e^+e^-e^+e^-$ . With such a small branching ratio the counting rate was only about 1.5 per week and this shows the limitations of the  $pd \rightarrow {}^3\text{He}\eta$  reaction to access rare decays, such as those associated with  $CP$  violation. Nevertheless, a search for possible  $CP$  violation was attempted in the study of the angular distribution between the  $\pi^+\pi^-$  and the  $e^+e^-$  decay planes in the rest frame of the  $\eta$ . No significant asymmetry was found but, once again, the limitation came from the statistical precision.

The Dalitz plot for the  $\eta \rightarrow \pi^+\pi^-\pi^0$  decay is clearly much richer than that for the  $\eta \rightarrow \pi^0\pi^0\pi^0$  because the pions are no longer identical particles and at least five parameters may be relevant. A study of the Dalitz plot for this decay was carried out with the initial  $1.2 \times 10^7$  events obtained using the  $pd \rightarrow {}^3\text{He}\eta$  reaction at 1.7 GeV/c [337]. The basic limitation compared to existing KLOE data [338] is the restricted statistics, which might eventually be expanded using  $pp \rightarrow pp\eta$  as the source of  $\eta$  mesons. Although it is claimed that the results are generally compatible with those of KLOE, there are deviations of more than  $2\sigma$  in a few of the parameters, though one has to realize that some of these were strongly correlated in the fits.

Superficially the decay  $\omega \rightarrow \pi^+\pi^-\pi^0$  looks very similar to the analogous  $\eta$  decay discussed earlier in this section, but there are two very important differences. The natural width of the  $\omega$  means that in any production experiment there will be a significant background, as illustrated in Fig. 49. This can be modeled in terms of explicit multipion production [171] or fitted empirically using information from data on either side of the  $\omega$  peak.

The big theoretical difference is that the  $\omega \rightarrow \pi^+\pi^-\pi^0$  decay is *allowed* by the strong interaction conservation laws and these show that each of the pion pairs must be in a relative  $p$ -wave and this has to be taken into account when modeling the Dalitz plot of the decay.

The three-pion decay of the  $\omega$  was studied in three runs by the WASA collaboration working at COSY [339].

The  $pd \rightarrow {}^3\text{He}\omega$  reaction was measured at proton beam energies of  $T_p = 1.45$  and 1.50 GeV and  $pp \rightarrow pp\omega$  at 2.063 GeV. In all three cases, combined fits were made for an  $\omega$  peak sitting on an empirical polynomial background.

Shortly after the  $\omega$  discovery it was pointed out that the simple  $p$ -wave form of the Dalitz plot would be distorted by the strong  $p$ -wave attraction between pion pairs, caused by the low mass tail of the  $\rho$  meson [340]. From the combined study of 44,000  $\omega \rightarrow \pi + \pi^-\pi^0$  decays, the WASA collaboration has found the first clear evidence of this effect at the  $4.1\sigma$  level and determined deviations from the simple  $p$ -wave Dalitz plot that are consistent with the expectations of a  $\rho$ -meson-type final-state interaction [339].

## 11.2 Dark photons

One of the early extensions to the Standard Model of particle physics that could accommodate some aspects of dark matter was the suggestion of an extra Abelian symmetry. This would give rise to a  $U(1)$  vector boson that could mix with the normal photon to form new eigenstates. This idea has gained traction in recent years because of the suggestion that such a *dark photon* might be the origin of the 3.6 standard deviations of the results of the muon  $g-2$  experiment from theoretical explanations. In view of the importance of finding physics beyond the Standard Model, searches for such *dark photons* have been initiated at many laboratories throughout the World.

The *dark photon* search at COSY involved the study of the Dalitz decay of the  $\pi^0$  meson [341] using the WASA detector that was described in sect. 2.2.3. The pions were produced in the  $pp \rightarrow pp\pi^0$  reaction at 550 MeV, which is below the two-pion threshold. However, the large excess energy of  $Q = 122$  MeV meant that the geometric acceptance for both protons to enter the WASA forward detector illustrated in Fig. 4 was only 19%.

The  $pp \rightarrow pp(\pi^0 \rightarrow e^+e^-\gamma)$  reaction was clearly identified by requesting, in addition to the two protons in the forward detector, two oppositely curved tracks in the MDC in the central detector of Fig. 4 with scattering angles between  $40^\circ$  and  $140^\circ$ . A photon hit cluster in the calorimeter with an energy deposit above 20 MeV was also demanded. Although the requirement of the mere presence of electron tracks improved significantly the background in the missing-mass spectrum, the most accurate identification of the  $\pi^0$  signal came from the  $e^+e^-\gamma$  invariant mass, where the  $\pi^0$  peak had a FWHM  $\approx 30$  MeV/ $c^2$  with almost no background. The peak was very well described by a Monte Carlo simulation where, in addition to the Dalitz decay, there was also a contribution from  $\pi^0 \rightarrow \gamma\gamma$  where one of the photons underwent an external conversion in the beryllium beam pipe. This contribution could be largely suppressed by identifying the origin of the  $e^+e^-$  pair and discarding events that lay outside the target region.

The invariant mass distribution of the  $e^+e^-$  pair from the Dalitz decay of the  $\pi^0$  can be predicted quite reliably, the only significant ambiguity being associated with

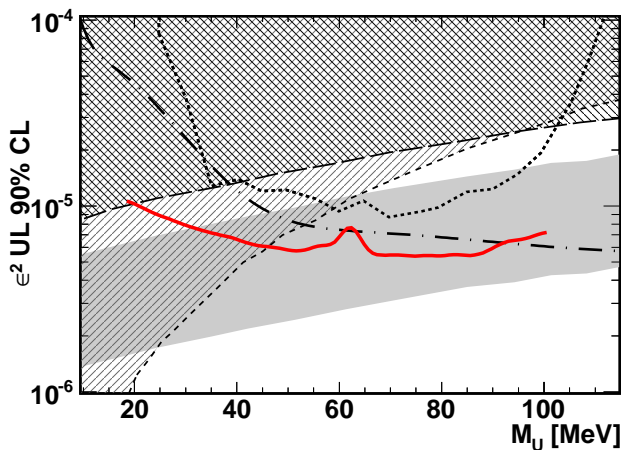


**Fig. 103.** Summary of the 90% confidential upper limits for the mixing parameter  $\epsilon^2$  as a function of the *dark photon* mass from the WASA experiment [341] (red solid line). Other lines represent similar upper limits from earlier experiments but the grey area represents the  $\pm 2\sigma$  preferred band around the present value of the muon ( $g-2$ ) measurement.

a form factor, whose effects are small and slowly varying. The  $5 \times 10^5$  events collected agree with the prediction up to at least  $0.1 \text{ GeV}/c^2$ , after which point random coincidences become relatively much more important. If there were a contribution from a dark photon in the decay  $\pi^0 \rightarrow \gamma (U \rightarrow e^+e^-)$  it should show up as a peak in this distribution, depending upon the  $(\gamma, U)$  mixing parameter  $\epsilon$  and the mass  $m_U$  of the state. No sign of such a peak was seen in the data and this allowed the group to put the upper limit on the dark photon that is shown in Fig. 103. Also shown in the figure is a grey area corresponding to the  $\pm 2\sigma$  band of values that could explain the  $g-2$  experimental data. From this it is seen that the WASA data would not rule out this possibility in certain regions in the plane.

Since dark matter is such an exciting area of current research, the WASA limit could not be the last word on the subject. In the year that followed there were measurements by collaborations at HADES [342], BaBar [343], MAMI [344], PHENIX [345], and NA48/2 [346] and the much stricter upper limits found by summing all these later results seem to exclude almost completely dark photons as being the origin of the  $g-2$  discrepancy. However, in general these were inclusive measurements and the WASA data still represents the best exclusive measurement of the Dalitz decay of the  $\pi^0$ .

## 12 Conclusions

Though the hadron physics programme has terminated, COSY has now embarked on a new career of precision measurements and we should here like to sketch what the future holds in this domain. Currently there are two main themes that are in different stages of preparation. The

principal one involves the search for an Electric Dipole Moment (EDM) of an elementary particle in an accelerator environment. The second is the search for the breaking of Time Reversal Invariance in COSY (TRIC) by measuring a particular spin correlation in proton-deuteron collisions. We give below outlines of these two important programmes.

The theory of the Big Bang postulates that, in the initial stages of the development of the Universe, matter and antimatter were produced in equal amounts. However, the Cosmic Microwave Background Probe has measured the ratio of the difference in the numbers of baryons and antibaryons compared to the number of relic photons in the visible part of the Universe and found a deviation of eight orders of magnitude compared to the predictions of the Standard Model of particle physics. This effect, the so-called Baryon Asymmetry of the Universe, represents one of the most serious challenges to the Standard Model. There is clearly a need for new sources of  $CP$  violation beyond the Standard Model to allow baryons to be generated at the expense of antibaryons.

Sakharov [347] set down three conditions that are necessary in order that baryonic matter should dominate the observable Universe:

- Baryon number conservation must be violated sufficiently strongly,
- $C$  and  $CP$  must be violated so that baryons and antibaryons are produced with different rates,
- The Universe must have evolved outside a realm of thermal equilibrium.

The COSY aim is therefore to try to find signals for the violation of  $CP$  conservation that are bigger than the well-known ones that are found, for example, in kaon decay. A permanent electric dipole moment of an elementary particle would simultaneously violate both parity  $P$  and time reversal symmetry  $T$ . Assuming that the  $CPT$  theorem holds, it means that an EDM would also violate the combined symmetry  $CP$  [348].

An EDM can arise due to the separation between the charges in a particle so that the natural scale for an EDM in atomic physics is  $10^{-8} \text{ e.cm}$  whereas the much smaller sizes in hadronic physics bring this down to  $10^{-13} \text{ e.cm}$ . A water molecule has an EDM of about  $2 \times 10^{-9} \text{ e.cm}$  and this is close to the natural scale because such objects have degenerate ground states of opposite parity and so parity violation does not lead to a big suppression. In contrast, the neutron does not have a partner with opposite parity and so it is not surprising that, despite steady improvements over the years, there is currently only an upper limit on its EDM of  $3 \times 10^{-26} \text{ e.cm}$  [349,350].

For a neutron at rest, there is no Coulomb force associated with an electric field which thus acts only through the neutron's EDM. This leads to precession frequency shifts that depend on the orientation of the neutron spin and hence its EDM. It might seem to be much more difficult to investigate an EDM of a charged particle under clean conditions but that is the goal of the JEDI collaboration at COSY [351]. In the short term an EDM measurement of a proton or deuteron will be undertaken at COSY but with

a limited sensitivity. On a longer time scale, the design of a dedicated storage ring will be undertaken. A highly sensitive accelerator-based experiment would allow the EDM of a charged particle to be inferred from its very slow spin precession in the presence of large electric fields, and could reach a limit of  $10^{-29}$  e.cm. This huge improvement over current neutron values is due mainly to the larger number of particles available in a stored beam, compared with the number of ultra-cold neutrons usually found in trap experiments, and also the potentially longer observation time that is possible because such experiments are not limited by the particle decay time. It must also be stressed that, knowing the EDM of just one particle, would not be sufficient to identify unambiguously the  $CP$ -violating source. For this reason the new design must allow for its use with a variety of light ions.

The basic ideas behind the COSY measurements are as follows. The proton/deuteron spin precesses in the horizontal plane at a rate determined by its magnetic dipole moment. If the particle has an EDM, the spin vector experiences an additional torque that will create a vertical spin component proportional to the size of the EDM. The main challenge of such kind of experiment is the very small expected vertical component of the spin excited by the EDM and the relatively large contributions from false spin rotations due to field and misalignments errors of accelerator elements.

The coherent buildup of the vertical polarization only takes place on a time scale where the spins of the particle ensemble stay aligned. Since the spin tune is a function of the betatron and synchrotron amplitudes of the particles in the six-dimensional phase space, spin decoherence, which is caused by beam emittance and momentum spread of the beam, leads to a gradual decrease of the polarization buildup rate in the vertical direction. To reach the anticipated statistical sensitivity of  $10^{-29}$  e.cm, a spin coherence time of 1000 s must be reached. This has been achieved for deuterons at COSY by a combination of beam bunching, electron cooling, sextupole field corrections, and the suppression of collective effects through beam current limitations [352,39].

There are many technical problems to overcome, even with the precursor experiment that aims to put limits on the deuteron EDM. For example, half the time a longitudinally polarized beam would have its polarization parallel to its momentum and half the time antiparallel, which could lead to no net EDM effect. This could be overcome by making the spin precession in the machine resonate with the orbital motion which might be done through the action of a judiciously tuned  $rf$  Wien filter, a possibility that is now being actively pursued. After other upgrades to COSY through, for example, the introduction of precise beam position monitors, it should be possible to make the first direct measurement of the deuteron EDM using the COSY ring. This will provide a proof-of-principle measurement for EDM searches of charged particles (and a first direct measurement of EDM limits for protons and deuterons) in storage rings. All the problems and challenges that have to be faced in turning this programme

into a reality will surely stimulate developments in storage ring technology.

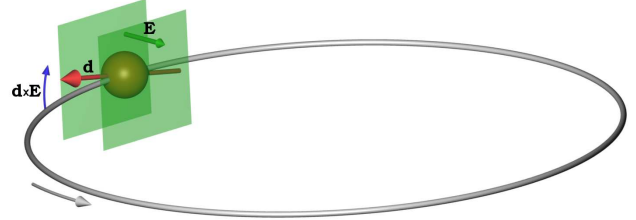


**Fig. 104.** In a dedicated experiment to measure the EDM of a charged particle, a radial electric field would be applied to an ensemble of particles circulating in a storage ring with polarisation vector aligned to their momentum. The existence of an EDM would generate a torque that would slowly rotate the spin out of the plane of the ring and into the vertical direction.

However, the use of the COSY ring, where the orbits are governed purely by magnetic fields, may not allow the EDM measurements of charged particles to reach the limits that are suggested to be theoretically *interesting*. For this purpose a new dedicated electric storage ring, as illustrated schematically in Fig. 104, might be required and its design will be the major tasks for the JEDI collaboration in the upcoming years. Such a precision storage ring for polarized light ions (proton, deuteron, and  $^3\text{He}$ ), possibly with two counter-rotating beams, would unquestionably present a multitude of new technical features. Preliminary estimates suggest that it might be possible to get down to the  $10^{-29}$  e.cm level for these light ions with such a facility.

In contrast to the EDM searches, the TRIC experiment seeks to find evidence for an interaction that breaks time reversal but conserves parity [353]. There is in fact an observable  $A_{y,xz}$  in proton-deuteron elastic scattering with polarized beam and target that would vanish in the absence of some  $T$ -odd  $P$ -even interaction. By the generalized optical theorem, the imaginary part of this observable in the forward direction is linked to the dependence of the proton-deuteron total cross section on these spin orientations. At COSY this could be studied by arranging the proton beam polarization along the perpendicular to the horizontal COSY plane while keeping the tensor polarization of the deuteron in the horizontal plane, with an angle of  $45^\circ$  between the polarization vector and the beam direction.

The principle of the experiment is illustrated in the c.m. frame in Fig. 105, where it is shown that the combined application of the time-reversal and rotation operators leads to the same initial configuration but with signs of the polarizations of either the proton or deuteron being reversed. Time reversal therefore means that the total cross section measured with configuration c) or d) should be identical to that obtained using a). The ability to invert either of these polarizations allows a useful check on the systematics of the experiment.

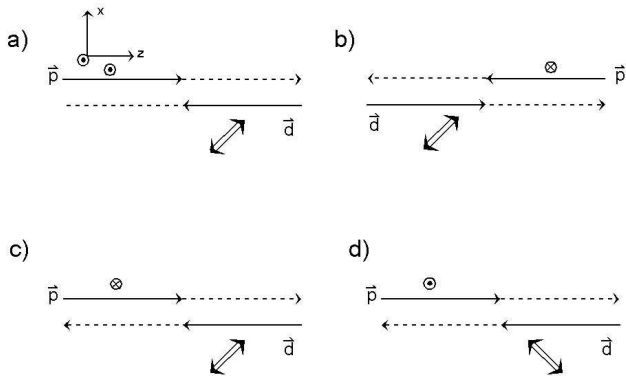


**Fig. 105.** Graphical illustration in the c.m. frame that a time-reversed situation can be prepared in double-polarized proton-deuteron total cross sections by flipping the spin of either the proton or deuteron [353]. a) The basic system is shown. b) The time-reversal operator is applied. In order to have a direct comparison between situation a) and b), rotations through  $180^\circ$  about either the  $y$ - or  $x$ -axis lead to configurations c) and d), respectively.  $\otimes$  proton spin up (in the  $y$ -direction),  $\odot$  proton spin down,  $\longleftrightarrow$  deuteron tensor polarization.

The measurement of such a  $\vec{p}\vec{d}$  total cross section in a transmission experiment with an external beam is problematic because of the difficulties in preparing a suitable polarized deuterium target. In COSY one can measure a total cross section by studying the lifetime of the beam as it passes through the target with a revolution frequency of up to 1.6 MHz.

The first test of using the COSY beam lifetime to study the spin dependence of a total cross section was carried out several years ago at COSY [60]. The total cross section asymmetry  $A_{y,y}$  in transversally polarized  $\vec{p}\vec{p}$  scattering has been measured at 1690 MeV/c with stochastic cooling and polarizations of the beam and target above 80%. This test measurement gave a total cross section difference of  $-3.2 \pm 9.6$  mb compared to that deduced from direct total cross section measurements of  $-3.0$  mb at this momentum [354]. The experimental conditions were rather poor and the error bar could have been reduced by a factor of 20 and even higher precision could be achieved now with the current equipment available at COSY. This will be further improved with the dedicated high precision beam current measurement system that is being specially built for the TRIC experiment.

In principle the TRIC measurement of  $A_{y,xz}$  could be undertaken at any proton beam energy, but there are good arguments for choosing  $T_p = 135$  MeV. It was predicted [355] that the sensitivity to  $T$ -violating forces should be maximal for  $T_p$  of the order of 150 MeV and this has been checked independently [356]. On the practical side, high quality polarimetry data for proton-deuteron elastic scattering are available at 135 MeV [357]. At this energy the electron cooler can continuously cool the COSY beam over the complete cycle of measurements. It should also

be noted that only one depolarizing resonance has to be crossed to arrive at this energy.

The TRIC experiment could be carried out at the PAX internal target station, which was discussed in sec. 2.4.3. This facility is located in one of the straight low- $\beta$  sections of COSY, which leads to a reduction in the beam emittance in the centre of the target. PAX is equipped with a high intensity Atomic Beam Source, storage cell, multi-purpose detector, holding field, and Breit-Rabi polarimeter. Using the new high precision beam current measurement system, COSY will serve as accelerator, storage ring, and ideal zero-degree spectrometer and detector for the TRIC experiment. However, the timescale is a little uncertain because TRIC is in competition for resources with the EDM project, which has perhaps more worldwide resonance.

As well as looking forward to the future, we must also look back at the past. Since the aim of this review is to emphasize some of the legacy left by the programme of hadron physics carried out at COSY over twenty years, it seems appropriate to finish by trying to identify some elements that will leave a lasting impression on the field. The ordering given below has no objective significance!

1. The systematic EDDA studies [37,66,67,68,69,70] of the differential cross section and a wide variety of spin observables in elastic proton-proton scattering over almost all the COSY energy range have led to radical changes in the extraction of isospin  $I = 1$  phase shifts. These data have been supplemented by measurements at small angles at ANKE but only of the differential cross section and analyzing power and at discrete energies [63,78]. Differential cross sections at even smaller angles have been measured by the PANDA collaboration with the KOALA detector [82] and, when good data become available in the Coulomb peak, this would lead to yet another independent means to normalize the cross sections.
2. The WASA measurements of two-pion production in the  $np \rightarrow d\pi^0\pi^0$  reaction [185,186,188,195] have had an electrifying influence on the whole field because of the evidence for the production of an isoscalar dibaryon resonance.
3. Extra evidence in support of the dibaryon hypothesis was found from the WASA measurements of the analyzing power in neutron-proton elastic scattering [84,85], which led to a revision of the SAID [65]  $I = 0$  amplitude analysis. There had already been indications from  $\vec{d}\vec{p} \rightarrow \{pp\}_s n$  measurements at ANKE [86] that the existing SAID  $np$  solution was defective at high energies. Far more measurements are needed in neutron-proton elastic scattering above 1 GeV to give definitive solutions.
4. The most ambitious programme of meson production was carried out at ANKE [120,137,125] where the aim was to perform a full amplitude analysis of the  $Np \rightarrow \{pp\}_s \pi$  reaction. Although there remain some discrete ambiguities, this is the most complete data set in the World to test theoretical models, be they phenomenological or more fundamental, e.g., effective field theory.

5. In order to constrain models in hyperon production in nucleon-nucleon collisions one needs fully exclusive measurements and the only facility for producing such data at COSY is the Time-of-Flight spectrometer. Of the many successful experiments carried out with COSY-TOF, the one that stands out is the measurement of  $pp \rightarrow K^+p\Lambda$  [219,220], which shows a prominent cusp at the  $\Sigma N$  thresholds due to the coupling to the  $pp \rightarrow K^+\Sigma N$  channels. Though the resolution in the  $K^+$  momentum was better in the HIRES inclusive  $pp \rightarrow K^+X$  measurement [232], it was not possible there to separate cleanly  $\Lambda$  from  $\Sigma$  production.
6. Although close to threshold the  $pp \rightarrow K^+p\Lambda$  reaction is dominated by the excitation of the  $N^*$  isobar  $S_{11}(1650)$ , it is only through the study of the different angular distributions away from threshold that one can confirm the importance of the higher  $N^*$ . Such angular distributions could only be measured at COSY with the help of the TOF detector [218,26,27], and this is also true for the associated spin dependence [222].
7. The COSY-11 and ANKE measurements of the  $pd \rightarrow {}^3\text{He}\eta$  cross section near threshold [172,173] have proved crucial in the search for  $\eta$ -mesic nuclei. After taking the beam momentum spread into account, the data show that there is a pole in the  $\eta$ - ${}^3\text{He}$  system within 1 MeV of threshold [173]. This is the best signal of an  $\eta$ -mesic nucleus in the literature.
8. The COSY-11 measurements completely revolutionized the database on the total cross sections for single meson production in proton-proton collisions near threshold. This is best illustrated with the study of  $pp \rightarrow pp\eta'$ , where the precision was such that an absolute value of the  $\eta'$  width could be obtained [177] and bounds deduced on the  $\eta'p$  scattering length [153].
9. COSY-11 data showed for the first time that the  $K^-$  in kaon pair production  $pp \rightarrow ppK^+K^-$  is strongly attracted to the proton [258] and this was made more quantitative in later ANKE experiments [263]. The interaction of  $K^-$  with protons and light nuclei is likely to remain an intriguing field for years to come.
10. The mass of the  $\eta$  meson was measured with unparalleled precision at ANKE [53] but this was only possible because a technique was found to determine the momentum of the deuteron beam to about  $10^{-5}$ . The  $\eta$  mass will probably stay with little impact at the head of the PDG tables for years to come but more important for the future at COSY is the determination of the beam momentum with such precision.

The choice shown in the list above is clearly subjective, but only time will tell whether some of the items selected will have sunk without trace or whether others, that have been overlooked, will flourish.

## Acknowledgements

This review was commissioned by the Directors of the Institut für Kernphysik working at the COSY laboratory and the author is grateful for the material and physics support offered by Professors Meißner, Ritman, and Ströher.

It would be invidious to list all the COSY colleagues who have supplied me with relevant information but I have to take personal responsibility for the inevitable oversights and misunderstandings that have crept into this paper. One of the colleagues insisted that the review was biased because it has been heavily influenced by the elements that I find “interesting”. I apologize — but this may indeed be the case!

## References

1. A. Boudard, P.-A. Chamouard (editors) *The 20 years of the synchrotron Saturne-2*, (World Scientific, Singapore, 2000).
2. A. Letourneau *et al.*, Nucl. Phys. A **712**, 133 (2002).
3. K. Nünighoff *et al.*, Nucl. Phys. News **12**(4), 33 (2002).
4. A. Bubak *et al.*, Phys. Rev. C **76**, 014618 (2007).
5. H. Machner, Pramana **66**, 867 (2005).
6. K.-Th. Brinkmann, Proceedings of MENU2007, Ed. H. Machner, S. Krewald; <http://www.slac.stanford.edu/econf/C070910/>.
7. R. Maier, Nucl. Instrum. Methods Phys. Res. A **390**, 1 (1997).
8. R. Weidmann *et al.*, Rev. Sci. Instrum. **67**, 1357 (1996).
9. O. Felden *et al.*, Proc. 9<sup>th</sup> Int. Workshop on Polarized Sources and Targets, Eds. V.P. Derenchuk, B. von Przewoski (World Scientific, Singapore, 2002) p. 200.
10. H. J. Stein *et al.*, Atomic Energy **94**, 24 (2003).
11. D. Prasuhn *et al.*, Nucl. Instrum. Methods Phys. Res. A **441**, 167 (2000).
12. A. Lehrach *et al.*, AIP Conf. Proc. **675**, 153 (2003).
13. S. Brauksiepe *et al.*, Nucl. Instrum. Methods Phys. Res. A **376**, 397 (1996).
14. H. Calén *et al.*, Phys. Rev. C **58**, 2667 (1998).
15. Chr. Bargholtz *et al.*, Instrum. Exp. Techn. **49**, 461 (2006).
16. J. Smyrski *et al.*, Phys. Lett. B **474**, 182 (2000).
17. P. Moskal *et al.*, Nucl. Instrum. Methods Phys. Res. A **466**, 448 (2001).
18. S. Barsov *et al.*, Nucl. Instrum. Methods Phys. Res. A **462**, 364 (2001).
19. M. Büscher *et al.*, Nucl. Instrum. Methods Phys. Res. A **481**, 378 (2002).
20. Chr. Bargholtz *et al.*, Nucl. Instrum. Methods Phys. Res. A **594**, 339 (2008).
21. H. H. Adam *et al.*, arXiv:nucl-ex/0411038 (2004).
22. P. Adlarson *et al.*, arXiv:1509.06588 [nucl-ex] (2015).
23. C. Ekström *et al.*, Nucl. Instrum. Methods Phys. Res. A **371**, 572 (1996).
24. A. Böhm *et al.*, Nucl. Instrum. Methods Phys. Res. A **443**, 238 (2000).
25. P. D. Barnes *et al.*, Nucl. Phys. A **526**, 575 (1991).
26. F. Hauenstein, PhD thesis, University of Erlangen-Nürnberg (2014).
27. S. Jowzaee *et al.*, Eur. Phys. J. A **52**, 7 (2016).
28. S. A. Martin *et al.*, Nucl. Instrum. Methods **214**, 281 (1983).
29. M. Drochner *et al.*, Nucl. Phys. A **643**, 55 (1998).
30. J. Bojowald *et al.*, Nucl. Instrum. Methods Phys. Res. A **487**, 314 (2002).
31. M. Betigeri *et al.*, Nucl. Instrum. Methods Phys. Res. A **421**, 447 (1999).
32. F. Bellemann *et al.*, Phys. Rev. C **60**, 061002 (1999).
33. F. Bellemann *et al.*, Phys. Rev. C **75**, 015204 (2007).
34. M. Betigeri *et al.*, Nucl. Instrum. Methods Phys. Res. A **578**, 198 (2007).
35. A. Budzanowski *et al.*, Phys. Rev. C **79**, 012201(R) (2009).
36. H. Machner, J. Phys. G **42**, 043001 (2015).
37. M. Altmeier *et al.*, Eur. Phys. J. A **23**, 351 (2005).
38. E. Weise, PhD thesis, University of Bonn (2000); <http://edda.hiskp.uni-bonn.de/dipldiss.html>.
39. G. Guidoboni *et al.*, Phys. Rev. Lett. **117**, 054801 (2016).
40. F. Lehar, E. A. Strakovsky, C. Wilkin, *Experimental physics with polarized protons, neutrons and deuterons*, (Czech Technical University in Prague, 2015).
41. M. Mikirtychyants *et al.*, Nucl. Instrum. Methods Phys. Res. A **721**, 83 (2013).
42. C. Weidemann *et al.*, Phys. Rev. S. T. Accel. Beams **18**, 020101 (2015).
43. W. Haerberli, Ann. Rev. Nucl. Sci. **17**, 373 (1967).
44. R. Engels *et al.*, Rev. Sci. Instrum. **76**, 053305 (2005).
45. E. Steffens, W. Haerberli, Rep. Prog. Phys. **66**, 1887 (2003).
46. A. Airapetian *et al.*, Nucl. Instrum. Methods Phys. Res. A **540**, 68 (2005).
47. S. Dymov, A. Kacharava, Status report on COSY proposal # 213; [http://collaborations.fz-juelich.de/ikp/anke/proposal/StatusReport\\_CW.pdf](http://collaborations.fz-juelich.de/ikp/anke/proposal/StatusReport_CW.pdf).
48. R. Schleichert *Private communication* (2016).
49. R. Schleichert *et al.*, IEEE Trans. Nucl. Sci. **50**, 301 (2003).
50. R. Bilger *et al.*, Nucl. Instrum. Methods Phys. Res. A **457**, 64 (2001).
51. Q. Hu *et al.*, Eur. Phys. J. A **50**, 156 (2014).
52. H. J. Stein *et al.*, Phys. Rev. S. T. Accel. Beams **11**, 052801 (2008).
53. P. Goslawski *et al.*, Phys. Rev. S. T. Accel. Beams **13**, 022803 (2010).
54. A. D. Krisch *et al.*, Phys. Rev. S. T. Accel. Beams **10**, 071001 (2007).
55. V. S. Morozov *et al.*, Phys. Rev. Lett. **102**, 244801 (2009).
56. A. D. Bukin *et al.*, Sov. J. Nucl. Phys. **27**, 516 (1978); A.S. Artamonov *et al.*, Phys. Lett. B **118**, 225 (1982); V.M. Aulchenko *et al.*, Phys. Lett. B **573**, 63 (2003).
57. M. G. Betigeri *et al.*, Nucl. Instrum. Methods Phys. Res. A **426**, 249 (1999).
58. PAX collaboration technical proposal for *Antiproton-Proton Scattering Experiments with Polarization* (2006), <http://collaborations.fz-juelich.de/ikp/pax>.
59. P. Lenisa, F. Rathmann, Nucl. Phys. News **23**, 27 (2013).
60. P. D. Eversheim *et al.*, Hyperfine Interactions **193**, 335 (2009).
61. F. Rathmann *et al.*, Phys. Rev. Lett. **71**, 1379 (1993).
62. W. Augustyniak *et al.*, Phys. Lett. B **718**, 64 (2012).
63. Z. Bagdasarian *et al.*, Phys. Lett. B **739**, 152 (2014).
64. D. Oellers *et al.*, Phys. Lett. B **674**, 269 (2009).
65. R. A. Arndt, I. I. Strakovsky, R. L. Workman, Phys. Rev. C **62**, 034005 (2000); R. A. Arndt, W. J. Briscoe, I. I. Strakovsky, R. L. Workman, Phys. Rev. C **76**, 025209 (2007); <http://gwdac.phys.gwu.edu>.
66. D. Albers *et al.*, Phys. Rev. Lett. **78**, 1652 (1997).
67. D. Albers *et al.*, Eur. Phys. J. A **22**, 125 (2004).
68. M. Altmeier *et al.*, Phys. Rev. Lett. **85**, 1819 (2000).
69. F. Bauer *et al.*, Phys. Rev. Lett. **90**, 142301 (2003).
70. F. Bauer *et al.*, Phys. Rev. C **71**, 054002 (2005).
71. M. Garçon *et al.*, Nucl. Phys. A **445**, 669 (1985).
72. A. J. Simon *et al.*, Phys. Rev. C **48**, 662 (1993).
73. R. L. Workman, W. J. Briscoe, I. I. Strakovsky, arXiv:1609.01741 (2016).
74. K. A. Jenkins *et al.*, Phys. Rev. D **21**, 2445 (1980).
75. M. W. McNaughton *et al.*, Phys. Rev. C **41**, 2809 (1990).
76. F. Lehar *et al.*, Nucl. Phys. B **294**, 1013 (1987).
77. C. E. Allgower *et al.*, Phys. Rev. C **62**, 064001 (2000).
78. D. Mchedlishvili *et al.*, Phys. Lett. B **755**, 92 (2016).



79. I. Ambats *et al.*, Phys. Rev. D **9**, 1179 (1974).
80. A. V. Dobrovolsky *et al.*, Nucl. Phys. B **214**, 1 (1983).
81. W. Grein, P. Kroll, Nucl. Phys. A **377**, 505 (1982).
82. Annual Report 2015, Jülich Centre for Hadron Physics/Institut für Kernphysik/COSY.
83. H. Xu *Private communication* (2016).
84. P. Adlarson *et al.*, Phys. Rev. Lett. **112**, 202301 (2014).
85. P. Adlarson *et al.*, Phys. Rev. C **90**, 035204 (2014).
86. D. Mchedlishvili, ANKE Report #28 (2013); <http://collaborations.fz-juelich.de/ikp/anke/>
87. R. L. Workman, W. J. Briscoe, I. I. Strakovsky, Phys. Rev. C **93**, 045201 (2016).
88. D. V. Bugg, C. Wilkin, Nucl. Phys. A **467**, 575 (1987).
89. J. Carbonell, M. B. Barbaro, C. Wilkin, Nucl. Phys. A **529**, 653 (1991).
90. D. Chiladze *et al.*, Phys. Rev. S. T. Accel. Beams **9**, 050101 (2006).
91. D. Chiladze *et al.*, Eur. Phys. J. A **40**, 23 (2009).
92. D. Mchedlishvili *et al.*, Eur. Phys. J. A **49**, 49 (2013).
93. D. Mchedlishvili, PhD thesis, Tbilisi State University (2013).
94. B. Gou *et al.*, Phys. Lett. B **741**, 305 (2015).
95. S. Barsov *et al.*, *In preparation*.
96. V. Komarov *et al.*, Phys. Lett. B **553**, 179 (2003).
97. S. Dymov *et al.*, Phys. Rev. C **81**, 044001 (2010).
98. N. S. Craigie, C. Wilkin, Nucl. Phys. B **14**, 477 (1969).
99. V. M. Kolybasov, N. Ya. Smorodinskaya, Sov. J. Nucl. Phys. **17**, 630 (1973).
100. Yu. N. Uzikov, J. Haidenbauer, C. Wilkin, Phys. Rev. C **75**, 014008 (2007).
101. S. Yaschenko *et al.*, Phys. Rev. Lett. **94**, 072304 (2005).
102. P. Moskal, M. Wolke, A. Khokkaz, W. Oelert, Prog. Part. Nucl. Phys. **49**, 1 (2002).
103. G. Fäldt, C. Wilkin, Phys. Lett. B **382**, 209 (1996).
104. A. Boudard, G. Fäldt, C. Wilkin, Phys. Lett. B **389**, 440 (1996).
105. G. Fäldt, C. Wilkin, Phys. Scripta **56**, 566 (1997).
106. G. Fäldt, C. Wilkin, Phys. Rev. C **56**, 2067 (1997).
107. A. Sibirtsev, J. Haidenbauer, H.-W. Hammer, U.-G. Meißner, Eur. Phys. J. A **29**, 363 (2006).
108. R. Bilger *et al.*, Phys. Lett. B **429**, 195 (1998).
109. A. Johansson, C. Wilkin, Phys. Lett. B **673**, 5 (2009), *Erratum* Phys. Lett. B **680**, 111 (2009).
110. A. Johansson, H. Haberzettl, K. Nakayama, C. Wilkin, Phys. Rev. C **83**, 054001 (2011).
111. V. Komarov *et al.*, Phys. Rev. Lett. **101**, 102501 (2008).
112. D. Tsirkov *et al.*, J. Phys. G **37**, 105005 (2010).
113. J. Złomanczuk, *Private communication* (2016).
114. C. Hanhart, Phys. Rept. **397**, 155 (2004).
115. S. Abd El-Samad *et al.*, Eur. Phys. J. A **17**, 595 (2003).
116. H. O. Meyer *et al.*, Nucl. Phys. A **539**, 633 (1992).
117. R. Bilger *et al.*, Nucl. Phys. A **693**, 633 (2001).
118. S. Abd El-Samad *et al.*, Eur. Phys. J. A **30**, 443 (2006).
119. S. Abd El-Samad *et al.*, Eur. Phys. J. A **39**, 281 (2009).
120. D. Tsirkov *et al.*, Phys. Lett. B **712**, 370 (2012).
121. P. Thörnqren Engblom *et al.*, Phys. Rev. C **76**, 011602(R) (2007).
122. R. A. Arndt, I. I. Strakovsky, R. L. Workman, D. V. Bugg, Phys. Rev. C **48**, 1926 (1993); <http://gwdac.phys.gwu.edu>.
123. M. Abdel-Bary *et al.*, Eur. Phys. J. A **29**, 353 (2006).
124. M. Abdel-Bary *et al.*, Eur. Phys. J. A **36**, 7 (2008).
125. S. Dymov *et al.*, Phys. Rev. C **88**, 014001 (2013).
126. M. Daum *et al.*, Eur. Phys. J. C **23**, 43 (2002).
127. R. Handler, Phys. Rev. B **138**, 1230 (1965).
128. M. Drochner *et al.*, Phys. Rev. Lett. **77**, 454 (1996).
129. E. Pedroni *et al.*, Nucl. Phys. A **300**, 321 (1978).
130. V. Shmakova *et al.*, Phys. Lett. B **726**, 634 (2013).
131. B. v. Przewoski *et al.*, Phys. Rev. C **61**, 064604 (2000).
132. S. Dymov *et al.*, Phys. Lett. B **635**, 270 (2006).
133. V. Kurbatov *et al.*, Phys. Lett. B **661**, 22 (2008).
134. J. A. Niskanen, Phys. Lett. B **642**, 34 (2006).
135. V. Komarov *et al.*, Phys. Rev. C **93**, 065206 (2016).
136. V. Baru, C. Hanhart, F. Myhrer, Int. J. Mod. Phys. E **23**, 1430004 (2014).
137. S. Dymov *et al.*, Phys. Lett. B **712**, 375 (2012).
138. V. Abaev *et al.*, Phys. Lett. B **521**, 158 (2001).
139. M. Abdel-Bary *et al.*, Phys. Lett. B **610**, 31 (2005).
140. A. Budzanowski *et al.*, Phys. Rev. C **79**, 061001(R) (2009).
141. E. Chiavassa *et al.*, Phys. Lett. B **322**, 270 (1994).
142. H. Calén *et al.*, Phys. Lett. B **366**, 39 (1996).
143. A. M. Bergdolt *et al.*, Phys. Rev. D **48**, R2969 (1993).
144. F. Hibou *et al.*, Phys. Lett. B **438**, 41 (1998).
145. P. Moskal *et al.*, Phys. Rev. C **69**, 025203 (2004).
146. P. Moskal *et al.*, Eur. Phys. J. A **43**, 131 (2010).
147. N. de Marco, *private communication* (2001).
148. G. Agakishiev *et al.*, Eur. Phys. J. A **48**, 74 (2012).
149. F. Balestra *et al.*, Phys. Lett. B **491**, 29 (2000).
150. P. Moskal *et al.*, Phys. Rev. Lett. **80**, 3202 (1998).
151. P. Moskal *et al.*, Phys. Lett. B **474**, 416 (2000).
152. A. Khokkaz *et al.*, Eur. Phys. J. A **20**, 345 (2004).
153. E. Czerwiński, P. Moskal, M. Silarski, S. D. Bass *et al.*, Phys. Rev. Lett. **113**, 062004 (2014).
154. H. Petrén *et al.*, Phys. Rev. C **82**, 055206 (2010).
155. M. Abdel-Bary *et al.*, Eur. Phys. J. A **16**, 127 (2003).
156. S. Dymov *et al.*, Phys. Rev. Lett. **102**, 192301 (2009).
157. I. Schätti-Ozerianska, PhD thesis, Jagiellonian University, Krakow (2015); I. Schätti-Ozerianska, P. Moskal, M. Zielinski, arXiv:1607.07261 [nucl-ex].
158. P. Winter *et al.*, Phys. Lett. B **544**, 251 (2002); *Erratum* Phys. Lett. B **553**, 339 (2003).
159. R. Czyżykiewicz *et al.*, Phys. Rev. Lett. **98**, 122003 (2007).
160. P. Moskal *et al.*, Phys. Rev. C **79**, 015208 (2009).
161. S. Dymov, *private communication* (2010).
162. A. Khokkaz and D. Schröer, COSY proposal #211 (2012).
163. D. Schröer, contribution to the 14<sup>th</sup> Int. Workshop Meson Production, Properties and Interaction, Cracow 2016.
164. K. A. Olive *et al.* (Particle Data Group), Chin. Phys. C **38**, 090001 (2014) and 2015 update.
165. F. Hibou *et al.*, Phys. Rev. Lett. **83**, 492 (1999).
166. S. Barsov *et al.*, Eur. Phys. J. A **31**, 95 (2007).
167. F. Balestra *et al.*, Phys. Rev. Lett. **81**, 4572 (1998).
168. F. Balestra *et al.*, Phys. Rev. C **63**, 024004 (2001).
169. S. Abd El-Samad *et al.*, Phys. Lett. B **522**, 16 (2001).
170. M. Abdel-Bary *et al.*, Phys. Lett. B **647**, 351 (2007).
171. M. Abdel-Bary *et al.*, Eur. Phys. J. A **44**, 7 (2010).
172. J. Smyrski *et al.*, Phys. Lett. B **649**, 258 (2007).
173. T. Mersmann *et al.*, Phys. Rev. Lett. **98**, 242301 (2007).
174. M. Abdel-Bary *et al.*, Phys. Lett. B **662**, 14 (2008).
175. S. Barsov *et al.*, Eur. Phys. J. A **21**, 521 (2004).
176. E. Czerwiński, P. Moskal, M. Silarski, Acta Phys. Polon. B **45**, 739 (2014).
177. E. Czerwiński, P. Moskal, D. Grzonka *et al.*, Phys. Rev. Lett. **105**, 122001 (2010).

178. A. Abashian, N. E. Booth, K. M. Crowe, *Phys. Rev. Lett.* **5**, 258 (1960).
179. S. Abd El-Bary *et al.*, *Eur. Phys. J. A* **37**, 267 (2008).
180. J. Pätzold *et al.*, *Phys. Rev. C* **67**, 052202(R) (2003).
181. C. D. Brunt *et al.*, *Phys. Rev.* **187**, 1856 (1969);  
D. R. F. Cochran *et al.*, *Phys. Rev. D* **6**, 3085 (1972);  
F. H. Cverna *et al.*, *Phys. Rev. C* **23**, 1698 (1981);  
F. Shimizu *et al.*, *Nucl. Phys. A* **386**, 571 (1982);  
L. G. Dakhno *et al.*, *Sov. J. Nucl. Phys.* **37**, 540 (1983);  
V. V. Sarantsev *et al.*, *Phys. Atom. Nucl.* **70**, 1885 (2007).
182. L. Alvarez-Ruso, E. Oset, E. Hernández, *Nucl. Phys. A* **633**, 519 (1998).
183. S. Abd El-Samad *et al.*, *Eur. Phys. J. A* **42**, 159 (2009).
184. P. Adlarson *et al.*, *Phys. Lett. B* **706**, 256 (2012).
185. M. Bashkanov *et al.*, *Phys. Rev. Lett.* **102**, 052301 (2009).
186. P. Adlarson *et al.*, *Phys. Rev. Lett.* **106**, 242302 (2011).
187. P. Adlarson *et al.*, *Phys. Lett. B* **721**, 229 (2013).
188. P. Adlarson *et al.*, *Eur. Phys. J. A* **52**, 147 (2016).
189. G. Fäldt, C. Wilkin, *Phys. Lett. B* **701**, 619 (2011).
190. M. Albaladejo, E. Oset, *Phys. Rev. C* **88**, 014006 (2013).
191. P. Adlarson *et al.*, *Phys. Lett. B* **743**, 325 (2015).
192. G. Agakishiev *et al.*, *Phys. Lett. B* **750**, 184 (2015).
193. T. Risser, M. D. Shuster, *Phys. Lett. B* **43**, 68 (1973).
194. S. Keleta *et al.*, *Nucl. Phys. A* **825**, 71 (2009).
195. P. Adlarson *et al.*, *Phys. Rev. C* **86**, 032201(R) (2012).
196. A. Gärdestig, G. Fäldt, C. Wilkin, *Phys. Rev. C* **59**, 2608 (1999).
197. R. Siebert *et al.*, *Nucl. Phys. A* **567**, 819 (1994).
198. J.-M. Laget, *Phys. Lett. B* **259**, 24 (1991).
199. A. Budzanowski *et al.*, *Phys. Lett. B* **687**, 31 (2010).
200. A. Budzanowski *et al.*, *Phys. Rev. D* **84**, 032002 (2011).
201. T. A. Armstrong *et al.*, *Phys. Rev. C* **47**, 1957 (1993).
202. W. Cassing *et al.*, *Eur. Phys. J. A* **16**, 549 (2003), and references contained therein.
203. M. J. Kim *et al.*, *Phys. Lett. B* **641**, 28 (2006).
204. X. Qiu *et al.*, arXiv:1212.1133 (2012), article withdrawn from the archive.
205. O. W. B. Schult *private communication* (2015).
206. V. Koptev *et al.*, *Phys. Rev. Lett.* **87**, 022301 (2001).
207. M. Nikipelov *et al.*, *Phys. Lett. B* **540**, 207 (2002).
208. M. Büscher *et al.*, *Eur. Phys. J. A* **22**, 301 (2004).
209. W. J. Fickinger, E. Pickup, D. K. Robinson, E. O. Salant, *Phys. Rev.* **125**, 2082 (1962).
210. J. T. Balewski *et al.*, *Phys. Lett. B* **420**, 211 (1998).
211. S. Sewerin *et al.*, *Phys. Rev. Lett.* **83**, 682 (1999).
212. P. Kowina *et al.*, *Eur. Phys. J. A* **22**, 293 (2004).
213. Yu. Valdau *et al.*, *Phys. Lett. B* **652**, 245 (2007).
214. Yu. Valdau *et al.*, *Phys. Rev. C* **81**, 045208 (2010).
215. R. Bilger *et al.*, *Phys. Lett. B* **420**, 217 (1998).
216. S. Abd El-Samad *et al.*, *Phys. Lett. B* **632**, 27 (2006).
217. S. Abd El-Samad *et al.*, *Phys. Lett. B* **688**, 142 (2010).
218. S. Abd El-Samad *et al.*, *Eur. Phys. J. A* **46**, 27 (2010).
219. S. Abd El-Samad *et al.*, *Eur. Phys. J. A* **49**, 41 (2013).
220. M. Röder *et al.*, *Eur. Phys. J. A* **49**, 157 (2013).
221. F. Balestra *et al.*, *Phys. Rev. Lett.* **83**, 1534 (1999).
222. F. Hauenstein *et al.*, *Eur. Phys. J. A* **52**, 337 (2016).
223. G. Fäldt, C. Wilkin, *Physica Scripta* **64**, 427 (2001).
224. A. Gasparyan, J. Haidenbauer, C. Hanhart, J. Speth, *Phys. Rev. C* **69**, 034006 (2004).
225. A. Gasparyan, J. Haidenbauer, C. Hanhart, *Phys. Rev. C* **72**, 034006 (2005).
226. F. Hauenstein *et al.*, arXiv:1607.04783 (2016).
227. G. Fäldt, C. Wilkin, arXiv:1611.06716 (2016).
228. A. Gal, E. V. Hungerford, D. J. Millener, *Rev. Mod. Phys.* **88**, 035004 (2016).
229. R. H. Dalitz, *Rev. Mod. Phys.* **33**, 471 (1982).
230. T. H. Tan, *Phys. Rev. Lett.* **23**, 395 (1969).
231. T. Rožek *et al.*, *Phys. Lett. B* **643**, 251 (2006).
232. A. Budzanowski *et al.*, *Phys. Lett. B* **692**, 10 (2010).
233. M. Abdel-Bary *et al.*, *Eur. Phys. J. A* **48**, 37 (2012).
234. M. Abdel-Bary *et al.*, *Eur. Phys. J. A* **48**, 23 (2012).
235. A. Sibirtsev, J. Haidenbauer, H. W. Hammer, U.-G. Meißner, *Eur. Phys. J. A* **32**, 229 (2007).
236. Yu. Valdau, C. Wilkin, *Phys. Lett. B* **696**, 23 (2011).
237. J. A. Oller, U.-G. Meißner, *Phys. Lett. B* **500**, 263 (2001).
238. D. Jido *et al.*, *Nucl. Phys. A* **725**, 181 (2003).
239. U.-G. Meißner, T. Hyodo, Note on “Pole structure of the  $\Lambda(1405)$  region” in the PDG compilation of Ref. [164], <http://pdg.lbl.gov/2015/reviews/rpp2015-rev-lam-1405-pole-struct>.
240. I. Zychor *et al.*, *Phys. Lett. B* **660**, 167 (2008).
241. G. Agakishiev *et al.*, *Phys. Rev. C* **87**, 025201 (2013).
242. I. Zychor *et al.*, *Phys. Rev. Lett.* **96**, 012002 (2006).
243. D. V. Bugg *et al.*, *Phys. Rev.* **168**, 1466 (1968).
244. R. L. Cool *et al.*, *Phys. Rev. D* **1**, 1887 (1970).
245. D. Diakonov, V. Petrov, M. Polyakov, *Z. Phys. A* **359**, 305 (1997).
246. M. Abdel-Bary *et al.*, *Phys. Lett. B* **595**, 127 (2004).
247. M. Abdel-Bary *et al.*, *Phys. Lett. B* **649**, 252 (2007).
248. M. Schulte-Wissermann *et al.*, *Eur. Phys. J. A* **50**, 109 (2014).
249. M. Nikipelov *et al.*, *J. Phys. G* **34**, 627 (2007).
250. R. Aaij *et al.*, *Phys. Rev. Lett.* **115**, 072001 (2015).
251. Yu. Valdau *et al.*, *Phys. Rev. C* **84**, 055207 (2011).
252. A. Dzyuba, V. P. Koptev, Yu. Valdau, COSY proposal #203 (2010).
253. E. Shikov, A. Dzyuba, S. Barsov, V. Koptev, *J. Phys. Conf. Ser.* **461**, 012041 (2013).
254. M. Krapp, PhD thesis, University of Erlangen-Nürnberg (2012).
255. E. Roderburg *et al.*, *in preparation* (2016).
256. M. Wolke, PhD thesis, Westfälische Wilhelms-Universität Münster (1997).
257. C. Quentmeier *et al.*, *Phys. Lett. B* **515**, 276 (2001).
258. P. Winter *et al.*, *Phys. Lett. B* **635**, 23 (2006).
259. M. Silarski, P. Moskal, *Phys. Rev. C* **88**, 025205 (2013).
260. M. Hartmann *et al.*, *Phys. Rev. Lett.* **96**, 242301 (2006).
261. Y. Maeda *et al.*, *Phys. Rev. C* **77**, 015204 (2008).
262. Q. J. Ye *et al.*, *Phys. Rev. C* **85**, 035211 (2012).
263. Q. J. Ye *et al.*, *Phys. Rev. C* **87**, 065203 (2013).
264. A. Sibirtsev, W. Cassing, C. M. Ko, *Z. Phys. A* **358**, 101 (1997).
265. D. Gil, *private communication* (2015); D. Gil, PhD thesis, Jagiellonian University, Krakow (2016).
266. C. Quentmeier, PhD thesis, Westfälische Wilhelms-Universität Münster (2001).
267. V. Bernard, N. Kaiser, U.-G. Meißner, *Eur. Phys. J. A* **4**, 259 (1999).
268. A. Dzyuba *et al.*, *Phys. Lett. B* **668**, 315 (2008).
269. J.-J. Xie, C. Wilkin, *Phys. Rev. C* **82**, 025210 (2010).
270. V. Kleber *et al.*, *Phys. Rev. Lett.* **91**, 172304 (2003).
271. A. Dzyuba *et al.*, *Eur. Phys. J. A* **29**, 245 (2006).
272. A. Dzyuba *et al.*, *Eur. Phys. J. A* **38**, 1 (2008).
273. Y. Maeda *et al.*, *Phys. Rev. C* **79**, 018201 (2009).
274. U.-G. Meißner, U. Raha, A. Rusetsky, *Eur. Phys. J. C* **47**, 473 (2006).
275. Y. Maeda *et al.*, *Phys. Rev. Lett.* **97**, 142301 (2006).

276. S. Okubo, Phys. Lett. **5**, 165 (1963); G. Zweig, CERN report TH-401 (1964); I. Iizuka, Prog. Theor. Phys. Suppl. **37**, 21 (1966).
277. A. Baldini, V. Flaminio, W. G. Moorhead, D. R. O. Morrison, in Landolt-Börnstein, New Series, Group 1, Vol. 12 (Springer-Verlag, Berlin, 1998).
278. A. Polyanskiy *et al.*, Phys. Lett. B **695**, 74 (2011).
279. M. Hartmann *et al.*, Phys. Rev. C **85**, 035206 (2012).
280. E. Ya. Paryev, J. Phys. G **36**, 015103 (2009).
281. Yu. T. Kiselev *et al.*, Phys. Rev. C **92**, 065201 (2015).
282. E. Ya. Paryev, M. Hartmann, Yu. T. Kiselev, J. Phys. G **42**, 075107 (2015).
283. A. Khoukaz, N. Hüskens, *private communication* (2016).
284. M. Betigeri *et al.*, Nucl. Phys. A **690**, 473 (2001).
285. S. Abdel-Samad *et al.*, Phys. Lett. B **553**, 31 (2003).
286. J. M. Cameron *et al.*, Nucl. Phys. A **472**, 718 (1987).
287. J.-F. Germond, C. Wilkin, J. Phys. G **16**, 381 (1990).
288. S. Dymov *et al.*, Phys. Lett. B **762**, 102 (2016).
289. W. R. Falk, Phys. Rev. C **61** (2000) 034005.
290. C. Kerboul *et al.*, Phys. Lett. B **181**, 28 (1986).
291. M. Betigeri *et al.*, Phys. Lett. B **472**, 267 (2000).
292. H.-H. Adam *et al.*, Phys. Rev. C **75**, 014004 (2007).
293. T. Rausmann *et al.*, Phys. Rev. C **80**, 017001 (2009).
294. P. Adlarson *et al.*, Eur. Phys. J. A **50**, 100 (2014).
295. K. Kilian, H. Nann, AIP Conf. Proc. **221**, 185 (1991).
296. G. Fäldt, C. Wilkin, Nucl. Phys. A **587**, 769 (1995).
297. R. Bilger *et al.*, Phys. Rev. C **65**, 044608 (2002).
298. J. Berger *et al.*, Phys. Rev. Lett. **61**, 919 (1988).
299. B. Mayer *et al.*, Phys. Rev. C **53**, 2068 (1996).
300. C. Wilkin, Phys. Rev. C **47**, R938 (1993).
301. Q. Haider, L.C. Liu, Phys. Lett. B **172**, 257 (1986).
302. Q. Haider, L.C. Liu, Phys. Rev. C **66**, 045208 (2002).
303. M. Papenbrock *et al.*, Phys. Lett. B **734**, 333 (2014).
304. C. Wilkin *et al.*, Phys. Lett. B **654**, 92 (2007).
305. F. Pheron *et al.*, Phys. Lett. B **709**, 21 (2012).
306. T. Mersmann *Private communication* (2016).
307. P. Goslawski *et al.*, Phys. Rev. D **85**, 112011 (2012).
308. C. Fritsch *Private communication* (2016).
309. M. Abdel-Bary *et al.*, Phys. Lett. B **619**, 281 (2005).
310. F. Plouin *et al.*, Phys. Lett. B **276**, 526 (1992).
311. C. Amsler *et al.* in J. Beringer *et al.*, Phys. Rev. D **86**, 010001 (2012).
312. G. Fäldt, A. Gärdestig, C. Wilkin, Phys. Lett. B **496**, 185 (2000).
313. F. Bellemann *et al.*, Phys. Rev. C **94**, 034618 (2016).
314. M. Bashkanov *et al.*, Phys. Lett. B **637**, 223 (2006).
315. P. Adlarson *et al.*, Phys. Rev. C **91**, 015201 (2015).
316. M. Mielke *et al.*, Eur. Phys. J. A **50**, 102 (2014).
317. K. Schönning *et al.*, Phys. Lett. B **668**, 258 (2008).
318. R. Wurzinger *et al.*, Phys. Lett. B **374**, 283 (1996).
319. X. Yuan *et al.*, Eur. Phys. J. A **42**, 1 (2009).
320. R. Frascaria *et al.*, Phys. Rev. C **50**, 537(R) (1994).
321. N. Willis *et al.*, Phys. Lett. B **406**, 14 (1997).
322. A. Wrońska *et al.*, Eur. Phys. J. A **26**, 421 (2005).
323. A. Budzanowski *et al.*, Nucl. Phys. A **821**, 193 (2009).
324. P. Adlarson *et al.*, arXiv:1611.01348 [nucl-ex] (2016).
325. S. Wycech, W. Krzemien, Acta Phys. Pol. B **45**, 745 (2014).
326. Q. Haider and L.C. Liu, Int. J. Mod. Phys. E **24**, 1530009 (2015).
327. L. Goldzahl *et al.*, Nucl. Phys. A **533**, 675 (1991).
328. D. Dobrokhotov, G. Fäldt, A. Gärdestig, C. Wilkin, Phys. Rev. Lett. **83**, 5246 (1999).
329. E. J. Stephenson *et al.*, Phys. Rev. Lett. **91**, 142302 (2003).
330. P. Adlarson *et al.*, Phys. Lett. B **739**, 44 (2014).
331. P. Adlarson *et al.*, Phys. Rev. C **88**, 014004 (2013).
332. M. K. Żurek, PhD thesis, Universität zu Köln (2016).
333. ETA collaboration, Nouvelles de Saturne **18**, 37 (2014).
334. M. Wolke and J. Złomanczuk, *Private communication* (2013).
335. C. Adolph *et al.*, Phys. Lett. B **677**, 24 (2009).
336. P. Adlarson *et al.*, Phys. Lett. B **707**, 243 (2012).
337. P. Adlarson *et al.*, Phys. Rev. C **90**, 045207 (2014).
338. F. Ambrosino *et al.*, J. High Energy Phys. **0805**, 006 (2008).
339. P. Adlarson *et al.*, arXiv:1610.02187 (2016).
340. M. Gell-Mann, D. Sharp, W. G. Wagner, Phys. Rev. Lett. **8**, 261 (1962).
341. P. Adlarson *et al.*, Phys. Lett. B **726**, 187 (2013).
342. G. Agakishiev *et al.*, Phys. Lett. B **731**, 265 (2014).
343. J. P. Lees *et al.*, Phys. Rev. Lett. **113**, 201801 (2014).
344. H. Merkel *et al.*, Phys. Rev. Lett. **112**, 221802 (2014).
345. A. Adare *et al.*, Phys. Rev. C **91**, 031901(R) (2015).
346. J. R. Batley *et al.*, Phys. Lett. B **746**, 178 (2015).
347. A. D. Sakharov, JETP Lett. **5**, 24 (1967).
348. P. Lenisa, J. Pretz, H. Ströher, CERN courier (2016); <http://cerncourier.com/cws/article/cern/65816>.
349. J. M. Pendlebury *et al.*, Phys. Rev. D **92**, 092003 (2015).
350. C. A. Baker *et al.*, Nucl. Instrum. Methods Phys. Res. A **736**, 184 (2014).
351. A. Lehrach, F. Rathmann, J. Pretz, COSY proposal #216 (2014), available from <http://collaborations.fz-juelich.de/ikp/jedi>.
352. D. Eversmann *et al.*, Phys. Rev. Lett. **115**, 094801 (2015).
353. P. D. Eversheim, Yu. Valdau, B. Lorentz, Hyperfine Interactions **214**, 127 (2013).
354. F. Perrot *et al.*, Nucl. Phys. B **278**, 881 (1986).
355. M. Beyer, Nucl. Phys. A **493**, 335 (1989).
356. Yu. N. Uzikov, A. A. Temerbayev, Phys. Rev. C **92**, 014002 (2015).
357. B. v. Przewoski *et al.*, Phys. Rev. C **74**, 064003 (2006).